Numerical modeling of two-phase flows with phase change : application to model cracks

Germain Davy

Thèse

présentée pour obtenir le grade de

Docteur de l'université Paris-Est

École doctorale n°531 : Sciences, Ingénierie, Environnement

Spécialité : Mécanique des fluides

par Germain Davy

Modélisation numérique d'écoulements diphasiques avec changement de phase : application au cas de fissures modèles

Numerical modeling of two-phase flows with phase change: application to model cracks

Soutenue le 29 mars 2022, devant le jury composé de

Présidente et rapp.	M^me^ Bérengère Podvin	Directrice de recherche CNRS, EM2C, CentraleSupélec
Rapporteur	M. Yann Bartosiewicz	Professeur, iMMC, UCLouvain
Examinateurs	M. Didier Lasseux	Directeur de recherche CNRS, I2M, Univ. Bordeaux
	M^me^ Marica Pelanti	Maître de conférences, IMSIA, ENSTA Paris
	M. Sébastien Tanguy	Maître de conférences, IMFT, Univ. Toulouse 3
Directeurs de thèse	M. Étienne Reyssat	Chargé de recherche CNRS, PMMH, ESPCI Paris
	M. Stéphane Vincent	Professeur, MSME, Univ. Gustave Eiffel (ex-UPEM)
Encadrant industriel	M. Stéphane Mimouni	Ingénieur-Chercheur expert, EDF R&D

Laboratoire Modélisation et Simulation Multi Echelle

Physique et Mécanique des Milieux Hétérogènes UMR 7636

Cette thèse a été réalisée dans le cadre du contrat CIFRE n°2018/1460 entre :

EDF R&D
Département Mécanique des Fluides, Energies, Environnement (MFEE)
Groupe Modèles et Etudes de Thermo-hydraulique Locale
6 quai Watier
78401 Chatou Cedex

Laboratoire Modélisation et Simulation Multi-Echelle (MSME)
CNRS UMR 8208
Equipe Transfert de Chaleur et de Matière
5 boulevard Descartes
77454 Marne-la-Vallée Cedex 2

Laboratoire Physique et Mécanique des Milieux Hétérogènes (PMMH)
CNRS UMR 7636
7 quai Saint-Bernard
75005 Paris

Les calculs ont été effectués au moyen des ressources informatiques d'EDF R&D.

Typeset using LaTeX

Remerciements

Ce document est le fruit de trois ans de thèse qui auront été pour moi très enrichissants, bien que très loin d'être de tout repos. Ces trois ans de thèse n'auraient pas pu être menés à leur terme sans l'aide de différentes personnes que je me dois de remercier.

Je tiens à remercier, en premier lieu, mon encadrant EDF, Stéphane Mimouni. Stéphane, ta confiance et ta disponibilité tout au long de la thèse m'ont été d'une grande utilité. J'ai beaucoup apprécié ton enthousiasme et ta capacité à rebondir dans les moments de doute. J'ai le sentiment d'avoir appris et progressé à tes côtés, aussi bien sur le plan scientifique que humain.

Je souhaite aussi chaleureusement remercier mes deux directeurs de thèse, Stéphane Vincent et Etienne Reyssat. Stéphane, merci pour ta pédagogie, ta patience et tes encouragements, lorsque les résultats étaient au rendez-vous comme lorsqu'ils ne l'étaient pas. Je te souhaite plein de succès pour la suite, sur le plan académique mais aussi entrepreneurial, vis-à-vis de la startup que tu as créée. Etienne, merci pour ta rigueur, ta patience et ta curiosité. Merci aussi pour ton joli discours lors de ma soutenance de thèse et pour les livres que tu m'as offerts. J'espère que cette immersion dans l'univers de la simulation numérique t'a plu et te sera utile pour la suite.

Je remercie vivement les personnes qui ont accepté de faire partie de mon jury de thèse : Yann Bartosiewicz et Bérengère Podvin, en qualité de rapporteur, ainsi que Didier Lasseux, Marica Pelanti et Sébastien Tanguy, en qualité d'examinateur. Merci à tous pour l'intérêt porté à mes travaux, pour votre temps, vos questions et vos remarques.

Je remercie les membres du projet EDF CIWAP3, dans lequel ma thèse s'est inscrite, avec qui j'ai été amené à collaborer : Jean-Luc Adia, Marina Bottoni et Sylvie Michel-Ponnelle. J'ajoute à cette liste Laurent Charpin, anciennement chef de ce projet devenu mon chef de groupe, qui a fait preuve de beaucoup de bienveillance à mon égard.

Côté EDF, mes remerciements vont également aux ingénieurs du groupe I8B et des équipes développement code_saturne et neptune_cfd. Je pense notamment à Chaï, Jérôme L., Nicolas M. et Yvan, qui m'ont aidé à plusieurs reprises, chacun à leur façon, sur le plan

technique, ainsi qu'à Didier, Dorothée, Hugo, Jean-Philippe, Joël, Jorge, Namane, Richard, Thomas F., Thomas N. et William, avec qui j'ai pris plaisir à échanger sur des sujets divers et variés en pause café, à la cantine ou au détour d'un couloir.

Je souhaite aussi remercier les personnes qui m'ont aidé d'un point de vue pratique pour la préparation de ma soutenance de thèse : Anne, Christophe et Sébastien.

Je remercie sincèrement l'ensemble des doctorants que j'ai côtoyés à EDF : Cécile, Clément C., Federico, Gaëtan, Hector, Jacques, Léa, Li, Luc, Lucie, Manon, Riccardo et Vladimir, ainsi qu'à MSME : Désir-André, Georges, Mathilde et Mohamed. J'ai une pensée particulière pour mes compagnons du "coin doctorants" du 1^{er} étage, à savoir Clément C., Gaëtan et Riccardo, avec qui j'ai passé de très bons moments. J'adresse une mention spéciale à Riccardo pour son aide et ses précieux "tips" en C, Git, LaTeX et Vim. Je n'oublie pas les stagiaires que j'ai eu l'occasion de rencontrer à EDF : Mocia, Quentin, Timothé, Alexandre, Anas, Aurélien, Romuald, Cédric, Clément L. et Colin. Au plaisir de vous revoir autour d'un verre !

Pour terminer, je remercie profondément ma famille, qui m'a toujours soutenu dans tout ce que j'ai entrepris, et mes amis, qui ont constitué une véritable source d'énergie pendant ces trois ans. Aussi, je remercie profondément celle qui partage ma vie depuis maintenant bien des années, pour sa présence, son écoute, ses conseils, son humour et sa joie de vivre, sans qui mes longues journées de télétravail n'auraient pas eu la même saveur. Tous ces êtres qui me sont chers ont, bien que sans beaucoup de connaissances en mécanique des fluides, eux aussi contribué à la réussite de cette thèse, et je leur suis infiniment reconnaissant.

Abstract – Résumé

Abstract

The understanding and modeling of two-phase flows in confined geometries like mini-channels and cracks is a major issue for many industries, including the nuclear industry. Indeed, in a nuclear power plant, in the event of a loss-of-coolant accident, steam and fission products would be released in the containment building. In the case of a double wall concrete containment building (without steel liner), the increase in pressure and temperature could lead to the opening of preexisting cracks and to the creation of new cracks (opening about 100 µm) in the inner wall, through which gas and fission products could escape. Two phenomena could have an impact on the gas leakage rate. The first is steam condensation on the inner wall and inside the cracks, which could result in their clogging by drops, films and/or slugs. The second is concrete thermal deformation, which could result in variations in the crack opening.

The present work focuses on steam condensation in model cracks of fixed geometry. Experiments have shown that, in confined geometries like mini-channels and cracks, depending on the opening and on the boundary conditions, condensation could lead to the formation of droplets of variable size, films and slugs (also called capillary bridges). A new model for flows with small droplets, small bubbles and large deformable interfaces is first proposed and implemented in the neptune_cfd code, developed by EDF R&D. This model combines a sub-grid approach for the droplets and bubbles, and an interface capturing approach for the large deformable interfaces, and therefore allows for cell sizes larger than the smallest flow structures. It is declined in two distinct versions, one using two computational fields and another using four computational fields.

Both versions of the model developed are then validated in different cases, involving droplets, bubbles and/or large interfaces. Among the cases studied is a case of steam condensation in the presence of air in an idealized rectilinear mini-channel with smooth walls. The model is found to correctly predict two-phase dynamics and heat transfer with phase change. It is also found to consistently capture the various flow regimes resulting

from condensation.

The two-field version of the model developed is then used to investigate the effect of roughness and tortuosity on laminar two-phase heat transfer with phase change in confined geometries. Such geometrical features are found to locally modify the various heat fluxes taking place at the wall, namely the condensation flux and the single-phase gas and liquid fluxes. The ratio of spatially-averaged condensation flux in the case of rough walls to spatially-average condensation flux in the case of smooth walls is found to increase with roughness element height and Reynolds number and to decrease with roughness element spacing. A similar behavior is obtained for the same ratio in the case of the gas heat flux, while the opposite is obtained for the same ratio in the case of the liquid heat flux. Correlations are derived for the various ratios.

Finally, a one-dimensional model is proposed as a practical alternative to the two- and four-field versions of the three-dimensional model initially developed, which remains computationally expensive and could hardly be used for industrial calculations. The one-dimensional model proposed builds up on the correlations developed in three dimensions for the impact of roughness on dynamics and heat transfer with phase change in the laminar flow regime. It is validated against the two-field version of the three-dimensional model in various geometrical configurations.

Keywords: condensation, crack, mini-channel, computational fluid dynamics, multi-regime, dispersed droplets, resolved interfaces, surface tension, roughness, tortuosity, upscaling

Résumé

La compréhension et la modélisation des écoulements diphasiques en milieu confiné (micro-canaux, mini-canaux ou fissures) est un problème majeur pour de nombreuses industries, dont l'industrie nucléaire. En effet, dans une centrale nucléaire, lors d'un accident par perte de réfrigérant primaire, de la vapeur d'eau et des produits de fission sont libérés dans l'enceinte de confinement. Dans le cas d'une enceinte à double paroi (sans liner métallique), l'augmentation de la température et de la pression peut conduire à l'ouverture de fissures pré-existantes et la formations de nouvelles fissures (ouverture d'environ 100 µm) dans la paroi interne, à travers lesquelles sont susceptibles de s'échapper des produits de fission. Deux phénomènes peuvent avoir un impact sur le débit de fuite de gaz. Le premier est la condensation de vapeur sur la paroi interne et dans les fissures, à l'origine du colmatage partiel ou total de ces dernières par le liquide. Le second est la dilatation thermique du béton, à l'origine d'une éventuelle modification de l'ouverture de fissure.

La présente thèse s'intéresse au phénomène de condensation de vapeur dans des fissures

modèles de géométrie fixée. L'expérience a montré que, en milieu confiné, selon l'ouverture et les conditions aux limites, la condensation pouvait conduire à la formation de gouttes, de films et/ou de slugs (bouchons liquides). Un nouveau modèle pour les écoulements à petites gouttes, petites bulles et grandes interfaces déformables est d'abord proposé et implémenté dans le code neptune_cfd, developpé par EDF R&D. Ce modèle combine une approche sous-maille pour les gouttes et les bulles, et une approche interface résolue pour les grandes interfaces déformables. Il présente l'avantage de permettre une taille de cellules supérieure à celle des plus petites structures de l'écoulement. Il est décliné en deux versions, l'une utilisant deux champs informatiques et l'autre utilisant quatre champs informatiques.

Les deux versions du modèle développé sont ensuite validées dans différents cas, impliquant gouttes, bulles et/ou grandes interfaces. Parmi les cas étudiés figure un cas de condensation de vapeur en présence d'air dans un mini-canal rectiligne aux parois lisses. Le modèle prédit correctement la dynamique et le transfert de chaleur avec changement de phase. En outre, il capture correctement les différents régimes d'écoulement résultant de la condensation.

La version deux champs du modèle développé est ensuite utilisée pour étudier l'effet de la rugosité et de la tortuosité sur le transfert de chaleur avec changement de phase en milieu confiné et en régime laminaire. Les géométries de paroi considérées modifient localement les différents flux de chaleur en paroi, à savoir le flux de condensation et les flux monophasiques gaz et liquide. Le ratio du flux de condensation moyenné spatialement dans le cas d'une paroi rugueuse sur le flux de condensation moyenné spatialement dans le cas d'une paroi lisse se révèle augmenter avec la hauteur des éléments de rugosité et le nombre de Reynolds et diminuer avec l'espacement des élements de rugosité. Un comportement similaire est obtenu pour ce même ratio dans le cas du flux monophasique gaz, alors que l'inverse est obtenu pour ce même ratio dans le cas du flux monophasique liquide. Des corrélations sont obtenues pour les différents ratios.

Enfin, un modèle unidimensionnel est proposé comme alternative aux versions deux et quatre champs du modèle trois dimensions développé initialement. En effet, ce dernier reste coûteux numériquement et serait donc difficilement utilisable pour des calculs en conditions industrielles. Le modèle une dimension proposé s'appuie sur les corrélations développées en trois dimensions pour inclure l'effet de la rugosité sur le transfert de chaleur avec changement de phase en régime laminaire. Il est validé par comparaison à la version deux champs du modèle trois dimensions dans différentes configurations géométriques.

Mots clés : condensation, fissure, mini-canal, mécanique des fluides numérique, multi-régime, gouttes dispersées, interfaces résolues, tension de surface, rugosité, tortuosité, remontée d'échelle

Contents

Nomenclature **15**

1 Introduction **19**

1.1 Contexte industriel 20

1.1.1 Le nucléaire en France 20

1.1.2 Les réacteurs à eau pressurisée 20

1.1.3 Problématique : l'étanchéité de l'enceinte 21

1.1.4 Le projet CIWAP3 24

1.2 Contexte scientifique 24

1.2.1 Etat des recherches d'EDF sur la fuite par les fissures 24

1.2.2 Stratégie de modélisation développée dans la thèse 27

1.3 Organisation du manuscrit 28

1.4 Valorisation des travaux 30

1.4.1 Publications 30

1.4.2 Conférences 31

2 Modeling approach **33**

2.1 General equations for two-phase flows 34

2.1.1 Single-phase flow equations 34

2.1.2 Jump conditions at the interface 34

2.1.3 Phase indicator function 35

2.1.4 Two-fluid approach 36

2.1.5 Single-fluid approach 38

2.2 Numerical simulation of two-phase flows 40

2.2.1 Resolved interfaces 40

2.2.2 Dispersed flows . . . 44
2.2.3 Multi-regime flows . . . 44
2.3 The neptune_cfd code . . . 45
2.3.1 Equations solved . . . 45
2.3.2 Standard Dispersed Model . . . 47
2.3.3 Large Interface Model and Large Bubble Model . . . 50
2.3.4 GLIM and LBM with bubbles . . . 52
2.4 Summary . . . 57

3 Validation of the proposed two- and four-field models 59
3.1 Introduction . . . 60
3.2 BHAGA validation case . . . 61
3.2.1 Problem setup . . . 61
3.2.2 Results . . . 61
3.3 STEFAN WITH NCG validation case . . . 64
3.3.1 Problem setup . . . 64
3.3.2 Results . . . 65
3.4 COPAIN validation case . . . 67
3.4.1 Problem setup . . . 67
3.4.2 Results . . . 69
3.5 BARTOLOMEI validation case . . . 70
3.5.1 Problem setup . . . 70
3.5.2 Results . . . 74
3.6 Summary . . . 75

4 Steam condensation in the presence of air in a smooth rectilinear model crack 79
4.1 Introduction . . . 80
4.2 Acticle published in *Int. J. Multiph. Flow* . . . 80
4.3 Complementary simulations . . . 110
4.3.1 Boundary conditions . . . 110
4.3.2 Results . . . 111
4.4 Summary . . . 112

5 Impact of roughness and tortuosity on small-scale two-phase heat transfer with phase change **115**

5.1 Impact of roughness on heat transfer with phase change 116

5.1.1 Introduction 116

5.1.2 Problem setup 118

5.1.3 Results 127

5.2 Impact of tortuosity on heat transfer with phase change 137

5.2.1 Introduction 137

5.2.2 Problem setup 139

5.2.3 Results 143

5.3 Summary 144

6 Development of a one-dimensional model based on the correlations derived in three dimensions **151**

6.1 Introduction 152

6.2 Model description 153

6.2.1 Preamble 153

6.2.2 Equations solved 153

6.2.3 Source and transfer terms 154

6.2.4 Note on the 1DM 158

6.3 Problem setup 159

6.3.1 Computational domain and boundary conditions 159

6.3.2 Averaging procedure for the 2D calculations used for comparison . . 159

6.3.3 Single-phase flow basic verifications 161

6.4 Results 162

6.4.1 High pressure 162

6.4.2 Low pressure 165

6.5 Summary 168

7 Conclusions and perspectives **171**

7.1 Conclusions 172

7.2 Perspectives 174

Bibliography **177**

A Stefan with NCG **193**

A.1 Prerequisites 193

A.2 Assumptions 194

A.3 Analytical solution 194

Nomenclature

Acronyms

1DM	1-Dimensional Model	
4FM	4-Field Model	
CFD	Computational Fluid Dynamics	
CIWAP3	Civil Work Assessment Project 3	
FGLIM	Full Generalized Large Interface Model	
GLIM	Generalized Large Interface Model	
LBM	Large Bubble Model	
SDM	Standard Dispersed Model	

Greek letters

α	Volume fraction	–
Δt	Time step	s
Δx, Δy, Δz	Grid spacing in x-, y-, z-direction	m
Δ	Distance from wall to center of boundary cell	m
Γ	Interfacial mass transfer	$\mathrm{kg\,m^{-3}\,s^{-1}}$
λ	Thermal conductivity	$\mathrm{W\,m^{-1}\,K^{-1}}$
μ	Molecular viscosity	$\mathrm{kg\,m^{-1}\,s^{-1}}$
ϕ^2	Two-phase multiplier	–
Π	Interfacial energy transfer	$\mathrm{W\,m^{-3}}$
ρ	Density	$\mathrm{kg\,m^{-3}}$
Σ	Stress tensor	$\mathrm{kg\,m^{-1}\,s^{-2}}$
σ	Surface tension	$\mathrm{kg\,s^{-2}}$
τ	Characteristic time for bubbles	s

θ	Drag relaxation coefficient	–
ε	Interface sharpening coefficient	m
φ	Wall energy transfer	$\mathrm{W\,m^{-2}}$

Roman letters

a^{int}	Interfacial area concentration	$\mathrm{m^{-1}}$
A_l	Fraction of area affected by the liquid	–
C	Force coefficient	–
c	Rescaling factor for h_{loc}	–
Cp	Specific heat capacity	$\mathrm{J\,kg^{-1}\,K^{-1}}$
D	Diffusion coefficient	$\mathrm{m^2\,s^{-1}}$
d	Diameter	m
D_h	Hydraulic diameter	m
F	Force density	$\mathrm{kg\,m^{-2}\,s^{-2}}$
f	Friction factor	–
f^θ	Function for drag computation	$\mathrm{kg\,m^{-3}\,s^{-1}}$
G	Mass flow rate per unit area	$\mathrm{kg\,m^{-2}\,s^{-1}}$
g	Gravity	$\mathrm{m\,s^{-2}}$
H	Total enthalpy	$\mathrm{J\,kg^{-1}}$
h	Heat transfer coefficient	$\mathrm{W\,m^{-2}\,K^{-1}}$
I	Interfacial momentum transfer	$\mathrm{kg\,m^{-2}\,s^{-2}}$
Ja^*	Modified Jakob number	–
n	Interface normal	–
n_{site}	Number of droplets per unit area	$\mathrm{m^{-2}}$
Nu	Nusselt number	–
P	Pressure	Pa
Pr	Prandtl number	–
Q	Heat flux density	$\mathrm{W\,m^{-2}}$
Re	Reynolds number	–
Sc	Schmidt number	–

Sh	Sherwood number	–
T	Temperature	K
U	Velocity	$\mathrm{m\,s^{-1}}$
X	Martinelli parameter	–
x, y, z	Cartesian coordinates	m
x_g	Flow quality	–
Y	Mass fraction	–
y^*	Dimensionless y-coordinate	–
MRE	Mean relative error	–

Subscripts and superscripts

a	Air	–
AM	Added mass	–
b	Bulk	–
c	Continuous	–
$cond$	Condensation	–
D	Drag	–
d	Dispersed	–
exp	Experimental	–
g	Gas	–
in	Inlet	–
int	Interfacial	–
L	Lift	–
l	Liquid	–
lat	Latent	–
loc	Local	–
num	Numerical	–
out	Outlet	–
pg	Gas particle	–
pl	Liquid particle	–

q	Quenching	–
Re	Reynolds	–
s	Steam	–
sat	Saturation	–
sp	Single-phase	–
ST	Surface tension	–
TD	Turbulent dispersion	–
tp	Two-phase	–
w, W	Wall	–
x, y, z	x-, y-, z-component	–

Chapter 1

Introduction

Contents

1.1 Contexte industriel 20
1.1.1 Le nucléaire en France 20
1.1.2 Les réacteurs à eau pressurisée 20
1.1.3 Problématique : l'étanchéité de l'enceinte 21
1.1.4 Le projet CIWAP3 24
1.2 Contexte scientifique 24
1.2.1 Etat des recherches d'EDF sur la fuite par les fissures 24
1.2.2 Stratégie de modélisation développée dans la thèse 27
1.3 Organisation du manuscrit 28
1.4 Valorisation des travaux 30
1.4.1 Publications 30
1.4.2 Conférences 31

1.1 Contexte industriel

1.1.1 Le nucléaire en France

En France, la majorité de la production d'électricité (67 % en 2020) est d'origine nucléaire (IRSN, 2021a; EDF, 2021a). En 2021, on dénombre un total de 56 réacteurs en activité et 1 réacteur en construction, répartis sur 18 sites, exploités par EDF. Ces réacteurs sont tous des réacteurs à eau pressurisée (REP). Leurs caractéristiques, à savoir le palier auquel ils appartiennent, la puissance qu'ils développent et la période pendant laquelle ils sont été construits, sont données dans la Table 1.1. Les premiers REP, construits entre 1971 et 1987, appartiennent aux paliers CP0 et CPY. Ils sont au nombre de 32 et fournissent chacun une puissance de 900 MWe. Les REP suivants, construits entre 1977 et 1993, correspondent aux paliers P4 et P'4. Ils sont au nombre de 20 et développent chacun une puissance de 1300 MWe. Les derniers REP en service ont été construits entre 1984 et 1999. Ils appartiennent au palier N4. Ils sont au nombre de 4 et fournissent chacun une puissance de 1450 MWe. Le réacteur en construction correspond à une nouvelle génération de REP, appelée EPR (European Pressurized Reactor). Une fois sa construction achevée, il développera une puissance de 1650 MWe. Le fonctionnement d'un REP est expliqué dans la section suivante.

Table 1.1: Caractéristiques des réacteurs nucléaires en activité ou en construction en 2021 en France (IRSN, 2021a; EDF, 2021a).

Palier (modèle)	Puissance [MWe]	Nombre	Construction
CP0 et CPY	900	32	1971-1987
P4 et P'4	1300	20	1977-1993
N4	1450	4	1984-1999
EPR	1650	1	2007-

1.1.2 Les réacteurs à eau pressurisée

Un schéma de principe de réacteur à eau pressurisée (REP) est fourni en Fig. 1.1. Le fonctionnement du réacteur est assuré par trois circuits d'eau distincts, échangeant de la chaleur mais pas de masse (IRSN, 2021b; EDF, 2021b). Parmi ces trois circuits, seul le circuit tertiaire est ouvert sur l'extérieur. L'eau du circuit primaire permet de récupérer la chaleur produite dans le cœur du réacteur, composé d'assemblages de crayons combustibles. Afin d'éviter qu'elle ne se vaporise, la pression est maintenue à une valeur supérieure à la pression de saturation. Ce circuit est intégralement contenu dans une enceinte de confinement, dont le rôle est détaillé dans la section suivante. La chaleur transportée par l'eau du

circuit primaire est transmise à l'eau du circuit secondaire dans un échangeur de chaleur, appelé générateur de vapeur. L'eau y entre à l'état liquide et en ressort à l'état vapeur. La vapeur produite met en mouvement une turbine, reliée à un alternateur, qui assure la conversion de l'énergie mécanique en énergie électrique. Un condenseur permet le retour du fluide à l'état liquide. Il constitue l'interface avec le circuit tertiaire : la vapeur cède sa chaleur à l'eau du cicuit tertiaire, qui circule dans des faisceaux de tubes. Cette dernière est finalement acheminée vers les tours aéroréfrigérantes, où elle est refroidie au contact direct d'un flux d'air ascendant. Une petite partie quitte les tours sous forme de vapeur. Le reste est recueilli dans un bassin et réinjecté dans le circuit. Les pertes sont compensées par prélèvement dans le fleuve ou la mer.

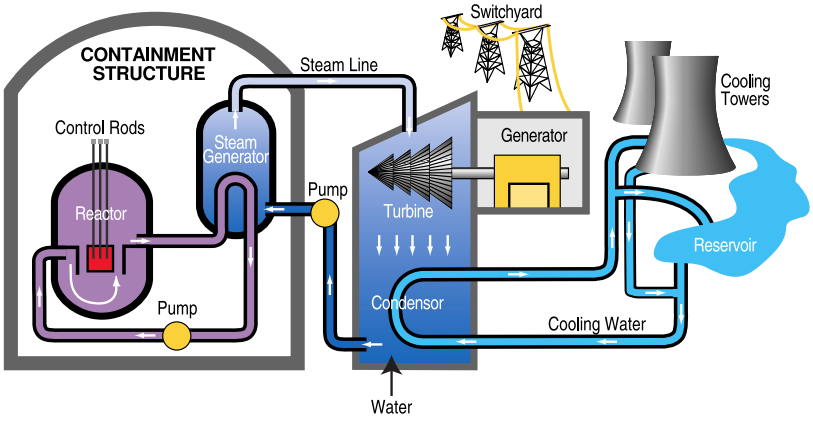

Figure 1.1: Principe de fonctionnement d'un réacteur à eau pressurisée (REP) (Wikipedia, 2021). Les circuits primaire, secondaire et tertiaire sont représentés en violet, bleu foncé et bleu clair, respectivement. Ces trois circuits échangent uniquement de la chaleur. Seul le circuit tertiaire est ouvert sur l'extérieur.

1.1.3 Problématique : l'étanchéité de l'enceinte

L'enceinte de confinement a pour objectifs de protéger le réacteur des agressions extérieures et d'empêcher la propagation d'éventuels produits de fission en cas d'accident. Il s'agit de la troisième barrière de confinement, après la gaine des crayons combustibles et le circuit primaire. En France, il existe deux types d'enceinte, représentés en Fig. 1.2 : (i) les enceintes à simple paroi, constituées d'une unique paroi en béton armé précontraint recouverte intérieurement d'une peau métallique (liner) en acier et (ii) les enceintes à double paroi, constituées d'une enceinte interne en béton armé précontraint, d'une enceinte externe en béton armé (non précontraint) et d'un espace entre enceintes permettant de collecter et filtrer les éventuelles fuites (Costaz, 1997). Dans le cas des enceintes à double paroi, qui sont l'objet d'étude de la présente thèse, deux types de fuite caractérisent la paroi de l'enceinte interne, comme schématisé en Fig. 1.3 : (i) les fuites diffuses, à travers les pores (ouverture

comprise entre 0.01 et 1 µm) et (ii) les fuites locales, à travers les fissures (ouverture de l'ordre de 100 µm) et autres défauts macroscopiques (Courtois, 2005).

Les centrales du parc français sont entièrement contrôlées tous les dix ans (IRSN, 2021c). Lors de ces visites décennales, deux épreuves majeures, déterminantes pour le redémarrage, sont réalisées : une épreuve hydraulique, qui consiste à contrôler l'intégrité de la cuve du réacteur et le circuit primaire et une épreuve enceinte, qui consiste à contrôler la résistance et l'étanchéité de l'enceinte de confinement. Lors de l'épreuve enceinte, celle-ci est soumise à sa pression de dimensionnement. Sa déformation et son taux de fuite sont mesurés et comparés aux valeurs limites. Une inspection de la surface externe de l'enceinte interne est réalisée, afin de localiser les principales zones de fuite.

Le taux de fuite limite de l'enceinte interne est fixé par le décret d'autorisation de création de la centrale (République française, 2021). Les décrets des centrales en activité indiquent une valeur de 1.5 % par jour de la masse de gaz contenue dans l'enceinte en situation d'accident de type APRP (Accident par Perte de Réfrigérant Primaire, caractérisé par l'ouverture d'une brèche dans le circuit primaire, conduisant à la libération d'eau passant instantanément à l'état vapeur, et à une augmentation de la pression et de la température). Cependant, comme les conditions de ce type d'accident ne sont pas reproductibles, lors des visites décennales, l'épreuve enceinte est réalisée en air sec et à température ambiante. Le critère précédent est transposé de la situation d'accident (air-vapeur, température élevée) à la situation d'épreuve (air sec, température ambiante). Le cœfficient de transposition, défini comme le rapport du taux de fuite en situation d'épreuve sur le taux de fuite en situation d'accident, est pris égal à 1.

L'objectif poursuivi par EDF est d'évaluer les marges existantes sur la valeur du coefficient de transposition et ainsi d'améliorer la prédiction des conséquences radiologiques d'un APRP. Les phénomènes physiques supposés avoir un impact sur le taux de fuite en situation d'accident sont la condensation de vapeur sur les parois, dans les fissures et dans les pores, qui pourrait conduire à la formation de bouchons liquides, ainsi que la dilatation thermique du béton, qui pourrait conduire à la refermeture de fissures. La présente thèse s'intéresse uniquement à la condensation et aux écoulements diphasiques dans les fissures. Elle a pour objectif le développement et la validation d'une nouvelle méthode pour la simulation de ce type d'écoulement, ainsi que sa mise en œuvre pour étudier la condensation en fissure. De plus amples informations concernant la stratégie et les objectifs de la thèse sont fournies dans la Section 1.2.

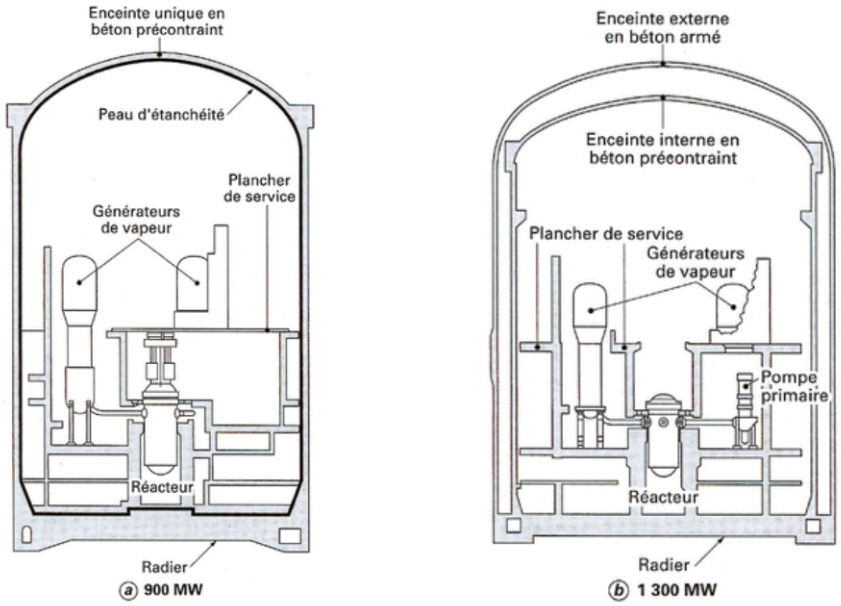

Figure 1.2: Enceintes de confinement à simple paroi (gauche) et à double paroi (droite) (Costaz, 1997). Les enceintes à simple paroi équipent les réacteurs 900 MWe, celles à double paroi les réacteurs 1300 et 1450 MWe.

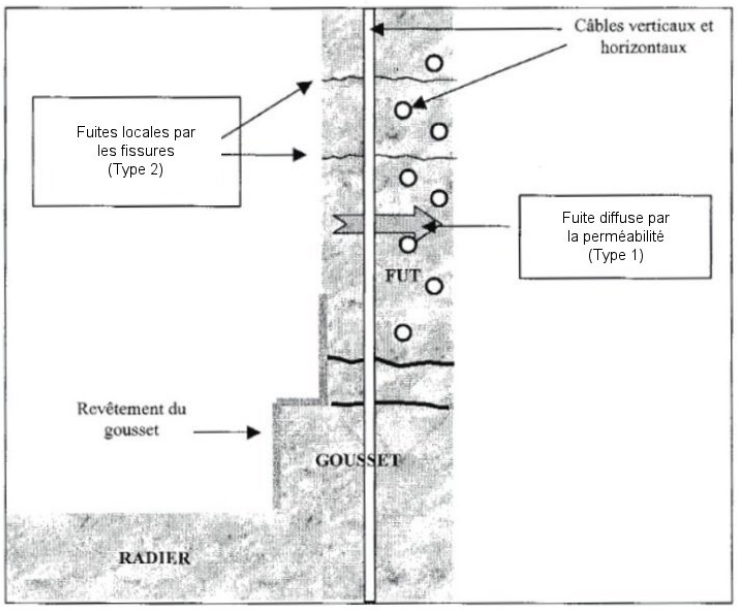

Figure 1.3: Fuites à travers l'enceinte interne d'une enceinte à double paroi (Courtois, 2005). Il en existe deux grands types : les fuites diffuses, à travers les pores du béton, et les fuites locales, à travers les fissures autres défauts macroscopiques.

1.1.4 Le projet CIWAP3

La thèse est intégrée au projet CIWAP3 (Civil Work Assessment Project 3), piloté par le département Matériaux et Mécanique des Composants d'EDF R&D (Charpin et al., 2020). Il s'inscrit dans la finalité "Durée de fonctionnement" des Programmes, qui regroupe l'ensemble des travaux de recherche menés dans le cadre de la prolongation de la durée de vie des centrales (passage de 40 à 60 ans). Il a pour objectifs principaux de (i) développer un outil numérique permettant de prédire la fuite d'une enceinte donnée en situation d'épreuve en prenant en compte son état de vieillissement, (ii) comprendre plus en détail les phénomènes physiques se produisant lors d'un accident (condensation et dilatation thermique) et (iii) évaluer l'efficacité de solutions innovantes pour la maintenance. Afin d'aider à atteindre ces objectifs, une maquette expérimentale inédite a été construite sur le site d'EDF Lab Les Renardières. Il s'agit de la maquette VeRCoRs (Vérification Réaliste du Confinement des Réacteurs) : une reproduction à l'échelle 1/3 des enceintes double paroi qui équipent les réacteurs 1300 MWe. En outre, plusieurs thèses ont été lancées, dont la présente thèse, qui doit permettre d'apporter des éléments de réponse à la problématique de la fuite en situation accidentelle.

1.2 Contexte scientifique

1.2.1 Etat des recherches d'EDF sur la fuite par les fissures

1.2.1.1 Etudes expérimentales

Plusieurs expériences concernant la fuite à travers les fissures ont été réalisées par EDF et ses partenaires dans le cadre de projets antérieurs à celui dans lequel s'inscrit la thèse (CIWAP3, voir Section 1.1.4). Deux types d'essais peuvent être distingués : les essais à petite échelle et les essais semi-intégraux, à une échelle plus proche de celle de la structure.

Parmi les essais à petite échelle, il y a eu les essais SIMIBE (SImulation de la MIgration air-vapeur dans une fissure en BEton) (Caroli et al., 1995). Ils portaient sur une fissure modélisée par deux plaques planes parallèles aux propriétés thermiques proches du béton, de longueur 50 cm et de largeur 12 cm, distantes de 50 à 370 µm. Un mélange d'air et de vapeur y était injecté pendant une durée de 2 ou 3 h (température comprise entre 20 et 130 °C, pression comprise entre 1.7 et 4 bar et fraction massique de vapeur comprise entre 0 et 0.85). Les débits d'air, de vapeur et d'eau étaient mesurés en sortie. La température de la paroi était mesurée tout le long du canal, afin de suivre le processus de condensation. Les résultats obtenus en air-vapeur ont montré (i) pour les petites ouvertures, que toute la vapeur se condensait et que le débit de fuite total était environ égal au débit de fuite en

air froid et (ii) pour les grandes ouvertures, que toute la vapeur ne se condensait pas et que le débit de fuite total était inférieur au débit de fuite en air froid. En outre, pour les petites ouvertures, ces essais ont mis en évidence la formation de gouttes déformables de taille caractéristique plusieurs millimètres, semblant s'accrocher aux parois et se déplaçant plus lentement que le gaz.

Parmis les essais à grande échelle, il y a les essais MAEVA (MAquette Echange Vapeur-Air) (Granger et al., 2001). Ils portaient sur une maquette d'enceinte constituée d'une paroi interne en béton précontraint et d'une paroi externe en métal. La hauteur de l'installation, le diamètre et l'épaisseur de l'enceinte interne étaient de 5 m, 16 m et 1.2 m, respectivement. La paroi interne était divisée en quandrants dont deux étaient revêtus d'une peau d'étanchéité. Au total, cinq campagnes d'essais ont eu lieu, chaque campagne regroupant au moins un essai en air sec et un essai en air-vapeur. Deux des essais en air-vapeur étaient basé sur un scénario de type APRP. Le dispositif de mesure du taux de fuite était composé essentiellement de capteurs de pression, température et humidité, installés à l'intérieur de l'enceinte interne et dans l'espace entre enceintes. Les résultats obtenus sur les deux quadrants sans peau d'étanchéité ont montré un cœfficient de transposition significativement supérieur à 1 pour les quatres premières campagnes et légèrement inférieur à 1 pour la cinquième campagne. Ces écarts s'expliquent par le fait que différents scénarios d'accident ont été envisagés.

Parmis les essais à grande échelle, il y a également les essais des dalles de Karlsruhe (Stegemann et al., 2005). Ils portaient sur une dalle parallélépipédique en béton armé, de longueur 2.7 m, de largeur 1.8 m et d'épaisseur 1.2 m. La dalle était fissurée par traction dans la direction de la longueur, à l'aide d'un système de vérins hydrauliques. L'ouverture était contrôlée en ajustant la force de traction. La face supérieure (2.7 m $\times$ 1.8 m) de la dalle était soumise à un chargement en pression et en température (air sec ou air-vapeur). Les débits de gaz et d'eau liquide, la température et l'humidité du gaz étaient mesurés aux niveau de la face opposée. Les résultats ont montré que le débit total en air-vapeur était très inférieur au débit en air sec.

Enfin, il y a les essais PACE-1450 (maquette de PArtie Courante d'Enceinte 1450 MWe) (Herrmann et al., 2016). Egalement réalisés par l'université de Karlsruhe, ces essais se rapprochent des essais précédents. Ils portaient sur une dalle incurvée en béton précontraint, de dimensions environ 2 m $\times$ 2 m $\times$ 1.2 m, représentative d'une portion de paroi interne de réacteur 1450 MWe. La précontrainte était diminuée d'essai en essai afin de simuler le vieillissement de l'enceinte. Au total, douze essais ont été réalisés, dont deux en air-vapeur. Etaient mesurés le débit de fuite et la déformation. Concernant la fuite en air-vapeur, dans un cas le débit total était environ égal au débit en air sec. Dans l'autre cas, le débit total était inférieur au débit en air sec.

Les différentes expériences réalisées ont apporté des informations intéressantes. Elles ont notamment mis en évidence l'effet de l'ouverture de fissure et du scénario d'accident envisagé sur le débit de fuite. Cependant, toutes ne permettent pas de conclure sur le cœfficient de transposition. C'est le cas de l'expérience SIMIBE. Les hypothèses faites dans cette expérience, en particulier celle consistant à négliger la tortuosité, font que les résultats ne sont pas directement applicables aux fissures qui caractérisent les enceintes. De nouvelles expériences sont prévues : à petite échelle (MACENA) et l'échelle intégrale (VeRCoRs, voir Section 1.1.4). L'accent est également mis sur la simulation numérique, qui fait l'objet de la section suivante.

1.2.1.2 Simulation numérique

Les calculs réalisés par EDF par le passé ont été effectués au moyen d'un couplage entre le code Ecrevisse (Ecoulement CRitique Eau-Vapeur dans les fISSurEs) pour la partie fluide et Code_Aster (Analyses des Structures et Thermo-mécanique pour des Etudes et des Recherches) pour la partie solide. Ces deux codes sont développés par EDF R&D (EDF, 2021c; Hervouet, 2004, 2012). Le premier est un code de thermo-hydraulique 1D basé sur une discrétisation de type différences finies. Il repose sur les hypothèses suivantes : écoulement stationnaire, fluide homogène dans le plan perpendiculaire à l'écoulement (la vitesse, la pression, la température et les propriétés physiques ne varient pas dans la section), même vitesse et même température pour tous les composants. Le second est un code de thermo-mécanique 2D et 3D basé sur une discrétisation de type éléments finis. Le couplage fonctionne de la façon suivante : à chaque itération, Ecrevisse calcule et transmet à Code_Aster la pression et le flux de chaleur sortant du fluide; Code_Aster calcule la diffusion de la chaleur dans le béton, sa dilatation thermique et la déformation mécanique due à la pression exercée par le fluide sur les parois; en sont déduits l'ouverture de fissure et la température de paroi, qui sont transmises à Ecrevisse en retour.

Parmis les essais décrits dans la Section 1.2.1.1, deux ont été simulés à l'aide du couplage entre Ecrevisse et Code_Aster. Il s'agit des essais SIMIBE et PACE-1450 (Granet, 2014, 2016). Dans SIMIBE, le débit en air sec à température ambiante s'est avéré être en bon accord avec l'expérience, contrairement à dans PACE-1450, où il s'est avéré être supérieur à l'expérience. Ceci s'explique par le fait qu'il est très sensible à l'ouverture et que, dans PACE-1450, l'ouverture initiale a dû être estimée à partir des valeurs mesurées en surface. Concernant les essais en air-vapeur, le débit obtenu dans SIMIBE pour les grandes ouvertures s'est avéré être en assez bon accord avec l'expérience. A l'inverse, le débit obtenu dans SIMIBE pour les petites ouvertures et dans PACE-1450 s'est avéré être inférieur à l'expérience. En outre, dans PACE-1450, les pics de débit d'eau observés expérimentalement à différents instants n'ont pas été reproduits numériquement.

Les résultats des calculs en air-vapeur posent la question de la pertinence de l'approche de modélisation utilisée dans Ecrevisse. En effet, si elle semble adaptée au cas de petites gouttes dispersées, comme dans SIMIBE pour les grandes ouvertures, elle peut être à l'origine d'écarts importants dans le cas de grosses gouttes et de ponts liquides, comme dans SIMIBE pour les petites ouvertures et dans PACE-1450. Il y a donc nécessité d'aller vers une modélisation plus réaliste, qui soit capable de prendre en compte la différence de vitesse et de température entre les deux phases ainsi que l'ensemble des phénomènes physiques pouvant avoir un impact sur l'écoulement, à savoir la capillarité, la rugosité et la tortuosité et la mouillabilité.

1.2.2 Stratégie de modélisation développée dans la thèse

Dans la présente thèse, l'approche de modélisation 1D proposée dans le code Ecrevisse est laissée de côté au profit d'une approche CFD 2D et 3D de type eulérienne. En CFD, il existe deux grands types de méthodes eulériennes permettant la simulation d'écoulements gaz-liquide : le type "interface résolue" ("interface capturing" ou "interface tracking methods" en anglais) et le type "dispersé" ("Eulerian dispersed models" en anglais). Ces deux types de méthodes sont présentés rapidement ci-dessous. Une description plus détaillée sera faite dans le chapitre suivant.

Les méthodes de type "interface résolue" permettent la simulation d'écoulements à phases séparées : films, poches ou gouttes s'étalant sur plusieurs cellules du maillage. A titre d'exemple, on peut citer les méthodes Volume-Of-Fluid (VOF) (Hirt and Nichols, 1981; DeBar, 1974; Noh and Woodward, 1976), Level-Set (LS) (Osher and Sethian, 1988) et Front-Tracking (FT) (Unverdi and Tryggvason, 1992). Dans ces méthodes, l'interface entre le gaz et le liquide est explicitement résolue. Elle a soit une épaisseur nulle (méthode FT et certaines méthodes VOF et LS), soit une épaisseur finie de quelques cellules (autres méthodes VOF et LS). Dans ce dernier cas, il y a trois possibilités pour chaque cellule : soit la cellule considérée ne contient que du gaz, ce qui signifie qu'on est dans la phase gaz, soit elle ne contient que du liquide, ce qui signifie qu'on est dans la phase liquide, soit elle contient à la fois du gaz et du liquide, ce qui signifie qu'on est au cœur de l'interface.

Les méthodes de type "dispersé" permettent la simulation d'écoulements à phase dispersée : petites bulles ou gouttelettes de taille inférieure ou environ égale à celle des cellules du maillage. Plusieurs formalismes, qui se distinguent par le nombre d'équations de conservation résolues, existent (Drew, 1983; Ishii, 1975; Manninen et al., 1996). Dans ces méthodes, l'interface n'est pas réellement resolue : les bulles ou gouttes sont sous-maille. Toutes les bulles ou gouttes d'une même cellule ont le même diamètre, la même vitesse et la même température. Le diamètre est soit pris constant soit obtenu via la résolution d'une équation

de transport d'aire interfaciale. Dans le cas d'un écoulement à bulles, il y a deux possibilités pour chaque cellule : soit la cellule considérée ne contient que du liquide, qui est la phase porteuse, soit elle contient à la fois du gaz et du liquide, le gaz représentant les bulles dispersées. Dans le cas d'un écoulement à gouttes, c'est l'inverse : soit la cellule considérée ne contient que du gaz, qui est la phase porteuse, soit elle contient à la fois du gaz et du liquide, le liquide représentant les gouttes dispersées.

L'inconvénient majeur des méthodes de type "interface résolue" est leur coût de calcul. En effet, elles requièrent d'avoir des cellules de taille inférieure à celle des plus petites structures de l'écoulement. Celui des méthodes de type "dispersé" est qu'elles ne permettent pas de prendre en compte certaines configurations d'écoulement (bulles déformables, annulaire, slug). Afin de pallier ces inconvénients, un troisième type d'approche a fait son apparition dans la littérature ces dernières années (Černe et al., 2001; Denèfle et al., 2015; De Santis et al., 2021; Fleau et al., 2015; Gada et al., 2017; Hänsch et al., 2012; Höhne and Vallée, 2010; Márques Damián, 2013; Mathur et al., 2019; Mérigoux et al., 2016; Štrubelj and Tiselj, 2011; Yan and Che, 2010). L'idée est d'alterner entre les approches "interface résolue" et "dispersé" en fonction de la configuration de l'écoulement. L'intérêt est de s'affranchir de la contrainte sur la taille des cellules imposée par l'approche "interface résolue", dans la mesure où les plus petites structures de l'écoulements sont traitées via l'approche "dispersé". EDF R&D a largement contribué au développement de ce type d'approche, au travers notamment du Large Bubble Model et du Generalized Large Interface Model, disponibles dans le code neptune_cfd (Denèfle et al., 2015; Fleau et al., 2015; Mérigoux et al., 2016).

Dans les fissures, l'expérience a montré que, selon l'ouverture et les conditions aux limites, il pouvait y avoir des petites gouttes et/ou des grosses gouttes et/ou des films liquides (voir Section 1.2.1.1 et Fig. 1.4). L'utilisation d'une approche hybride "interface résolue"-"dispersé" paraît donc pertinente. Cependant, les modèles mentionnés précédemment pour ce type d'approche ne sont pas valables dans le cas de gouttes dispersées : ils permettent uniquement de traiter des écoulements avec grandes interfaces et bulles dispersées. Le premier objectif de la thèse est d'étendre ces modèles au cas de gouttes dispersées, afin d'être capable de traiter des écoulements avec grandes interfaces, bulles dispersées et gouttes dispersées, comme dans les fissures. Le second objectif est de caractériser, à l'aide de ces modèles, l'impact de la rugosité et de la tortuosité sur la condensation en fissure.

1.3 Organisation du manuscrit

Le reste de ce manuscrit est constitué de six chapitres, rédigés en anglais afin de toucher un plus large public. Ces chapitres sont brièvement introduits ci-dessous.

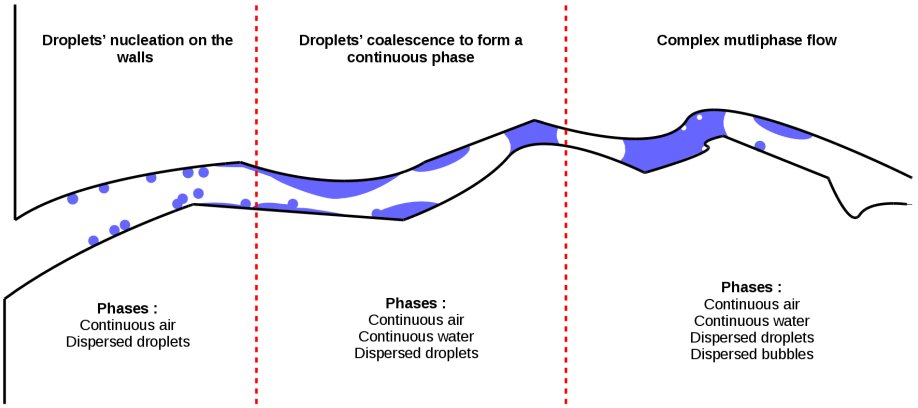

Figure 1.4: Ensemble des structures diphasiques pouvant être formées suite à la condensation de vapeur dans une fissure : gouttes, films liquides, slugs (ponts capillaires) et bulles.

Le Chapitre 2 présente les deux grands types d'approches pour la simulation des écoulements diphasiques, à savoir l'approche à deux fluides et l'approche à un fluide. Les équations résolues dans ces deux approches sont d'abord obtenues à partir des équations locales instantannées valables dans chaque phase et des conditions de saut à l'interface. Elles sont ensuite moyennées en volume. Les modèles et méthodes numériques de la litérature utilisant ces équations moyennées sont alors passées en revue. Le reste du chapitre s'intéresse au code neptune_cfd. Dans un premier temps, les modèles de transfert de masse, de quantité de mouvement et d'énergie disponibles dans le code, permettant de traiter les écoulements à gouttes/bulles/grandes interfaces/bulles et grandes interfaces, sont détaillés. Dans un second temps, les modèles hybrides 2 champs et 4 champs développés dans la thèse, permettant de traiter les écoulements à gouttes, bulles et grandes interfaces, sont explicités.

Le Chapitre 3 correspond à la validation des modèles hybrides 2 et 4 champs développés dans la thèse, dans des cas faisant intervenir gouttes dispersées, bulles dispersées ou grandes interfaces. Pour chaque modèle, une étude paramétrique est effectuée sur la base des différents cas de validation, afin d'optimiser les paramètres permettant d'alterner entre les transferts de type gouttes dispersées, ceux de type bulles dispersées et ceux de type grandes interfaces.

Le Chapitre 4 correspond à la validation du modèle hybride 2 champs dans un cas faisant intervenir simultanément gouttes dispersées et grandes interfaces. Ce cas correspond à la condensation de vapeur en présence d'air dans un mini-cannal lisse et rectiligne d'ouverture 100 µm. Des vérifications sur le nombre de Nusselt en monophasique sont d'abord effectuées. Les résultats des calculs diphasiques sont ensuite comparées à toute une série de corrélations expérimentales de la littérature fournissant la perte de charge ou le nombre de Nusselt. A noter que ce chapitre a fait l'objet d'un article, intitulé "Euler-Euler simulations of condensing two-phase flow in mini-channel: combination of a sub-grid approach and an

interface capturing approach", dans la revue à comité de lecture *International Journal of Multiphase Flow* (Davy et al., 2020).

Le Chapitre 5 s'intéresse aux effets – inconnus dans la littérature – de la rugosité et de la tortuosité, c'est-à-dire de singularités géométriques, sur le transfert de chaleur avec changement de phase en milieu confiné et en régime laminaire. Les résultats de calculs réalisés avec le modèle 2 champs, dans lesquelles la rugosité/tortuosité est modélisée de façon directe, sont présentés. Des vérifications sur les pertes de charges en monophasique sont d'abord effectuées. L'effet des singularités géométriques sur le transfert de chaleur avec changement de phase est ensuite caractérisé localement, puis globalement. Des corrélations sont proposées, l'objectif étant à terme d'éviter de modéliser directement rugosité et tortuosité.

Le Chapitre 6 porte sur le développement d'un modèle une dimension, qui pourrait être utilisé pour des simulations en conditions d'accident, car moins couteux numériquement que les modèles trois dimensions 2 et 4 champs proposés dans le Chapitre 1. La première partie du chapitre détaille les équations résolues et les relations employées pour les termes de transfert de masse, de quantité de mouvement et d'énergie, parmis lesquelles les corrélations proposées dans le chapitre précédent. Le modèle est ensuite validé dans différentes configurations, par comparaison au modèle 2 champs. L'impact des corrélations issues du chapitre précédent sur les résultats est étudié.

Le Chapitre 7 synthétise l'ensemble des résultats obtenus dans les chapitres précédents. Il donne également des perspectives pour la suite.

1.4 Valorisation des travaux

1.4.1 Publications

Les travaux réalisés dans le cadre de la présente thèse ont fait l'objet de plusieurs publications :

- S. Mimouni, P. Baconnier, and G. Davy. Overview of mitigation models dedicated to severe accidents and consequences on flow rate through concrete containment structures. 10th International Conference on Fracture Mechanics of Concrete and Concrete Structures (FraMCoS-X), Bayonne, France, 2019.
- S. Mimouni, P. Baconnier, and G. Davy. Overview of mitigation models dedicated to severe accidents and consequences on flow rate through concrete containment structures. 18th International Topical Meeting on Nuclear Reactor Thermal Hydraulics

(NURETH-18), Portland, USA, 2019

- G. Davy, E. Reyssat, S. Vincent, and S. Mimouni. CFD modeling of two-phase flows in cracks. 8th Workshop on Computational Fluid Dynamics for Nuclear Reactor Safety (CFD4NRS-8), Paris, France, 2020
- G. Davy, E. Reyssat, S. Vincent, and S. Mimouni. Euler-Euler simulations of condensing two-phase flows in mini-channel: Combination of a sub-grid approach and an interface capturing approach. *Int. J. Multiph. Flow*, 149:103964, 2022
- S. Mimouni, and G. Davy. Overview on vapor condensation phenomenon at the wall in a CFD tool. 19th International Topical Meeting on Nuclear Reactor Thermal Hydraulics (NURETH-19), Brussels, Belgium, 2022.
- S. Mimouni, and G. Davy. Pattern flow maps and multiphase flow simulations. 19th International Topical Meeting on Nuclear Reactor Thermal Hydraulics (NURETH-19), Brussels, Belgium, 2022.

1.4.2 Conférences

En outre, les travaux ont été présentés dans les conférences suivantes :

- 10^{th} International Conference on Fracture Mechanics of Concrete and Concrete Structures (FraMCoS-X), Bayonne, France, 2019 : article et communication orale.
- 3^{rd} Workshop on Surface Wettability Effects on Phase Change Phenomena (SWEP 2020), Brighton, UK, 2020 : communication orale.
- 8^{th} Workshop on Computational Fluid Dynamics for Nuclear Reactor Safety (CFD4NRS-8), Paris, France, 2020 : article et communication orale.
- Joint 14^{th} World Congress in Computational Mechanics and ECCOMAS Congress 2020 (WCCM-ECCOMAS 2020), Paris, France, 2021 : communication orale.
- 25^{th} International Conference on Theoretical and Applied Mechanics (ICTAM 2020), Milan, Italie, 2021 : communication orale.

Chapter 2

Modeling approach

Contents

2.1 General equations for two-phase flows 34

2.1.1 Single-phase flow equations 34

2.1.2 Jump conditions at the interface 34

2.1.3 Phase indicator function 35

2.1.4 Two-fluid approach 36

2.1.5 Single-fluid approach 38

2.2 Numerical simulation of two-phase flows 40

2.2.1 Resolved interfaces 40

2.2.2 Dispersed flows 44

2.2.3 Multi-regime flows 44

2.3 The neptune_cfd code 45

2.3.1 Equations solved 45

2.3.2 Standard Dispersed Model 47

2.3.3 Large Interface Model and Large Bubble Model 50

2.3.4 GLIM and LBM with bubbles 52

2.4 Summary 57

2.1 General equations for two-phase flows

2.1.1 Single-phase flow equations

Consider a system composed two phases: phase 1 and phase 2. Conservation of mass, momentum and energy of phase k with $k = 1, 2$ read:

$$\frac{\partial \rho_k}{\partial t} + \underline{\nabla} \cdot (\rho_k \underline{u}_k) = 0\,, \tag{2.1}$$

$$\frac{\partial \rho_k \underline{u}_k}{\partial t} + \underline{\nabla} \cdot (\rho_k \underline{u}_k \otimes \underline{u}_k) = -\underline{\nabla} p_k + \underline{\nabla} \cdot \underline{\underline{\tau}}_k + \rho_k \underline{g}\,, \tag{2.2}$$

$$\frac{\partial}{\partial t}(\rho_k h_k - p_k) + \underline{\nabla} \cdot (\rho_k h_k \underline{u}_k) = -\underline{\nabla} \cdot \underline{q}_k + \underline{\nabla} \cdot \left(\underline{\underline{\tau}}_k \cdot \underline{u}_k\right) + \rho_k \underline{g} \cdot \underline{u}_k\,. \tag{2.3}$$

h_k, p_k, $\underline{q}_k$, $\underline{u}_k$, ρ_k, $\underline{\underline{\tau}}_k$ are, respectively, the total enthalpy, pressure, heat flux density, velocity, density and viscous stress tensor of phase k. $\underline{g}$ is the gravity. The above equations are the same as those used for single-phase flows. They apply at any point within phase k but not at the interface with the other phase, where exchanges can take place. This is the object of the following section.

2.1.2 Jump conditions at the interface

Conservation equations can also be written for the mass, momentum and energy of the interface. Since the mass of the interface is zero, these equations simplify as follows:

$$0 = \sum_{k=1}^{2} \rho_k \left(\underline{u}_k - \underline{u}^{int}\right) \cdot \underline{n}_k\,, \tag{2.4}$$

$$0 = \underline{\nabla}^{int} \sigma - 2\sigma\kappa \underline{n}^{int} + \sum_{k=1}^{2} \left(\rho_k \underline{u}_k \otimes \left(\underline{u}_k - \underline{u}^{int}\right) + p_k \underline{\underline{I}} - \underline{\underline{\tau}}_k\right) \cdot \underline{n}_k\,, \tag{2.5}$$

$$\frac{\partial e^{int}}{\partial t} + \underline{\nabla}^{int} \cdot \left(e^{int} \underline{u}^{int}\right) = \underline{\nabla}^{int} \cdot \left(\sigma \underline{u}^{int}\right) - 2\sigma\kappa \underline{u}^{int} \cdot \underline{n}^{int} + \sum_{k=1}^{2} \left(\rho_k h_k \left(\underline{u}_k - \underline{u}^{int}\right) + \underline{q}_k + p_k \underline{u}^{int} - \underline{\underline{\tau}}_k \cdot \underline{u}_k\right) \cdot \underline{n}_k\,. \tag{2.6}$$

e^{int}, $\underline{u}^{int}$ and κ are, respectively, the interface energy, velocity and curvature. $\underline{\underline{I}}$ is the identity tensor. $\underline{n}_k$ and $\underline{n}^{int}$ are, respectively, the outer normal from phase k and the interface normal. σ is the surface tension. These equations are usually called jump conditions. The quantity $\rho_k \left(\underline{u}_k - \underline{u}^{int}\right) \cdot \underline{n}_k$ in Eq. (2.4) corresponds to the mass flux leaving phase k. This quantity can also be found in Eqs. (2.5) and (2.6), indicating that the mass transfer from phase k has an impact on both the momentum transfer and the energy transfer. A common

assumption is to neglect the two terms on the left side of Eq. (2.6) and the two first terms on the right side of this same equation.

For resolved interfaces, a first approach, called direct numerical simulation (DNS), consists in solving Eqs. (2.1) to (2.3) for $k = 1$ in the cells containing phase 1 and $k = 2$ in the cells containing phase 2, and Eqs. (2.4) to (2.6) at the interface. It requires the use of a moving grid that fits the interface, which is computationally expensive. An alternative to DNS is to use a fixed-grid approach. The two existing ones are introduced below. More details on DNS will be provided Section 2.2.1.1.

2.1.3 Phase indicator function

To solve Eqs. (2.1) to (2.3) on a fixed grid, the first step is to extend their validity to the whole domain. This is achieved using a phase indicator function, defined as:

$$\chi_k\left(\underline{x},t\right) = \begin{cases} 1 & \text{if } \underline{x} \in \Omega_k\left(t\right) \\ 0 & \text{otherwise} \end{cases}, \tag{2.7}$$

with $\Omega_k\left(t\right)$ the volume occupied by phase k at time t. This function has the following properties:

$$\sum_{k=1}^{2} \chi_k = 1\,, \tag{2.8}$$

$$\chi_k \chi_k = \chi_k\,, \tag{2.9}$$

$$\underline{\nabla}\,\chi_k = -\underline{n}_k \delta^{int}\,, \tag{2.10}$$

with δ^{int} the Dirac delta function centered on the interface. It also satisfies:

$$\frac{\partial \chi_k}{\partial t} + \underline{u}^{int} \cdot \underline{\nabla}\,\chi_k = 0\,, \tag{2.11}$$

which expresses the fact that χ_k is conserved with the motion of the interface. Two systems of equations valid on the whole domain can be derived from Eqs. (2.1) to (2.3) and the above equations for the phase indicator function. They result in two approaches for the simulation of two-phase flows: the two-fluid approach and the single-fluid approach. These are the subject of the following two sections.

2.1.4 Two-fluid approach

2.1.4.1 Local equations

A first system of equations valid on the whole domain can be obtained by multiplying Eqs. (2.1) to (2.3) by χ_k:

$$\chi_k \left(\frac{\partial \rho_k}{\partial t} + \underline{\nabla} \cdot (\rho_k \underline{u}_k) \right) = \chi_k (0) \ , \tag{2.12}$$

$$\chi_k \left(\frac{\partial \rho_k \underline{u}_k}{\partial t} + \underline{\nabla} \cdot (\rho_k \underline{u}_k \otimes \underline{u}_k) \right) = \chi_k \left(-\underline{\nabla} p_k + \underline{\nabla} \cdot \underline{\underline{\tau}}_k + \rho_k \underline{g} \right) \ , \tag{2.13}$$

$$\chi_k \left(\frac{\partial}{\partial t} (\rho_k h_k - p_k) + \underline{\nabla} \cdot (\rho_k h_k \underline{u}_k) \right) = \chi_k \left(-\underline{\nabla} \cdot \underline{q}_k + \underline{\nabla} \cdot \left(\underline{\underline{\tau}}_k \cdot \underline{u}_k \right) + \rho_k \underline{g} \cdot \underline{u}_k \right) \ . \tag{2.14}$$

Using Eqs. (2.10) and (2.11), we finally get:

$$\frac{\partial \chi_k \rho_k}{\partial t} + \underline{\nabla} \cdot (\chi_k \rho_k \underline{u}_k) = -\rho_k \left(\underline{u}_k - \underline{u}^{int} \right) \cdot \underline{n}_k \delta^{int} \ , \tag{2.15}$$

$$\begin{aligned} \frac{\partial \chi_k \rho_k \underline{u}_k}{\partial t} + \underline{\nabla} \cdot (\chi_k \rho_k \underline{u}_k \otimes \underline{u}_k) = & -\underline{\nabla} (\chi_k p_k) + \underline{\nabla} \cdot \left(\chi_k \underline{\underline{\tau}}_k \right) + \chi_k \rho_k \underline{g} \\ & - \left(\rho_k \underline{u}_k \otimes \left(\underline{u}_k - \underline{u}^{int} \right) \right) \cdot \underline{n}_k \delta^{int} \\ & - \left(p_k \underline{\underline{I}} - \underline{\underline{\tau}}_k \right) \cdot \underline{n}_k \delta^{int} \ , \end{aligned} \tag{2.16}$$

$$\begin{aligned} \frac{\partial}{\partial t} (\chi_k (\rho_k h_k - p_k)) + \underline{\nabla} \cdot (\chi_k \rho_k h_k \underline{u}_k) = & -\underline{\nabla} \cdot \left(\chi_k \underline{q}_k \right) + \underline{\nabla} \cdot \left(\chi_k \underline{\underline{\tau}}_k \cdot \underline{u}_k \right) + \chi_k \rho_k \underline{g} \cdot \underline{u}_k \\ & - \left(\rho_k h_k \left(\underline{u}_k - \underline{u}^{int} \right) \right) \cdot \underline{n}_k \delta^{int} \\ & - \left(\underline{q}_k + p_k \underline{u}^{int} - \underline{\underline{\tau}}_k \cdot \underline{u}_k \right) \cdot \underline{n}_k \delta^{int} \ . \end{aligned} \tag{2.17}$$

In Eqs. (2.15) to (2.17), the conserved quantities are $\chi_k \rho_k$, $\chi_k \rho_k \underline{u}_k$ and $\chi_k \rho_k h_k$. In comparison with Eqs. (2.1) to (2.3), additional terms have appeared. $-\rho_k \left(\underline{u}_k - \underline{u}^{int} \right) \cdot \underline{n}_k \delta^{int}$ represents the interfacial mass transfer. The interfacial momentum transfer can be decomposed into three contributions: $-\rho_k \underline{u}_k \otimes \left(\underline{u}_k - \underline{u}^{int} \right) \cdot \underline{n}_k \delta^{int}$, $-p_k \underline{n}_k \delta^{int}$ and $\underline{\underline{\tau}}_k \cdot \underline{n}_k \delta^{int}$. The first contribution results from mass transfer, while the other two are independent of mass transfer. The same apply for the interfacial energy transfer. Eqs. (2.15) to (2.17) cannot be solved as they stand due to the fact that they depend on the phase indicator function χ_k, which is discontinuous. This problem can be overcome by averaging them in time or space. In the following, spatial averaging, which is the most widely used in computational fluid dynamics, is adopted. The corresponding operator is denoted $\langle \cdot \rangle$. By definition, $\langle \chi_k \rangle = \alpha_k$, with α_k the volume fraction of phase k. In addition, for a given function f_k, $\langle \chi_k f_k \rangle = \alpha_k \langle f_k \rangle$.

2.1.4.2 Averaged equations

Applying the operator $\langle\cdot\rangle$ to Eqs. (2.15) to (2.17) gives:

$$\frac{\partial \alpha_k \langle\rho_k\rangle}{\partial t} + \underline{\nabla}\cdot\left(\alpha_k \langle\rho_k \underline{u}_k\rangle\right) = -\left\langle \rho_k \left(\underline{u}_k - \underline{u}^{int}\right)\cdot \underline{n}_k \delta^{int}\right\rangle , \tag{2.18}$$

$$\begin{aligned}\frac{\partial \alpha_k \langle\rho_k \underline{u}_k\rangle}{\partial t} + \underline{\nabla}\cdot\left(\alpha_k \langle\rho_k \underline{u}_k \otimes \underline{u}_k\rangle\right) = &-\underline{\nabla}\left(\alpha_k \langle p_k\rangle\right) + \underline{\nabla}\cdot\left(\alpha_k \left\langle \underline{\underline{\tau}}_k\right\rangle\right) + \alpha_k \langle\rho_k\rangle \underline{g} \\ &- \left\langle \left(\rho_k \underline{u}_k \otimes \left(\underline{u}_k - \underline{u}^{int}\right)\right)\cdot \underline{n}_k \delta^{int}\right\rangle \\ &- \left\langle \left(p_k \underline{\underline{I}} - \underline{\underline{\tau}}_k\right)\cdot \underline{n}_k \delta^{int}\right\rangle ,\end{aligned} \tag{2.19}$$

$$\begin{aligned}\frac{\partial}{\partial t}\left(\alpha_k \langle\rho_k h_k - p_k\rangle\right) + \underline{\nabla}\cdot\left(\alpha_k \langle\rho_k h_k \underline{u}_k\rangle\right) = &-\underline{\nabla}\cdot\left(\alpha_k \left\langle \underline{q}_k\right\rangle\right) + \underline{\nabla}\cdot\left(\alpha_k \left\langle \underline{\underline{\tau}}_k\cdot \underline{u}_k\right\rangle\right) + \alpha_k \left\langle \rho_k \underline{g}\cdot \underline{u}_k\right\rangle \\ &- \left\langle \left(\rho_k h_k \left(\underline{u}_k - \underline{u}^{int}\right)\right)\cdot \underline{n}_k \delta^{int}\right\rangle \\ &- \left\langle \left(\underline{q}_k + p_k \underline{u}^{int} - \underline{\underline{\tau}}_k\cdot \underline{u}_k\right)\cdot \underline{n}_k \delta^{int}\right\rangle .\end{aligned} \tag{2.20}$$

Except for highly compressible flows, $\langle\rho_k \underline{u}_k\rangle \approx \langle\rho_k\rangle\langle\underline{u}_k\rangle$ and $\langle\rho_k h_k\rangle \approx \langle\rho_k\rangle\langle h_k\rangle$.[1] The following equations thus apply:

$$\langle\rho_k \underline{u}_k \otimes \underline{u}_k\rangle = \langle\rho_k\rangle\langle\underline{u}_k\rangle \otimes \langle\underline{u}_k\rangle + \langle\rho_k \left(\underline{u}_k - \langle\underline{u}_k\rangle\right)\otimes\left(\underline{u}_k - \langle\underline{u}_k\rangle\right)\rangle , \tag{2.21}$$

$$\langle\rho_k h_k \underline{u}_k\rangle = \langle\rho_k\rangle\langle h_k\rangle\langle\underline{u}_k\rangle + \langle\rho_k \left(h_k - \langle h_k\rangle\right)\left(\underline{u}_k - \langle\underline{u}_k\rangle\right)\rangle , \tag{2.22}$$

$$\left\langle \underline{\underline{\tau}}_k\cdot \underline{u}_k\right\rangle = \left\langle \underline{\underline{\tau}}_k\right\rangle\cdot\langle\underline{u}_k\rangle + \left\langle \underline{\underline{\tau}}_k\cdot\left(\underline{u}_k - \langle\underline{u}_k\rangle\right)\right\rangle . \tag{2.23}$$

The quantities $\underline{u}_k - \langle\underline{u}_k\rangle$ and $h_k - \langle h_k\rangle$ correspond to velocity and enthalpy fluctuations due to the presence of interfaces in the control volume and/or to turbulence (these quantities are often denoted $\underline{u}'_k$ and h'_k).[2] Eqs. (2.18) to (2.20) correspond to the conservation equations solved in the two-fluid approach (note that they are solved for $k = 1$ and $k = 2$). These equations are solved together with the average jump conditions that can be obtained by applying the operator $\langle\cdot\rangle$ to Eqs. (2.4) to (2.6). The two-fluid approach is usually employed for dispersed flows, with small (sub-grid) gas, liquid or solid inclusions. It is also sometimes used for resolved interfaces. In both cases, closure laws have to be provided by the user for the interfacial and fluctuation terms. For dispersed flows, the two terms relating to surface tension in the momentum jump condition are not taken into account.

[1] For highly compressible flows, Favre's average is usually employed. It is defined as $\tilde{f}_k = \langle\rho_k f_k\rangle/\langle\rho_k\rangle$.

[2] Eq. (2.23) is used instead of $\left\langle \underline{\underline{\tau}}_k\cdot \underline{u}_k\right\rangle = \left\langle \underline{\underline{\tau}}_k\right\rangle\cdot\langle\underline{u}_k\rangle + \left\langle \left(\underline{\underline{\tau}}_k - \left\langle \underline{\underline{\tau}}_k\right\rangle\right)\cdot\left(\underline{u}_k - \langle\underline{u}_k\rangle\right)\right\rangle$ to avoid introducing $\underline{\underline{\tau}}_k - \left\langle \underline{\underline{\tau}}_k\right\rangle$.

2.1.5 Single-fluid approach

2.1.5.1 Local equations

A system of equations different from that consisting of Eqs. (2.15) to (2.17) but also valid on the whole domain, can be obtained by multiplying Eqs. (2.1) to (2.3) by χ_k and then summing over the two phases:

$$\sum_{k=1}^{2} \frac{\partial \chi_k \rho_k}{\partial t} + \underline{\nabla} \cdot (\chi_k \rho_k \underline{u}_k) = \sum_{k=1}^{2} -\rho_k \left(\underline{u}_k - \underline{u}^{int}\right) \cdot \underline{n}_k \delta^{int}\,, \tag{2.24}$$

$$\begin{aligned}\sum_{k=1}^{2} \frac{\partial \chi_k \rho_k \underline{u}_k}{\partial t} + \underline{\nabla} \cdot (\chi_k \rho_k \underline{u}_k \otimes \underline{u}_k) = &\sum_{k=1}^{2} -\underline{\nabla} (\chi_k p_k) + \underline{\nabla} \cdot \left(\chi_k \underline{\underline{\tau}}_k\right) + \chi_k \rho_k \underline{g} \\ &- \sum_{k=1}^{2} \left(\rho_k \underline{u}_k \otimes \left(\underline{u}_k - \underline{u}^{int}\right)\right) \cdot \underline{n}_k \delta^{int} \\ &- \sum_{k=1}^{2} \left(p_k \underline{\underline{I}} - \underline{\underline{\tau}}_k\right) \cdot \underline{n}_k \delta^{int}\,,\end{aligned} \tag{2.25}$$

$$\begin{aligned}\sum_{k=1}^{2} \frac{\partial}{\partial t} (\chi_k (\rho_k H_k - p_k)) + \underline{\nabla} \cdot (\chi_k \rho_k H_k \underline{u}_k) = &\sum_{k=1}^{2} -\underline{\nabla} \cdot \left(\chi_k \underline{q}_k\right) + \underline{\nabla} \cdot \left(\chi_k \underline{\underline{\tau}}_k \cdot \underline{u}_k\right) + \chi_k \rho_k \underline{g} \cdot \underline{u}_k \\ &- \sum_{k=1}^{2} \left(\rho_k h_k \left(\underline{u}_k - \underline{u}^{int}\right)\right) \cdot \underline{n}_k \delta^{int} \\ &- \sum_{k=1}^{2} \left(\underline{q}_k + p_k \underline{u}^{int} - \underline{\underline{\tau}}_k \cdot \underline{u}_k\right) \cdot \underline{n}_k \delta^{int}\,.\end{aligned} \tag{2.26}$$

Using the jump conditions given by Eqs. (2.4) to (2.6), we finally get:

$$\frac{\partial \rho}{\partial t} + \underline{\nabla} \cdot (\rho \underline{u}) = 0\,, \tag{2.27}$$

$$\frac{\partial \rho \underline{u}}{\partial t} + \underline{\nabla} \cdot (\rho \underline{u} \otimes \underline{u}) = -\underline{\nabla} p + \underline{\nabla} \cdot \underline{\underline{\tau}} + \rho \underline{g} + \left(\underline{\nabla}^{int} (\sigma) - 2\sigma\kappa \underline{n}^{int}\right) \delta^{int}\,, \tag{2.28}$$

$$\frac{\partial}{\partial t} (\rho h - p) + \underline{\nabla} \cdot (\rho h \underline{u}) = -\underline{\nabla} \cdot \underline{q} + \underline{\nabla} \cdot \left(\underline{\underline{\tau}} \cdot \underline{u}\right) + \rho \underline{g} \cdot \underline{u}\,. \tag{2.29}$$

with $h = \sum_{k=1}^{2} \chi_k h_k$, $p = \sum_{k=1}^{2} \chi_k p_k$, $\underline{q} = \sum_{k=1}^{2} \chi_k \underline{q}_k$, $\underline{u} = \sum_{k=1}^{2} \chi_k \underline{u}_k$, $\rho = \sum_{k=1}^{2} \chi_k \rho_k$ and $\underline{\underline{\tau}} = \sum_{k=1}^{2} \chi_k \underline{\underline{\tau}}_k$. In Eqs. (2.27) to (2.29), the conserved quantities are ρ, $\rho\underline{u}$ and ρh. Like Eqs. (2.15) to (2.17), Eqs. (2.27) to (2.29) depend on χ_k. They are therefore also averaged in space.

2.1.5.2 Averaged equations

Applying the operator $\langle\cdot\rangle$ to Eqs. (2.27) to (2.29) gives:

$$\frac{\partial \rho}{\partial t} + \underline{\nabla} \cdot (\rho \underline{u}) = 0 \,, \tag{2.30}$$

$$\frac{\partial \rho \underline{u}}{\partial t} + \underline{\nabla} \cdot (\rho \underline{u} \otimes \underline{u} + \underline{J}_u) = -\underline{\nabla} p + \underline{\nabla} \cdot \underline{\underline{\tau}} + \rho \underline{g} + \left\langle \left(\underline{\nabla}^{int} \ (\sigma) - 2\sigma\kappa \underline{n}^{int} \right) \delta^{int} \right\rangle \,, \tag{2.31}$$

$$\frac{\partial}{\partial t} (\rho h - p) + \underline{\nabla} \cdot (\rho h \underline{u} + \underline{J}_h) = -\underline{\nabla} \cdot \underline{q} + \underline{\nabla} \cdot \left(\underline{\underline{\tau}} \cdot \underline{u} + \underline{J}'_h \right) + \rho \underline{g} \cdot \underline{u} \,. \tag{2.32}$$

The variables h, p, $\underline{q}$, $\underline{u}$, ρ and $\underline{\underline{\tau}}$ are redefined as follows: $\rho h = \sum_{k=1}^{2} \alpha_k \langle \rho_k h_k \rangle$, $p = \sum_{k=1}^{2} \alpha_k \langle p_k \rangle$, $\underline{q} = \sum_{k=1}^{2} \alpha_k \left\langle \underline{q}_k \right\rangle$, $\rho \underline{u} = \sum_{k=1}^{2} \alpha_k \langle \rho_k \underline{u}_k \rangle$, $\rho = \sum_{k=1}^{2} \alpha_k \langle \rho_k \rangle$, $\underline{\underline{\tau}} = \sum_{k=1}^{2} \alpha_k \left\langle \underline{\underline{\tau}}_k \right\rangle$. Assuming that $\langle \rho_k \underline{u}_k \rangle \approx \langle \rho_k \rangle \langle \underline{u}_k \rangle$ and $\langle \rho_k h_k \rangle \approx \langle \rho_k \rangle \langle h_k \rangle$, $\underline{J}_u$, $\underline{J}_h$ and $\underline{J}'_h$ can be put into the form:

$$\begin{aligned}
\rho \underline{J}_u = {} & \alpha_1 \rho \langle \rho_1 (\underline{u}_1 - \langle \underline{u}_1 \rangle) \otimes (\underline{u}_1 - \langle \underline{u}_1 \rangle) \rangle \\
& + \alpha_2 \rho \langle \rho_2 (\underline{u}_2 - \langle \underline{u}_2 \rangle) \otimes (\underline{u}_2 - \langle \underline{u}_2 \rangle) \rangle \\
& + \alpha_1 \alpha_2 \langle \rho_1 \rangle \langle \rho_2 \rangle (\langle \underline{u}_2 \rangle - \langle \underline{u}_1 \rangle) \otimes (\langle \underline{u}_2 \rangle - \langle \underline{u}_1 \rangle) \,,
\end{aligned} \tag{2.33}$$

$$\begin{aligned}
\rho \underline{J}_h = {} & \alpha_1 \rho \langle \rho_1 (h_1 - \langle h_1 \rangle) (\underline{u}_1 - \langle \underline{u}_1 \rangle) \rangle \\
& + \alpha_2 \rho \langle \rho_2 (h_2 - \langle h_2 \rangle) (\underline{u}_2 - \langle \underline{u}_2 \rangle) \rangle \\
& + \alpha_1 \alpha_2 \langle \rho_1 \rangle \langle \rho_2 \rangle (\langle h_2 \rangle - \langle h_1 \rangle) (\langle \underline{u}_2 \rangle - \langle \underline{u}_1 \rangle) \,,
\end{aligned} \tag{2.34}$$

$$\begin{aligned}
\rho \underline{J}'_h = {} & \alpha_1 \rho \left\langle \underline{\underline{\tau}}_1 \cdot (\underline{u}_1 - \langle \underline{u}_1 \rangle) \right\rangle \\
& + \alpha_2 \rho \left\langle \underline{\underline{\tau}}_2 \cdot (\underline{u}_2 - \langle \underline{u}_2 \rangle) \right\rangle \\
& + \alpha_1 \alpha_2 \left(\langle \rho_1 \rangle \left\langle \underline{\underline{\tau}}_2 \right\rangle - \langle \rho_2 \rangle \left\langle \underline{\underline{\tau}}_1 \right\rangle \right) \cdot (\langle \underline{u}_2 \rangle - \langle \underline{u}_1 \rangle) \,.
\end{aligned} \tag{2.35}$$

They each consist of two fluctuation terms, involving the quantities $\underline{u}_k - \langle \underline{u}_k \rangle$ and $h_k - \langle h_k \rangle$ discussed in Section 2.1.4.2, and another term depending on the relative (or slip) velocity $\langle \underline{u}_2 \rangle - \langle \underline{u}_1 \rangle$. For the sake of consistency with Section 2.1.4, Eqs. (2.30) to (2.32) have been obtained by multiplying Eqs. (2.1) to (2.3) by χ_k, summing over the two phases and applying the space average filter. They could have been obtained in a more simple way by summing Eqs. (2.18) to (2.20) over the two phases. Eqs. (2.30) to (2.32) correspond to the conservation equations solved in the single-fluid approach. These equations are solved together with an additional equation for the volume fraction, namely Eq. (2.18) with $k = 1$ or $k = 2$. In terms of mixture velocity and relative velocity, the latter reads:

$$\begin{aligned}
\frac{\partial \alpha_k \langle \rho_k \rangle}{\partial t} + \underline{\nabla} \cdot (\alpha_k \langle \rho_k \rangle \underline{u}) = {} & -\underline{\nabla} \cdot \left(\alpha_k \alpha_p \frac{\langle \rho_k \rangle \langle \rho_p \rangle}{\rho_m} \left(\langle \underline{u}_k \rangle - \left\langle \underline{u}_p \right\rangle \right) \right) \\
& - \left\langle \rho_k \left(\underline{u}_k - \underline{u}^{int} \right) \cdot \underline{n}_k \delta^{int} \right\rangle \,.
\end{aligned} \tag{2.36}$$

The single-fluid approach can be used for both dispersed flows and resolved interfaces. For dispersed flows, a closure law is used for the relative velocity $\langle \underline{u}_2 \rangle - \langle \underline{u}_1 \rangle$. In addition, the two terms relating to surface tension in Eq. (2.31) are not taken into account. For resolved interfaces, the assumption is made that the two phases share the same velocity ($\langle \underline{u}_1 \rangle = \langle \underline{u}_2 \rangle = \underline{u}$). Therefore, the terms depending on $\langle \underline{u}_2 \rangle - \langle \underline{u}_1 \rangle$ in Eqs. (2.33) to (2.36) vanish. Note that solving Eq. (2.36) allows to capture the interface. Alternatives to this equation exist. They will be presented in Section 2.2.1.

2.2 Numerical simulation of two-phase flows

The three approaches discussed before (DNS, two-fluid and single-fluid) come in various methods and models, which are briefly introduced below. These apply to resolved interfaces and/or dispersed flows. "Resolved interfaces" refers to interfaces spreading over several grid cells, while "dispersed flows" refers to small (sub-grid) gas, liquid or solid inclusions. For dispersed flows, only Eulerian methods will be considered.

2.2.1 Resolved interfaces

2.2.1.1 Direct numerical simulation (DNS)

In the context of two-phase flows, DNS consists in solving the conservation equations for single-phase flows in the gas bulk and in the liquid bulk, and the jump conditions at the interface (see Sections 2.1.1 and 2.1.2). It requires the use of a moving grid that fits the interface. Moving-grid methods can be classified into three categories: the full Lagrangian methods, in which all the grid points are moved with the flow, the boundary-fitted methods, in which the mesh is built orthogonal to the interface (Ryskin and Leal, 1984) and the arbitrary Lagrangian-Eulerian methods, in which only the mesh close to the interface is moved with the flow (Hirt et al., 1997; Ganesan and Tobiska, 2006). The advantage of DNS is its accuracy. Indeed, it does not involve the volume fraction (phase indicator function) and does not require averaging of the physical properties (hence the name of "direct numerical simulation", which comes from the field of turbulence and means that all the scales of turbulence are solved and no turbulence model is used). The drawback of DNS is the need for a moving grid. Indeed, meshing algorithms are complex to implement, especially in 3D, and computationally expensive.

2.2.1.2 Volume-Of-Fluid (VOF) method

The Volume-Of-Fluid method (VOF) has been introduced by Hirt and Nichols (1981); DeBar (1974); Noh and Woodward (1976). It is based on the single-fluid approach (see Section 2.1.5.2). The interface is captured via the volume fraction and advected by Eq. (2.36) (with $\langle \underline{u}_k \rangle - \left\langle \underline{u}_p \right\rangle = 0$). Two main types of VOF methods can be distinguished: geometric and algebraic. In the geometric VOF methods, Eq. (2.36) is solved by means of geometric techniques, which requires to first reconstruct the interface from the volume fraction field in each computational cell. The most commonly used method for interface reconstruction is the PLIC (Piecewise Linear Interface Calculation) method (Debar, 1974), in which, in each interfacial cell, the interface is approximated as a line (in 2D) or a plane (in 3D). In the algebraic VOF methods, Eq. (2.36) is solved based on algebraic considerations. Therefore, no reconstruction step is needed. However, specific schemes are required to avoid numerical diffusion of the interface. In comparison with the following methods, the advantage of the VOF method is that it intrinsically ensures mass conservation.

2.2.1.3 Level-Set (LS) method

The Level-Set (LS) method has been introduced by Osher and Sethian (1988). As the VOF method, it is based on the single-fluid approach (see Section 2.1.5.2). However, unlike in the VOF method, the interface is not captured via the volume fraction but via a specific function, called level-set function. This function takes the value d in one phase, 0 at the interface and $-d$ in the other phase, with d the distance from the center of the considered cell to the interface. At each iteration, a volume fraction field is reconstructed from the level-set function ($\alpha_k = 0$ if $\phi < -\varepsilon$, $\alpha_k = 1$ if $\phi > \varepsilon$ and $\alpha_k = f(\phi, \varepsilon)$ otherwise, with ϕ the level-set function, ε a parameter defining the thickness of the interface and f a function comprised between 0 and 1). The volume fraction is then used to compute the physical properties according to the expression provided in Section 2.1.5.2. The LS method allows an accurate computation of the surface tension force, which is obtained from the gradient of the level-set function, which is a smooth function. The drawbacks of the LS method are that the level-set function can be deformed during advection and that the conservation of mass is not ensured (the level-set function does not represent any physical quantity). The method thus requires the use of specific procedures to maintain the level-set function as a signed distance to the interface (which is called redistancing) and to conserve mass.

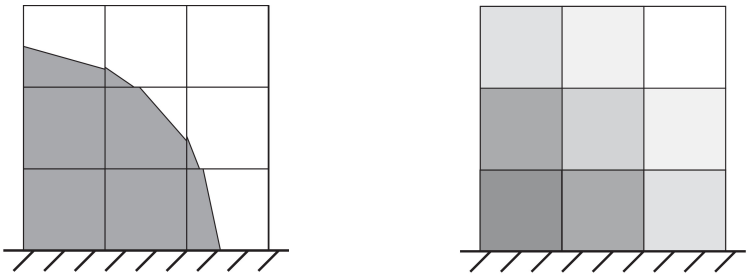

(b) Geometric VOF (FS3D). (c) Algebraic VOF (interFoam).

Figure 2.1: Principle of the Volume-Of-Fluid method (Gründing et al., 2020). Two approaches can be distinguished: the geometric approach (left), which consists in reconstructing the interface and solving Eq. (2.36) using geometric techniques, and the algebraic approach (right), which consists in solving Eq. (2.36) based on algebraic considerations.

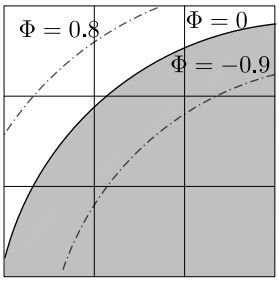

Figure 2.2: Principle of the Level-Set method Tavares (2019). The quantity advected is not $\alpha_k \langle \rho_k \rangle$ but an auxiliary function, called level-set function (denoted Φ in this figure). This function takes the value d in one phase, 0 at the interface and $-d$ in the other phase, where d is the distance to the interface.

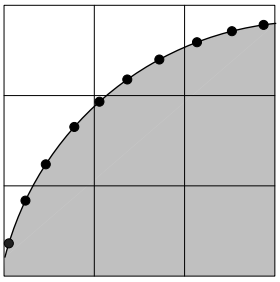

Figure 2.3: Principle of the Front-Tracking method Tavares (2019). Markers are used to describe the interface. These markers are advected in a Lagrangian way with velocities interpolated from the stationary Eulerian grid used to solve the fluid conservation equations.

2.2.1.4 Front-Tracking (FT) method

The Front-Tracking (FT) method has been introduced by Unverdi and Tryggvason (1992). As the VOF and LS methods, it is based on the single-fluid approach (see Section 2.1.5.2). The difference is that the interface is described by markers that are advected in a Lagrangian way. Their velocity is interpolated from the Eulerian grid used for the fluid conservation equations. To ensure a constant spacing between them, markers can be added or deleted during the simulation. At each iteration, a volume fraction field is derived from a pairing between the markers and the Eulerian grid. The volume fraction is then employed to compute the physical properties. As the LS method, the FT method allows for an accurate computation of the interface curvature and the surface tension force. One of its limitation is the management of coalescence and break-up, which is complex, especially in 3D. In addition, the equation solved for the transport of the markers does not guarantee the conservation of mass. The method thus requires the use of specific algorithms with correction of the position of the markers in order to satisfy the mass balance equation.

2.2.1.5 VOF-like method based on the two-fluid model

Unlike the previous ones, this method is based on the two fluid approach (see Section 2.1.4.2). It has been employed by several authors, including Coste (2013); Denèfle et al. (2015); De Santis et al. (2021); Fleau et al. (2015); Gada et al. (2017); Höhne and Vallée (2010); Marschall and Hinrichsen (2013); Mathur et al. (2019); Štrubelj and Tiselj (2011). It has similarities with the VOF method. As in this method, the interface is captured via the volume fraction. However, it is obtained by solving Eq. (2.19) for $k = 1$ and $k = 2$ instead of Eqs. (2.30) and (2.36). In the works of Denèfle et al. (2015); De Santis et al. (2021); Fleau et al. (2015); Mathur et al. (2019); Štrubelj and Tiselj (2011), the surface tension force is taken into account and a compressive term is used to prevent numerical diffusion of the interface and allow an accurate computation of the interface curvature, involved in the surface tension force. This term is included in the mass conservation equation, as in the algebraic VOF method, or in an additional equation, called interface sharpening equation. However, unlike in the VOF method, a closure law is required for the interfacial momentum transfer. The latter generally consists in a friction force (sometimes called drag force). This method is implemented in the neptune_cfd code (Coste, 2013; Denèfle et al., 2015; Fleau et al., 2015). More details will be provided in Section 2.3.

2.2.2 Dispersed flows

2.2.2.1 Mixture models

Among the most widely used mixture models are the homogeneous equilibrium model (HEM), the homogeneous relaxation model (HRM) and the drift-flux model. They are based on the single-fluid approach (see Section 2.1.5.2). The HEM assumes that the gas and the liquid are in kinematic equilibrium, which implies that they have the same velocity, and in thermodynamic equilibrium, which implies that they both are at saturated conditions. The volume fraction is obtained from the mixture density and the saturated gas and liquid densities. Therefore, Eq. (2.36) is not considered. The HRM also assumes that the two phases are in kinematic equilibrium, but allows for a thermal disequilibrium. The original formulation of the model considers saturated gas and superheated (metastable) liquid. The mass transfer term (second term on the right) in Eq. (2.36) is modeled using a relaxation time, which has been experimentally correlated to the void fraction, the local pressure and the saturation pressure. Finally, the drift-flux model allows the gas and the liquid to move at different velocities. For this purpose, a correlation is used for the slip velocity $\langle \underline{u}_2 \rangle - \langle \underline{u}_1 \rangle$. Concerning energy, the two phases can be assumed to be in thermodynamic equilibrium as in the HEM or in thermal disequilibrium as in the HRM.

2.2.2.2 Two-fluid model

As its name indicates, the two-fluid model is based on the two-fluid approach (see Section 2.1.4.2). The interfacial momentum transfer $\langle \underline{\underline{\tau}}_k \cdot \underline{n}_k \delta^{int} \rangle$ is usually computed as the sum of a drag force (caused by the motion of the inclusion through the carrier fluid), a lift force (due to velocity gradients in the carrier fluid) and an added mass force (due to acceleration of the inclusion with respect to the carrier fluid). Each of these forces depend on a specific coefficient. Each coefficient is obtained from a correlation. The existing correlations are functions of, among other parameters, the inclusion diameter. The latter is usually obtained by solving an additional transport equation on the interfacial area concentration. The two-fluid model is implemented in the neptune_cfd code. More details will be provided in Section 2.3.

2.2.3 Multi-regime flows

The methods in Section 2.2.2 only apply to dispersed flows. On the contrary, the methods in Section 2.2.1 can in theory be used for any kind of flow regime. However, they require the grid cells to be smaller than the smallest flow structures. Therefore, in practice, they are

only used for flows with large interfaces, such as separate flows or flows with large bubbles or droplets. Few years ago, hybrid methods appeared in the literature, with the aim of simulating flows with both small and large structures, without the constraint of having the cells smaller than the smallest flow structures. For example, Černe et al. (2001); Yan and Che (2010) coupled the two-fluid method with the VOF method. Márques Damián (2013) coupled the mixture method with the VOF method. Denèfle et al. (2015); De Santis et al. (2021); Fleau et al. (2015); Gada et al. (2017); Hänsch et al. (2012); Höhne and Vallée (2010); Mathur et al. (2019); Mérigoux et al. (2016); Štrubelj and Tiselj (2011) coupled the two-fluid method with the two-fluid method for large interfaces.

Depending on the authors, the methods were not coupled the same way. Černe et al. (2001) solved Eq. (2.19) for $k = 1$ and $k = 2$ in the cells with dispersed bubbles and Eq. (2.31) in the cells with a large interface, while Yan and Che (2010) solved Eq. (2.19) for $k = 1$ and Eq. (2.31) in all the cells. De Santis et al. (2021); Gada et al. (2017); Höhne and Vallée (2010); Mathur et al. (2019); Mérigoux et al. (2016); Štrubelj and Tiselj (2011) solved Eq. (2.19) for $k = 1$ and $k = 2$ and applied the appropriate interfacial transfer terms depending on whether the cell contains dispersed bubbles or a large interface, while Denèfle et al. (2015); Fleau et al. (2015); Hänsch et al. (2012) considered the dispersed bubbles as a separate phase ($k = 3$) and solved Eq. (2.19) for $k = 1$ to $k = 3$.

In the various works mentioned, a criterion was required to switch from one method to the other. In the works of Černe et al. (2001); Štrubelj and Tiselj (2011), this criterion was based on a dispersion function. In the work of Márques Damián (2013), it was based on the gradient of the volume fraction. In the works of Denèfle et al. (2015); Fleau et al. (2015); Gada et al. (2017); Hänsch et al. (2012); Höhne and Vallée (2010); Mathur et al. (2019); Mérigoux et al. (2016), it was based on the volume fraction (and the resolved interface curvature for the first two references). In the work of De Santis et al. (2021), it is based on the resolved interface curvature and on the dispersed inclusions diameter. Note that none of the authors cited above considered flows with dispersed droplets (only resolved interfaces and dispersed bubbles). In addition, except Gada et al. (2017), they all considered adiabatic flows. The hybrid methods employed in the works of Denèfle et al. (2015); Fleau et al. (2015) correspond to those in the neptune_cfd code. More details will be provided in Section 2.3.

2.3 The neptune_cfd code

2.3.1 Equations solved

The equations solved in the neptune_cfd code are based on those provided in Section 2.1.4.2. The terms $\langle \rho_k \underline{u}_k \otimes (\underline{u}_k - \underline{u}^{int}) \cdot \underline{n}_k \delta^{int} \rangle$ and $p_k \underline{n}_k \delta^{int}$ in the momentum conservation equa-

tion, the terms $p_k \underline{u}^{int} \cdot \underline{n}_k \delta^{int}$ and $\left(\underline{\underline{\tau}}_k \cdot \underline{u}_k\right) \cdot \underline{n}_k \delta^{int}$ in the energy conservation equation and the term $\left\langle \underline{\nabla}^{int} \sigma \right\rangle$ in the momentum jump condition are not taken into account. Using the notations in Table 2.1 and introducing the terms $\Gamma_{w\to k}$ and $\varphi_{w\to k}$ for the transfers at the wall, the conservation equations become:

$$\frac{\partial}{\partial t}\left(\alpha_k \rho_k\right) + \underline{\nabla} \cdot \left(\alpha_k \rho_k \underline{U}_k\right) = \Gamma_{p\to k} + \Gamma_{w\to k}\,, \tag{2.37}$$

$$\begin{aligned}\frac{\partial}{\partial t}\left(\alpha_k \rho_k \underline{U}_k\right) + \underline{\nabla} \cdot \left(\alpha_k \rho_k \underline{U}_k \otimes \underline{U}_k\right) = &-\alpha_k \underline{\nabla} P + \underline{\nabla} \cdot \left[\alpha_k \left(\underline{\underline{\Sigma}}_k + \underline{\underline{\Sigma}}_k^{Re}\right)\right] \\ &+ \alpha_k \rho_k \underline{g} + \underline{I}_{p\to k}\,,\end{aligned} \tag{2.38}$$

$$\begin{aligned}\frac{\partial}{\partial t}\left(\alpha_k \rho_k H_k\right) + \underline{\nabla} \cdot \left(\alpha_k \rho_k H_k \underline{U}_k\right) = &\alpha_k \frac{\partial P}{\partial t} - \underline{\nabla} \cdot \left[\alpha_k \left(\underline{Q}_k + \underline{Q}_k^{Re}\right)\right] + \underline{\nabla} \cdot \left(\alpha_k \underline{\underline{\Sigma}}_k \cdot \underline{U}_k\right) \\ &+ \alpha_k \rho_k \underline{g} \cdot \underline{U}_k + \Pi_{p\to k}^{\Gamma} + \Pi_{p\to k} + \varphi_{w\to k}\,.\end{aligned} \tag{2.39}$$

For the jump conditions, we get:

$$\sum_{k=1}^{2} \Gamma_{p\to k} = 0\,, \tag{2.40}$$

$$\sum_{k=1}^{2} \underline{I}_{p\to k} = \underline{F}_{pk}^{ST}\,, \tag{2.41}$$

$$\sum_{k=1}^{2} \Pi_{p\to k}^{\Gamma} + \Pi_{p\to k} = 0\,. \tag{2.42}$$

The term $\varphi_{w\to k}$ in Eq. (2.39) represents the total (latent and/or sensible) energy transfer from the wall to phase k and the term $\Gamma_{w\to k}$ in Eq. (2.37) represents the mass transfer from phase p to phase k associated with the wall latent energy transfer. These two terms verify:

$$\sum_{k=1}^{2} \Gamma_{w\to k} = 0\,, \tag{2.43}$$

$$\sum_{k=1}^{2} \varphi_{w\to k} = \varphi_w\,, \tag{2.44}$$

with φ_w the total wall heat flux. In practice, the terms $\underline{I}'_{p\to k}$, $\Pi'_{p\to k}$ (or $\Gamma_{p\to k}$), $\Gamma_{w\to k}$ and $\underline{F}_{pk}^{ST}$ are obtained from closure laws. These depend on the model used. The Standard Dispersed Model uses closure laws specific to droplets/bubbles. Surface tension is not taken into account. An additional equation is solved for the droplet/bubble interfacial area. The Large Interface Model and the Large Bubble Model use closure laws specific to resolved interfaces. Surface tension can be taken into account. An additional equation is solved for both phases, to prevent numerical diffusion of the interface. The Generalized Large Interface Model and the Large Bubble Model with bubbles are hybrid models allowing to take into account resolved interfaces and dispersed bubbles at the same time. In the latter model, the gas phase is decomposed into a continuous gas field and a dispersed gas field, unlike in the other models, where the gas is either continuous or dispersed. Each field can exchange with the two others. Therefore, the terms $\Gamma_{p\to k}$, $\underline{I}_{p\to k}$, $\Pi_{p\to k}^{\Gamma}$, $\Pi_{p\to k}$ in Eqs. (2.37) to (2.42) are rewritten as $\sum_{p\neq k} \Gamma_{p\to k}$, $\sum_{p\neq k} \underline{I}_{p\to k}$, $\sum_{p\neq k} \Pi_{p\to k}^{\Gamma}$, $\sum_{p\neq k} \Pi_{p\to k}$.

Note that, for the needs of the PhD, the GLIM and the LBMb have been extended to dispersed droplets. Regardless of the model used, the term $\Pi^{\Gamma}_{p\to k}$ is computed as $\Gamma_{p\to k}H_k$. $\Gamma_{p\to k}$ (or $\Pi_{p\to k}$) is deduced from Eq. (2.42). The contribution to $\varphi_{w\to k}$ corresponding to sensible heat is obtained from Newton's law of cooling. That corresponding to latent heat (if any) is obtained from the product $\Gamma_{w\to k}H_{lat}$, with H_{lat} the latent heat of vaporization/ condensation. Depending on the physics, other equations than those mentioned above can be solved, e.g., for non-condensable gases and/or turbulence. More information is provided in the following. All the equations are discretized using the finite volume method. They are solved using a SIMPLE-like algorithm.

Table 2.1: Correspondance between Eqs. (2.18) to (2.20) and Eqs. (2.37) to (2.39).

Symbol	Expression
$\underline{F}^{ST}_{pk}$	$-\left\langle 2\sigma\kappa\underline{n}^{int}\right\rangle$
H_k	$\left\langle h_k\right\rangle$
$\underline{I}'_{p\to k}$	$\left\langle \underline{\underline{\tau}}_k\cdot\underline{n}_k\delta^{int}\right\rangle$
P	$\left\langle p_k\right\rangle$
$\underline{Q}_k$	$\left\langle \underline{q}_k\right\rangle$
$\underline{Q}^{Re}_k$	$\left\langle \rho_k\left(h_k-\left\langle h_k\right\rangle\right)\left(\underline{u}_k-\left\langle \underline{u}_k\right\rangle\right)\right\rangle-\left\langle \underline{\underline{\tau}}_k\cdot\left(\underline{u}_k-\left\langle \underline{u}_k\right\rangle\right)\right\rangle$
$\underline{U}_k$	$\left\langle \underline{u}_k\right\rangle$
$\Gamma_{p\to k}$	$-\left\langle \rho_k\left(\underline{u}_k-\underline{u}^{int}\right)\cdot\underline{n}_k\delta^{int}\right\rangle$
$\Pi'_{p\to k}$	$-\left\langle \underline{q}_k\cdot\underline{n}_k\delta^{int}\right\rangle$
$\Pi^{\Gamma}_{p\to k}$	$-\left\langle \rho_k h_k\left(\underline{u}_k-\underline{u}^{int}\right)\cdot\underline{n}_k\delta^{int}\right\rangle$
ρ_k	$\left\langle \rho_k\right\rangle$
$\underline{\underline{\Sigma}}_k$	$\left\langle \underline{\underline{\tau}}_k\right\rangle$
$\underline{\underline{\Sigma}}^{Re}_k$	$-\left\langle \rho_k\left(\underline{u}_k-\left\langle \underline{u}_k\right\rangle\right)\otimes\left(\underline{u}_k-\left\langle \underline{u}_k\right\rangle\right)\right\rangle$

2.3.2 Standard Dispersed Model

2.3.2.1 Interfacial momentum transfers for bubbles and droplets

As in the Standard Dispersed Model, for bubbles and droplets, the momentum transfers read as the sum of a drag force $\underline{F}^{D}$, an added mass force $\underline{F}^{AM}$, a lift force $\underline{F}^{L}$, a wall force $\underline{F}^{W}$ and a turbulent dispersion force $\underline{F}^{TD}$:

$$\underline{I}_{c\to d}=-\underline{I}_{d\to c}=\underline{F}^{D}_{c\to d}+\underline{F}^{AM}_{c\to d}+\underline{F}^{L}_{c\to d}+\underline{F}^{W}_{c\to d}+\underline{F}^{TD}_{c\to d}\,, \tag{2.45}$$

where the subscript c stands for "continuous" and the subscript d for "dispersed". In the following, for droplets ($c=g$ and $d=l$), only the drag force is taken into account. The drag

Table 2.2: Expressions used for the drag, added mass and lift forces. $C_X = \{C_D, C_{AM}, C_L\}$.

Force	Expression	C_X for droplets	C_X for bubbles
$\underline{F}^D_{c\to d}$	$-\frac{6}{8}\frac{\alpha_d}{d_d}C_D\rho_c \left\|\underline{U}_d - \underline{U}_c\right\| (\underline{U}_d - \underline{U}_c)$	Gobin et al. (2003)	Ishii and Zuber (1979)
$\underline{F}^{AM}_{c\to d}$	$-\alpha_d C_{AM}\rho_c \left(\frac{D\underline{U}_d}{Dt} - \frac{D\underline{U}_c}{Dt}\right)$	–	Zuber (1964)
$\underline{F}^L_{c\to d}$	$-\alpha_d C_L\rho_c (\underline{U}_d - \underline{U}_c) \wedge (\underline{\nabla} \wedge \underline{U}_c)$	–	Tomiyama et al. (2002)

coefficient is obtained from the correlation of Gobin et al. (2003). For bubbles ($c = l$ and $d = g$), only the drag, added mass and lift forces are taken into account. The drag, added mass and lift coefficients are obtained from the correlations of Ishii and Zuber (1979), Zuber (1964) and Tomiyama et al. (2002), respectively. Expressions of these forces are given in Table 5.4, where d_d refers to the droplet/bubble diameter. It is given by: $d_d = {}^{6\alpha_d}/_{a_d^{int}}$, with a_d^{int} the interfacial area concentration. The latter is obtained by solving an additional transport equation, which takes into account size variation due to phase change for droplets (Mimouni et al., 2010, 2011) and due to phase change, coalescence and break-up for bubbles (Guelfi et al., 2007). The model of Ruyer et al. (2007) is used for bubble coalescence and break-up.

2.3.2.2 Interfacial energy and mass transfers for droplets

For droplets, the energy and mass transfers from the liquid to the gas are computed using the expressions proposed by Mimouni et al. (2010, 2011):

$$\Pi_{l\to g} = \frac{6\alpha_l}{d_l^2} \cdot Nu_g \cdot \lambda_g \cdot (T_l - T_g) \ , \tag{2.46}$$

$$\Gamma_{l\to g} = \frac{6\alpha_l}{d_l^2} \cdot Sh_g \cdot D \cdot (\rho_{s,sat}(T_l) - Y_s\rho_g) \ . \tag{2.47}$$

D is the diffusion coefficient of steam in air. It is obtained from the correlation of Oran and Boris (1981): $D = 4.88 \times 10^{-4} {}^{T^{3/2}}/_P$, with T computed as an average between the gas temperature T_g and the liquid temperature T_l. Nu_g and Sh_g are the gas Nusselt and Sherwood numbers. They are obtained from the correlations of Ranz and Marshall (1952): $Nu_g = 2 + 0.56 Re_{pl}^{1/2} Pr_g^{1/3}$ and $Sh_g = 2 + 0.56 Re_{pl}^{1/2} Sc_g^{1/3}$, with $Re_{pl} = {}^{\rho_g \left\|\underline{U}_g - \underline{U}_l\right\| d_l}/_{\mu_g}$ the liquid particle Reynolds number, $Pr_g = {}^{\mu_g Cp_g}/_{\lambda_g}$ the gas Prandtl number and $Sc_g = \frac{\mu_g}{\rho_g D}$ the gas Schmidt number. Cp_g, λ_g and μ_g are the gas heat capacity, thermal conductivity and molecular viscosity. Y_s and $\rho_{s,sat} = \rho_s(P_{sat}, T)$ are the steam mass fraction and saturation density. The steam mass fraction is given by: $Y_s = 1 - Y_a$, with Y_a the air mass fraction, obtained by solving an additional transport equation (Mimouni et al., 2010, 2011).

The energy and mass transfers from the gas to the liquid are deduced from:

$$\Pi_{g\to l} = -\Pi_{l\to g} - \Gamma_{l\to g} H_{lat}\,, \tag{2.48}$$

$$\Gamma_{g\to l} = -\Gamma_{l\to g}\,. \tag{2.49}$$

H_{lat} is the latent heat. It is given by: $H_{lat} = H_g - H_l$.

2.3.2.3 Interfacial energy and mass transfers for bubbles

For bubbles, the energy transfer from the gas to the liquid is computed using the expression proposed by Manon (2000):

$$\Pi_{g\to l} = \frac{6\alpha_g}{d_g^2} \cdot Nu_l \cdot \lambda_l \cdot (T_{sat} - T_l)\ . \tag{2.50}$$

Like the gas Nusselt number, the liquid Nusselt number Nu_l is obtained from the correlation of Ranz and Marshall (1952): $Nu_l = 2 + 0.56 Re_{pg}^{1/2} Pr_l^{1/3}$, with $Re_{pg} = \rho_l \left\| \underline{U}_g - \underline{U}_l \right\| d_g/\mu_l$ the gas particle Reynolds number and $Pr_l = \mu_l Cp_l/\lambda_l$ the liquid Prandtl number. Cp_l, λ_l and μ_l are the liquid heat capacity, thermal conductivity and molecular viscosity. T_{sat} is the saturation temperature.

The energy transfer from the liquid to the gas is computed as:

$$\Pi_{l\to g} = \alpha_g \alpha_l \frac{\rho_g Cp_g}{\tau_{relax}} (T_{sat} - T_g)\ . \tag{2.51}$$

Actually, this term is a penalty term, whose purpose is that the gas temperature remains close to the saturation temperature. Therefore, the characteristic time τ_{relax} has no physical meaning. It is chosen equal to the time step, so that $T_g \approx T_{sat}$ is met at each iteration in cells with bubbles.

The mass transfers are deduced from:

$$\Gamma_{g\to l} = -\Gamma_{l\to g} = \frac{\Pi_{g\to l} + \Pi_{l\to g}}{H_{lat}}\,. \tag{2.52}$$

2.3.2.4 Wall energy and mass transfers for droplets

At the wall, the mass transfers are computed using the expression proposed by Mimouni et al. (2010, 2011):

$$\Gamma_{w\to g} = -\Gamma_{w\to l} = \frac{S}{V} \cdot n_{site} \cdot \pi \cdot Sh_g \cdot D \cdot \frac{d_l}{2} \cdot (\rho_{s,sat}(T_w) - Y_s \rho_g)\ . \tag{2.53}$$

n_{site} is the number of droplets formed at nucleation sites per unit area. It is given by: $n_{site} = \frac{4A_l}{\pi d_l^2}$, with A_l the fraction of area affected by the liquid. Also, S/V is the ratio of the surface of the boundary face to the volume of the boundary cell. T_w is the wall temperature.

The energy transfers are computed as:

$$\varphi_{w\to g} = \varphi_{cond} + \varphi_{sp,g}\,, \tag{2.54}$$

$$\varphi_{w\to l} = \varphi_{sp,l}\,. \tag{2.55}$$

φ_{cond} is the condensation flux. It is deduced from: $\varphi_{cond} = \Gamma_{w\to g} H_{lat}$. $\varphi_{sp,g}$ and $\varphi_{sp,l}$ are the single-phase gas and liquid heat fluxes. They are obtained from: $\varphi_{sp,g} = (1 - A_l)\, h_{loc,g}\,(T_w - T_g)$ and $\varphi_{sp,l} = A_l h_{loc,l}\,(T_w - T_l)$, with $h_{loc,g}$ and $h_{loc,l}$ the gas and liquid local heat transfer coefficients. These coefficients are given by: $h_{loc,k} = \lambda_k/\Delta \cdot c_k$, with Δ the distance from the wall to the center of the boundary cell and c_k a dimensionless rescaling factor equal to unity in the laminar flow regime and provided by an analytical wall function in the turbulent flow regime.

2.3.3 Large Interface Model and Large Bubble Model

2.3.3.1 Interfacial momentum transfers

For large interfaces, the momentum transfers read as the sum of a generalized drag force $\underline{F}^D$, which allows to couple the gas and liquid velocities, and a surface tension force $\underline{F}^{ST}$:

$$\underline{I}_{l\to g} = \underline{F}^D_{l\to g} + \underline{F}^{ST}_g\,, \tag{2.56}$$

$$\underline{I}_{g\to l} = \underline{F}^D_{g\to l} + \underline{F}^{ST}_l\,. \tag{2.57}$$

$\underline{F}^D$ is computed using a combination of the expression proposed by Coste (2013) in the framework of the Large Interface Model and the expression proposed by Mimouni et al. (2017) in the framework of the Large Bubble Model:

$$\underline{F}^D_{l\to g} = \alpha_g \alpha_l \left[f_l^\theta + \theta\left(f_g^\theta - f_l^\theta\right)\right]\left(\underline{U}_l - \underline{U}_g\right)\,. \tag{2.58}$$

f_l^θ, f_g^θ and θ are given by: $f_l^\theta = 18^{\mu_g}/_{d_l^2}\,(1 + 0.15 Re_{pl})$, $f_g^\theta = 18^{\mu_l}/_{d_g^2}\,(1 + 0.15 Re_{pg})$ and $\theta = {}^1/_2\,(1 - \cos[\pi\alpha_l)]$, with Re_{pl} and Re_{pg} defined in Section 2.3.2.2 and Section 2.3.2.3, respectively. Originally introduced in the Large Bubble Model, $\underline{F}^{ST}$ is computed the same way as in this model:

$$\underline{F}^{ST}_k = \alpha_k \underline{F}^{ST}_{tot}\,, \tag{2.59}$$

with $\underline{F}_{tot}^{ST}$ obtained from the Continuum Surface Force approach of Brackbill et al. (1992):

$$\underline{F}_{tot}^{ST} = -\sigma \underline{\nabla} \cdot (\underline{n}_l) \, \underline{\nabla} \, \alpha_l \, . \tag{2.60}$$

$\underline{n}_l$ is the interface normal pointing towards g. It is given by: $\underline{n}_l = {}^{\underline{\nabla} \alpha_l}/_{\| \underline{\nabla} \alpha_l \|}$. σ is the surface tension. In order to maintain constant interface thickness, which is required to accurately compute the interface normal, an additional equation, called interface-sharpening equation, is solved for each field k in the cells assumed to contain a portion of large interface:

$$\frac{\partial \alpha_k}{\partial \tau} + \underline{\nabla} \cdot [\alpha_k \, (1 - \alpha_k) \, \underline{n}_k] = \varepsilon \underline{\nabla}^2 \, \alpha_k \, , \tag{2.61}$$

τ is an artificial time, different from the actual time t. ε allows to control the balance between compression (second term on the left-hand side) and diffusion (right-hand side). The time step $\Delta\tau$ and ε are set to ${}^{\Delta x}/_{32}$ and ${}^{\Delta x}/_{2}$, respectively, which results in an interface thickness of 5 cells.

2.3.3.2 Interfacial energy and mass transfers

For large interfaces, the energy transfers are computed using the expressions proposed by Fleau (2017) in the framework of the Large Bubble Model:

$$\Pi_{l \to g} = \alpha_g \alpha_l \lambda_g \underline{\nabla} \, T_g \cdot \underline{\nabla} \, \alpha_g \, , \tag{2.62}$$

$$\Pi_{g \to l} = \alpha_g \alpha_l \lambda_l \underline{\nabla} \, T_l \cdot \underline{\nabla} \, \alpha_l \, . \tag{2.63}$$

In the neptune_cfd code, a five-cell stencil is used for the gradients. Fleau (2017) showed that this could be a problem for temperature. Indeed, for a given interface cell, the stencil used to compute say the liquid temperature gradient could include cells with only gas, in which the liquid temperature does not make sense. As an alternative, the author proposed the following modified expression, based on the fact that condensing steam or evaporating liquid must be at saturation temperature: $\underline{\nabla} \, T_k = (T_{sat} - T_k) \, ({}^{\underline{e}_x}/_{\Delta x} + {}^{\underline{e}_y}/_{\Delta y} + {}^{\underline{e}_z}/_{\Delta z})$.

In the present work, since air is present, Eqs. (2.62) and (2.63) are weighted by Y_s. The resulting expressions are successfully validated by comparison with analytical data in a 1D phase change case based on the Stefan problem. However, for the sake of brevity, the results are not provided.

The mass transfers are deduced from the same equation as Eq. (2.52).

2.3.4 GLIM and LBM with bubbles

2.3.4.1 GLIM – Original and extended model

The Generalized Large Interface Model (GLIM) has been introduced by Mérigoux et al. (2016). It corresponds to a coupling between the LIM and the SDM. It uses two fields: one for the gas (g) and another for the liquid (l). Like the LBM with bubbles, which will be presented in the following section, it has originally been conceived for flows with resolved interfaces and dispersed bubbles. For the needs of the PhD, it has been extended to the case of dispersed droplets. The distinction between resolved interface, dispersed bubbles and dispersed droplets is made by applying the correct interfacial transfers depending on the composition of the cell. The interfacial transfers read as follows:

$$\Gamma_{p\to k} = \gamma \cdot \Gamma^{bub}_{p\to k} + \varepsilon \cdot \Gamma^{drop}_{p\to k} + (1-\gamma-\varepsilon)\cdot \Gamma^{li}_{p\to k}\,, \tag{2.64}$$

$$\underline{I}_{p\to k} = \gamma \cdot \underline{I}^{bub}_{p\to k} + \varepsilon \cdot \underline{I}^{drop}_{p\to k} + (1-\gamma-\varepsilon)\cdot \underline{I}^{li}_{p\to k}\,, \tag{2.65}$$

$$\Pi_{p\to k} = \gamma \cdot \Pi^{bub}_{p\to k} + \varepsilon \cdot \Pi^{drop}_{p\to k} + (1-\gamma-\varepsilon)\cdot \Pi^{li}_{p\to k}\,, \tag{2.66}$$

with $\gamma, \varepsilon, \gamma+\varepsilon \in [0,1]$. The expressions for $\Gamma^{drop}_{p\to k}$, $\underline{I}^{drop}_{p\to k}$ and $\Pi^{drop}_{p\to k}$ are provided in Sections 2.3.2.1, 2.3.2.2 and 2.3.2.4. Those for $\Gamma^{bub}_{p\to k}$, $\underline{I}^{bub}_{p\to k}$ and $\Pi^{bub}_{p\to k}$ are provided in Sections 2.3.2.1 and 2.3.2.3. Finally, those for $\Gamma^{li}_{p\to k}$, $\underline{I}^{li}_{p\to k}$ and $\Pi^{li}_{p\to k}$ are provided in Section 2.3.3. The diameter of the droplets and bubbles is obtained by solving two distinct interfacial area equations, one for the droplets and another for the bubbles. In addition, the interface sharpening Eq. (2.61) is solved for both the gas and the liquid. To be consistent with Eqs. (2.64) to (2.66), the compressive and diffusive terms are weighted by $(1-\gamma-\varepsilon)$. In the original GLIM, the coefficient ε did not exist, due to the fact that the droplets were not included in the model. The coefficient γ was obtained from: $\gamma = \beta\cdot\beta'$ (2.67). The coefficient β was defined as: $\beta = 0$ if $\alpha_l < \alpha_l^{li}$, $\beta = 1$ if $\alpha_l > \alpha_l^{bub}$, $\beta = {}^{\alpha_l - \alpha_l^{li}}/_{\alpha_l^{bub} - \alpha_l^{li}}$ otherwise (2.68). α_l^{li} was set to 0.5 and α_l^{bub} to 0.7. These values were optimized based on the results obtained in various adiabatic validation cases. The coefficient β', used to detect a potential large interface in the cases where $\beta \neq 0$, was obtained from: $\beta' = 1 - \min\left({}^{\|\underline{\nabla}\alpha\|}/_{\nabla\alpha_{max}}, 1\right)$ (2.69) with, for an interface thickness of 5 cells, $\nabla\alpha_{max} = {}^{1}/_{5\Delta x}$. Eqs. (2.67) and (2.68) as well as $\alpha_l^{li} = 0.5$ are kept for use in the extended GLIM. The coefficient ε is obtained from: $\varepsilon = \delta\cdot\beta'$ (2.70). The coefficient δ is computed as: $\delta = 1$ if $\alpha_l < \alpha_l^{drop}$, $\delta = 0$ if $\alpha_l > \alpha_l^{li}$, $\delta = {}^{\alpha_l - \alpha_l^{li}}/_{\alpha_l^{drop} - \alpha_l^{li}}$ otherwise (2.71). α_l^{drop} is defined in a symmetric way to α_l^{bub}: $\alpha_l^{drop} = 1 - \alpha_l^{bub}$. Since the validation cases in the following include heat transfer with phase change, there is no guarantee that the previous values for β' and α_l^{bub} are still optimal. Therefore, different combinations will be tested. They are given in Table 2.3. Combinations 1-2 and 3-4 differ in the value for α_l^{bub} and α_l^{drop}, while combinations 1-3 and 2-4 differ in the values for β'.

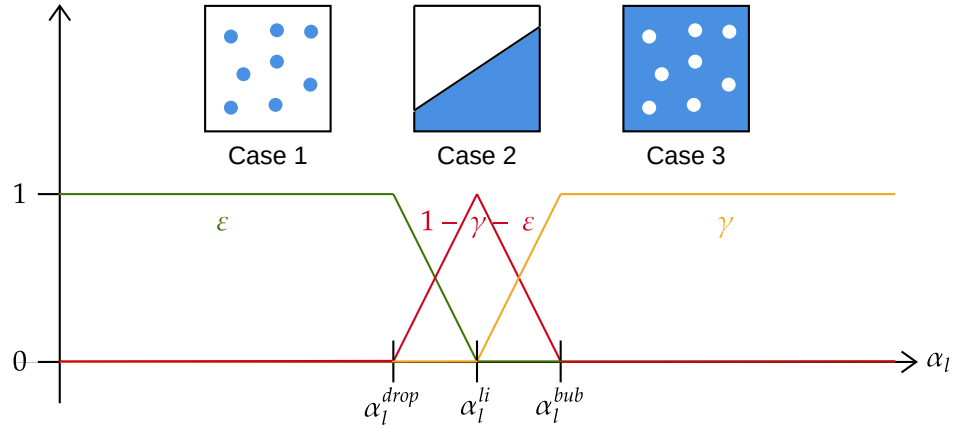

(a) β' in the limit $\|\underline{\nabla}\,\alpha\| \approx 0$ or $\beta' = 1$

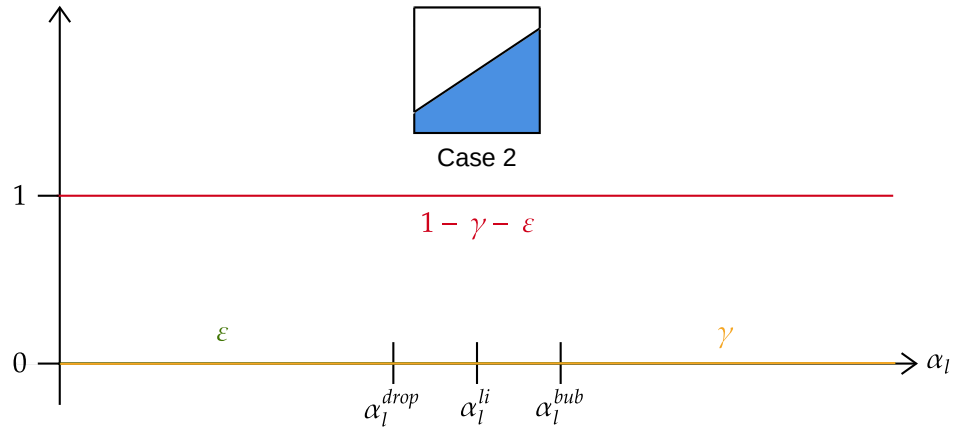

(b) β' in the limit $\|\underline{\nabla}\,\alpha\| \approx {}^{S}/_{V}$

Figure 2.4: Principle of the FGLIM. The model uses a sub-grid approach in Cases 1 and 3 and an interface capturing approach in Case 2. Closures for mass, momentum and energy used in Cases 1 and 3 come from the Standard Dispersed Model for droplets and the Standard Dispersed Model for bubbles, respectively. Those used in Case 2 come from the Large Interface Model.

Table 2.3: Combinations tested for the parameter β' (Eqs. (2.67) and (2.70)) and the parameters α_l^{drop}, α_l^{li} and α_l^{bub} (Eqs. (2.68) and (2.71)).

Criterion	β'	α_l^{drop}	α_l^{li}	α_l^{bub}	Illustrating figure
1	Eq. (2.69)	0.3	0.5	0.7	Figs. 2.4a and 2.4b
2	Eq. (2.69)	0.4	0.5	0.6	Figs. 2.4a and 2.4b
3	1	0.3	0.5	0.7	Fig. 2.4a
4	1	0.4	0.5	0.6	Fig. 2.4a

2.3.4.2 LBM with bubbles – Original and extended model

The Large Bubble Model with bubbles (LBMb) has been introduced by Denèfle et al. (2015); Fleau et al. (2015). It corresponds to a coupling between the LBM and the SDM. Like the GLIM, it has originally been developed for flows with resolved interfaces and dispersed bubbles. The difference is that the dispersed bubbles are considered as a separate field (see Fig. 2.5). During the PhD, it has also been extended to dispersed droplets. In the extended LBMb, as shown in Fig. 2.6, four fields are used: a continuous gas field (cg), a dispersed gas field (dg), a continuous liquid field (cl) and a dispersed liquid field (dl). Each field has its own interfacial transfers. Therefore, no weighting is required as in the GLIM. The expressions for the transfers between the continuous gas and the dispersed liquid are provided in Sections 2.3.2.1, 2.3.2.2 and 2.3.2.4, those for the transfers between the continuous liquid and the dispersed gas are provided in Sections 2.3.2.1 and 2.3.2.3 and those for the transfers between the continuous gas and the continuous liquid are provided in Section 2.3.3. Two interfacial area equations are solved, one for the dispersed droplets and another for the dispersed bubbles. In addition, the interface sharpening Eq. (2.61) is solved for both the continuous gas and the continuous liquid. In the original LBM, one transfer term was used used for the transfer from the continuous gas to the dispersed gas, and another was used for the transfer from the dispersed gas to the continuous gas. These were obtained from the following expressions:

$$\Gamma_{dg\to cg} = \alpha_{dg}\frac{\rho_{dg}}{\Delta t}C_{dg\to cg}H\left(\delta_{dg\to cg}\right) , \tag{2.72}$$

$$\Gamma_{cg\to dg} = \alpha_{cg}\frac{\rho_{cg}}{\Delta t}C_{cg\to dg}H\left(\delta_{cg\to dg}\right) . \tag{2.73}$$

with H the Heaviside function, which is such that $H\left(\delta\right) = 0$ if $\delta < 0$ and $H\left(\delta\right) = 1$ if $\delta > 0$. Unlike in the GLIM, it was thus possible to distinguish the criteria to switch from dispersed gas to continuous gas from the criteria to switch from continuous gas to dispersed gas. The quantity $\delta_{dg\to cg}$ was set to $\alpha_{dg} - 0.3$ and the quantity $\delta_{cg\to dg}$ to $\kappa \left\|\underline{\nabla}\,\alpha_{cg}\right\| V_\Omega - {}^{\Delta x}/_{20}$. The limiting value 0.3 was empirical, based on experiments from the literature (Taitel et al., 1980;

Table 2.4: Combinations tested for the parameters $\delta_{dg\to cg}$, $\delta_{cg\to dg}$, $\delta_{dl\to cl}$ and $\delta_{cl\to dl}$ (Eqs. (2.72) to (2.75)).

Criterion	$\delta_{dg\to cg}$	$\delta_{cg\to dg}$	$\delta_{dl\to cl}$	$\delta_{cl\to dl}$
1	$\alpha_{dg} - 0.3$	$\kappa \left\|\underline{\nabla}\,\alpha_{cg}\right\| V_\Omega - {}^{\Delta x}/_{20}$	$\alpha_{dl} - 0.3$	$\kappa \left\|\underline{\nabla}\,\alpha_{cl}\right\| V_\Omega - {}^{\Delta x}/_{20}$
3	$\alpha_{dg} - 0.3$	$0.3 - \alpha_{cg}$	$\alpha_{dl} - 0.3$	$0.3 - \alpha_{cl}$

Griffith and Synder, 1964). The idea of the other criterion was to switch from continuous gas to dispersed gas when the curvature of the resolved interface is too large and can no longer be described correctly by the mesh (see Denèfle et al. (2015) for derivation). Note that the limiting value ${}^{\Delta x}/_{20}$ assumes that the interface has a thickness of 5 cells. The dimensionless coefficients $C_{dg\to cg}$ and $C_{cg\to dg}$, used to control the intensity of the transfers, were set to 0.05 and 0.01. Eqs. (2.72) and (2.73) are kept for use in the extended LBM. Equivalent expressions are used for the transfers between the dispersed liquid and the continuous liquid:

$$\Gamma_{dl\to cl} = \alpha_{dl}\frac{\rho_{dl}}{\Delta t}C_{dl\to cl}H\left(\delta_{dl\to cl}\right) , \tag{2.74}$$

$$\Gamma_{cl\to dl} = \alpha_{cl}\frac{\rho_{cl}}{\Delta t}C_{cl\to dl}H\left(\delta_{cl\to dl}\right) , \tag{2.75}$$

As previously in the extended GLIM, different combinations will be tested for $\delta_{dg\to cg}$, $\delta_{cg\to dg}$, $\delta_{dl\to cl}$ and $\delta_{cl\to dl}$. They are presented in Table 2.4. The first combination uses the above expressions for $\delta_{dg\to cg}$ and $\delta_{cg\to dg}$ and similar expressions for $\delta_{dl\to cl}$ and $\delta_{cl\to dl}$. The second combination use the same criteria for the transfer from the dispersed gas/liquid to the continuous gas/liquid and for the transfer from the continuous gas/liquid to the dispersed gas/liquid. It is equivalent to combination 3 in the extended GLIM (see Table 2.3).

2.3.4.3 Discussion on the extended GLIM and the extended LBMb

In the following, for the sake of clarity, the extended GLIM will be called FGLIM (Full Generalized Large Interface Model) and the extended LBMb will be called 4FM (4-Field Model). These two models constitute original contributions. From a theoretical point of view, they are almost equivalent. They are designed to allow for the simulation of a wide range of flow regimes, including droplet flow, unlike most of the hybrid models discussed in Section 2.2.3. The main interest is that several flow regimes can occur simultaneously at various places in the domain. The difference between the two models is that the FGLIM cannot handle cells with at the same time droplets, bubbles and large interfaces. However, in practice, this situation is expected to be rarely encoutered.

The models and therefore the criteria Tables 2.3 and 2.4 for switching between the

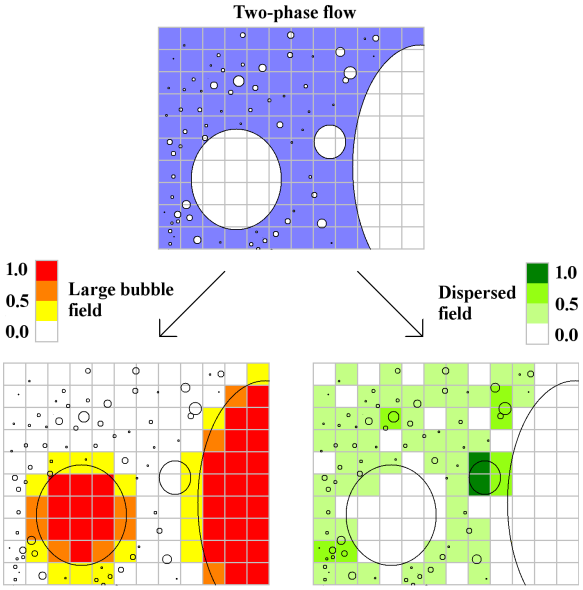

Figure 2.5: Original Large Bubble Model with bubbles developed by Denèfle et al. (2015); Fleau (2017). Three computational fields are used: a continuous liquid field (in blue), a continuous gas field (in red, orange, yellow), and a dispersed gas field (in green). Picture from Fleau (2017).

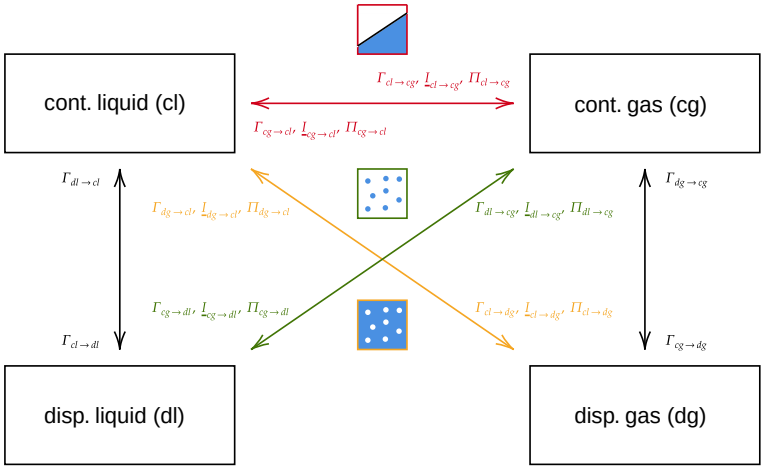

Figure 2.6: Extended Large Bubble Model developed in the present thesis. Four computational fields are used: a continuous liquid field (top left), a continuous gas field (top right), a dispersed liquid field (bottom left) and a dispersed gas field (bottom right). The transfer terms are given (i) in Sections 2.3.2.1, 2.3.2.2 and 2.3.2.4 for the transfers between the continuous gas and the dispersed liquid (in green), (ii) in Sections 2.3.2.1 and 2.3.2.3 for the transfers between the continuous liquid and the dispersed gas (in yellow), (iii) in Section 2.3.3 for the transfers between the continuous gas and the continuous liquid (in red), (iv) by Eqs. (2.72) and (2.73) for the transfers between the continuous liquid and the dispersed liquid (in black) and (v) by Eqs. (2.74) and (2.75) for the transfers between the continuous gas and the dispersed gas (in black).

dispersed approach and the interface capturing approach will be validated in the following chapter. Except Criterion 1 in Table 2.4, which also rely on the mesh resolution, they all rely on the volume fraction, which is a debatable assumption. Other choices could have been made. For instance, all the criteria could have use only the mesh resolution, like in the model of De Santis et al. (2021). However, this is also questionable, since the mesh size does not guarantee that, physically speaking, the conditions are met to switch from droplets or bubbles to a large interface for instance. The best would be to use both the mesh resolution and dimensionless numbers. Numerous criteria for break-up of large bubbles and droplets based on dimensionless numbers are available in the literature – see Clift et al. (1978); Hinze (1955) and the review of Jain (2017) for additional references. Note that these dimensionless numbers depend on the flow conditions (Capillary number for viscous-dominated flow, Eötvos number for gravity-dominated flow and Weber number for turbulent flow) and their critical value vary according whether a bubble or a droplet is considered. Much less criteria are available for coalescence, especially for droplets – see for instance Chen et al. (2009a), but the results are restricted to relatively large droplets. Some of the criteria available for bubble break-up in the turbulent flow regime have been implemented in the code in the framework of the master's thesis of Leau (2020). Further work is required for the laminar flow regime, and also for the droplets, but this was beyond the scope of the present thesis.

It is worth noting that the FGLIM and the 4FM have required significant developments in the code, performed in collaboration with the development team. An important number of routines have been impacted and some other parts of the code have been reorganized for compatibility.

2.4 Summary

In this chapter, the two existing approaches for the simulation of two-phase flows were presented. In the two-fluid approach, the conservation equations are solved for each phase at each point of the domain. The equations include interfacial transfer terms that have to be modeled. These must satisfy the jump conditions at the interface, e.g., the sum of the momentum transfers must equal the surface tension force. In the single-fluid approach, a single set of equations is solved using the properties of the phase present at the considered point. An additional equation is required to capture the interface. The jumps of mass, momentum and energy at the interface are either included as source terms in the equations or solved as jump conditions. The formulation corresponding to the former case was called standard homogeneous formulation, while that corresponding to the latter case was called jump condition formulation.

For dispersed flows, the available Eulerian methods include the two-fluid method, based on the two-fluid approach, and the drift-flux method, based on the single-fluid approach with standard homogeneous formulation. For resolved interfaces, the available models include the VOF, LS and FT methods, which differ in the equation solved to capture the interface, and the two-fluid method for resolved interfaces. The former methods are based on the single-fluid approach and can be used with either the standard homogeneous formulation or the jump condition formulation, while the latter method is based on the two-fluid approach.

In addition, the equations solved and the models available in the neptune_cfd code, employed in the PhD, have been presented. The equations solved correspond to those of the two-fluid approach, with additional terms for the exchanges at the wall. The models available include a model for dispersed droplets or bubbles and two models for resolved interfaces. Each one uses a specific set of closure laws for the interfacial transfers. Two hybrid models for resolved interfaces and dispersed bubbles are also available. They combine the closure laws used in the previous models. For the needs of the PhD, the two hybrid models have been extended to dispersed droplets. The extended models constitute an original contribution, since they in principle allow for the simulation of any kind of flow regime. The next chapter is devoted to their validation against different test cases.

Chapter 3

Validation of the proposed two- and four-field models

Contents

3.1 Introduction 60

3.2 BHAGA validation case 61

3.2.1 Problem setup 61

3.2.2 Results 61

3.3 STEFAN WITH NCG validation case 64

3.3.1 Problem setup 64

3.3.2 Results 65

3.4 COPAIN validation case 67

3.4.1 Problem setup 67

3.4.2 Results 69

3.5 BARTOLOMEI validation case 70

3.5.1 Problem setup 70

3.5.2 Results 74

3.6 Summary 75

3.1 Introduction

In the previous chapter, the FGLIM and the 4FM, developed in the framework of the present thesis, were introduced. As a reminder, both combine a sub-grid approach and an interface capturing approach, and allow for the simulation of flows with droplets, bubbles and large interfaces. The main difference between them is that the 4FM uses four computational fields, while the FGLIM only uses two computational fields. The purposes of this chapter are (i) to assess the validity of the developments performed in the code in cases involving droplets, bubbles or larges interfaces – cases involving simultaneously droplets, bubbles and larges interfaces will be considered in the next chapter – and (ii) to choose a criterion to switch between the sub-grid approach and the interface capturing approach among those proposed in the previous chapter – see Tables 2.3 and 2.4.

The industrial problem discussed in Chapter 1 corresponds to steam condensation in confined geometries in the presence of air, which is a non-condensable gas. Infortunately, no experiment of phase change in a confined geometry, involving droplets/bubbles/larges interfaces together with air could be found in the literature. As a consequence, the cases studied in the present chapter do not correspond to confined geometries. However, some of them involve air. All are listed in Table 3.1. The BHAGA case, based on the experiments of Bhaga and Weber (1981), corresponds to a two-dimensional axisymmetric problem in which a large bubble of air rises in a viscous liquid. The STEFAN WITH NCG case, inspired from the classical Stefan problem – see for instance Lienhard IV and Lienhard V (2017) – and based on the analytical work of Law (2006), corresponds to a one-dimensional problem in which a large interface moves horizontally due to direct contact condensation of steam, in the presence of air. The COPAIN case, based on the experiments of Cheng et al. (2001), corresponds to a three-dimensional problem in which superheated steam condenses, in the presence of air, in the form of small droplets on a vertical plate. Finally, the BARTOLOMEI case, based on the experiments of Bartolomei et al. (1982), corresponds to a two-dimensional axisymmetric problem in which subcooled water evaporates in the form of small bubbles in a vertical pipe.[1]

The BHAGA, COPAIN and BARTOLOMEI cases have already been studied numerically in the past – see for instance Bonometti and Magnaudet (2007); Denèfle et al. (2015); Fleau (2017); Pianet et al. (2010) for the BHAGA case, Bian et al. (2019); Dehbi et al. (2013); Mimouni et al. (2011) for the COPAIN case and Pal and K (2021); Lavieville et al. (2017); Murallidharan et al. (2016) for the BARTOLOMEI case. Note that Denèfle et al. (2015); Fleau (2017); Lavieville et al. (2017); Mimouni et al. (2011) used the neptune_cfd code but employed the Standard Dispersed Model or the Large Bubble Model. The STE-

[1]The wall mass and energy transfers in Chapter 2 correspond to droplets. For bubbles, only involved in the BARTOLOMEI case, the reader is referred to Mimouni et al. (2010, 2011).

Table 3.1: Validation cases considered in the present chapter.

Case name	Flow structure	Reference
BHAGA	Large interface	Bhaga and Weber (1981)
STEFAN WITH NCG	Large interface	Law (2006)
COPAIN	Dispersed droplets	Cheng et al. (2001)
BARTOLOMEI	Dispersed bubbles	Bartolomei et al. (1982)

FAN WITH NCG has already been studied analytically but, to our knowledge, never been studied numerically, unlike the classical Stefan problem with pure steam – see for instance Fleau (2017); Sato and Ničeno (2013). Among the cases mentioned, the BHAGA and the STEFAN WITH NCG cases will be of great interest for the FGLIM. Indeed, they will allow to characterize the impact of the application of the closures for the droplets and the bubbles in cells supposed to be part of a large interface – see the weighting in Eqs. (2.64) to (2.66).

3.2 BHAGA validation case

3.2.1 Problem setup

The case in the present section is based on the experiments of Bhaga and Weber (1981), corresponding to the rise of a large bubble of air – of volume $9.3\,\mathrm{cm}^3$ – in viscous liquid. The axisymmetric computational domain shown in Fig. 3.1, of length 31.2 cm and radius 10.4 cm, is considered. A pressure boundary condition is imposed at the outlet. The pressure is set to 1.013 bar. Since the flow is laminar, no turbulence model is required. A uniform mesh, composed of 540×179 cells, is used. The bubble is initialized as a half-disc of center $(0, 3.9)$ cm and radius 1.3 cm. Constant physical properties are used. The surface tension coefficient is set to $0.0785\,\mathrm{N\,m^{-1}}$. The gas density and viscosity are set to $1.35\,\mathrm{kg\,m^{-3}}$ and $1.8 \times 10^{-5}\,\mathrm{Pa\,s}$, respectively. The liquid density is set to $1350\,\mathrm{kg\,m^{-3}}$. The liquid viscosity – deduced from the experimental Morton number (ratio of viscous to surface tension forces) – is given in Table 3.2. A constant time step is used. It is set to 10^{-4} s, leading to a Courant number – defined as $\|\underline{U}_k\| \frac{\Delta t}{\Delta x}$, with Δt the time step and Δx the grid spacing – below 1 for both the gas and the liquid. The calculations are run for 0.6 s.

3.2.2 Results

The parameters of interest are the bubble steady-state shape and velocity. Only the FGLIM is considered. The bubble steady-state shape is obtained by extracting the $\alpha_l = 0.5$ isosur-

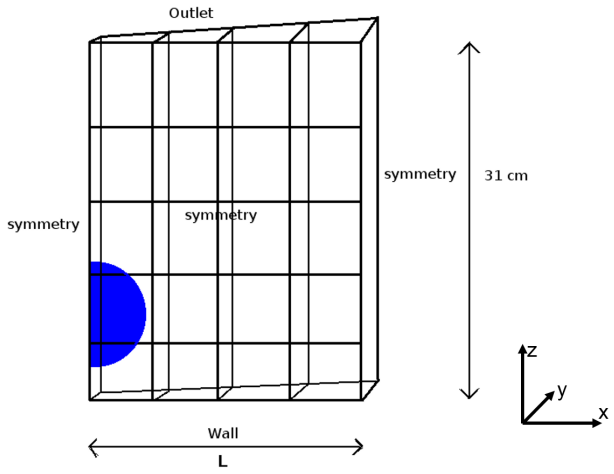

Figure 3.1: Computational domain used in the BHAGA case. The domain is two-dimensional and axisymmetric, and has a height of 31.2 cm and a width of 10.4 cm. Pressure is imposed at the outlet. Picture from Fleau (2017).

Table 3.2: Experimental values of the Morton number (ratio of viscous to surface tension force) considered in the BHAGA case and resulting values of the liquid viscosity.

Calculation name	Experimental Morton number	Liquid viscosity [Pa s]
b	266	2.02
d	5.51	0.77

face. The bubble steady-state velocity U_g^{st} is obtained from the following equation:

$$U_g^{st} = \frac{\int_{V_\Omega} \alpha_g U_{g,z} \mathrm{d}V_\Omega}{\int_{V_\Omega} \alpha_g \mathrm{d}V_\Omega} \,. \tag{3.1}$$

A comparison is made with the available experimental data – the experimental bubble velocity is deduced from the experimental Reynolds, see Table 3.3 after. For the sake of brievety, only the results of Calculation d are presented.

The steady-state bubble shape obtained with the FGLIM is shown in Figs. 3.2 and 3.3 for Case b. All the criteria in Table 2.3 are considered. The corresponding values of the steady-sate bubble velocity are provided in Table 3.3. For the steady-state bubble shape, no clear distinction can be made between the various criteria. The bubble is a little flatter than in the experiment but overall a good agreement is achieved. For the steady-state bubble velocity, differences exist but they are not significant. Again, a good agreement is obtained with the experiment. For Criteria 3 and 4, it is interesting to note the good agreement obtained for both the bubble shape and velocity. Indeed, for these two criteria, such a good agreement was not expected since they do not use the coefficient β' (see Section 2.3.4.1) –

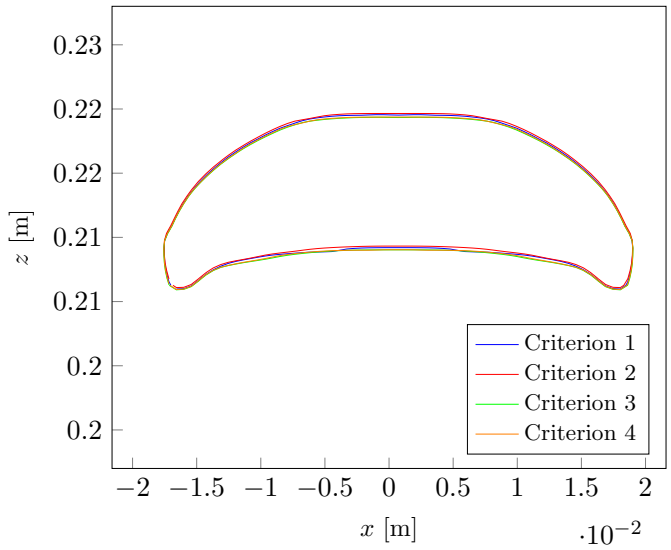

Figure 3.2: Steady-state interface shape obtained in the BHAGA case with the FGLIM for Calculation d. The interface is defined as the $\alpha_l = 0.5$ isosurface. A comparison is made between the criteria in Table 2.3.

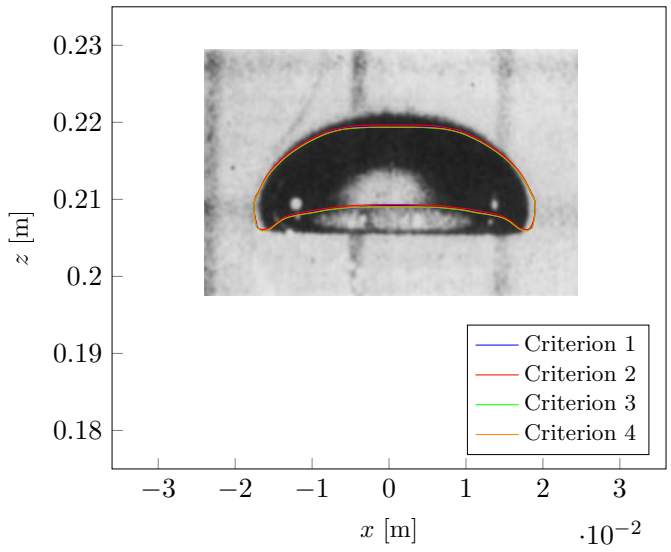

Figure 3.3: Steady-state interface shape obtained in the BHAGA case with the FGLIM for Calculation d. The interface is defined as the $\alpha_l = 0.5$ isosurface. All the criteria in Table 2.3 are considered. A comparison is made with the available experimental data (Bhaga and Weber, 1981). The experimental picture is scaled so that the grid in the background, of size 2×2 cm, matches the dimensions of the graph.

Table 3.3: Experimental value of the Reynolds number corresponding to Calculation d in the BHAGA case and resulting value of the steady-state bubble velocity, along with numerical values of the steady-state velocity (Eq. (3.1)) obtained with the FGLIM for the various criteria in Table 2.3.

Calc. name	Exp. Reynolds	Exp. vel. [$\mathrm{m\,s^{-1}}$]	U_g^{st} [$\mathrm{m\,s^{-1}}$]			
			Crit. 1	Crit. 2	Crit. 3	Crit. 4
d	13.3	0.29	0.286302	0.286925	0.285928	0.285832

introduced in order to decrease the contributions of the droplets and bubbles in the zones with a high volume fraction gradient, supposed to correspond to large interfaces.

3.3 STEFAN WITH NCG validation case

3.3.1 Problem setup

The case in this section is based on the classical one-dimensional Stefan problem, which has been widely studied in the literature, both analytically – see for instance Lienhard IV and Lienhard V (2017) – and numerically – see for instance Fleau (2017); Sato and Ničeno (2013). This problem aims to "describe the evolution of the boundary between two phases of a material undergoing phase change". Unlike most of the cases in the literature, which considered the process of evaporation or melting of pure water, the present case considers the phenomenon of water vapor condensation in the presence of air. The computational domain, of length 0.3 cm, is shown in Fig. 3.4. The left part is filled with water, which is cooled by the adjacent wall. The right part is filled with a mixture of water vapor and air, and the water vapor condenses on the liquid-vapor interface. Pressure and composition boundary conditions are imposed at the outlet and a temperature boundary condition is imposed at the wall. The boundary condition values are given in Table 3.4. Since the flow is laminar, no turbulence model is required. To save computational time, surface tension is deactivated. Two uniform Cartesian meshes, composed of 200 and 400 cells, are used. At initial state, the first three cells are full of water, the five following cells have a water volume fraction of, respectively, 0.875, 0.75, 0.5, 0.25 and 0.125, and the other cells are full of vapor. The physical properties are automatically computed using the CATHARE tables (Emonot et al., 2011). A constant time step is used. It is set to 5×10^{-5} s for the coarse mesh and 10^{-5} s for the fine mesh, leading to Courant and Fourier numbers – defined as $\|\underline{U}_k\| \frac{\Delta t}{\Delta x}$ and $\frac{\lambda_k}{\rho_k C p_k} \frac{\Delta t}{\Delta x}$, with Δt the time step and Δx the grid spacing – below 1 and 10 for both the gas and the liquid. The calculations are run for 500 s, which is found to be sufficient to observe a significant displacement of the interface.

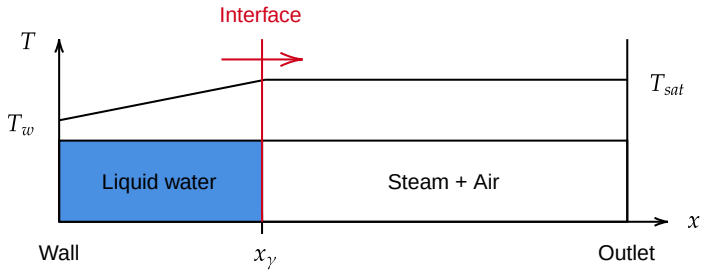

Figure 3.4: Computational domain used in the STEFAN WITH NCG case. The domain is one-dimensional and has a length of 0.3 cm. Pressure and composition are imposed at the outlet and temperature is imposed at the wall.

Table 3.4: Values of the outlet pressure and air molar fraction, and wall temperature considered in the STEFAN with NCG case.

Outlet		Wall
Pressure [bar]	Air molar fraction	Temperature [K]
1.013	0.065	348.15

3.3.2 Results

The quantity of interest is the interface position x_γ, which vary over time. It is obtained by extracting the $\alpha_l = 0.5$ isosurface for the FGLIM and the $\alpha_{cl} + \alpha_{dl} = 0.5$ isosurface for the 4FM. A comparison is made with a semi-analytical solution, derived in Appendix A, and based on the work of Law (2006). To summarize the appendix, one can show analytically that x_γ verify:

$$\frac{dx_\gamma}{dt} = \frac{\lambda_l}{\rho_l L} \frac{T_\gamma - T_w}{x_\gamma} . \tag{3.2}$$

with L the latent heat of condensation, T_γ the interface temperature, T_w the wall temperature, λ_l the liquid thermal conductivity and ρ_l the liquid density. The interface temperature T_γ is solution of the following equation, based on Clapeyron's law:

$$1 - X_{a,b} \exp\left[\frac{\lambda_l}{\rho_v D L} \frac{T_w - T_\gamma}{x_\gamma} (x_\gamma - x_b)\right] = \frac{P_0}{P} \exp\left[\frac{L M_{H_2O}}{R}\left(\frac{1}{T_0} - \frac{1}{T_\gamma}\right)\right] , \tag{3.3}$$

with D the coefficient of diffusion of steam in air, M_{H_2O} the water molar mass, P the pressure, P_0 the reference pressure, R the perfect gas constant, T_0 the reference temperature associated with P_0, $X_{a,b}$ the air molar fraction imposed at the outlet, x_b the x-coordinate corresponding to the outlet and ρ_v the gas density. Eq. (3.2) is solved in the following form,

Table 3.5: Physical properties used in the computation of the analytical solution to the STEFAN WITH NCG problem (Eqs. (3.3) and (3.4)).

λ_l	ρ_l	ρ_v	D	L	M_{H_2O}	R
$[\mathrm{W\,m^{-1}\,K^{-1}}]$	$[\mathrm{kg\,m^{-3}}]$	$[\mathrm{kg\,m^{-3}}]$	$[\mathrm{m^2\,s^{-1}}]$	$[\mathrm{J\,kg^{-1}}]$	$[\mathrm{kg\,mol^{-1}}]$	$[\mathrm{J\,mol^{-1}\,K^{-1}}]$
0.678	969	0.593	2.86×10^{-5}	2.30×10^{6}	0.0180	8.31

using MATLAB:

$$x_\gamma^{n+1} \approx x_\gamma^n + \frac{\lambda_l}{\rho_l L} \frac{T_\gamma^n - T_w}{x_\gamma^n} \Delta t \,, \tag{3.4}$$

with n the current iteration number and Δt the time step. The interface temperature at iteration n T_γ^n is obtained from Eq. (3.3). The physical properties, assumed to be constant, are given in Table 3.5. Δt is set to 10^{-2} and the total number of iterations to 6×10^4.

Mesh convergence is studied with the FGLIM only. Criteria 2 in Table 2.3 is arbitrarily used. The results are shown in Fig. 3.5. It is interesting to observe that the mesh with the lowest number of cells leads to an accurate prediction of the interface position. Increasing the number of cells has the effect that the numerical solution is closer to the analytical one. The drawback is that, since the time step is reduced, the computation time increases. The mesh composed of 200 cells being a good compromise between accuracy and calculation cost, it is kept for use in subsequent calculations.

The results obtained with the FGLIM for all the critera in Table 2.3 are shown in Fig. 3.6. The interface position is found to be almost the same for Criteria 1 and 2 and for Criteria 3 and 4. In all cases, a good agreement is obtained with the analytical solution. However, the agreement is found to be slightly better for Criteria 1 and 2 than for Criteria 3 and 4. This is due to the fact that Criteria 1 and 2 use the coefficient β' (see Section 2.3.4.1) – introduced in order to decrease the contributions of the droplets and bubbles in the zones with a high volume fraction gradient, supposed to correspond to large interfaces. It is still interesting to note that predictive results are achieved for Criteria 3 and 4, although they do not depend on the coefficient β'.

The results obtained with the 4FM for the criteria in Table 2.4 are shown in Fig. 3.7. Criteria 1 and 3 give almost identical results from about 300 s. Before that time, Criterion 1 gives results similar to Criteria 1 and 2 in the FGLIM and Criterion 3 results similar to Criteria 3 and 4 in the FGLIM. As previously with the FGLIM, a good agreement is achieved with the analytical data for all the criteria studied. The agreement is slightly less good for Criterion 1, which is attributed to the fact that a part of the mass of the condensation front is transferred from the continuous to the dispersed fields and therefore treated with different closures laws for phase change. For Criterion 3, such a transfer does not occur since the condensation front remains flat and therefore $\delta_{cg\to dg}$ and $\delta_{cg\to dg}$, which

involve the interface curvature, remain null.

3.4 COPAIN validation case

3.4.1 Problem setup

The case in this section is based on the COPAIN facility, designed to study wall condensation in the presence of non-condensable gases (Cheng et al., 2001). This facility has already been studied numerically by several authors in the literature, including Bian et al. (2019); Dehbi et al. (2013); Mimouni et al. (2011) – Mimouni et al. (2011) used the neptune_cfd code but employed the Standard Dispersed Model for droplets. The computational domain, consisting of a rectangular channel of length 2.5 m, width 0.6 m and depth 0.5 m, is shown in Fig. 3.8. A mixture of steam and air is injected at the inlet, and steam condenses on the vertical plate – of length 2 m and width 0.6 m – on the left, which is maintained at a constant temperature below the saturation temperature. Velocity, temperature and composition boundary conditions are imposed at the inlet, a pressure boundary condition is imposed at the outlet and a temperature boundary condition is imposed at the wall corresponding to the plate. The boundary condition values are given in Table 3.6. As in Mimouni et al. (2011), the gas phase is assumed to be turbulent and the liquid phase to be laminar. For the gas phase, a $k-\varepsilon$ model is used. A uniform Cartesian mesh consisting of $60 \times 50 \times 50$ cells is used. The dimensionless distance from the wall to the center of the adjacent cells – defined, for the gas phase, as:

$$y_g^+ = \frac{y u_{\tau,g}}{\nu_g}, \tag{3.5}$$

with $\nu_g = \mu_g/\rho_g$ and $u_{\tau,g} = \sqrt{\tau_{w,g}/\rho_g}$, $\tau_{w,g}$ being the wall shear stress – is found to be greater than 30, as required by the turbulence model[2] – in Calculation P344 for instance, it is about 37 in average over the wall. The physical properties are automatically computed using the CATHARE tables (Emonot et al., 2011). An adaptive time-stepping strategy is adopted. The maximum Courant and Fourier numbers – defined as $\|\underline{U}_k\| \frac{\Delta t}{\Delta x}$ and $\frac{\lambda_k}{\rho_k C p_k} \frac{\Delta t}{\Delta x}$, with Δt the time step and Δx the grid spacing – are set to 1 and 10 for both the gas and the liquid. The calculations are run for 15 s, which is found to be sufficient to reach a permanent flow regime.

[2]This value corresponding to the transition between the buffer layer and the log-law region.

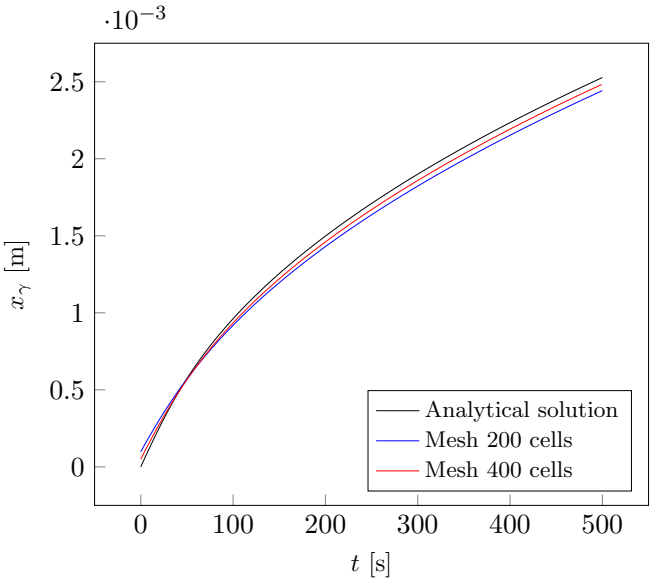

Figure 3.5: Evolution of the interface position over time in the STEFAN WITH NCG case with the FGLIM. The interface is defined as the $\alpha_l = 0.5$ isosurface. Criteria 2, among those proposed in Table 2.3, is arbitrarily used. Both the mesh with 200 cells and that with 400 cells are considered. A comparison is made with the analytical solution given by Eqs. (3.3) and (3.4).

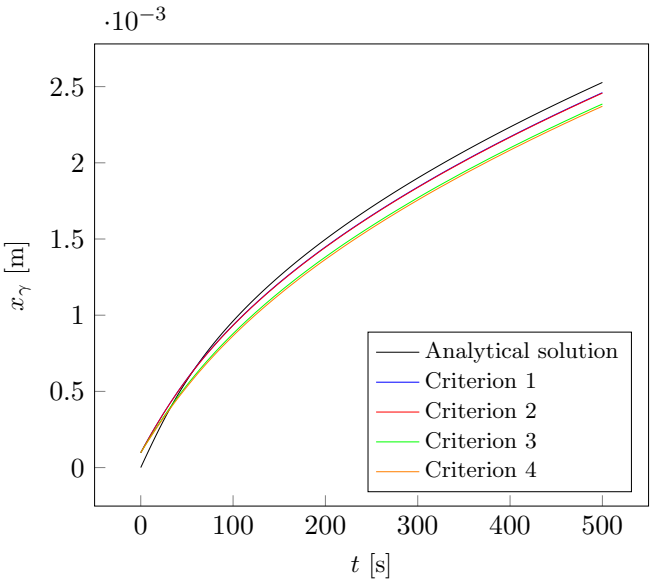

Figure 3.6: Evolution of the interface position over time in the STEFAN WITH NCG case with the FGLIM. The interface is defined as the $\alpha_l = 0.5$ isosurface. The mesh with 200 cells is used. All the criteria in Table 2.3 are considered. A comparison is made with the analytical solution given by Eqs. (3.3) and (3.4).

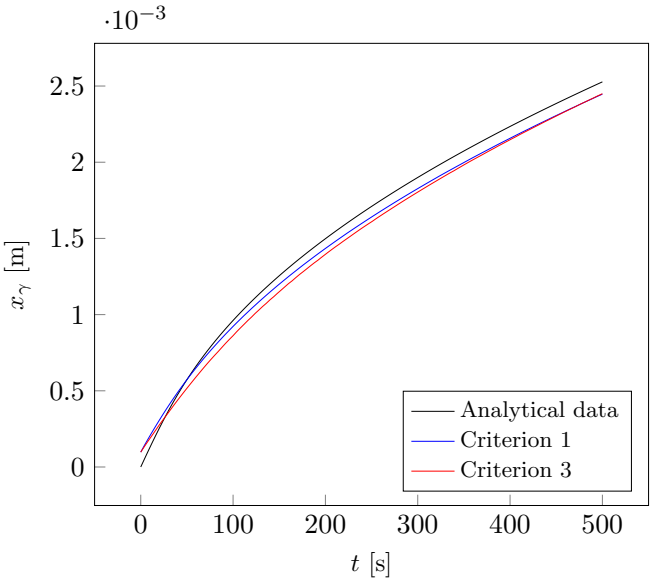

Figure 3.7: Evolution of the interface position over time in the STEFAN WITH NCG case with the 4FM. The interface is defined as the $\alpha_{cl} + \alpha_{dl} = 0.5$ isosurface. The mesh with 200 cells is used. All the criteria in Table 2.4 are considered. A comparison is made with the analytical solution given by Eqs. (3.3) and (3.4).

3.4.2 Results

The quantities of interest, which vary with the position on the vertical plate, are the total heat flux echanged at the wall, equal to $\varphi_{w\to g} + \varphi_{w\to l}$ for the FGLIM and to $\varphi_{w\to cg} + \varphi_{w\to dl}$ for the 4FM – obtained from Eqs. (2.54) and (2.55) – the droplet drag coefficient, denoted C_D – obtained from Table 2.2 – the droplet diameter, denoted d_l – obtained from Section 2.3.2.1 – and the liquid volume fraction, equal to α_l for the FGLIM and to $\alpha_{cl} + \alpha_{dl}$ for the 4FM – obtained by solving Eqs. (2.37) to (2.39). A comparison is made with the experimental data, which is only available for the total heat flux. For the sake of brievety, only the results corresponding to Calculation P344 are presented.

The results obtained at steady-state with the FGLIM are shown as a function of the y-coordinate in Fig. 3.9, for $x = 0.25\,\text{m}$. The four criteria in Table 2.3 are considered. No distinction can be made between them. A good agreement is obtained between numerical and experimental data for the total wall heat flux. The other quantities resulting from simulation behave as expected. Due to condensation, the liquid volume fraction and therefore the droplet diameter increase. As a consequence of the increase in the droplet diameter, the droplet drag coefficient decreases. The fact that no distinction can be made between the various criteria is due to the low amount of liquid formed in the experiment and thus in the calculation, leading the model to systematically and exclusively use the closures for

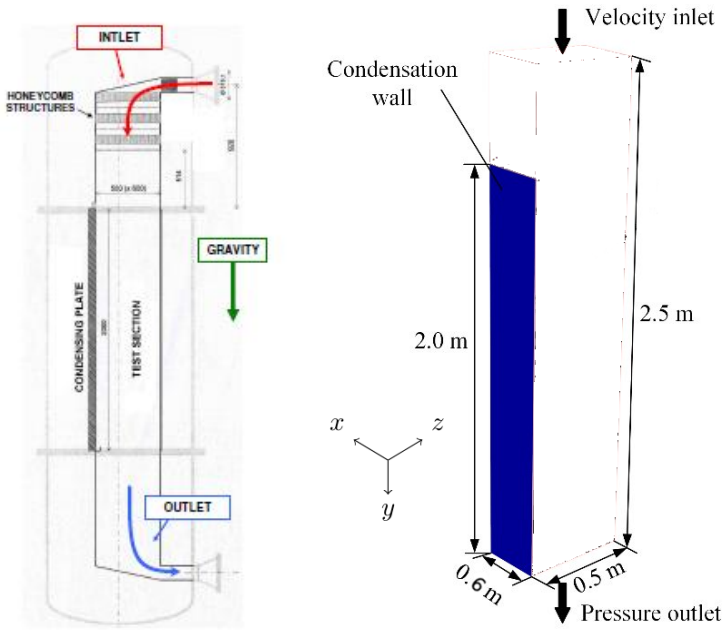

Figure 3.8: Computational domain used in the COPAIN case. The domain is three-dimensional and has a length of 2.5 m, a width of 0.6 m and a depth of 0.5 m. Velocity, temperature and composition are imposed at the inlet, pressure is imposed at the outlet and temperature is imposed at the wall corresponding to the condensation plate.

the droplets.

The results obtained with the 4FM are shown in Fig. 3.10. The two criteria in Table 2.4 are considered. The results are similar to those obtained with the FGLIM, and therefore in good agreement with the available experimental data. For the same reason as before, no distinction can be made between the criteria studied.

3.5 BARTOLOMEI validation case

3.5.1 Problem setup

The case in the present section is based on the experiments of Bartolomei et al. (1982), corresponding to the boiling of water in a vertical pipe with circular cross-section. These experiments have already been simulated by several authors in the literature, including Pal and K (2021); Lavieville et al. (2017); Murallidharan et al. (2016) – Lavieville et al. (2017) used the neptune_cfd code but employed the Standard Dispersed Model for bubbles. The axisymmetric computational domain shown in Fig. 3.11, of height 1.4 m and radius $R = {}^{12.03}/_{2}$ mm, is considered. Subcooled water is injected at the inlet, and evaporates in the first part of the pipe – comprised between 0 and 1 m. Mass flow rate and temperature

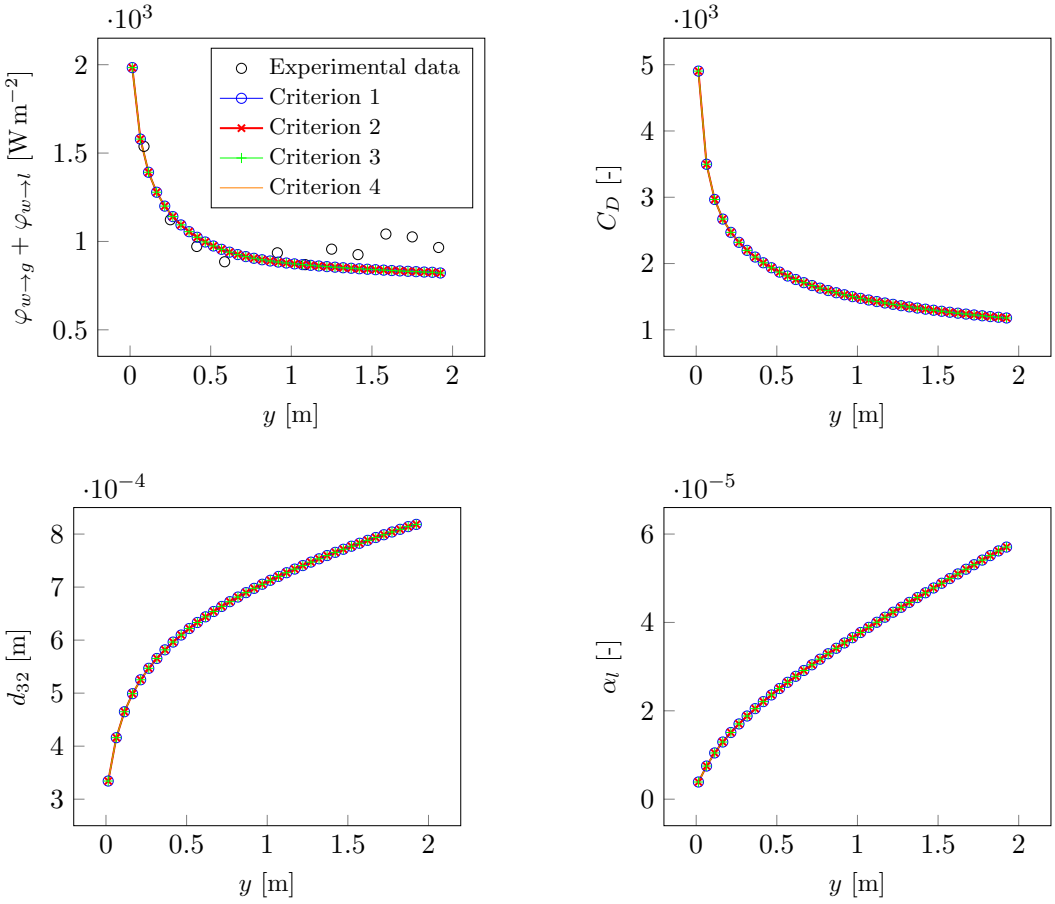

Figure 3.9: Evolution of the steady-state total wall heat flux, droplet drag coefficient, droplet diameter and liquid volume fraction as a function of the y-coordinate in the COPAIN case with the FGLIM for Calculation P344 at $x = 0.25\,\text{m}$. All the criteria in Table 2.3 are considered. For the wall heat flux, a comparison is made with the available experimental data (Cheng et al., 2001).

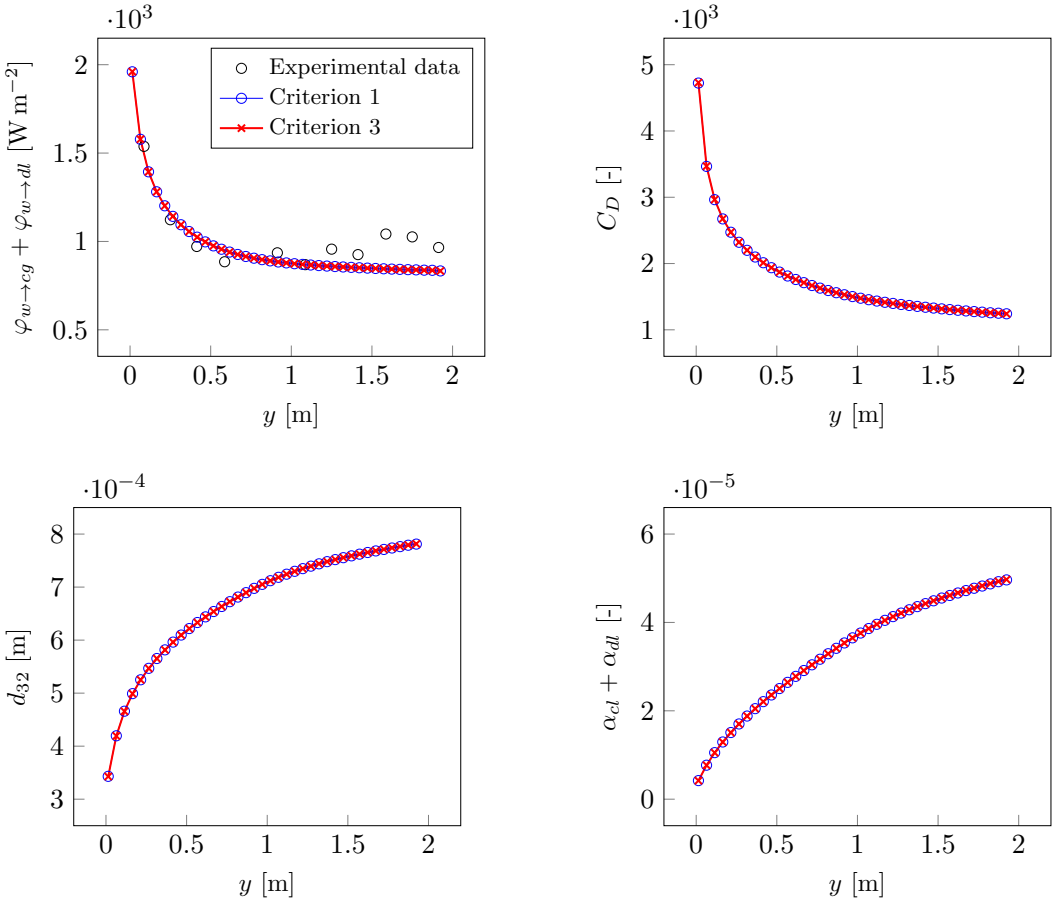

Figure 3.10: Evolution of the steady-state total wall heat flux, droplet drag coefficient, droplet diameter and liquid volume fraction as a function of the y-coordinate in the COPAIN case with the 4FM for Calculation P344 at $x = 0.25\,\text{m}$. All the criteria in Table 2.4 are considered. For the wall heat flux, a comparison is made with the available experimental data (Cheng et al., 2001).

Table 3.6: Values of the gas inlet velocity and temperature, air mass fraction, outlet pressure and wall temperature considered in the COPAIN case.

#	Inlet			Outlet	Wall
	Velocity [m s^{-1}]	Temperature [K]	Air mass fraction	Pressure [bar]	Temperature [K]
P344	0.3	344.03	0.864	1.21	322
P441	3	353.23	0.767	1.02	307.4
P443	1	353.33	0.772	1.02	300.06
P444	0.5	351.53	0.773	1.02	299.7

Table 3.7: Values of the inlet mass flow rate, liquid inlet temperature and wall total heat flux considered in the BARTOLOMEI case.

#	Inlet		Wall
	Mass flow rate [kg m^{-2} s^{-1}]	Temperature [K]	Heat flux [MW m^{-2}]
2	1500	495	1.2
3	1500	519	0.8
5	1000	503	0.8

boundary conditions are imposed at the inlet, a pressure boundary condition is imposed at the outlet and a heat flux boundary condition is imposed at the wall in the first part of the pipe. The pressure is set to 68.9 bar. The other boundary condition values are given in Table 3.7. As in Lavieville et al. (2017), the gas phase is assumed to be laminar and the liquid phase to be turbulent. For the latter phase, a $R_{ij} - \varepsilon$ model is used. A uniform mesh consisting of 840×20 cells is used. The dimensionless distance from the wall to the center of the adjacent cells – obtained from Eq. (3.5) by replacing the subscript g by l – is found, as previously in the COPAIN case, to be greater than 30, indicating compatibility with the turbulence model – in Calculation 2 for example, it is about 116 in average over the wall. The physical properties are automatically computed using the CATHARE tables (Emonot et al., 2011). A constant time step is used. It is set to 10^{-3} s, leading to Courant and Fourier numbers – defined as $\|\underline{U}_k\| \frac{\Delta t}{\Delta x}$ and $\frac{\lambda_k}{\rho_k C p_k} \frac{\Delta t}{\Delta x}$, with Δt the time step and Δx the grid spacing – below 1 and 10 for both the gas and the liquid. The calculations are run for 5 s.

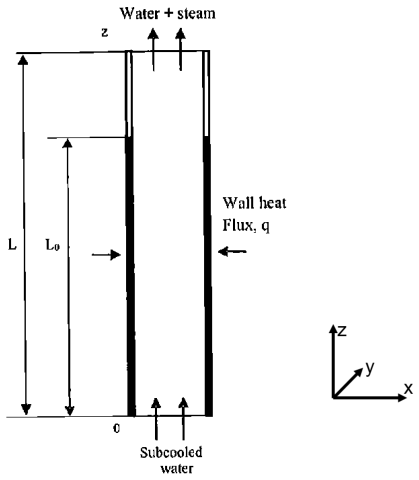

Figure 3.11: Computational domain used in the BARTOLOMEI case. The domain is two-dimensional and axisymmetric, and has a height of 1.4 m and a radius of $^{12.03}/_{2}$ mm. Mass flow rate and composition are imposed at the outlet, pressure is imposed at the outlet and total heat flux is imposed at the wall for z comprised between 0 and 1 m.

3.5.2 Results

The quantity of interest is the cross-sectional averaged gas volume fraction, equal to $\overline{\alpha_g}$ for the FGLIM and to $\overline{\alpha_{cg}} + \overline{\alpha_{dg}}$ for the 4FM, with:

$$\overline{\alpha_k} = \frac{1}{R}\int_0^R \alpha_k \mathrm{d}x \,. \tag{3.6}$$

A comparison is made with the available experimental data. For the sake of brievety, only the results of Calculation 2 are presented.

The results obtained at steady-state with the FGLIM are shown as a function of the z-coordinate in Fig. 3.12. Again, the four criteria in Table 2.3 are considered. For Criteria 3 and 4, the gas volume fraction is found to be almost the same and to be in good agreement with the experiment. For Criteria 1 and 2, however, the gas volume fraction is significantly overestimated. Also, important oscillations are observed on almost all the domain. The reason is that Criteria 1 and 2 use the coefficient β' (see Section 2.3.4.1) – introduced in order to decrease the contributions of the droplets and bubbles in the zones with a high volume fraction gradient, supposed to correspond to large interfaces. In the present case, this coefficient gives an unexpected importance to the large interfaces due to unexpected large values of the volume fraction gradient.

The results obtained with the 4FM are shown in Fig. 3.13. Again, the two criteria in Table 2.4 are considered. For $z \leq 1$ m, the gas volume fraction is similar to that obtained with the FGLIM for Criteria 3 and 4, and therefore in good agreement with the experimental

data. For $z \geq 1\,\mathrm{m}$, however, the gas volume fraction is different from that obtained with the FGLIM. Although qualitatively in good agreement with the experimental data, it is found to be overestimated by the model for both Criteria 1 and 3. This is related to the recondensation phenomenon occuring near the wall. With the FGLIM, recondensation occurs with the gas phase in the form of bubbles, while, with the 4FM, recondensation mostly occurs with the gas phase in the form of a large interface, which seems to lead to an underestimation of the amount of liquid formed.

3.6 Summary

The purpose of this chapter was to validate the two models developed in the framework of the present thesis, namely the FGLIM and the 4FM, in cases involving droplets, bubbles or large interfaces – cases involving simultaneously droplets, bubbles and large interfaces will be the object of the following chapter. The two models combining a sub-grid approach and an interface capturing approach, the purpose of the chapter was also to choose a criterion among those proposed in the previous chapter to switch between these approaches. Four cases were considered: the BHAGA case, corresponding to the rising of a large bubble of air in viscous liquid, the STEFAN WITH NCG case, corresponding to the horizontal displacement of a large interface due to direct contact condensation of steam in the presence of air, the COPAIN case, corresponding to condensation of steam, in the presence of air, in the form of small droplets on a vertical plate, and the BARTOLOMEI case, corresponding to water evaporation in the form of small bubbles in a vertical pipe.

The results obtained with the FGLIM were found to be in good agreement with the analytical/experimental data for all the criteria in Table 2.3, except for Criteria 1 and 2 in the BARTOLOMEI case. Also, for all the criteria, the large interfaces were found to be well described by the model in the BHAGA and STEFAN WITH NCG cases. For criteria 3 and 4, it was not evident that a good agreement would be achieved and that the large interfaces would be well described, due to the fact that these two criteria do not use the coefficient β' (see Section 2.3.4.1) – introduced in order to decrease the contributions of the droplets and bubbles in the zones with a high volume fraction gradient, supposed to correspond to large interfaces. Since Criteria 1 and 2 were found to be in bad agreement with the experiment in the BARTOLOMEI case, they could not be retained, despite the fact that they showed a slightly better agreement than Criteria 3 and 4 in the STEFAN WITH NCG case. Criteria 3 or 4, providing almost identical results, should be preferred.

The results obtained with the 4FM were also found to be in good agreement with the analytical/experimental data for all the criteria in Table 2.4, except for Criteria 3 in the STEFAN WITH NCG case. If a criteria should be retained among those two, it would

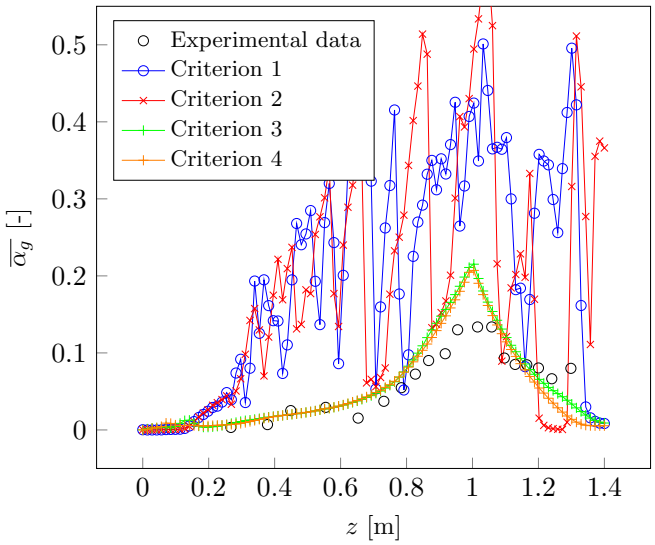

Figure 3.12: Evolution of the steady-state cross-sectional averaged liquid volume fraction as a function of the z-coordinate in the BARTOLOMEI case with the FGLIM for Calculation 2. All the criteria in Table 2.3 are considered. A comparison is made with the available experimental data (Bartolomei et al., 1982).

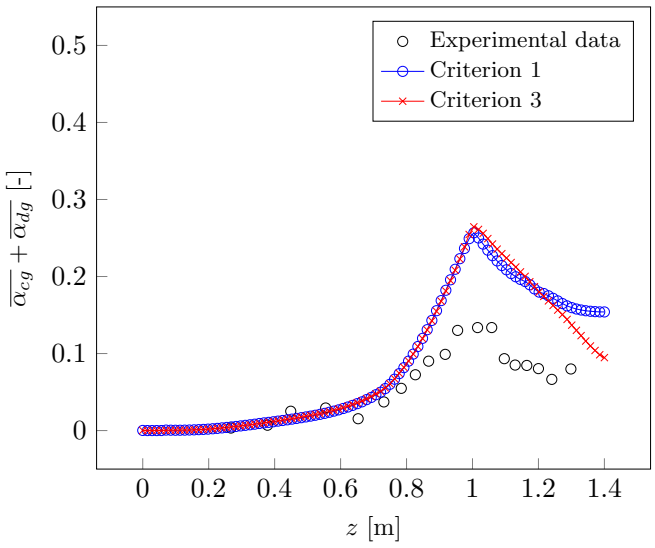

Figure 3.13: Evolution of the steady-state cross-sectional averaged liquid volume fraction as a function of the z-coordinate in the BARTOLOMEI case with the 4FM for Calculation 2. All the criteria in Table 2.4 are considered. A comparison is made with the available experimental data (Bartolomei et al., 1982).

therefore be Criteria 1, which includes the expressions for the transfers between the two gas fields initially proposed by Denèfle et al. (2015) in the framework of the LBMb.

The calculations performed for this chapter indicate that the FGLIM and the 4FM provide similar results in cases that do not involve cells with at the same time droplets, bubbles and large interfaces. Also, they show that the FGLIM is computationally cheaper than the 4FM, which was expected since only two computational fields are used. For the sake of information, the calculation time in the 4FM increased by 165 % in the STEFAN WITH NCG case, 398 % in the COPAIN case and 307 % in the BARTOLOMEI case. In the rest of the PhD, the simulations are expected to involve simultaneously droplets, bubbles and large interfaces but the cells are expected to not contain the three at the same time. As a consequence, the FGLIM will be used, with Criteria 4.

Chapter 4

Steam condensation in the presence of air in a smooth rectilinear model crack

Contents

4.1 Introduction 80

4.2 Acticle published in *Int. J. Multiph. Flow* 80

4.3 Complementary simulations 110

4.3.1 Boundary conditions 110

4.3.2 Results 111

4.4 Summary 112

4.1 Introduction

In the previous chapter, the FGLIM and the 4FM were validated in cases involving either dispersed droplets, dispersed bubbles or large interfaces. In this chapter, the FGLIM is validated in a case involving both dispersed droplets and large interfaces. The case studied, which is directly linked with the industrial problem considered in the thesis (see Chapter 1), corresponds to steam condensation in the presence of air in an idealized rectilinear mini-channel with smooth walls.

The originality of the chapter lies in several aspects. It constitutes a first attempt to simulate steam condensation in a mini-channel with an model combining a sub-grid approach and an interface capturing approach (see Chapter 2). Indeed, the few studies on condensation in mini-channel found in the literature have used the volume-of-fluid method, which only allow for large interfaces and therefore requires the cells to be smaller than the smallest flow structures. The other point is the presence of air, which is a non-condensable gas. Except one, all the studies available in the literature considered the case of pure steam, which is less complex to handle.

The chapter is presented in the form of the article entitled "Euler-Euler simulations of condensing two phase flow in mini-channel: combination of a sub-grid approach and an interface capturing approach", published in the peer-reviewed *International Journal of Multiphase Flow* (Davy et al., 2022). For the sake of completeness, the paper is provided in its entirety, including abstract, introduction, conclusion and references. Results of complementary simulations at low pressure and a short conclusion are given in separate sections.

4.2 Acticle published in *Int. J. Multiph. Flow*

Euler-Euler simulations of condensing two-phase flows in mini-channel: Combination of a sub-grid approach and an interface capturing approach

Germain Davy[a,b,c,*], Etienne Reyssat[c], Stéphane Vincent[b], Stéphane Mimouni[a]

[a] *R&D Division, Electricité de France (EDF), Chatou, France*
[b] *Laboratoire Modélisation et Simulation Multi-Echelle (MSME), CNRS, Université Paris-Est Créteil, Université Gustave Eiffel, Marne-la-Vallée, France*
[c] *Laboratoire Physique et Mécanique des Milieux Hétérogènes (PMMH), CNRS, ESPCI Paris, Université PSL, Sorbonne Université, Université Paris Diderot, Paris, France*

Abstract

A new model implemented in the neptune_cfd code is used to study steam condensation in the presence of air in a mini-channel of opening 100 µm. This model is the Full Generalized Large Interface Model. It combines a sub-grid approach and an interface capturing approach. The sub-grid approach is used to compute the small flow structures, which can be small bubbles or droplets, while the interface capturing approach is used to compute the large flow structures, which can be gas or liquid films, large bubbles or large drops. It is conceived to simulate a wide range of flow configurations, without the need for the grid cells to be smaller than the smallest flow structures. The results show that the model is able to reproduce all the flow patterns experimentally observed in mini-channels in the analyzed range of control parameters. Both the pressure drop and the Nusselt number (dimensionless wall heat flux) are found to be in good agreement with experimental correlations from the literature.

Keywords: condensation, mini-channel, computational fluid dynamics, multi-regime, pressure drop, Nusselt number

1. Introduction

The understanding and modeling of two-phase flows in confined geometries like mini-channels and cracks is a major issue for many industries. Examples include the electronics, automotive, aeronautics and chemical industries (Chen et al., 2014; Da Riva et al., 2012; Ganapathy et al., 2013; Hu and Chao, 2007; Wu and Cheng, 2005; Yin et al., 2015; Zhang et al., 2016b; Zhao et al., 2015), with systems such as compact heat exchangers, micro-pumps and micro-reactors, but also the nuclear industry (Davy et al., 2020; Mimouni et al., 2019; Rastiello et al., 2015). Indeed, in a nuclear power plant, in the event of a loss-of-coolant accident, steam and fission products would be released in the containment building. In the case of a double wall concrete containment (no steel liner), the increase in pressure and temperature could lead to the opening of preexisting cracks and to the creation of new cracks (opening of the order of 100 µm) in the inner wall, through which gas and fission products could escape. Two phenomena could have an impact on the gas leakage rate. The first is steam condensation on the inner wall and inside the cracks, which could result in their clogging by drops, films and/or slugs. The second is concrete thermal deformation, which could result in variations in the crack opening.

The present work focuses on the first of the two phenomena described above, i.e., steam condensation in confined geometries. Recent numerical work on condensation in mini-channels is summarized in Table 1. Da Riva and Del Col

*Corresponding author
Email address: germain.davy@univ-eiffel.fr (Germain Davy)
URL: https://msme.univ-gustave-eiffel.fr (Germain Davy)

(2011, 2012); Da Riva et al. (2012) carried out a series of studies on condensation of R134a (1,1,1,2-tetrafluoroethane) in a 1 mm diameter circular mini-channel. They found that, at high mass fluxes, the heat transfer coefficient (ratio of wall heat flux to difference in temperature between the solid surface and the surrounding fluid area) can only be predicted correctly if liquid turbulence is taken into account. Yin et al. (2015) studied condensation of water vapor in a 1 mm diameter circular mini-channel in the presence of a non-condensable gas (air, oxygen, helium or hydrogen). They found that the existence of a non-condensable gas led to a decrease in the interfacial mass transfer rate (mass exchanged at the gas-liquid interface per unit area and per unit time) and in the heat transfer coefficient. Zhang et al. (2016a,b, 2017) conducted a series of studies on condensation of R410A (mixture of difluoromethane and pentafluoroethane) in mini-channels of various shapes and sizes. They found that the heat transfer was stronger in flattened and helical microfin tubes than in smooth circular tubes. Based on the results obtained for smooth circular tubes, they proposed two new correlations, one for the frictional pressure drop and another for the heat transfer coefficient. Zhao et al. (2015) studied condensation of R22 (chlorodifluoromethane) in a 0.91 mm hydraulic diameter mini-channel. They developed a flow regime map and proposed new correlations for the frictional pressure drop and the heat transfer coefficient. In all these studies, the flow regime is annular. The volume-of-fluid (VOF) method is used under steady-state assumption. The mass and energy transfer terms, computed using the model of Lee (1980), are based on a constant that is problem-dependent.

Two other studies worth mentioning are those of Chen et al. (2014) and Ganapathy et al. (2013). Chen et al. (2014) studied condensation of FC-72 (perfluorohexane) in a 1 mm hydraulic diameter mini-channel. They were able to observe various flow regimes, including smooth annular, wavy annular, slug and bubbly flow. They found these flow patterns to be consistent with the experimental data of Kim et al. (2012) and Wang et al. (2002). Ganapathy et al. (2013) investigated condensation of R134a (1,1,1,2-tetrafluoroethane) in a 0.1 mm hydraulic diameter mini-channel. They observed flow patterns similar to those mentioned previously (with, in addition, droplet flow). They found the frictional pressure drop and the Nusselt number (dimensionless heat transfer coefficient) to be in good agreement with a number of correlations from the literature. In these two studies, the VOF method is also used. Unlike previously, no steady-state assumption is made. Concerning phase change, the model used by Chen et al. (2014) is similar to that of Lee (1980). The model used by Ganapathy et al. (2013) is close to that presented in Section 2.4.2.

It is important to note that, in the studies mentioned previously, all the gas-liquid interfaces are supposed to be fully resolved, even the smallest ones. The main drawback of this kind of approach is its computational cost, since it requires the use of very fine meshes and thus very small time steps.

The present work aims to assess the ability of a new model implemented in the neptune_cfd code[1] to correctly predict steam condensation and resulting flow patterns in mini-channels. This model is the Full Generalized Large Interface Model (Davy et al., 2020). It combines a sub-grid approach and an interface capturing approach. The sub-grid approach is used to compute the small flow structures, which can be small bubbles or droplets, while the interface capturing approach is used to compute the large flow structures, which can be gas or liquid films, large bubbles or large drops. It is conceived to simulate a wide range of flow configurations, without the need for the grid cells to be smaller than the smallest flow structures. It also has the advantage that no empirical constant is used for phase change.

The document is organized as follows. The balance equations solved by the code are given in Section 2.1. The model employed is presented in Sections 2.2 to 2.4. The numerical setup and the assumptions done are detailed in Section 3. In

[1]The neptune_cfd code is jointly developed by EDF, CEA, Framatome and IRSN

Table 1: Computational condensation studies found in the literature. 2D stands for "two dimensions", 3D for "three dimensions", A for "annular flow", B for "bubbly flow", C for "circular cross-section", CF for "circular flattened cross-section", D for "droplet flow", H for "horizontal", I for "infinite cross-section", M for "microfin tube", NCG for "non-condensable gases", R for "rectangular cross-section", S for "slug flow", SC for "semi-circular cross-section", V for "vertical" and VOF for "volume-of-fluid method".

Authors	Orientation, geometry, diameter, fluid	Regime(s)	Approach
Chen et al. (2014)	H, R, 1 mm, FC-72	D, A, S, B	3D, VOF
Da Riva and Del Col (2011)	H and V, C, 1 mm, R134a	A	3D, VOF, steady
Da Riva and Del Col (2012)	H, C, 1 mm, R134a	A	3D, VOF, steady
Da Riva et al. (2012)	H, C, 1 mm, R134a	A	3D, VOF, steady
Ganapathy et al. (2013)	H, I, 0.1 mm, R134a	A, S, B	2D, VOF
Yin et al. (2015)	H, C, 1 mm, water and NCG	A	3D, VOF, steady
Zhang et al. (2016a)	H, C, 0.25-4 mm, R410A	A	3D, VOF, steady
Zhang et al. (2016b)	H, CF, 3.78 mm, R410A or R134a	A	3D, VOF, steady
Zhang et al. (2017)	H, C and M, 4.54 mm, R410A	A	3D, VOF, steady
Zhao et al. (2015)	n/a, SC, 0.91 mm, R22	A	3D, VOF, steady

Section 4, the flow patterns obtained by simulation are qualitatively compared with experimental views from the literature. In addition, the pressure drop and the Nusselt number are quantitatively compared with experimental correlations. Conclusions are drawn in Section 5.

2. Modeling strategy

2.1. Governing equations

Two computational fields are used: a gas field (g) and a liquid field (l). The following mass, momentum and energy balance equations are considered for $k = g$ and $k = l$:

$$\frac{\partial}{\partial t}\left(\alpha_k \rho_k\right) + \underline{\nabla}\cdot\left(\alpha_k \rho_k \underline{U}_k\right) = \Gamma_{p\to k} + \Gamma_{w\to k}\,, \tag{1}$$

$$\frac{\partial}{\partial t}\left(\alpha_k \rho_k \underline{U}_k\right) + \underline{\nabla}\cdot\left(\alpha_k \rho_k \underline{U}_k \otimes \underline{U}_k\right) = -\alpha_k \underline{\nabla} P + \underline{\nabla}\cdot\left[\alpha_k\left(\underline{\underline{\Sigma}}_k + \underline{\underline{\Sigma}}_k^{Re}\right)\right] + \alpha_k \rho_k \underline{g} + \underline{I}_{p\to k}\,, \tag{2}$$

$$\frac{\partial}{\partial t}\left(\alpha_k \rho_k H_k\right) + \underline{\nabla}\cdot\left(\alpha_k \rho_k H_k \underline{U}_k\right) = \alpha_k \frac{\partial P}{\partial t} - \underline{\nabla}\cdot\left(\alpha_k \underline{Q}_k + \underline{Q}_k^{Re}\right) + \Gamma_{p\to k} H_k + \Pi_{p\to k} + \varphi_{w\to k}\,. \tag{3}$$

H_k, $\underline{Q}_k$, $\underline{Q}_k^{Re}$, $\underline{U}_k$, α_k, ρ_k, $\underline{\underline{\Sigma}}_k$ and $\underline{\underline{\Sigma}}_k^{Re}$ are, respectively, the average total enthalpy, heat flux density, turbulent heat flux density, average velocity, volume fraction, density, viscous stress tensor and Reynolds stress tensor of phase k. $\underline{g}$ is the gravity. P is the pressure (assumed to be the same for both fields). $\underline{I}_{p\to k}$, $\Gamma_{p\to k}$, and $\Pi_{p\to k}$ denote, respectively, the momentum, mass and energy transfers from phase p to phase k. $\Gamma_{w\to k}$ denotes the mass contribution to phase k induced by wall condensation and $\varphi_{w\to k}$ denotes the energy contribution to phase k induced by wall condensation and/or wall sensible heat transfer. These equations are solved with the neptune_cfd code. This code is based on the finite volume discretization method and uses a SIMPLE (Semi-Implicit Method for Pressure Linked Equations) algorithm as solution procedure.

2.2. The Full Generalized Large Interface Model

The models available in the code are listed in Table 2. The model used in the present work is the newly developed Full Generalized Large Interface Model (FGLIM) (Davy et al., 2020). This model uses both a sub-grid approach, like in the Standard Dispersed Model (Mimouni et al., 2010, 2011), and an interface capturing approach, like in the Large Interface Model (Coste and Lavieville, 2008, 2009; Coste, 2013), and switches between the two according to the composition of the considered cell. Closures for sub-grid droplets, corresponding to Case 1 in Fig. 1, are applied in the cells with a liquid volume fraction lower than α_l^{lim}, and closures for sub-grid bubbles, corresponding to Case 3 in Fig. 1, are applied in the cells with a liquid volume fraction greater than α_l^{lim}. In both cases, the interface is not explicitly modeled. In a cell, all the droplets/bubbles have the same diameter, velocity and temperature. The diameter is obtained by solving a transport equation on the interfacial area. Closures for large interfaces (i.e., interfaces "captured" by several cells), corresponding to Case 2 in Fig. 1, are applied in the cells with a liquid volume fraction between α_l^{inf} and α_l^{sup}. An additional equation, called interface sharpening equation, is solved to maintain constant the thickness of large interfaces. However, unlike in codes based on the one-fluid formalism, no additional equation is required for large interface advection, since a mass balance is solved for each phase (see Section 2.1). To avoid superimposing closures corresponding to the sub-grid approach and to the interface capturing approach, a weighting is done between the closures for the sub-grid droplets (respectively, sub-grid bubbles) and the closures for the large interfaces in the cells with a liquid volume fraction between α_l^{inf} and α_l^{lim} (respectively, between α_l^{lim} and α_l^{sup}).

The FGLIM can be seen as an extension of the Generalized Large Interface Model (Mérigoux et al., 2016; Mer et al., 2018), the latter including Cases 2 and 3 but not Case 1 and using different closure laws for mass, momentum and energy. It is worth noting that the two models completely rely on the volume fraction. Cells with $\alpha_l > \alpha_l^{lim}$ cannot be treated as droplets, cells with $\alpha_l < \alpha_l^{lim}$ cannot be treated as bubbles and cells with $\alpha_l < \alpha_l^{inf}$ or $\alpha_l > \alpha_l^{sup}$ cannot be treated as large interfaces. It is also worth noting that the FGLIM has already been validated on several test cases, involving droplets, bubbles and/or large interfaces (not provided here for consistency, since they do not involve mini-channels). Different combinations for α_l^{inf}, α_l^{lim} and α_l^{sup} were tested and the best results were obtained for $\alpha_l^{inf} = 0.4$, $\alpha_l^{lim} = 0.5$ and $\alpha_l^{sup} = 0.6$. Therefore, these values are kept for use in the present work.

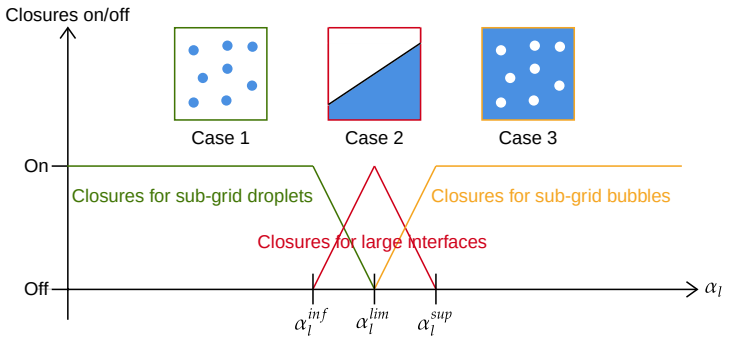

Figure 1: Principle of the Full Generalized Large Interface Model. The model uses a sub-grid approach in Cases 1 and 3 and an interface capturing approach in Case 2. Closures for mass, momentum and energy used in Cases 1 and 3 come from the Standard Dispersed Model for droplets and the Standard Dispersed Model for bubbles, respectively. Those used in Case 2 come from the Large Interface Model. α_l^{inf}, α_l^{lim} and α_l^{sup} are set to 0.4, 0.5 and 0.6, respectively.

Table 2: Models for gas-liquid flows available in the neptune_cfd code. FGLIM stands for "Full Generalized Large Interface Model", GLIM for "Generalized Large Interface Model", LBM for "Large Bubble Model", LI for "large interface", LIM for "Large Interface Model" and SDM for "Standard Dispersed Model".

Model	Reference(s)	Bubbles	Droplets	LI
SDM (bubbles)	Mimouni et al. (2010, 2011)	Yes	No	No
SDM (droplets)	Mimouni et al. (2010, 2011)	No	Yes	No
LIM	Coste and Lavieville (2008, 2009); Coste (2013)	No	No	Yes
LBM	Denèfle et al. (2015); Fleau et al. (2015)	Yes	No	Yes
GLIM	Mérigoux et al. (2016); Mer et al. (2018)	Yes	No	Yes
FGLIM	Davy et al. (2020)	Yes	Yes	Yes

2.3. Closure laws for bubbles and droplets

2.3.1. Interfacial momentum transfers for bubbles and droplets

As in the Standard Dispersed Model, for bubbles and droplets, the momentum transfers read as the sum of a drag force $\underline{F}^D$, an added mass force $\underline{F}^{AM}$, a lift force $\underline{F}^L$, a wall force $\underline{F}^W$ and a turbulent dispersion force $\underline{F}^{TD}$:

$$\underline{I}_{c\to d} = -\underline{I}_{d\to c} = \underline{F}^D_{c\to d} + \underline{F}^{AM}_{c\to d} + \underline{F}^L_{c\to d} + \underline{F}^W_{c\to d} + \underline{F}^{TD}_{c\to d}\,, \tag{4}$$

where the subscript c stands for "continuous" and the subscript d for "dispersed". In the following, for droplets ($c = g$ and $d = l$), only the drag force is taken into account. The drag coefficient is obtained from the correlation of Gobin et al. (2003). For bubbles ($c = l$ and $d = g$), only the drag, added mass and lift forces are taken into account. The drag, added mass and lift coefficients are obtained from the correlations of Ishii and Zuber (1979), Zuber (1964) and Tomiyama et al. (2002), respectively. Expressions of these forces are given in Table 3, where d_d refers to the droplet/bubble diameter. It is given by: $d_d = {}^{6\alpha_d}/_{a_d^{int}}$, with a_d^{int} the interfacial area concentration. The latter is obtained by solving an additional transport equation, which takes into account size variation due to phase change for droplets (Mimouni et al., 2010, 2011) and due to phase change, coalescence and break-up for bubbles (Guelfi et al., 2007). The model of Ruyer et al. (2007) is used for bubble coalescence and break-up.

2.3.2. Interfacial energy and mass transfers for droplets

For droplets, the energy and mass transfers from the liquid to the gas are computed using the expressions proposed by Mimouni et al. (2010, 2011):

$$\Pi_{l\to g} = \frac{6\alpha_l}{d_l^2}\cdot Nu_g \cdot \lambda_g \cdot (T_l - T_g)\,, \tag{5}$$

$$\Gamma_{l\to g} = \frac{6\alpha_l}{d_l^2}\cdot Sh_g \cdot D \cdot (\rho_{s,sat}(T_l) - Y_s\rho_g)\,. \tag{6}$$

D is the diffusion coefficient of steam in air. It is obtained from the correlation of Oran and Boris (1981): $D = 4.88\times10^{-4}{T^{3/2}}/{P}$, with T computed as an average between the gas temperature T_g and the liquid temperature T_l. Nu_g and Sh_g are the gas Nusselt and Sherwood numbers. They are obtained from the correlations of Ranz and Marshall (1952): $Nu_g = 2 + 0.56 Re_{pl}^{1/2} Pr_g^{1/3}$ and $Sh_g = 2 + 0.56 Re_{pl}^{1/2} Sc_g^{1/3}$, with $Re_{pl} = {\rho_g \left\|\underline{U}_g - \underline{U}_l\right\| d_l}/{\mu_g}$ the liquid particle Reynolds number, $Pr_g = {\mu_g Cp_g}/{\lambda_g}$ the gas Prandtl number and $Sc_g = \frac{\mu_g}{\rho_g D}$ the gas Schmidt number. Cp_g, λ_g and μ_g are the gas heat capacity,

Table 3: Expressions used for the drag, added mass and lift forces. $C_X = \{C_D, C_{AM}, C_L\}$.

Force	Expression	C_X for droplets	C_X for bubbles
$\underline{F}^D_{c\to d}$	$-\frac{6}{8}\frac{\alpha_d}{d_d}C_D\rho_c\left\|\underline{U}_d-\underline{U}_c\right\|(\underline{U}_d-\underline{U}_c)$	Gobin et al. (2003)	Ishii and Zuber (1979)
$\underline{F}^{AM}_{c\to d}$	$-\alpha_d C_{AM}\rho_c\left(\frac{D\underline{U}_d}{Dt}-\frac{D\underline{U}_c}{Dt}\right)$	–	Zuber (1964)
$\underline{F}^L_{c\to d}$	$-\alpha_d C_L\rho_c(\underline{U}_d-\underline{U}_c)\wedge(\underline{\nabla}\wedge\underline{U}_c)$	–	Tomiyama et al. (2002)

thermal conductivity and molecular viscosity. Y_s and $\rho_{s,sat} = \rho_s(P_{sat}, T)$ are the steam mass fraction and saturation density. The steam mass fraction is given by: $Y_s = 1 - Y_a$, with Y_a the air mass fraction, obtained by solving an additional transport equation (Mimouni et al., 2010, 2011).

The energy and mass transfers from the gas to the liquid are deduced from:

$$\Pi_{g\to l} = -\Pi_{l\to g} - \Gamma_{l\to g}H_{lat}\,, \tag{7}$$

$$\Gamma_{g\to l} = -\Gamma_{l\to g}\,. \tag{8}$$

H_{lat} is the latent heat. It is given by: $H_{lat} = H_g - H_l$.

2.3.3. Interfacial energy and mass transfers for bubbles

For bubbles, the energy transfer from the gas to the liquid is computed using the expression proposed by Manon (2000):

$$\Pi_{g\to l} = \frac{6\alpha_g}{d_g^2}\cdot Nu_l\cdot\lambda_l\cdot(T_{sat}-T_l)\,. \tag{9}$$

Like the gas Nusselt number, the liquid Nusselt number Nu_l is obtained from the correlation of Ranz and Marshall (1952): $Nu_l = 2 + 0.56Re_{pg}^{1/2}Pr_l^{1/3}$, with $Re_{pg} = \rho_l\left\|\underline{U}_g-\underline{U}_l\right\|d_g/\mu_l$ the gas particle Reynolds number and $Pr_l = \mu_l Cp_l/\lambda_l$ the liquid Prandtl number. Cp_l, λ_l and μ_l are the liquid heat capacity, thermal conductivity and molecular viscosity. T_{sat} is the saturation temperature.

The energy transfer from the liquid to the gas is computed as:

$$\Pi_{l\to g} = \alpha_g\alpha_l\frac{\rho_g Cp_g}{\tau_{relax}}(T_{sat}-T_g)\,. \tag{10}$$

Actually, this term is a penalty term, whose purpose is that the gas temperature remains close to the saturation temperature. Therefore, the characteristic time τ_{relax} has no physical meaning. It is chosen equal to the time step, so that $T_g \approx T_{sat}$ is met at each iteration in cells with bubbles.

The mass transfers are deduced from:

$$\Gamma_{g\to l} = -\Gamma_{l\to g} = \frac{\Pi_{g\to l}+\Pi_{l\to g}}{H_{lat}}\,. \tag{11}$$

2.3.4. Wall energy and mass transfers for droplets

At the wall, the mass transfers are computed using the expression proposed by Mimouni et al. (2010, 2011):

$$\Gamma_{w\to g} = -\Gamma_{w\to l} = \frac{S}{V}\cdot n_{site}\cdot\pi\cdot Sh_g\cdot D\cdot\frac{d_l}{2}\cdot(\rho_{s,sat}(T_w)-Y_s\rho_g)\,. \tag{12}$$

n_{site} is the number of droplets formed at nucleation sites per unit area. It is given by: $n_{site} = \frac{4A_l}{\pi d_l^2}$, with A_l the fraction of area affected by the liquid. Also, S/V is the ratio of the surface of the boundary face to the volume of the boundary cell. T_w is the wall temperature.

The energy transfers are computed as:

$$\varphi_{w\to g} = \varphi_{cond} + \varphi_{sp,g}\,, \tag{13}$$

$$\varphi_{w\to l} = \varphi_{sp,l}\,. \tag{14}$$

φ_{cond} is the condensation flux. It is deduced from: $\varphi_{cond} = \Gamma_{w\to g} H_{lat}$. $\varphi_{sp,g}$ and $\varphi_{sp,l}$ are the single-phase gas and liquid heat fluxes. They are obtained from: $\varphi_{sp,g} = (1 - A_l)\, h_{loc,g}\, (T_w - T_g)$ and $\varphi_{sp,l} = A_l h_{loc,l}\, (T_w - T_l)$, with $h_{loc,g}$ and $h_{loc,l}$ the gas and liquid local heat transfer coefficients. These coefficients are given by: $h_{loc,k} = {}^{\lambda_k}/_{\Delta} \cdot c_k$, with Δ the distance from the wall to the center of the boundary cell and c_k a dimensionless rescaling factor equal to unity in the laminar flow regime and provided by an analytical wall function in the turbulent flow regime.

2.4. Closure laws for large interfaces

2.4.1. Interfacial momentum transfers

For large interfaces, the momentum transfers read as the sum of a generalized drag force $\underline{F}^D$, which allows to couple the gas and liquid velocities, and a surface tension force $\underline{F}^{ST}$:

$$\underline{I}_{l\to g} = \underline{F}^D_{l\to g} + \underline{F}^{ST}_g\,, \tag{15}$$

$$\underline{I}_{g\to l} = \underline{F}^D_{g\to l} + \underline{F}^{ST}_l\,. \tag{16}$$

$\underline{F}^D$ is computed using a combination of the expression proposed by Coste (2013) in the framework of the Large Interface Model and the expression proposed by Mimouni et al. (2017) in the framework of the Large Bubble Model:

$$\underline{F}^D_{l\to g} = \alpha_g \alpha_l \left[f^\theta_l + \theta \left(f^\theta_g - f^\theta_l\right)\right] \left(\underline{U}_l - \underline{U}_g\right)\,. \tag{17}$$

f^θ_l, f^θ_g and θ are given by: $f^\theta_l = 18^{\mu_g}/_{d_l^2}\,(1 + 0.15 Re_{pl})$, $f^\theta_g = 18^{\mu_l}/_{d_g^2}\,(1 + 0.15 Re_{pg})$ and $\theta = {}^1/_2\,(1 - \cos[\pi\alpha_l)]$, with Re_{pl} and Re_{pg} defined in Section 2.3.2 and Section 2.3.3, respectively. Originally introduced in the Large Bubble Model, $\underline{F}^{ST}$ is computed the same way as in this model:

$$\underline{F}^{ST}_k = \alpha_k \underline{F}^{ST}_{tot}\,, \tag{18}$$

with $\underline{F}^{ST}_{tot}$ obtained from the Continuum Surface Force approach of Brackbill et al. (1992):

$$\underline{F}^{ST}_{tot} = -\sigma \underline{\nabla} \cdot (\underline{n}_l)\, \underline{\nabla}\, \alpha_l\,. \tag{19}$$

$\underline{n}_l$ is the interface normal pointing towards g. It is given by: $\underline{n}_l = {}^{\underline{\nabla}\,\alpha_l}/_{\|\underline{\nabla}\,\alpha_l\|}$. σ is the surface tension. In order to maintain constant interface thickness, which is required to accurately compute the interface normal, an additional equation, called interface-sharpening equation, is solved for each field k in the cells assumed to contain a portion of large interface:

$$\frac{\partial \alpha_k}{\partial \tau} + \underline{\nabla} \cdot \left[\alpha_k \left(1 - \alpha_k\right] \underline{n}_k\right) = \varepsilon \underline{\nabla}^2\, \alpha_k\,, \tag{20}$$

τ is an artificial time, different from the actual time t. ε allows to control the balance between compression (second term on the left-hand side) and diffusion (right-hand side). The time step $\Delta\tau$ and ε are set to ${}^{\Delta x}/_{32}$ and ${}^{\Delta x}/_{2}$, respectively, which results in an interface thickness of 5 cells.

2.4.2. Interfacial energy and mass transfers

For large interfaces, the energy transfers are computed using the expressions proposed by Fleau (2017) in the framework of the Large Bubble Model:

$$\Pi_{l\to g} = \alpha_g \alpha_l \lambda_g \underline{\nabla} T_g \cdot \underline{\nabla} \alpha_g \,, \tag{21}$$

$$\Pi_{g\to l} = \alpha_g \alpha_l \lambda_l \underline{\nabla} T_l \cdot \underline{\nabla} \alpha_l \,. \tag{22}$$

In the neptune_cfd code, a five-cell stencil is used for the gradients. Fleau (2017) showed that this could be a problem for temperature. Indeed, for a given interface cell, the stencil used to compute say the liquid temperature gradient could include cells with only gas, in which the liquid temperature does not make sense. As an alternative, the author proposed the following modified expression, based on the fact that condensing steam or evaporating liquid must be at saturation temperature: $\underline{\nabla} T_k = (T_{sat} - T_k)\,(\underline{e}_x/\Delta x + \underline{e}_y/\Delta y + \underline{e}_z/\Delta z)$.

In the present work, since air is present, Eqs. (21) and (22) are weighted by Y_s. The resulting expressions are successfully validated by comparison with analytical data in a 1D phase change case based on the Stefan problem. However, for the sake of brevity, the results are not provided.

The mass transfers are deduced from the same equation as Eq. (11).

3. Problem setup

3.1. Computational domain and boundary conditions

An air-steam mixture is injected into the two-dimensional mini-channel of opening $d = 100\,\mu\text{m}$ and length $l = 3\,\text{cm}$ presented in Fig. 2. Flow rate, temperature and composition boundary conditions are imposed at the inlet, a pressure boundary condition is imposed at the outlet and a temperature boundary condition is imposed at the walls. The outlet pressure P^{out} is set to 140 bar. Indeed, the final purpose is to assess the performance of the FGLIM at both low and high pressures, but the present work is restricted to high pressures. The air inlet mass fraction Y_a^{in} is set to 1 %. This low value aims to prove the ability of the FGLIM to take into account non-condensable gases while ensuring an important level of condensation. The other boundary condition values are given in Table 4. The gas inlet temperature T_g^{in} is set to $T_{sat} + 12\,\text{K}$ and the wall temperature T_w to either $T_{sat} - 15\,\text{K}$ or $T_{sat} - 25\,\text{K}$ (an exception is made for Calculation 0, which will be used for a single-phase flow verification; in this calculation, to avoid the formation of liquid, both T_g^{in} and T_w are set above T_{sat}). The gas inlet mass flow rate per unit area G is varied between 20 and $50\,\text{kg}\,\text{m}^{-2}\,\text{s}^{-1}$, to be able to observe a wide range of flow regimes. The physical properties are automatically computed using the CATHARE tables (Emonot et al., 2011). For the sake of information, the values at saturation are provided in Table 5. An adaptive time-stepping strategy is adopted. The maximum Courant and Fourier numbers, defined as $\|\underline{U}_k\| \frac{\Delta t}{\Delta x}$ and $\frac{\lambda_k}{\rho_k C p_k} \frac{\Delta t}{\Delta x}$, with Δt the time step and Δx the grid spacing, are set to 1 and 10 for both the gas and the liquid.

3.2. Turbulence

In the present work, the gas and liquid Reynolds numbers are defined as:

$$Re_g = \frac{G x_g D_h}{\mu_g} \,, \tag{23}$$

$$Re_l = \frac{G\,(1 - x_g)\,D_h}{\mu_l} \,, \tag{24}$$

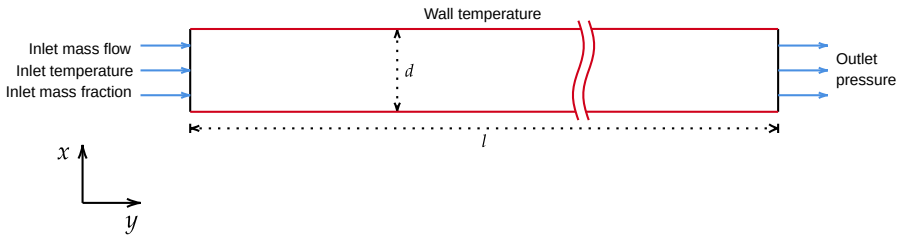

Figure 2: Computational domain and boundary conditions. Dimensions are: $d = 100\,\mu\text{m}$ and $l = 3\,\text{cm}$. Mass flow rate, temperature and composition are imposed at the inlet, pressure is imposed at the outlet and temperature is imposed at the walls.

Table 4: Boundary condition values for the various calculations performed in the present work. G is the gas inlet mass flow rate per unit area, T_g^{in} the gas inlet temperature and T_w the wall temperature.

Calculation number	Inlet		Walls
	G [kg m^{-2} s^{-1}]	T_g^{in} [K]	T_w [K]
0	20	650	620
1	20	622	595
2	30	622	595
3	40	622	595
4	50	622	595
5	20	622	585
6	30	622	585
7	40	622	585
8	50	622	585

Table 5: Physical properties at saturation. During the computation, the physical properties are automatically computed using the CATHARE tables (Emonot et al., 2011).

Property	$k = g$	$k = l$	Two phases
σ [N m^{-1}]	–	–	7.2×10^{-3}
λ_k [W m^{-1} K]	0.0707	0.472	–
μ_k [Pa s]	2.29×10^{-5}	8.14×10^{-5}	–
ρ_k [kg m^{-3}]	86.8	624	–
Cp_k [J kg^{-1} K^{-1}]	11 424	7752.6	–

with $D_h = 2d$ the hydraulic diameter and x_g the flow quality, i.e., the ratio of vapor mass flow rate to total mass flow rate (see Section 3.6 in the following). An estimation of the gas Reynolds number at the inlet (where $x_g = 1$) Re_g^{in} is given in Table 6. For all the calculations, Re_g^{in} is far below the critical value of about 2000 for smooth pipes, above which the flow is considered to be turbulent. Therefore, no turbulence model is used for the gas field. No turbulence model is used for the liquid field either, since Re_l is expected to be lower than Re_g.

3.3. Gravity, roughness and wettability

Gravity is neglected. Indeed, the Eötvos number, defined as the ratio of gravitational to surface tension forces, is below the critical value of 0.88 proposed by Suo and Griffith (1964). Other criteria can be found in the literature (Brauner and Moalem-Maron, 1992; Cornwell and Kew, 1993), but this one is the most restrictive.

In the following, the results are compared with experimental correlations. Most of the experiments have used slightly rough and slightly hydrophilic surfaces. In the present work, for the sake of simplicity, roughness is neglected. Concerning wettability, for the large interfaces, a neutral contact angle of 90° is used. The advantage is that no contact angle model is required, the value of 90° being enforced via the null flux condition applied by the code to the volume fraction at the wall.

3.4. Mesh

A mesh convergence study is performed. Four Cartesian meshes are considered. To maintain a constant interface resolution, cubic cells are used. The number of cells in the x-direction N_x is varied between 10 and 30 (the number of cells in the y-direction is modified accordingly in order to have cubic cells). Calculation 4 is used for comparison between the various meshes. The quantities of interest are the gas and liquid volume fractions, velocities and temperatures. These are averaged over time according to the following formulas: $\overline{\alpha}_k = \langle \alpha_k \rangle$, $\overline{U}_k = {}^{\langle \alpha_k \rho_k U_k \rangle}/_{\langle \alpha_k \rho_k \rangle}$ and $\overline{T}_k = {}^{\langle \alpha_k \rho_k C p_k T_k \rangle}/_{\langle \alpha_k \rho_k C p_k \rangle}$, where $\langle \cdot \rangle$ denotes the time average. The results are shown in Fig. 3 for the gas phase. Convergence is reached for $N_x = 25$, and almost reached for $N_x = 20$. The mesh corresponding to $N_x = 20$ being the best compromise between accuracy and calculation time, it is kept for use in subsequent calculations. It ensures that the hydrodynamic and thermal boundary layers are properly solved. It is worth noting that, with this mesh, the time steps used by the code, resulting from the conditions on the Courant and Fourier numbers set in Section 3.1, are of the order of 10^{-6} s, which is very small. It is also worth noting that the models used for dynamics and phase change (presented in Sections 2.3 and 2.4) act differently according to the mesh resolution. However, the present results show that, once convergence is reached, similar levels of volume fraction, velocity and temperature are obtained.

3.5. Averaging procedure

In the following, the correlations to which are compared the results are one-dimensional correlations. Therefore, the problem variables are averaged over the cross-section. The expressions used are given in Table 7. An area-weighted average is performed for volume fraction, surface tension and pressure. A volume-fraction-weighted average is performed for thermal conductivity, viscosity, density and specific heat capacity, to take into account only the regions where phase k is present. A volume-fraction- and density-weighted average is performed for velocity, since the conserved quantity is $\alpha_k \rho_k U_k$. A volume-fraction-, density- and heat-capacity-weighted average is performed for temperature, since the conserved quantity is $\alpha_k \rho_k H_k = \alpha_k \rho_k C p_k T_k$.

Table 6: Estimation of the gas Reynolds number (Eq. (23)) at the inlet.

Calculation number	0	1	2	3	4	5	6	7	8
Re_g^{in}	174	174	261	348	435	174	261	348	435

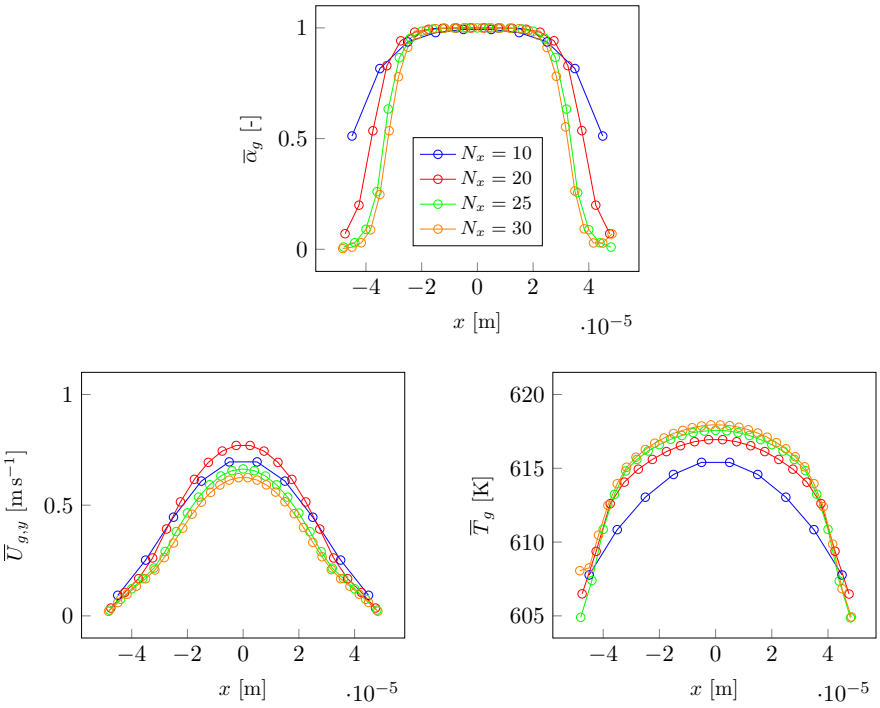

Figure 3: Time-averaged profiles of gas volume fraction (top), y-component of the gas velocity (bottom left) and gas temperature (bottom right) obtained in Calculation 4 at $y = 0.01$ m for the various meshes studied

Table 7: One-dimensional quantities used in the following.

ϕ_k	Cross-sectional averaged ϕ_k
α_k, σ, P	$\frac{1}{d}\int_x \phi_k \mathrm{d}x$
λ_k, μ_k, ρ_k, Cp_k	$\frac{\int_x \alpha_k \phi_k \mathrm{d}x}{\int_x \alpha_k \mathrm{d}x}$
$U_{k,y}$	$\frac{\int_x \alpha_k \rho_k \phi_k \mathrm{d}x}{\int_x \alpha_k \rho_k \mathrm{d}x}$
T_k	$\frac{\int_x \alpha_k \rho_k Cp_k \phi_k \mathrm{d}x}{\int_x \alpha_k \rho_k Cp_k \mathrm{d}x}$

3.6. Flow quality

Another quantity used in the following is the flow quality, defined as the ratio of vapor mass flow rate to total mass flow rate:

$$x_g = \frac{\int_x \alpha_g \rho_g U_{g,y} \mathrm{d}x}{\int_x \left(\alpha_g \rho_g U_{g,y} + \alpha_l \rho_l U_{l,y}\right) \mathrm{d}x} \,. \tag{25}$$

Using the cross-sectional averaged quantities in Table 7, Eq. (25) can be rewritten as:

$$x_g = \left(1 + \frac{U_{l,y}}{U_{g,y}} \frac{\alpha_l}{\alpha_g} \frac{\rho_l}{\rho_g}\right)^{-1} \,. \tag{26}$$

A usual assumption is that the ratio of gas to liquid velocity, called slip ratio, is unity. The flow quality then simply corresponds to the static vapor quality (vapor mass fraction). This assumption is valid for flow regimes like droplet flow and bubbly flow, but is not valid for flow regimes like slug/plug flow, where there is a liquid film surrounding the vapor slugs. In the present work, as the latter flow regime is expected to occur, no assumption is made on the slip ratio.

3.7. Single-phase flow verification

Before detailing the results for two-phase flow, a verification is first performed for single-phase flow. The purpose is to ensure that single-phase heat transfer is correctly computed and to help understanding the results provided in the following. Calculation 0, in which no liquid is formed, is used. The quantity considered is the Nusselt number, which, in the present section, is computed as:

$$Nu_{sp,g} = \frac{h_{sp} D_h}{\lambda_g} \,, \tag{27}$$

with $h_{sp,g}$ the single-phase gas heat transfer coefficient, obtained from:

$$h_{sp,g} = \frac{\varphi_{sp,g}}{T_w - T_g} \,. \tag{28}$$

$\varphi_{sp,g}$, T_w and T_g are given, respectively, in Section 2.3.4, Table 4 and Table 7. Fig. 4 shows $Nu_{sp,g}$ as a function of ${}^{4y}/_{Re_g Pr_g D_h}$. Two regions can be distinguished: a region in which $Nu_{sp,g}$ decreases, corresponding to the development of the hydrodynamic and thermal boundary layers and referred to as hydrodynamic and thermal developing region, and a region in which $Nu_{sp,g}$ is constant, referred to as fully developed region. A good agreement is obtained with the analytical solution of Kays and Crawford (1993):

$$Nu_{sp,g} = 7.54 \,, \tag{29}$$

which is valid only in the fully developed region. Fig. 5 shows ${}^{1}/_{y} \int_0^y Nu_{sp,g} \mathrm{d}y'$ as a function of ${}^{4y}/_{Re_g Pr_g D_h}$. A good agreement is obtained with the analytical solution of Mercer et al. (1967):

$$\frac{1}{2y} \int_0^y Nu_{sp,g} \mathrm{d}y' = 3.77 + \frac{0.066 \left(\frac{Re_g Pr_g D_h}{4y}\right)^{1.2}}{1 + 0.1 Pr_g^{0.87} \left(\frac{Re_g Pr_g D_h}{4y}\right)^{0.7}} \,, \tag{30}$$

which is valid in both the hydrodynamic and thermal developing region and the fully develop region. Note that it is consistent with Eq. (29) ($2 \times 3.77 = 7.54$). These results indicate that single-phase heat transfer is correctly computed. Two-phase heat transfer is investigated in the following.

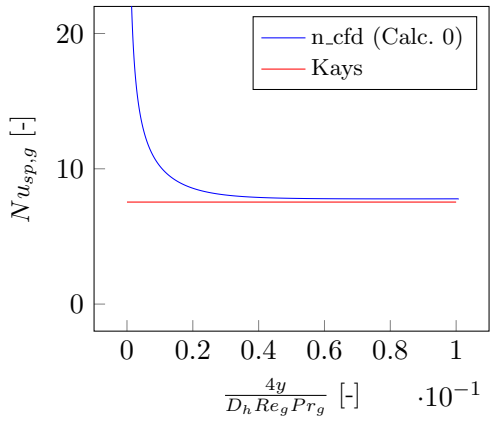

Figure 4: Evolution of $Nu_{sp,g}$ (Eqs. (27) and (28)) as a function of $^{4y}/_{Re_g Pr_g D_h}$ for Calculation 0. Comparison is made with the analytical solution of Kays and Crawford (1993) (Eq. (29)) in the fully developed region.

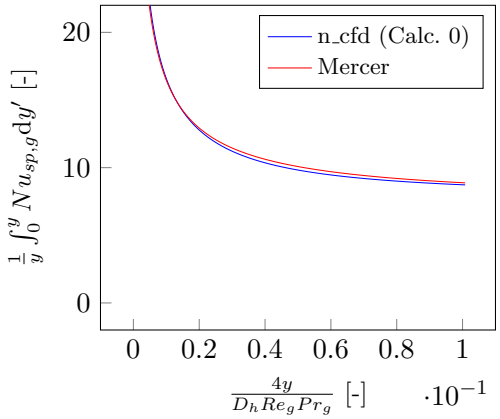

Figure 5: Evolution of $^1/_y \int_0^y Nu_{sp,g} dy'$ (with $Nu_{sp,g}$ given by Eqs. (27) and (28)) as a function of $^{4y}/_{Re_g Pr_g D_h}$ for Calculation 0. Comparison is made with the analytical solution of Mercer et al. (1967) (Eq. (30)) in both the hydrodynamic and thermal developing region and the fully developed region.

4. Results

4.1. Flow patterns

4.1.1. Droplet flow regime

The droplet flow regime is observed in all the calculations performed. It is shown in Fig. 6a. It is characterized by the nucleation of small droplets on the walls. Once formed, these droplets are entrained by the gas and slide along the walls. They are sub-grid droplets, which means that, at this location, the model uses the closures in Sections 2.3.1, 2.3.2 and 2.3.4.

4.1.2. Smooth and wavy annular flow regimes

The smooth and wavy annular flow regimes are also observed in all the calculations performed. As shown in Figs. 6b and 6c, the liquid flows on the walls as a film while the gas flows in the center. The two regimes can be distinguished by the shape of the interfaces, flat in one case and wavy in the other. Waves might result from a Kelvin-Helmholtz instability (Carey, 1992). Unlike in the droplet flow regime, the interfaces can be distinguished. Therefore, at this location, the model uses the closures in Section 2.4.

4.1.3. Slug flow regime

The length of the zone in which the previous flow regimes occur increases with flow rate. As a consequence, the slug flow regime is only observed in Calculations 1, 2, 5 and 6. It is shown in Fig. 6d. It is characterized by an alternation between large bubbles and liquid slugs, the liquid slugs resulting from the merging of two high-amplitude waves (see Fig. 7). Like in the smooth and wavy annular flow regimes, the interfaces can be distinguished, which means that, at this location, the model uses the closures in Section 2.4.

4.1.4. Comparison with experimental flow patterns

A qualitative comparison is made with the experiments of Hu and Chao (2007) and Wu and Cheng (2005). The channel geometry used in these experiments is close to that of the present work (hydraulic diameter between 73 and 237 µm and length of 2.8 cm for Hu and Chao (2007); hydraulic diameter of 82.8 µm and length of 3 cm for Wu and Cheng (2005)). The working fluid is the same. However, the operating conditions are different. Flow regimes similar as those mentioned previously are observed, which indicates that the model is able to capture all the flow regimes that would occur in a real system.

4.2. Frictional pressure drop

4.2.1. Computation and correlations used for comparison

The frictional pressure drop is quantified using the model of Lockhart and Martinelli (1947), in which:

$$\phi_l^2 = \frac{\left(\frac{dP}{dy}\right)_f}{\left(\frac{dP}{dy}\right)_{f,l}}, \tag{31}$$

$$\phi_g^2 = \frac{\left(\frac{dP}{dy}\right)_f}{\left(\frac{dP}{dy}\right)_{f,g}}, \tag{32}$$

$$X = \sqrt{\frac{\phi_g^2}{\phi_l^2}}. \tag{33}$$

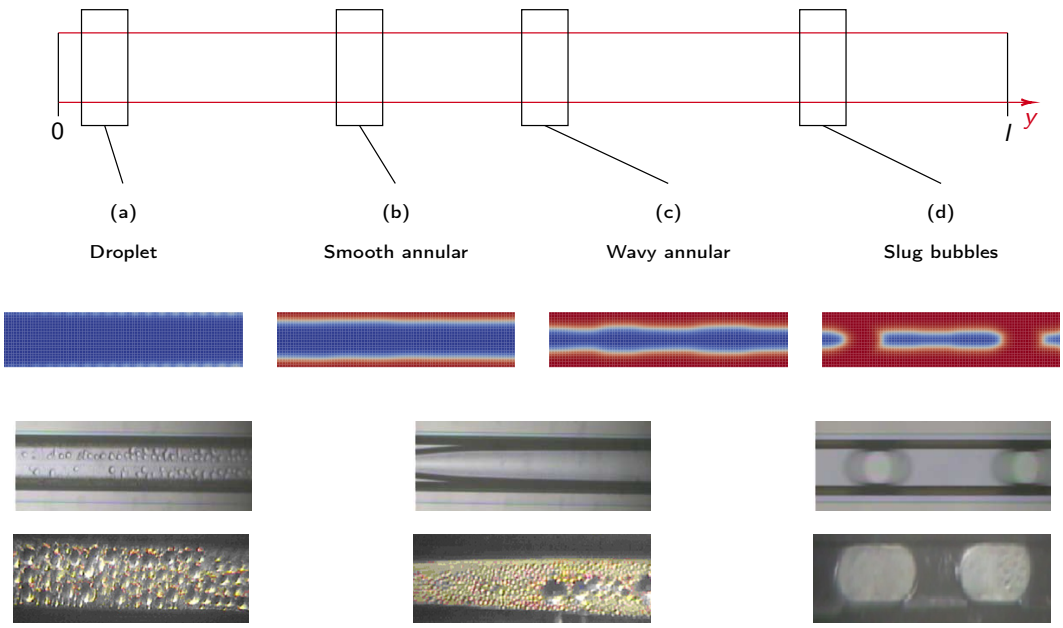

Figure 6: Flow patterns obtained in the present work (top line; gas in blue; liquid in red; flow from left to right). Qualitative comparison is made with the experiments of Wu and Cheng (2005) (middle line; flow from right to left) and Hu and Chao (2007) (bottom line; flow from right to left).

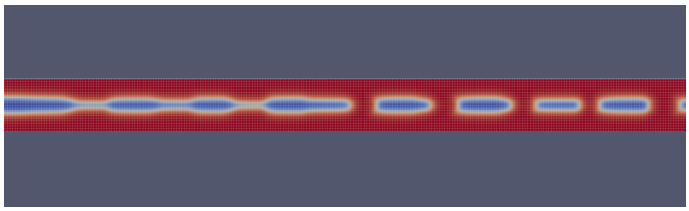

Figure 7: Transition from wavy annular to slug flow (gas in blue; liquid in red).

ϕ_l^2 and ϕ_g^2 are called two-phase multipliers and X is called Martinelli parameter. $\left({}^{dP}/_{dy}\right)_{f,l}$ is the frictional pressure gradient assuming the liquid flows alone in the tube, $\left({}^{dP}/_{dy}\right)_{f,g}$ the frictional pressure gradient assuming the gas flows alone in the tube and $\left({}^{dP}/_{dy}\right)_f$ the actual frictional pressure gradient. $\left({}^{dP}/_{dy}\right)_{f,g}$ and $\left({}^{dP}/_{dy}\right)_{f,l}$ are computed as:

$$\left(\frac{dP}{dy}\right)_{f,l} = \frac{f_l G^2 \left(1-x_g\right)^2}{2\rho_l D_h}\,, \tag{34}$$

$$\left(\frac{dP}{dy}\right)_{f,g} = \frac{f_g G^2 x_g^2}{2\rho_g D_h}\,, \tag{35}$$

with f_g and f_l the gas and liquid friction factors, obtained from:

$$f_l = \frac{96}{Re_l}\,, \tag{36}$$

$$f_g = \frac{96}{Re_g}\,. \tag{37}$$

$\left({}^{dP}/_{dy}\right)_f$ is computed as:

$$\left(\frac{dP}{dy}\right)_f = \left(\frac{dP}{dy}\right)_t - \left(\frac{dP}{dy}\right)_a\,, \tag{38}$$

with $\left({}^{dP}/_{dy}\right)_t$ the total pressure gradient, obtained from the pressure P solved by the code, and $\left({}^{dP}/_{dy}\right)_a$ the acceleration pressure gradient, obtained from the expression proposed by Martinelli and Nelson (1948):

$$\left(\frac{dP}{dy}\right)_a = G^2 \frac{d}{dy}\left(\frac{x_g^2}{\alpha_g \rho_g} + \frac{\left(1-x_g\right)^2}{\left(1-\alpha_g\right)\rho_l}\right)\,. \tag{39}$$

The multiplier ϕ_l^2 given by Eq. (31) is compared with that given by:

$$\phi_l^2 = 1 + \frac{C}{X} + \frac{1}{X^2}\,, \tag{40}$$

with X obtained from Eq. (33) and C obtained from the correlations in Table 8. These correlations have been established using data points coming from phase change experiments conducted in mini-channels. The correlations used are those of Hwang and Kim (2006), Kim and Mudawar (2012), Li and Wu (2010), Mishima and Hibiki (1996) and Zhang et al. (2010). An additional correlation, corresponding to the average of the previous ones, is employed. In the following, the multiplier ϕ_l^2 given by Eq. (31) is denoted $\phi_{l,num}^2$ while that given by Eq. (40) is denoted $\phi_{l,exp}^{2\,k}$, $k \in [\![1,6]\!]$. Both are averaged over time. The mean relative error is computed as:

$$\mathrm{MRE}_k = \frac{1}{8}\sum_{i=1}^{8}\frac{1}{N_y}\sum_{j=1}^{N_y}\frac{\phi_{l,num}^2 - \phi_{l,exp}^{2\,k}}{\phi_{l,exp}^{2\,k}}\,, \tag{41}$$

with N_y the number of points (cells) in the y-direction.

4.2.2. Discussion of the results

Figs. 8 and 9 show, respectively, $\phi_{l,num}^2$ and the flow quality as a function of y for all the calculations performed. $\phi_{l,num}^2$ decreases to unity as the flow quality, inversely related to the amount of liquid, decreases to zero, which is consistent. At given y, $\phi_{l,num}^2$ increases with flow rate, due to the fact that the flow quality increases and thus the amount of liquid decreases.

Fig. 10 shows $\phi_{l,num}^2$ and $\phi_{l,exp}^{2\,k}$, $k \in [\![1,6]\!]$ as a function of y for Calculations 5 to 8. A good agreement is obtained between the two quantities.

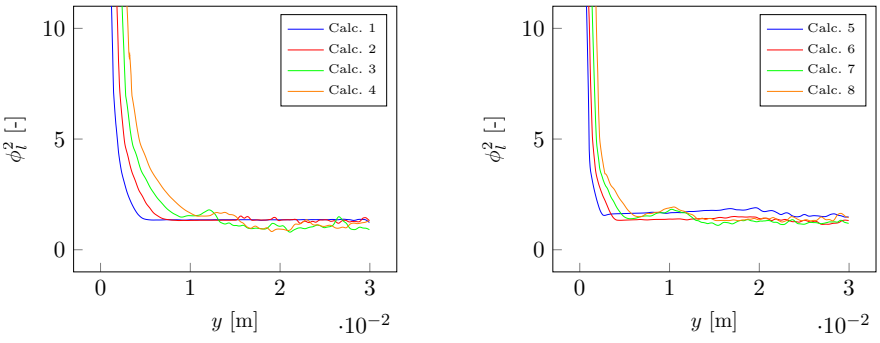

Figure 8: Evolution of $\phi^2_{l,num}$ (Eq. (31)) along the mini-channel for all the calculations performed.

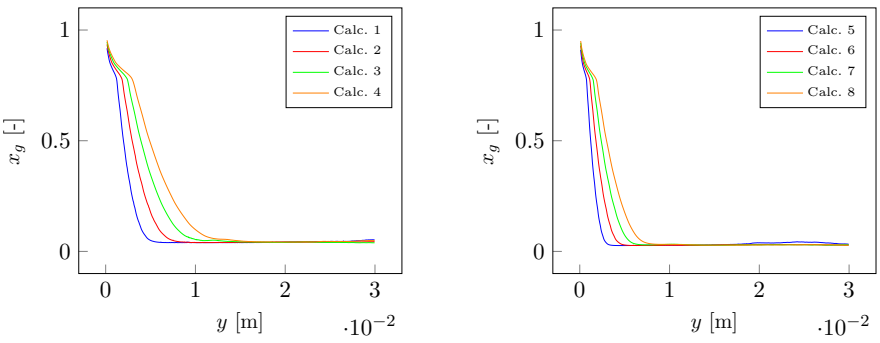

Figure 9: Evolution of the flow quality (Eq. (26)) along the mini-channel for all the calculations performed.

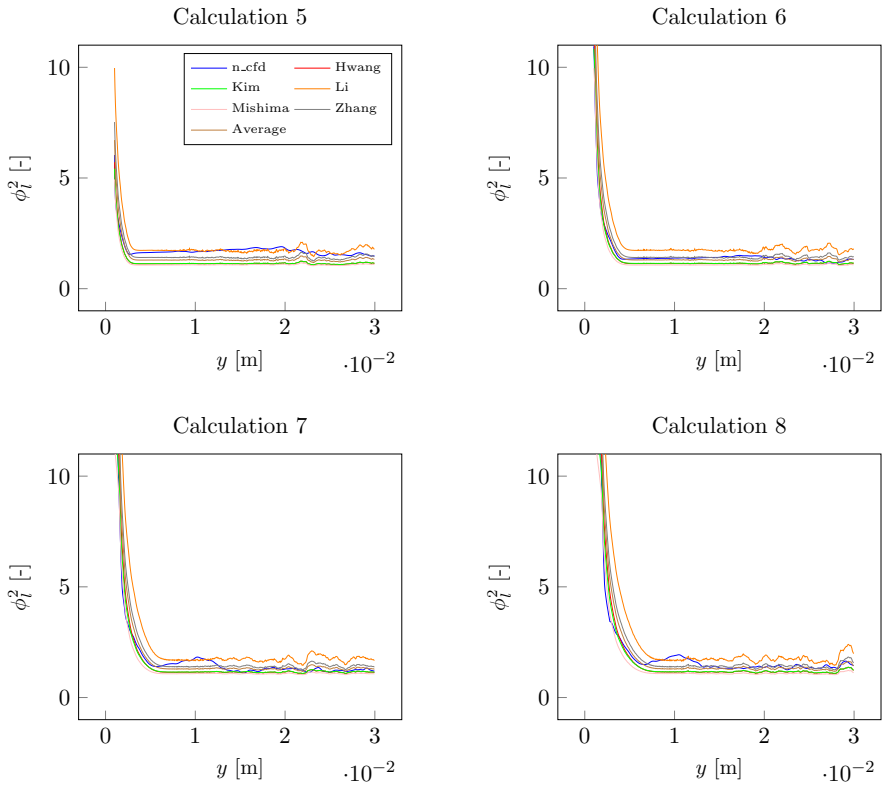

Figure 10: Comparison between $\phi^2_{l,num}$ and $\phi^{2\,k}_{l,exp}$, $k \in [\![1,6]\!]$ for Calculations 5 to 8. $\phi^2_{l,num}$ is obtained from Eq. (31) while $\phi^{2\,k}_{l,exp}$, $k \in [\![1,6]\!]$ is obtained from Eq. (40) and Table 8.

Table 8: Correlations for C in Eq. (40). The corresponding ϕ_l^2 is denoted $\phi_{l,exp}^{2\,k}$, $k \in [\![1,6]\!]$.

Correlation	D_h [mm]	Fluid(s)	Points	Expression for C
Hwang and Kim (2006)	0.244–0.792	R134a	77	$0.227 Re_{lo}^{0.452} X^{-0.32} N^{-0.82}$
Kim and Mudawar (2012)	0.0695–6.22	22 fluids	7115	$3.5 \times 10^{-5} Re_{lo}^{0.44} La_g^{0.5} \left(\frac{\rho_L}{\rho_g}\right)^{0.48}$
Li and Wu (2010)	0.148–3.25	12 fluids	769	$11.9 Bo^{0.45}$
Mishima and Hibiki (1996)	1.05–4.08	Air-Water	299	$21\left(1 - e^{-0.319 D_h}\right)$
Zhang et al. (2010)	0.07–6.2	10 fluids	2201	$21\left(1 - e^{-0.358/N}\right)$
Average correlation	–	–	–	–

$Bo = {}^{g(\rho_l - \rho_g)D_h^2}/_{\sigma}$ (Bond number); $La_g = {}^{\rho_g \sigma D_h}/_{\mu_g^2}$ (Laplace number based on gas); $N = \sqrt{{}^{\sigma}/_{g(\rho_l - \rho_g)D_h^2}}$ (confinement number); $Re_{lo} = {}^{GD_h}/_{\mu_l}$ (Reynolds number assuming only liquid).

19

Table 9: Mean relative error (MRE) on ϕ_l^2 (Eq. (41)).

Correlation	MRE [%]
Hwang and Kim (2006)	13.8
Kim and Mudawar (2012)	13.0
Li and Wu (2010)	−26.6
Mishima and Hibiki (1996)	21.6
Zhang et al. (2010)	−9.27
Average correlation	−1.08

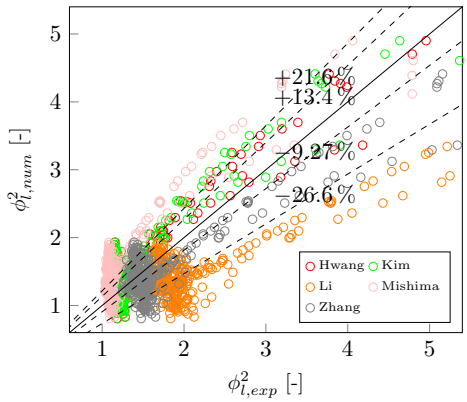

Figure 11: Parity plot of $\phi^{2\,k}_{l,exp}$, $k \in [\![1,6]\!]$ versus $\phi^2_{l,num}$ at various locations along the mini-channel. $\phi^2_{l,num}$ is obtained from Eq. (31) while $\phi^{2\,k}_{l,exp}$, $k \in [\![1,6]\!]$ is obtained from Eq. (40) and Table 8.

The mean relative error is given in Table 9 and shown on the parity plot in Fig. 11. It is interesting to observe the relatively good accuracy of the correlation of Mishima and Hibiki (1996), which does not depend on the flow characteristics (it does not depend on any dimensionless number) and is, in principle, not suited for horizontal configurations. A very good agreement is obtained with the correlation of Zhang et al. (2010). However, it is difficult to know if this correlation is more reliable than the others. Indeed, it is one of the most appropriate in terms of fluids and number of data points but one of the least appropriate in terms of diameter. Overall, the mean relative error is comprised between $-26.6\,\%$ and $21.6\,\%$, which is comparable with the values found in the literature for pressure drop. The mean relative error obtained with the average correlation is $-1.08\,\%$, which is very low. Therefore, the frictional pressure drop and more globally flow dynamics is considered to be well predicted by the model.

4.3. Nusselt number

4.3.1. Computation and correlations used for comparison

In this section, the Nusselt number is computed as:

$$Nu_{tp} = \frac{h_{tp} D_h}{\lambda_b}\,, \tag{42}$$

with h_{tp} the two-phase heat transfer coefficient, obtained from:

$$h_{tp} = \frac{\varphi_{w\to g} + \varphi_{w\to l}}{T_w - T_b}\,. \tag{43}$$

$\varphi_{w\to g}$ and $\varphi_{w\to l}$ are given in Section 2.3.4 and T_w is given in Table 4. The bulk thermal conductivity λ_b and the bulk temperature T_b are given by:

$$\lambda_b = \frac{1}{d}\int_x (\alpha_g \lambda_g + \alpha_l \lambda_l)\,\mathrm{d}x\,, \tag{44}$$

$$T_b = \frac{\int_x (\alpha_g \rho_g Cp_g T_g + \alpha_l \rho_l Cp_l T_l)\,\mathrm{d}x}{\int_x (\alpha_g \rho_g Cp_g + \alpha_l \rho_l Cp_l)\,\mathrm{d}x}\,. \tag{45}$$

As previously, a comparison is made with experimental correlations. The correlations used, provided in Table 10, are those of Chato (1962), Kaushik and Azer (1988), Shah (2009) and Singh et al. (1996). Since they originally do not depend

on the amount of air, as usually done in the literature, they are weighted by a so-called degradation factor, denoted f_{nc}. The latter is obtained from the expression proposed by Kunh et al. (1997):

$$f_{nc} = f_{nc,1} f_{nc,2} \,, \tag{46}$$

with $f_{nc,1}$ and $f_{nc,2}$ given by:

$$f_{nc,1} = \frac{\delta_{Nu}}{\delta_{shear}} \left(1 + 7.32 \times 10^{-4} Re_l\right) \,, \tag{47}$$

$$f_{nc,2} = \begin{cases} 1 - 2.601 Y_a^{0.708} & \text{if } Y_a < 0.1 \\ 1 - Y_a^{0.292} & \text{otherwise} \end{cases} \,, \tag{48}$$

$\delta_{Nu}/\delta_{shear}$ being the ratio of liquid thickness with interfacial shear to liquid thickness without interfacial shear, assumed to be close to unity here due to small shear stress at the interface. An additional correlation, corresponding to the average of the previous ones, is employed. In the following, the Nusselt number obtained from Eqs. (42) to (45) is denoted $Nu_{tp,num}$ while that obtained from the correlations in Table 10 is denoted $Nu^k_{tp,exp}$, $k \in [\![1,5]\!]$. Both are averaged over time. The mean relative error is computed as:

$$\text{MRE}_k = \frac{1}{8} \sum_{i=1}^{8} \frac{1}{N_y} \sum_{j=1}^{N_y} \frac{Nu_{tp,num} - Nu^k_{tp,exp}}{Nu^k_{tp,exp}} \,. \tag{49}$$

4.3.2. Discussion of the results

Fig. 12 shows $Nu_{tp,num}$ as a function of y for all the calculations performed. The profiles can be decomposed into four regions: two developing regions, where $Nu_{tp,num}$ decreases, and two developed regions, where $Nu_{tp,num}$ is constant or almost constant, the first being very short. The transition from the first developed region to the second developing region occurs when $\varphi_{w\to g} + \varphi_{w\to l} \approx \varphi_{w\to l}$, $\lambda_b \approx \frac{1}{d}\int_x \alpha_l \lambda_l \mathrm{d}x$ and $T_b \approx \int_x \alpha_l \rho_l C p_l T_l \mathrm{d}x / \int_x \alpha_l \rho_l C p_l \mathrm{d}x$. The constant value reached by $Nu_{tp,num}$ in the second developed region is close to that predicted by single-phase flow theory (see the verification in Section 3.7). At given y in the entrance region (first developing region), $Nu_{tp,num}$ increases with flow rate, due to the fact that both φ_{cond} and $\varphi_{sp,g}$ increase.

Fig. 13 shows $Nu_{tp,num}$ and $Nu^k_{tp,exp}$, $k \in [\![1,5]\!]$ as a function of y for Calculations 1 to 4. Since the correlations assume the flow to be fully developed, $Nu^k_{tp,exp}$, $k \in [\![1,5]\!]$ is only shown in the second developed region. Qualitatively speaking, a good agreement is obtained between $Nu_{tp,num}$ and $Nu^k_{tp,exp}$, $k \in [\![1,5]\!]$.

The mean relative error is given in Table 11 and shown on the parity plot in Fig. 14. Good agreement is obtained with the correlations of Chato (1962), Kaushik and Azer (1988) and Singh et al. (1996). The correlation of Chato (1962) is considered to be the most reliable for the present calculations. Indeed, it is completely based on the analytical solution of Nusselt (1916) for laminar condensation on a plate. The worst agreement is obtained with the correlation of Shah (2009). However, less confidence is placed in this correlation than in the others. Indeed, even if few authors, such as Borchman (1967), have found it to give acceptable predictions in the laminar flow regime, the fact remains that it has originally not been developed for laminar flows (a large part of the data on which it is based corresponds to the turbulent flow regime). Excluding this correlation, the mean relative error is comprised between $-15.9\,\%$ and $15.8\,\%$, which is of the same order of what can be found in the literature. The mean relative error obtained with the average correlation is $5.82\,\%$, which is low. Therefore, the Nusselt number and more generally heat transfer is considered to be correctly predicted by the model.

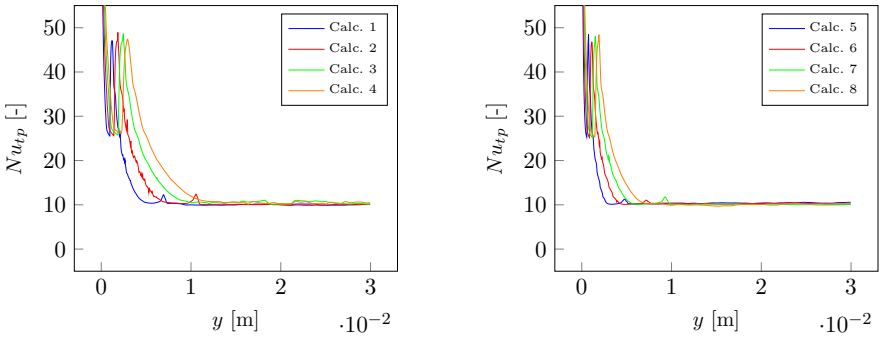

Figure 12: Evolution of $Nu_{tp,num}$ (Eqs. (42) to (45)) along the mini-channel for all the calculations performed.

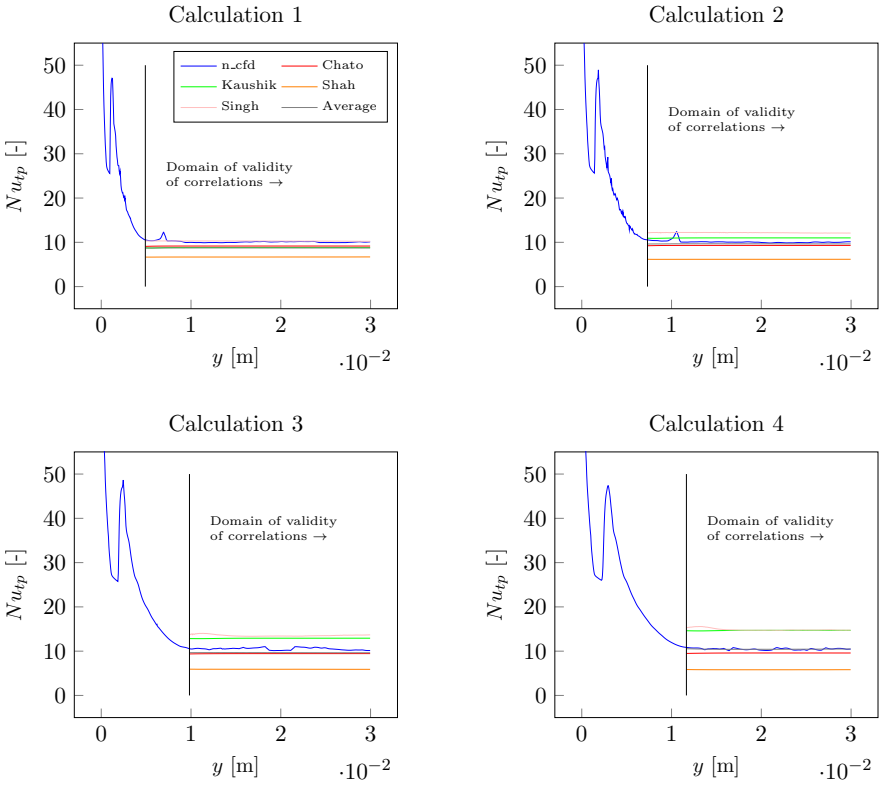

Figure 13: Comparison between $Nu_{tp,num}$ and $Nu^k_{tp,exp}$, $k \in [\![1,5]\!]$ for Calculations 1 to 4. $Nu_{tp,num}$ is obtained from Eqs. (42) to (45) while $Nu^k_{tp,exp}$, $k \in [\![1,5]\!]$ is obtained from Table 10.

Table 10: Correlations for the Nusselt number. The corresponding Nusselt number is denoted $Nu^k_{tp,exp}$, $k \in [\![1,5]\!]$.

Correlation	D_h [mm]	Fluid(s)	Points	Expression for $Nu_{tp,exp}$
Chato (1962)	14.5–27.9	Water, R113	n/a	$f_{nc} \cdot 0.555 \left(\frac{GaPr_l}{Ja}\right)^{1/4}$
Kaushik and Azer (1988)	12.5–17.8	R11, R113	n/a	$f_{nc} \cdot 2.078 Re_{eq}^{0.507} Pr_l^{1/3} \left(\frac{\Delta x_g D_h}{l}\right)^{0.198} P_r^{-0.14}$
Shah (2009)	2–49	17 fluids	1189	$f_{nc} \cdot \left[0.023 Re_{lo}^{0.8} Pr_l^{0.4} \left(\frac{\mu_l}{14\mu_g}\right)^n \alpha + 1.32 Re_{lo}^{-1/3} Ga^{1/3}\right]$
Singh et al. (1996)	11	R134a	n/a	$f_{nc} \cdot \left[0.2339 Re_l^{0.5} Pr_l^{0.33} \theta + 0.0925 \left(\frac{GaPr_l}{Ja}\right)^{1/4} (2\pi - \theta)\right]$
Average correlation	–	–	–	–

$Ga = {}^{g\rho_l(\rho_l - \rho_g)D_h^3}/_{\mu_l^2}$ (Galileo number); $Ja = {}^{Cp_l(T_{sat} - T_w)}/_{H_{lat}}$ (Jakob number); $n = 0.0058 + 0.557 P_r$ (exponent); $P_r = {}^{P}/_{P_c}$ with P_c the critical pressure (reduced pressure); $Re_{eq} = {}^{G_{eq} D_h}/_{\mu_l}$ with $G_{eq} = G(1 - x_g) + G x_g \sqrt{{}^{\rho_l}/_{\rho_g}}$ (equivalent Reynolds number); $\alpha = (1 - x_g)^{0.8} + {}^{3.8 x_g^{0.76}(1 - x_g)^{0.04}}/_{P_r^{0.38}}$ (coefficient); $\Delta x_g = x_g^{in} - x_g^{out}$ (flow quality variation); $\theta = 2 \arccos(2\alpha_g - 1)$ (coefficient).

Table 11: Mean relative error (MRE) on the Nusselt number (Eq. (49)).

Correlation	MRE [%]
Chato (1962)	15.8
Kaushik and Azer (1988)	−8.67
Shah (2009)	67.1
Singh et al. (1996)	−15.9
Average correlation	5.82

4.4. Generalization of the results obtained for the Nusselt number

The purpose of this section is to find a relevant dimensionless coordinate for plotting the Nusselt number defined by Eqs. (42) to (45). As shown in Fig. 15, the dimensionless coordinate $^{4y}/_{D_h Re_g Pr_g}$ used for single-phase flow (see Section 3.7) is not appropriate. Indeed, the curves corresponding to Calculations 1 to 4, characterized by $T_g^{in} - T_w = 27\,\mathrm{K}$, do not overlap with those corresponding to Calculations 5 to 8, characterized by $T_g^{in} - T_w = 37\,\mathrm{K}$. This is due to condensation, which depends on both T_g^{in} and T_w. Based on these considerations, the following new dimensionless coordinate is proposed:

$$y^* = \frac{4yJa^*}{D_h Re_g Pr_g}\,, \tag{50}$$

with Ja^* a modified Jakob number based on $T_g^{in} - T_w$:

$$Ja^* = \frac{Cp_l\left(T_g^{in} - T_w\right)}{H_{lat}}\,. \tag{51}$$

As shown is Fig. 16, this new dimensionless coordinate allows all the curves to overlap. An expression could be derived by curve fitting and could then be used for one-dimensional (1D) calculations. Note that this expression would only be valid for $Y_a^{in} = 1\,\%$ and $T_g^{in} - T_w > 27\,\mathrm{K}$. A more general analysis should be conducted to provide an expression valid for all values of Y_a^{in} and $T_g^{in} - T_w$.

5. Conclusion

A new model implemented in the neptune_cfd code was used to simulate steam condensation in the presence of air in a mini-channel of opening 100 µm. Various flow patterns, including droplet, smooth annular, wavy annular and slug flow, were observed. These flow patterns were found to be consistent in nature with those observed experimentally. The results were compared with various experimental correlations from the literature. The considered quantities were the pressure drop and the Nusselt number. They were predicted with minimal absolute mean relative errors of, respectively, 9.27 % and 15.8 %, which was considered indicative of a reasonably good accuracy of the model. The present work shows the relevance of the proposed model for the simulation of condensing two-phase flows in mini-channels, and more generally for the simulation of two-phase flows with phase change involving large deformable interfaces, small dispersed bubbles and small dispersed droplets. Its application to model cracks for the prediction of the leakage rate in the event of an accident is possible, but corresponding calculations would be time consuming, due to the fact that most of the accident scenarios last several days and that the dimensions of the problem imply the use of small time steps. A solution could be to perform 1D calculations, allowing for larger cells and thus larger time steps. The gas and liquid frictional pressure drops, as well as the gas and liquid wall heat fluxes, could be obtained from standard laws and the condensation flux deduced from the law $Nu_{tp} = f\left(y^*\right)$ proposed in Section 4.4.

CRediT authorship statement

Germain Davy: Conceptualization, Investigation, Methodology, Software, Validation, Visualization, Writing – Original Draft – Review & Editing. **Etienne Reyssat:** Supervision, Writing – Review & Editing. **Stéphane Vincent:** Supervision, Writing – Review & Editing. **Stéphane Mimouni:** Supervision, Writing – Review & Editing.

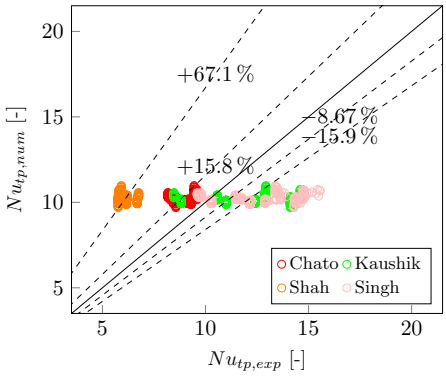

Figure 14: Parity plot of $Nu^k_{tp,exp}$, $k \in [\![1,5]\!]$ versus $Nu_{tp,num}$ at various locations along the mini-channel. $Nu_{tp,num}$ is obtained from Eqs. (42) to (45) while $Nu^k_{tp,exp}$, $k \in [\![1,5]\!]$ is obtained from Table 10.

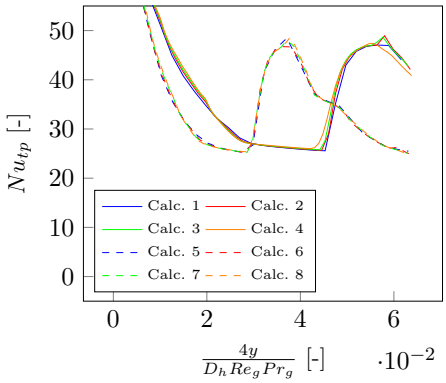

Figure 15: Evolution of $Nu_{tp,num}$ (Eqs. (42) to (45)) as a function of $^{4y}/_{Re_g Pr_g D_h}$ for all the calculations performed.

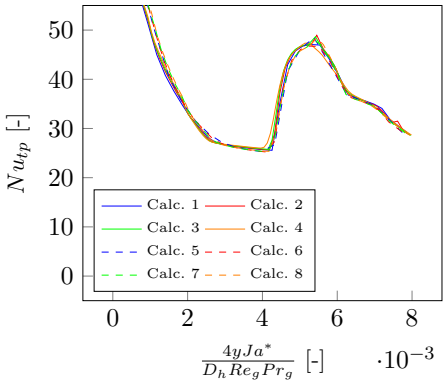

Figure 16: Evolution of $Nu_{tp,num}$ (Eqs. (42) to (45)) as a function of $^{4yJa^*}/_{Re_g Pr_g D_h}$ for all the calculations performed.

Declaration of interests

The authors declare that they have no known competing financial interests or personal relationships that could have appeared to influence the work reported in this paper.

Acknowledgements

This work has been achieved in the framework of the CIWAP3 project, financially supported by EDF. The neptune_cfd code is being developed in the framework of the NEPTUNE project, financially supported by EDF, Commissariat à l'Energie Atomique et aux Energies Alternatives (CEA), Institut de Radioprotection et de Sûreté Nucléaire (IRSN) and Framatome.

References

Borchman, J., 1967. Heat transfer of high velocity vapor condensing in annuli. ASHRAE Trans. 73.

Brackbill, J.U., Kothe, D.B., Zemach, C., 1992. A continuum method for modeling surface tension. J. Comput. Phys. 100, 335–54.

Brauner, N., Moalem-Maron, D., 1992. Identification of the range of 'small diameters' conduits, regarding two-phase flow pattern transitions. Int. Commun. Heat Mass Transf. 19, 29–39.

Carey, V.P., 1992. Liquid-vapor phase change phenomena: An introduction to the thermophysics of vaporization and condensation process in heat transfer equipment. Hemisphere.

Chato, J.C., 1962. Laminar condensation in horizontal and inclined tubes. ASHRAE J. 4, 52–60.

Chen, M., Yang, Z., Duan, Y., Chen, Y., Wu, D., 2014. Simulation of condensation flow in a rectangular microchannel. Int. Commun. Heat Mass Transf. 76, 60–9.

Cornwell, K., Kew, P.A., 1993. Boiling in small parallel channels. Elsevier Applied Science.

Coste, P., 2013. A large interface model for two-phase CFD. Nucl. Eng. Des. 255, 38–50.

Coste, P., Lavieville, J., 2008. A two-phase approach to the PTS problem evaluated on COSI experiment. 16th International Conference on Nuclear Engineering (ICONE-16), Orlando, USA.

Coste, P., Lavieville, J., 2009. A wall function-like approach for two-phase CFD condensation modeling of the pressurized thermal shock. 13th International Topical Meeting on Nuclear Reactor Thermal Hydraulics (NURETH-13), Kanazawa, Japan.

Da Riva, E., Del Col, D., 2011. Effect of gravity during condensation of R134a in a circular minichannel. Microgravity Sci. Technol. 23, 87–97.

Da Riva, E., Del Col, D., 2012. Numerical simulation of laminar liquid film condensation in a horizontal circular minichannel. J. Heat Transf. 134, 051019.

Da Riva, E., Del Col, D., Garimella, S.V., Cavallini, A., 2012. The importance of turbulence during condensation in a horizontal circular minichannel. Int. J. Heat Mass Transf. 55, 3470–81.

Davy, G., Reyssat, E., Vincent, S., Mimouni, S., 2020. CFD modeling of two-phase flows in cracks. 8th Workshop on Computational Fluid Dynamics for Nuclear Reactor Safety (CFD4NRS-8), Paris, France.

Denèfle, R., Mimouni, S., Caltagirone, J.P., Vincent, S., 2015. Multifield hybrid approach for two-phase flow modeling – Part 1: Adiabatic flows. Comput. Fluids 113, 106–11.

Emonot, P., Souyri, A., Grandrille, J.L., Barré, F., 2011. CATHARE-3: A new system code for thermal-hydraulics in the context of the NEPTUNE project. Nucl. Eng. Des. 241, 4476–81.

Fleau, S., 2017. Multifield approach and interface locating method for two-phase flows in nuclear power plant. Ph.D. thesis. Université Paris-Est.

Fleau, S., Mimouni, S., Mérigoux, N., Vincent, S., 2015. Validation of multifield approach for the simulations of two-phase flows. Comput. Therm. Sci. 7, 441–57.

Ganapathy, H., Shooshtari, A., Choo, K., Dessiatoun, S., Alshehhi, M., Ohadi, M., 2013. Volume of fluid-based numerical modeling of condensation heat transfer and fluid flow characteristics in microchannels. Int. J. Heat Mass Transf. 65, 62–72.

Gobin, A., Neau, H., Simonin, O., Llinas, J.R., Reiling, V., Selo, J.L., 2003. Fluid dynamic numerical simulation of a gas phase polymerization reactor. Int. J. Numer. Methods Fluids 43, 1199–220.

Guelfi, A., Bestion, D., Boucker, M., Boudier, P., Fillion, P., Grandotto, M., Hérard, J.M., Hervieu, E., Péturaud, P., 2007. NEPTUNE: A new software platform for advanced nuclear thermal hydraulics. Nucl. Sci. Eng. 156, 281–324.

Hu, J.S., Chao, C.Y.H., 2007. An experimental study of the fluid flow and heat transfer characteristics in micro-condensers with slug-bubbly flow. Int. J. Refrig. 30, 1309–18.

Hwang, Y.W., Kim, M.S., 2006. The pressure drop in microtubes and the correlation development. Int. J. Heat Mass Transf. 49, 1804–12.

Ishii, M., Zuber, N., 1979. Drag coefficient and relative velocity in bubbly, droplet or particulate flows. AIChE J. 25, 843–55.

Kaushik, N., Azer, N.Z., 1988. A general heat transfer correlation for condensation inside internally finned tubes. ASHRAE Trans. 94, 261–79.

Kays, W.M., Crawford, M.E., 1993. Convection heat and mass transfer. McGraw-Hill.

Kim, S.M., Kim, J., Mudawar, I., 2012. Flow condensation in parallel micro-channels – Part 1: Experimental results and assessment of pressure drop correlations. Int. J. Heat Mass Transf. 55, 971–83.

Kim, S.M., Mudawar, I., 2012. Universal approach to predicting two-phase frictional pressure drop for adiabatic and condensing mini/micro-channel flows. Int. J. Heat Mass Transf. 55, 3246–61.

Kunh, S.Z., Schrock, V.E., Peterson, P.F., 1997. An investigation of condensation from steam-gas mixture flow downward inside a vertical tube. Nucl. Eng. Des. 177, 53–69.

Lee, W.H., 1980. A pressure iteration scheme for two-phase flow modeling. Hemisphere.

Li, W., Wu, Z., 2010. A general correlation for adiabatic two-phase pressure drop in micro/mini-channels. Int. J. Heat Mass Transf. 53, 2732–9.

Lockhart, R.W., Martinelli, R.C., 1947. Proposed correlation of data for isothermal two-phase, two-component flow in pipes. Chem. Eng. Prog. 45, 39–48.

Manon, E., 2000. Contribution à l'analyse et à la modélisation locale des écoulements bouillants sous-saturés dans les conditions des Réacteurs à Eau sous Pression. Ph.D. thesis. Ecole Centrale Paris.

Martinelli, R.C., Nelson, B., 1948. Prediction of pressure drop during forced-circulation boiling water. Trans. ASME 70, 695–702.

Mer, S., Praud, O., Neau, H., Mérigoux, N., Magnaudet, J., Roig, V., 2018. The emptying of a bottle as a test case for assessing interfacial momentum exchange models for Euler–Euler simulations of multi-scale gas-liquid flows. Int. J. Multiph. Flow 106, 109–24.

Mercer, W.E., Pearce, W.M., Hitchcock, J.E., 1967. Laminar forced convection in the entrance region between parallel flat plates. J. Heat Transf. 89, 251–6.

Mérigoux, N., Lavieville, J., Mimouni, S., Guingo, M., Baudry, C., 2016. A generalized large interface to dispersed bubbly flow approach to model two-phase flows in nuclear power plant. 6th Workshop on Computational Fluid Dynamics for Nuclear Reactor Safety (CFD4NRS-6), Cambridge, USA.

Mimouni, S., Baconnier, P., Davy, G., 2019. Overview of mitigation models dedicated to severe accidents and consequences on flow rate through concrete containment structures. 18th International Topical Meeting on Nuclear Reactor Thermal Hydraulics (NURETH-18), Portland, USA.

Mimouni, S., Fleau, S., Vincent, S., 2017. CFD calculations of flow pattern maps and LES of multiphase flows. Nucl. Eng. Des. 321, 118–31.

Mimouni, S., Foissac, A., Lavieville, J., 2011. CFD modelling of wall steam condensation by a two-phase flow approach. Nucl. Eng. Des. 241, 4445–55.

Mimouni, S., Lamy, J.S., Lavieville, J., Guieu, S., Martin, M., 2010. Modelling of sprays in containment applications with a CMFD code. Nucl. Eng. Des. 240, 2260–70.

Mishima, K., Hibiki, T., 1996. Some characteristics of air-water two-phase flow in small diameter vertical tubes. Int. J. Multiph. Flow 22, 703–12.

Nusselt, W., 1916. Die oberflachenkondensation des wasserdampfes. Z. Ver. D. Ing. 60, 541–6.

Oran, E.S., Boris, J.P., 1981. Detailed modelling of combustion systems. Prog. Energy Combust. Sci. 7, 1–72.

Ranz, W.E., Marshall, W.R., 1952. Evaporation from drops. Chem. Eng. Prog. 48, 141–6.

Rastiello, G., Leclaire, S., Belarbi, R., Bennacer, R., 2015. Unstable two-phase flow rate in micro-channels and cracks under imposed pressure difference. Int. J. Multiph. Flow 77, 131–41.

Ruyer, P., Seiler, N., Weiss, M., Weiss, F.P., 2007. A bubble size distribution model for the simulation of bubbly flows. 6th International Conference on Multiphase Flow (ICMF-6), Leipzig, Germany.

Shah, M.M., 2009. An improved and extended general correlation for heat transfer during condensation in plain tubes. HVAC&R Res. 15, 889–913.

Singh, A., Ohadi, M.M., Dessiatoun, S.V., 1996. Empirical modeling of stratified-wavy flow condensation heat transfer in smooth horizontal tubes. ASHRAE Trans. 102, 596–603.

Suo, M., Griffith, P., 1964. Two-phase flow in capillary tubes. J. Basic Eng. 86, 576–82.

Tomiyama, A., Tamai, H., Zun, I., Hosokawa, S., 2002. Transverse migration of single bubbles in simple shear flows. Chem. Eng. Sci. 57, 1849–58.

Wang, W.W., Radcliff, T.D., Christensen, R.N., 2002. A condensation heat transfer correlation for millimeter-scale tubing with flow regime transition. Exp. Therm. Fluid Sci. 26, 473–85.

Wu, C., Cheng, P., 2005. Condensation flow patterns in silicon microchannels. Int. J. Heat Mass Transf. 48, 2186–97.

Yin, Z., Guo, Y., Suden, B., Wang, Q., Zeng, M., 2015. Numerical simulation of laminar film condensation in a horizontal minitube with and without non-condensable gas by the VOF method. Numer. Heat Transf. A: Appl. 68, 958–77.

Zhang, J., Li, W., Minkowycz, W.J., 2016a. Numerical simulation of condensation for R410A at varying saturation temperatures in mini/micro tubes. Numer. Heat Transf. A: Appl. 69, 464–78.

Zhang, J., Li, W., Minkowycz, W.J., 2017. Numerical simulation of R410A condensation in horizontal microfin tubes. Numer. Heat Transf. A: Appl. 71, 361–76.

Zhang, J., Li, W., Sherif, S.A., 2016b. A numerical study of condensation heat transfer and pressure drop in horizontal round and flattened minichannels. Int. J. Therm. Sci. 106, 80–93.

Zhang, W., Hibiki, T., Mishima, K., 2010. Correlations of two-phase frictional pressure drop and void fraction in mini-channel. Int. J. Heat Mass Transf. 53, 453–65.

Zhao, Z., Zhang, Y., Chen, X., Ma, X., Yanga, S., Li, S., 2015. A numerical study on condensation flow and heat transfer of refrigerant in minichannels of printed circuit heat exchanger. Int. J. Refrig. 102, 96–111.

Zuber, N., 1964. On the dispersed two-phase flow in the laminar flow regime. Chem. Eng. Sci. 19, 897–917.

4.3 Complementary simulations

4.3.1 Boundary conditions

As mentioned in Section 4.2, the final purpose is to validate the FGLIM in a case involving dispersed droplets and large interfaces at both low and high pressure. While Section 4.2 focused on high pressure, the present section focuses on low pressure. The reason why the results corresponding to high pressures have been provided first is that they were obtained first, requiring larger time steps and therefore resulting in shorter computation times (see demonstration after).

The pressure P^{out} is set to 5 bar. For the same reason as mentioned in the article, namely to prove the ability of the FGLIM to take into account non-condensable gases while ensuring an important level of condensation, the air inlet mass fraction Y_a^{in} is set to 1 %. The values of the gas inlet temperature T_g^{in}, the wall temperature T_w and the gas inlet mass flow rate per unit area G are given in Table 4.1. As before, the physical properties are automatically computed using the CATHARE tables (Emonot et al., 2011). Also, an adaptive time-stepping strategy is used. The maximum Courant and Fourier numbers, defined as $\|\underline{U}_k\| \frac{\Delta t}{\Delta x}$ and $\frac{\lambda_k}{\rho_k C p_k} \frac{\Delta t}{\Delta x}$, with Δt the time step and Δx the grid spacing, are set to 1 and 10 for both the gas and the liquid.

When mass transfer occurs, a criterion other than those corresponding to the Courant and Fourier number, not mentioned in the article, has to be met. In our calculations, it is found to be the most restrictive. The corresponding limiting value of the time step is obtained from the mass balance equation, by neglecting the convection term:

$$\rho_k \frac{\Delta \alpha_k}{\Delta t} \approx \Gamma_{p\to k} + \Gamma_{w\to k}\,, \tag{4.1}$$

with Δt the time step and $\Delta \alpha_k$ the volume fraction increment. The density ρ_k is obtained from the CATHARE tables and the mass transfers $\Gamma_{p\to k}$ and $\Gamma_{w\to k}$ from the model employed. A good practice is to have $\Delta \alpha_k \approx 10\,\%$. From Eq. (4.1), it is possible to quantify the ratio of time step at high pressure to time step at low pressure. Using the superscript 1 for high pressure and 2 for low pressure, we write:

$$\frac{\Delta t^1}{\Delta t^2} \approx \frac{\rho_k^1}{\rho_k^2} \frac{\Delta \alpha_k^1}{\Delta \alpha_k^2} \frac{\Gamma_{p\to k}^2 + \Gamma_{w\to k}^2}{\Gamma_{p\to k}^1 + \Gamma_{w\to k}^1}\,. \tag{4.2}$$

Assuming that $\Delta \alpha_k^1 \approx \Delta \alpha_k^2$ and $\Gamma_{p\to k}^1 + \Gamma_{w\to k}^1 \approx \Gamma_{p\to k}^2 + \Gamma_{w\to k}^2$, Eq. (4.2) simplifies in:

$$\frac{\Delta t^1}{\Delta t^2} \approx \frac{\rho_k^1}{\rho_k^2}\,. \tag{4.3}$$

Considering the pressures of 140 bar (article) and 5 bar (present section), $^{\Delta t^1}/_{\Delta t^2} \approx 36$. Therefore, in this section, the time step can be expected to be more than one order of magnitude lower than that in the article, i.e., less than 10^{-7} s, which is extremely small and will imply very large computation times.

Table 4.1: Boundary conditions values for the simulations performed in Section 4.3 and estimation of the Reynolds number at the inlet. G is the gas inlet mass flow rate per unit area, T_g^{in} the gas inlet temperature and T_w the wall temperature. Re_g^{in} is the inlet Reynolds number.

Calculation number	Inlet		Walls	Re_g^{in}
	G [kg m^{-2} s^{-1}]	T_g^{in} [K]	T_w [K]	
1	15	467	400	188

Table 4.2: Physical properties at saturation. During the computation, the physical properties are automatically computed using the CATHARE tables (Emonot et al., 2011).

Property	$k = g$	$k = l$	Two phases
σ [N m^{-1}]	–	–	4.6×10^{-2}
λ_k [W m^{-1} K]	0.0310	0.695	–
μ_k [Pa s]	1.59×10^{-5}	1.79×10^{-4}	–
ρ_k [kg m^{-3}]	2.65	915	–
Cp_k [J kg^{-1} K^{-1}]	1619	4336	–

4.3.2 Results

Fig. 4.1 shows $\phi^2_{l,num}$ and $\phi^{2\,k}_{l,exp}$, $k \in [\![1, 6]\!]$ as a function of y for Calculations 1. The corresponding mean relative errors are given in Table 4.3. As at high pressure, a very good agreement is obtained with the correlations of Kim and Mudawar (2012); Zhang et al. (2010b). The agreement obtained with the correlation of Li and Wu (2010) is better than at high pressure. However, that obtained with the correlation of Hwang and Kim (2006) is not as good as at high pressure. This is also the case for the correlation of Mishima and Hibiki (1996), but less confidence is placed in this correlation than in the others, since it does not depend on the flow properties and it is in principle not suited for horizontal configurations. The mean relative error obtained with the average correlation is 13.4 %, which is reasonable, and indicates that the frictional pressure drop and more globally flow dynamics is correctly predicted by the model at low pressure.

Fig. 4.1 also shows $Nu_{tp,num}$ and $Nu^k_{tp,exp}$, $k \in [\![1, 5]\!]$ as a function of y. The corresponding mean relative errors are given in Table 4.4. As at high pressure, a good agreement is

obtained with the correlations of Chato (1962) and Singh et al. (1996). A relatively good agreement is also obtained with the correlation of Shah (2009), which was unexpected since this correlation has originally been developed for turbulent flows and since a bad agreement has been obtained at high pressure. The worst agreement is obtained with the correlation of Kaushik and Azer (1988), which was also unexpected since a good agreement has been obtained at high pressure and since the correlation explicitly depends on the pressure – in the other correlations, the pressure is indirectly taken into account via the physical properties in the dimensionless numbers. The mean relative error obtained with the average correlation is $-3.13\,\%$, which is low, and indicates that the Nusselt number and therefore wall heat transfer is well predicted by the model at low pressure.

4.4 Summary

The purpose of this chapter was to validate the FGLIM in a case involving dispersed droplets and large interfaces. The problem studied was steam condensation in the presence of air in a smooth rectilinear model crack, at low and high pressure.

Several flow regimes were observed, including droplet, smooth annular, wavy annular and slug flow. These flow regimes were found to be consistent in nature with the various experimental flow patterns found in the literature. The results were also analyzed quantitatively in terms of both frictional pressure drop and Nusselt number. They were found to be in relatively good agreement with various experimental correlations from the literature.

Due to the scale of the problem, and to important mass transfers, small time steps were required. This resulted in large but acceptable computation times, since small physical durations were considered – note that the computation time would have been even greater with the 4FM, based on the results obtained at large scale in Chapter 3. For industrial-type simulations, characterized by large physical durations, the time steps employed would result in unacceptable computation times. As a consequence, the FGLIM could hardly be used for this kind of simulation. An alternative would be to keep a one-dimensional model, but to improve the existing correlations or develop new ones for better accuracy. In the following chapter, the FGLIM will be used to investigate the effect of roughness and tortuosity on laminar small-scale heat transfer with phase change, and possibly propose correlations that could be employed in 1D.

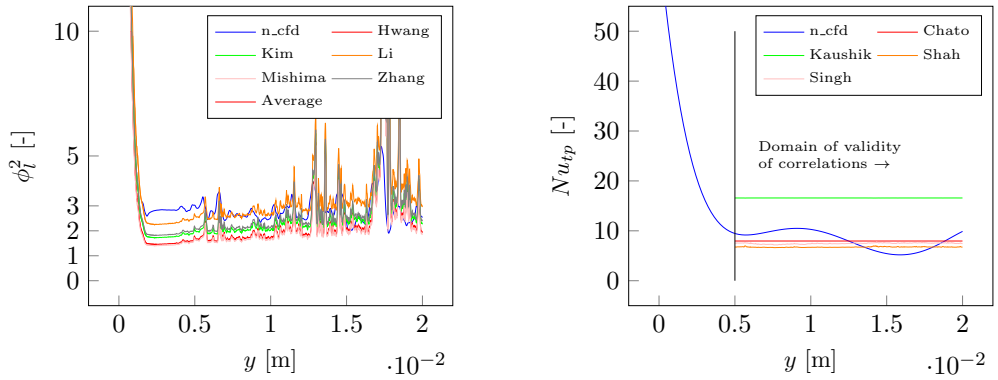

Figure 4.1: Comparison between $\phi^2_{l,num}$ and $\phi^{2\,k}_{l,exp}$, $k \in [\![1, 6]\!]$ and $Nu_{tp,num}$ and $Nu^k_{tp,exp}$, $k \in [\![1, 5]\!]$ for Calculations 1. $\phi^2_{l,num}$ and $Nu_{tp,num}$ are obtained from Eq. (31) and Eq. (42) while $\phi^{2\,k}_{l,exp}$ and $Nu^k_{tp,exp}$ are obtained from Table 8 and Table 10.

Table 4.3: Mean relative error (MRE) on ϕ_l^2 (Eq. (41)).

Correlation	MRE [%]
Hwang and Kim (2006)	28.8
Kim and Mudawar (2012)	11.2
Li and Wu (2010)	−12.9
Mishima and Hibiki (1996)	34.0
Zhang et al. (2010b)	6.02
Average correlation	13.4

Table 4.4: Mean relative error (MRE) on the Nusselt number (Eq. (49)).

Correlation	MRE [%]
Chato (1962)	3.84
Kaushik and Azer (1988)	−50.2
Shah (2009)	22.8
Singh et al. (1996)	11.1
Average correlation	−3.13

Chapter 5

Impact of roughness and tortuosity on small-scale two-phase heat transfer with phase change

Contents

5.1 Impact of roughness on heat transfer with phase change 116

5.1.1 Introduction 116

5.1.2 Problem setup 118

5.1.3 Results 127

5.2 Impact of tortuosity on heat transfer with phase change 137

5.2.1 Introduction 137

5.2.2 Problem setup 139

5.2.3 Results 143

5.3 Summary 144

5.1 Impact of roughness on heat transfer with phase change

5.1.1 Introduction

Surface roughness corresponds to the "finer irregularities of surface texture that are inherent in the materials or production process" (Taylor et al., 2006). Relative roughness, defined as the ratio of roughness size to channel diameter, is significantly larger in micro-channels, mini-channels and cracks than in channels of conventional size. Therefore, in micro-channels, mini-channels and cracks, it is to be expected that roughness will have a significant impact on dynamics and heat transfer.

A number of experimental studies on the impact of roughness on single-phase dynamics and/or heat transfer in mini-channels at low Reynolds number are available in the literature. Among them are those of Celata et al. (2007); Grohmann (2005); Kandlikar et al. (2003); Li et al. (2007); Liu et al. (2007); Qu et al. (2000); Shen et al. (2006); Wu and Cheng (2003). The hydraulic diameter was between 51 and 1570 µm. The wall roughness was inherent to the material used. The relative roughness was between 0.4 and 6 %. When considered by the authors, the friction factor (ratio of pressure gradient to kinetic energy of the fluid) was found to increase with relative roughness. The results on the Nusselt number (dimensionless wall heat flux) are summarized in Fig. 5.1. The latter shows the ratio of the average Nusselt number obtained in rough-wall conditions to the average Nusselt number obtained in smooth-wall conditions (referred to as Nu_{smooth} if the value comes from the experiment or Nu_{conv} if the value has been obtained from a correlation) as a function of the relative roughness. This ratio is found to increase in the works of Qu et al. (2000); Kandlikar et al. (2003); Li et al. (2007), to decrease in the work of Wu and Cheng (2005) and to remain constant in the works of Grohmann (2005); Shen et al. (2006); Celata et al. (2007); Liu et al. (2007).

In addition to the previous experimental studies, various numerical studies can also be found in the literature. Ji et al. (2006) studied heat transfer and flow characteristics of rarefied and compressible gases in rough micro-channels of height between 2 and 4 µm. Wall roughness was modeled by rectangular elements. The relative roughness was between 0.75 and 6 %. The friction factor was found to increase and the average Nusselt number to decrease with the relative roughness. The impact of roughness on the friction factor was found to be more important than that on the Nusselt number. In addition, the impact of roughness on the Nusselt number was found to be more important for the rarefied gas than for the compressible gas. Chen et al. (2010) studied the impact of wall roughness on heat transfer in a mini-channel of height 100 µm. Roughness was generated by a fractal approach (Cantor structures). The relative roughness was between 0.5 and 2 %. The average Nusselt

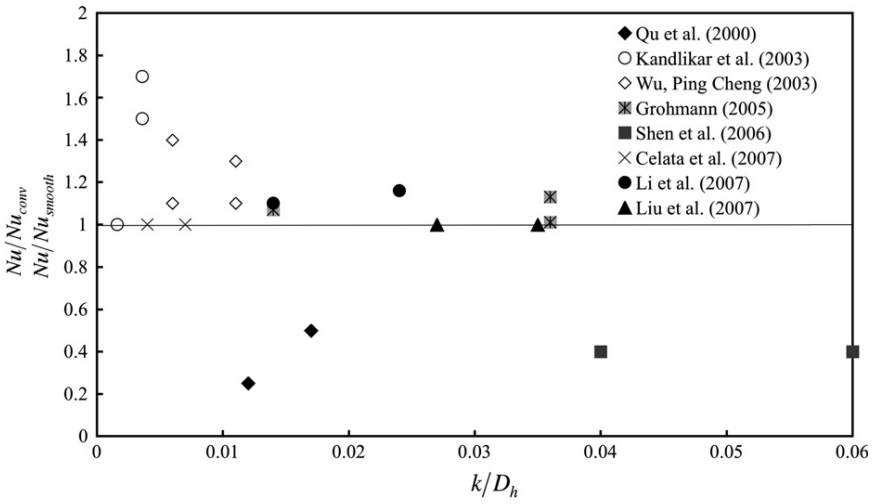

Figure 5.1: Results of the experiments of Celata et al. (2007); Grohmann (2005); Kandlikar et al. (2003); Li et al. (2007); Liu et al. (2007); Qu et al. (2000); Shen et al. (2006); Wu and Cheng (2003): Ratio of the average Nusselt number obtained in rough-wall conditions (Nu) to the average Nusselt number obtained in smooth-wall conditions (Nu_{smooth} if the value comes from the experiment or Nu_{conv} if the value has been obtained from a correlation) as a function of relative roughness (k/D_h, with k the element heigh and D_h the hydraulic diameter). Graph from Gamrat et al. (2009).

number was found to increase with relative roughness (at given fractal dimension) and with fractal dimension (at given relative roughness). Croce and D'Agaro (2004, 2005) studied the effect of roughness on pressure drop and heat transfer in channels of diameter ranging from 50 to 150 µm. Roughness was modeled by rectangular or triangular elements of random size. The relative roughness was between 0.5 and 5.3 %. The friction factor was found to increase with relative roughness. Compared to the smooth case, the Nusselt number was found to increase on the peaks (top of the roughness elements) and to decrease in the valleys (regions between the peaks). In average, it was found to decrease with relative roughness. The triangular elements were found to result in a lower average Nusselt number than the rectangular elements. Zhang et al. (2010a) studied heat transfer and flow characteristics of liquid ammonia in a rough mini-channel of height 100 µm. Roughness was modeled by semi-circular, rectangular or triangular elements. The relative roughness was between 1 and 4 %. Both the friction factor and the average Nusselt number were found to increase with roughness element height and to decrease with roughness element spacing. The impact of roughness on these numbers was found to be less important for the rectangular elements than for the semi-circular and triangular elements.

All the previous studies agree on the fact that the friction factor increases with relative roughness. It is worth noting that this behavior does not apply to channels of conventional size, characterized by a constant friction factor in the laminar flow regime and in the fully

developed region. Concerning the Nusselt number, the conclusions vary from one author to another. Some of them found it to increase with relative roughness, while the others found it to decrease with relative roughness.

This section investigates the effect of roughness on laminar single- and two-phase dynamics and heat transfer in mini-channel. Indeed, the previous studies show that the issue of single-phase heat transfer in this kind of geometry has not been fully addressed yet. In addition, these studies were restricted to single-phase flow and to relative roughness values below 6 %, while, in the present thesis, the case of two-phase flows with phase change is considered, and the application material is concrete, which is characterized by relative roughness values larger than 6 %.

5.1.2 Problem setup

5.1.2.1 Computational domain and boundary conditions

The computational domain is shown in Fig. 5.2. It represents a rough rectilinear mini-channel of maximum height h and length l_{rect}. Roughness is explicitly modeled by uniform rectangular elements of height p, width w and spacing s. The flow rate, the temperature and the composition are imposed at the inlet, the pressure is imposed at the outlet and the temperature is imposed at the walls. A total of 70 calculations is performed (see Table 5.1). h is set to 100 µm and l_{rect} to 3 cm. The values of p, w and s are based on those provided by Rastiello et al. (2015) for concrete. To simplify the problem, w is set to 10 µm. p is varied between 3.33 and 10 µm and s between 20 and 60 µm. Since there is no guarantee that roughness will have an impact on heat transfer with phase change, to save computational time, the investigations are performed at high pressure (see Chapter 4 for information on the link between pressure and computational time). The outlet pressure P^{out} is set to 140 bar. The air inlet mass fraction Y_a^{in} is varied between 1 and 7.5 %. The gas inlet temperature T_g^{in} and wall temperature T_w are set to $T_{sat} + 12\,\mathrm{K}$ and $T_{sat} - 15\,\mathrm{K}$, respectively. The inlet mass flow rate per unit area G is varied between 100 and 250 $\mathrm{kg\,m^{-2}\,s^{-1}}$. The physical properties are computed using the CATHARE tables (Emonot et al., 2011). An adaptive time-stepping strategy is adopted. The maximum Courant and Fourier numbers, defined as $\|\underline{U}_k\| \frac{\Delta t}{\Delta x}$ and $\frac{\lambda_k}{\rho_k C p_k} \frac{\Delta t}{\Delta x}$, with Δt the time step and Δx the grid spacing, are set to 1 and 10 for both the gas and the liquid.

5.1.2.2 Gravity and wettability

As in Chapter 4, gravity is neglected, since the Eotvos number (ratio of gravitational to surface tension forces) is below the critical values proposed by Suo and Griffith (1964);

Table 5.1: Roughness parameter and boundary condition values for the various calculations performed in Section 5.1. $^{p}/_{h}$ is the element relative height and $^{s}/_{h}$ the element relative spacing. G is the gas inlet mass flow rate per unit area, T_g^{in} the gas inlet temperature, Y_a^{in} the air inlet mass fraction and T_w the wall temperature.

$\varepsilon = {}^{p}/_{h}$	${}^{s}/_{h}$	T_g^{in} [K]	T_w [K]	Y_a^{in} [%]	G [kg m^{-2} s^{-1}]			
					100	150	200	250
0	–	650	620	1	–	–	n°00	–
0.033	0.3	650	620	1	–	–	n°01	–
0.05	0.3	650	620	1	–	–	n°02	–
0.1	0.3	650	620	1	–	–	n°03	–
0	–	622	595	1	n°1	n°17	n°33	n°55
0	–	622	595	2.5	–	–	n°34	–
0	–	622	595	5	–	–	n°35	–
0	–	622	595	7.5	–	–	n°36	–
0.033	0.2	622	595	1	n°2	n°18	n°37	n°56
0.033	0.3	622	595	1	n°3	n°19	n°38	n°57
0.033	0.4	622	595	1	n°4	n°20	n°39	n°58
0.033	0.5	622	595	1	n°5	n°21	n°40	n°59
0.033	0.6	622	595	1	n°6	n°22	n°41	n°60
0.05	0.2	622	595	1	n°7	n°23	n°42	n°61
0.05	0.3	622	595	1	n°8	n°24	n°43	n°62
0.05	0.4	622	595	1	n°9	n°25	n°44	n°63
0.05	0.5	622	595	1	n°10	n°26	n°45	n°64
0.05	0.6	622	595	1	n°11	n°27	n°46	n°65
0.1	0.2	622	595	1	n°12	n°28	n°47	n°66
0.1	0.3	622	595	1	n°13	n°29	n°48	n°67
0.1	0.3	622	595	2.5	–	–	n°49	–
0.1	0.3	622	595	5	–	–	n°50	–
0.1	0.3	622	595	7.5	–	–	n°51	–
0.1	0.4	622	595	1	n°14	n°30	n°52	n°68
0.1	0.5	622	595	1	n°15	n°31	n°53	n°69
0.1	0.6	622	595	1	n°16	n°32	n°54	n°70

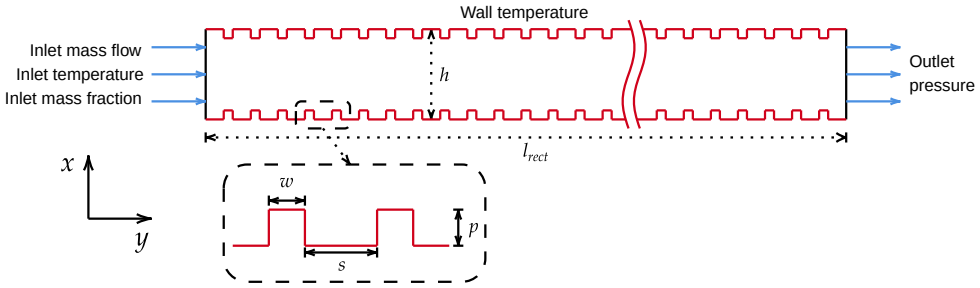

Figure 5.2: Computational domain and boundary conditions. The domain represents a rough mini-channel of (maximum) height $h = 100\,\mu m$ and length $l_{rect} = 3\,cm$. Roughness is directly modeled by rectangular elements of height p, width w and spacing s. Mass flow rate, temperature and composition are imposed at the inlet, pressure is imposed at the outlet and temperature is imposed at the walls. The dimensions of the roughness elements and the values of the boundary conditions are given in Table 5.1.

Brauner and Moalem-Maron (1992); Cornwell and Kew (1993). Also, as in this chapter we are not interested by the effect of wettability, a neutral contact angle of 90° is used for the large interfaces. It is worth noting that no contact angle model is required, the value of 90° being enforced via the null flux condition applied by the code to the volume fraction at the wall.

5.1.2.3 Turbulence and mesh

In smooth circular channels of any size, the critical Reynolds number, above which the flow is considered to be turbulent, is about 2000. In rough mini- and micro-channels, several authors found the transition from laminar to turbulent flow to occur at lower values of the Reynolds number (Brackbill and Kandlikar, 2007; Kandlikar et al., 2005; Rastiello et al., 2015; Schmitt and Kandlikar, 2005; Wu and Little, 1983). As an example, Schmitt and Kandlikar (2005) carried out experiments using sawtooth roughened channels and air and water as working fluids. Based on their experimental data, shown in Fig. 5.3, they proposed the following correlation for the critical Reynolds number:

$$Re_{cf} = \begin{cases} 2300 - 18\,750\,(p/D_{h,cf}) & \text{if } p/D_{h,cf} \in]0, 0.08] \\ 800 - 3270\,(p/D_{h,cf} - 0.08) & \text{if } p/D_{h,cf} \in]0.08, 0.15] \end{cases}, \tag{5.1}$$

with p the roughness element height and $D_{h,cf}$ the constricted hydraulic diameter.

In the present case, the roughness elements do not have a sawtooth shape but a rectangular shape. Eq. (5.1) can still be used to give an approximation of the minimum critical

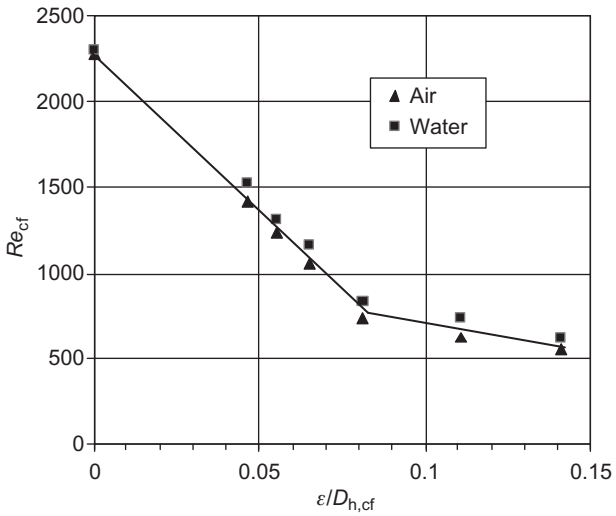

Figure 5.3: Results of the experiments of Schmitt and Kandlikar (2005): Critical Reynolds number (Re_{cf}) as a function of relative roughness based on constricted hydraulic diameter ($\varepsilon/D_{h,cf}$, with ε the element height and $D_{h,cf}$ the constricted hydraulic diameter).

Reynolds number. The constricted hydraulic diameter reads: $D_{h,cf} = D_h - 4p = 2\,(h - 2p)$, with D_h the hydraulic diameter. The maximum roughness element height is $p = 10\,\mu\text{m}$. The value of Re_{cf} obtained from Eq. (5.1) is 857. An estimation of the inlet Reynolds number, defined as:

$$Re_g^{in} = \frac{GD_h}{\mu_g}\,, \tag{5.2}$$

is given in Table 5.2. The corresponding values are found to be greater than or approximately equal to 857, indicating that turbulence may occur. This has to be taken into account in the modeling.

The different ways to deal with turbulent flow in CFD are briefly described in Appendix 2. Here, the choice is made to use the $R_{ij} - \varepsilon$ EBRSM model (Manceau and Hanjalić, 2002), which is a low Reynolds number model. It is applied to both the gas and liquid phases. This model belongs to the class of methods called RANS (Reynolds Stress Average Navier-Stokes). "Low Reynolds number" does not refer to the flow at a global scale, but to a model that uses damping functions to force the decay of turbulence near the wall, where the mesh is supposed to be fine enough to solve the viscous sublayer. Cartesian gris are used in the following. They can be decomposed into three parts, with different resolution: two symmetric parts of height $p+5\,\mu\text{m}$, associated with the two horizontal edges of the channel, characterized by $\Delta y = {}^{l}/_{18000}$ and $\Delta x = {}^{h}/_{60}$, and a central part of height $h - 2\,(p+5)\,\mu\text{m}$, characterized by $\Delta y = {}^{l}/_{6000}$ and Δx varying linearly from ${}^{h}/_{20}$ in the center to ${}^{h}/_{60}$ at the boundaries with the two symmetric parts. The dimensionless distance from the wall to the

Table 5.2: Values of the gas Reynolds number at the inlet (Eq. (5.2)), of the dimensionless wall distance defined with respect to the gas and of the dimensionless wall distance defined with respect to the liquid (Eq. (5.3)) for the calculations in Table 5.1. The dimensionless wall distances are averaged in space and over the calculations corresponding to the same Reynolds number.

Calculation number	1 to 16	17 to 32	00 to 03 and 33 to 54	55 to 70
Re_g^{in}	833	1250	1667	2083
y_g^+	0.27	0.37	0.48	0.63
y_l^+	0.081	0.15	0.24	0.34

center of the adjacent cells, defined as:

$$y_k^+ = \frac{y u_{\tau,k}}{\nu_k}\,, \tag{5.3}$$

with $\nu_k = \mu_k/\rho_k$ and $u_{\tau,k} = \sqrt{\tau_{w,k}/\rho_k}$ – $\tau_{w,k}$ being the wall shear stress – is given in Table 5.2. For both the gas and the liquid, it is found to be lower than unity, meaning that the wall cells are effectively located in the viscous sublayer, which extends from 0 to about 5.

5.1.2.4 Single-phase flow verifications

The Darcy (or Darcy-Weisbach or Moody) friction factor f is defined, for the gas phase, as (Darcy, 1857; Moody, 1944; Weisbach, 1850):

$$\frac{\Delta P}{l'} = \frac{1}{2}\frac{f_g}{D_h}\rho_g U_g^2\,, \tag{5.4}$$

with ΔP the pressure difference between two arbitrary sections and l' the distance between them. It has to be distinguished from the Fanning friction factor, which is defined as a function of the wall shear stress instead of the pressure drop. For single-phase flow in smooth channels of any size, using Eq. (5.4), one can show analytically that, in the laminar flow regime and in the fully developped region (Incropera et al., 2007):

$$f_g = \frac{C_f}{Re_g}\,. \tag{5.5}$$

C_f is a constant depending on the cross-section geometry – $C_f = 64$ for a circular cross-section and $C_f = 96$ for a semi-infinite cross-section – and Re_g is the gas Reynolds number, which is constant and equal to Re_g^{in} in Eq. (5.2). In channels of conventional size, it is well known that, in the laminar flow regime and in the fully developed region, roughness has no significant impact on the friction factor. Therefore, Eq. (5.5) still apply. For mini- and

Table 5.3: Correlations of Churchill (1977) and Colebrook and White (1937). These correlations are compared with the present results, in addition to Eq. (5.5) and Eq. (5.6).

Author	Expression	Validity
Churchill (1977)	$f_k = 8\left(\left(\frac{8}{Re_k}\right)^{12} + \frac{1}{(A+B)^{1.5}}\right)^{1/12}$	All Re_g
Colebrook and White (1937)	$\frac{1}{\sqrt{f_k}} = -2\log_{10}\left(\frac{2.51}{Re_k\sqrt{f_k}} + \frac{1}{3.7}\frac{\varepsilon}{D_h}\right)$	$Re_g > 3200$

$A = 2.457\ln\left(1/(7/Re_k)^{0.9} + 0.27\varepsilon/D_h\right)^{16}$; $B = (37530/Re_k)^{16}$.

micro-channels, however, it was found that, in the fully developed region, the friction factor increases with relative roughness (Gamrat et al., 2008; Herwig et al., 2008; Liu et al., 2019; Sentürk and Smits, 2019; Wagner and Kandlikar, 2012). The consequence is that Eq. (5.5) does not apply anymore.

The purpose of this section is to verify that the latter behavior is effectively and correctly captured by the code. For this purpose, Calcs. 01 to 03, in which no liquid is formed, are used. The friction factor is obtained from Eq. (5.4). It is shown as a function of ε in Fig. 5.4a. A behavior similar to that described above is obtained. For a relative roughness equal to zero, f_g matches the theoretical value obtained from Eq. (5.5). For a relative roughness different from zero, f_g is higher than the value obtained from Eq. (5.5). In addition, f_g increases with relative roughness.

This behavior is characteristic of the turbulent flow regime, and might be due to the fact that transition to turbulence occurs at lower Reynolds numbers (see previous section). However, the correlations of Churchill (1977) and Colebrook and White (1937), given in Table 5.3, which are among the most widely used correlations for the friction factor in rough channels in the turbulent flow regime, fail to correctly predict the results obtained from simulation. For Churchill (1977), this is attributed to the fact that the correlation reduces to Eq. (5.5) for $Re_g < 2200$, and for Colebrook and White (1937), to the fact that it is only applicable for $Re_g > 3200$.

The fact that neither Eq. (5.5) nor the usual correlations for turbulent flows are able to reproduce the results obtained in rough mini-channels at moderate Reynolds number led authors to develop their own correlation. This is the case of Sentürk and Smits (2019). They performed direct numerical simulation of the flow in a circular micro-channel with relative roughness varying from 0.5 to 5 %. Their results are shown in Fig. 5.4b. Correspondence between their notations and the notations in the present work is as follows: $k/D = \varepsilon$ and $\lambda/w = (s+w)/w$. The curve referred to as "smooth" corresponds to $64/Re_g$. The correlation

they proposed is:

$$f_g = \frac{a_1 \varepsilon^2 + \left(a_2 + a_3 \frac{s+w}{w}\right) \varepsilon + C_f}{Re_g} , \tag{5.6}$$

with $a_1 = 3000$, $a_2 = 520$, $a_3 = -35$. Note that, in this expression, Re_g is still equal to Re_g^{in} in Eq. (5.2), and therefore does not depend on the constricted hydraulic diameter $D_{h,cf}$ but on the hydraulic diameter D_h. A comparison is made between the results obtained in the present work and the above correlation, as well as the results corresponding to $\lambda/w = 4$ in Fig. 5.4b. The results of the comparison are presented in Fig. 5.5. The quantity used is $f_g Re_g - C_f$, with $C_f = 64$ or $C_f = 96$ depending on the geometry. A good agreement is obtained with both Eq. (5.6) and the results from Fig. 5.4b. This indicates that single-phase pressure drop, and more generally single-phase dynamics, is correctly computed by the neptune_cfd code in rough-wall conditions.

5.1.2.5 Dependence of the wall energy transfers

As a reminder of Chapter 2, the energy transfer from the wall to the gas is computed using Eq. (2.54), i.e., as the sum of a condensation heat flux φ_{cond} and a single-phase heat flux $\varphi_{sp,g}$, and the energy transfer from the wall to the liquid is computed using Eq. (2.55), i.e., as a single-phase heat flux $\varphi_{sp,l}$. Let us define ϕ such that $\phi \in \{\varphi_{cond}, \varphi_{sp,g}, \varphi_{sp,l}\}$ and ϕ^0 such that $\phi^0 \in \left\{\varphi^0_{cond}, \varphi^0_{sp,g}, \varphi^0_{sp,l}\right\}$, ϕ referring to rough-wall conditions and ϕ^0 to smooth-wall conditions. The purpose of the following section is to characterize the impact of the problem variables, especially the roughness parameters, on the quantities ϕ and $\phi^{av}/\phi^{0,av}$, the superscript av referring to the average over the length:

$$\phi^{av} = \frac{1}{l} \int_0^l \phi \, \mathrm{d}y_{curv} , \tag{5.7}$$

$$\phi^{0,av} = \frac{1}{l} \int_0^l \phi^0 \, \mathrm{d}y . \tag{5.8}$$

Using the general non-dimensionalization technique proposed by Ipsen (1960), taking into account the fact that the roughness element width w is maintained constant, it is found that ϕ and ϕ^0 can depend on the following dimensionless quantities:

$$\phi = f_\phi \left(\varepsilon = \frac{p}{h}, \frac{s}{h}, \frac{y_{curv}}{h}, Re_g^{in}, Ec, Pr, Y_a^{in}\right) , \tag{5.9}$$

$$\phi^0 = f_\phi^0 \left(\frac{y}{h}, Re_g^{in}, Ec, Pr, Y_a^{in}\right) , \tag{5.10}$$

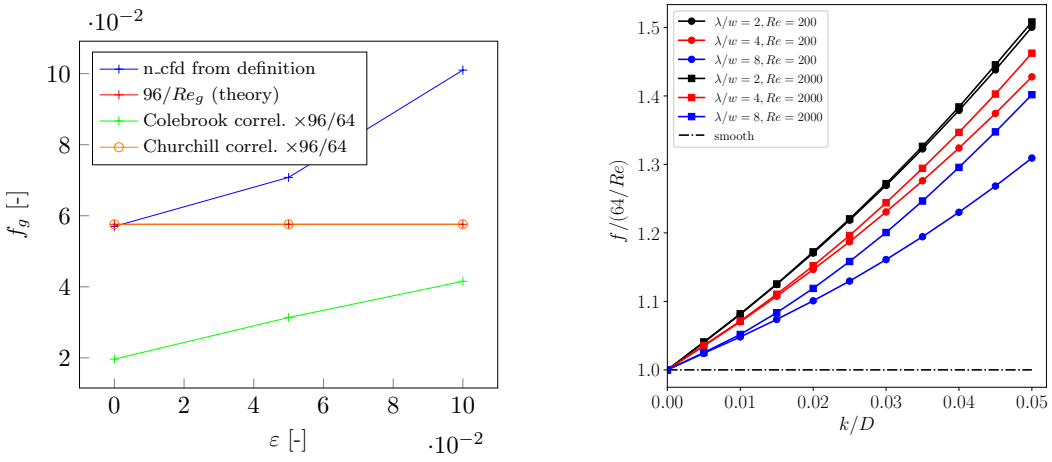

(a) (b)

Figure 5.4: Evolution of the friction factor with element relative height. (a) Calcs. 01 to 03; comparison is made with Eq. (5.5) with $C_f = 96$ and with the correlations of Churchill (1977) and Colebrook and White (1937). (b) Work of Sentürk and Smits (2019); comparison is made with Eq. (5.5) with $C_f = 64$.

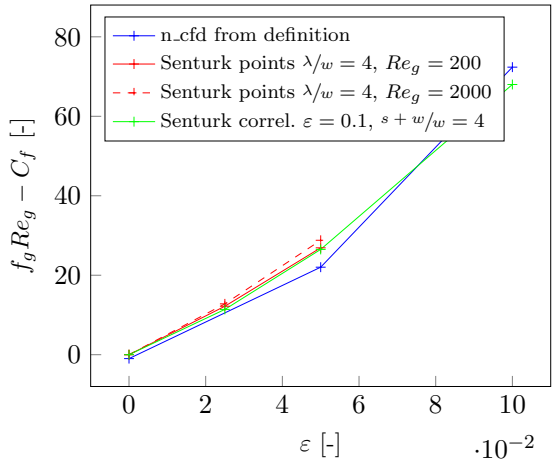

Figure 5.5: Evolution of the quantity $f_g Re_g - C_f$ with element relative height for Calcs. 01 to 03. Comparison is made between the present results ($C_f = 96$) and the original data and correlation by Sentürk and Smits (2019) ($C_f = 64$).

with f_ϕ and f_ϕ^0 unknown functions, and Ec and Pr the Eckert and Prandlt numbers:

$$Ec = \frac{U_y^2}{Cp\left(T_g^{in} - T_w\right)}\,, \tag{5.11}$$

$$Pr = \frac{\mu Cp}{\lambda}\,. \tag{5.12}$$

As Pr is almost constant, the dependance to this number is neglected. Due to spatial averaging, ϕ^{av}, $\phi^{av,0}$ and therefore $\phi^{av}/\phi^{0,av}$ are expected to not depend on y_{curv}/h or y/h but on l/h. Based on the work Dierich and Nikrityuk (2013), who numerically studied the impact of roughness on single-phase heat transfer around a cylindrical particle, the assumption is made that $\phi^{av}/\phi^{0,av}$ is independent of Ec, i.e., that the variations of ϕ^{av} and $\phi^{0,av}$ with Ec are identical. In doing so, the following theoretical dependence is established for $\phi^{av}/\phi^{0,av}$:

$$\frac{\phi^{av}}{\phi^{0,av}} = g_\phi\left(\varepsilon = \frac{p}{h}, \frac{s}{h}, \frac{l}{h}, Re_g^{in}, Y_a^{in}\right)\,, \tag{5.13}$$

with g_ϕ an unknown function. In the following section, the sensitivity of ϕ to y_{curv}/h will be assessed. The sensitivity of $\phi^{av}/\phi^{0,av}$ to l/h, ε, s/h, Re_g^{in} and Y_a^{in} will also be investiagted.

5.1.2.6 Dependence of the interfacial mass transfer

As a reminder of Chapter 2, the interfacial mass transfer $\Gamma_{p\to k}$ is computed using Eqs. (2.47) and (2.49) in case of droplets, Eq. (2.52) in case of bubbles and Eqs. (2.62) and (2.63) in case of large interfaces. It will also be considered in the following, for rough-wall conditions only. Unlike φ_{cond}, $\varphi_{sp,g}$ and $\varphi_{sp,l}$, it does not apply to the wall boundary but to the core flow. Therefore, it will be averaged over the cross-section:

$$\Gamma_{p\to k}^{av} = \frac{1}{h_y}\int_x \Gamma_{p\to k}\mathrm{d}x\,. \tag{5.14}$$

Using the same non-dimensionalization technique as before, it is found that:

$$\Gamma_{p\to k}^{av} = h_\phi\left(\frac{y}{h}, Re_g^{in}, Ec, Pr, Y_a^{in}\right)\,, \tag{5.15}$$

with h_ϕ an unknown function. The sensitivity of $\Gamma_{g\to l}^{av}$ to y/h will be assessed in the following section, in addition to that of ϕ to y_{curv}/h and to that of $\phi^{av}/\phi^{0,av}$ to l/h, ε, s/h, Re_g^{in} and Y_a^{in}.

5.1.3 Results

5.1.3.1 Local impact

This section focuses on the sensitivity of $\phi \in \{\varphi_{cond}, \varphi_{sp,g}, \varphi_{sp,l}\}$ to y/h and y_{curv}/h and the sensitivity of $\Gamma^{av}_{g\to l}$ to y/h. ϕ and $\Gamma^{av}_{g\to l}$ are averaged over time, and absolute values are used.

The various quantities are shown as a function of y in Fig. 5.6 for Calc. 13. For φ_{cond}, $\varphi_{sp,g}$ and $\varphi_{sp,l}$, the bottom wall is considered. The range $y \in [2.017 \times 10^{-4}, 3.683 \times 10^{-4}]$ m is used for φ_{cond} and $\varphi_{sp,g}$, since at this location the gas phase predominates at the wall, and the range $y \in [9.882 \times 10^{-3}, 1.005 \times 10^{-2}]$ m is used for $\varphi_{sp,l}$, since at this location the liquid phase predominates at the wall. The range $y \in [1.768 \times 10^{-2}, 1.784 \times 10^{-2}]$ m is arbitrarily used for $\Gamma^{av}_{g\to l}$. It observed that roughness is responsible for significant fluctuations in φ_{cond}, $\varphi_{sp,g}$ and $\varphi_{sp,l}$. Fluctuations are also observed for $\Gamma^{av}_{g\to l}$, but they are less important than for the other quantities.

φ_{cond}, $\varphi_{sp,g}$ and $\varphi_{sp,l}$ are shown as a function of y_{curv} in Fig. 5.7 for the same calculation as before. A comparison is made with Calc. 1, corresponding to smooth-wall conditions. The three quantities are found to decrease in the region between the roughness elements and to increase on the roughness elements. Note that these effects corresponds to the intrinsic impact of roughness (remember that the results are shown as a function of y_{curv} and not as a function of y). The magnitude and the exact number of points concerned by the increase/decrease vary according to the quantity considered. For example, for φ_{cond}, a majority of points show an increase and the magnitude of the increase is much more important than that of the decrease. Therefore, it is likely that $\varphi^{av}_{cond}/\varphi^{0,av}_{cond}$ will increase with relative roughness. Applying the same reasoning to $\varphi_{sp,g}$, it can be expected that $\varphi^{av}_{sp,g}/\varphi^{0,av}_{sp,g}$ will increase with relative roughness. It is more difficult to guess an average behavior for $\varphi_{sp,l}$. This will be discussed in the following section.

The fact that φ_{cond}, $\varphi_{sp,g}$ and $\varphi_{sp,l}$ decrease between the roughness elements seems to be due to the generation of recirculations. A part of the fluid is trapped between the roughness elements and the difference in temperature with the wall decreases in comparison with the case with no roughness. Pictures of liquid recirculations in Calcs. 62, 66, 67 and 70 are shown in Fig. 5.8. The size of the recirculations essentially depends on the geometrical characteristics of the roughness elements (height, width and spacing). The recirculations can be classified into two types. The first type, which can be seen in Figs. 5.8b and 5.8c, corresponds to recirculations occupying the entire space between the roughness elements, and leading to almost no disturbance of the bulk flow. It is favored by an increase in the roughness element height and a decrease in the roughness element spacing. The second type, which can be seen in Figs. 5.8a and 5.8d, corresponds to recirculations occupying only

the left part of the space between the roughness elements, the right part consisting in a reattachment of the bulk flow. In contrast to the previous type, it is favored by a decrease in the roughness element height and an increase in the roughness element spacing. These two types of recirculations have already been observed for single-phase flow by some authors in the literature, both experimentally and numerically, and both in the laminar and in the turbulent flow regime (Chen et al., 2009b, 2010; Croce and D'Agaro, 2004, 2005; Ji et al., 2006; Perry et al., 1969; Zhang et al., 2010a). Perry et al. (1969), who studied the impact of roughness on the friction factor in the turbulent flow regime, called roughness leading to recirculations occupying the entire space between the roughness elements *d*-type roughness, and roughness leading to recirculations occupying only a part of the space between the roughness elements *k*-type roughness. These names are related to the roughness function $-\Delta u^+$, usually added in the logarithmic law of the wall to virtually account for roughness: $u^+ = {}^1/_\kappa \log\left(y^+\right) + \text{cte} - \Delta u^+$. Indeed, they found that, for *k*-type roughness, Δu^+ is proportional to ${}^{ku_\tau}/_\nu$, with k the roughness element height, and that, for *d*-type roughness, Δu^+ is proportional to ${}^{du_\tau}/_\nu$, with d the channel diameter.

5.1.3.2 Global impact

Previously, it was found that $\phi \in \{\varphi_{cond}, \varphi_{sp,g}, \varphi_{sp,l}\}$ tends to decrease where recirculations occur and to increase on top of the roughness elements, suggesting that ${}^{\phi^{av}}/_{\phi^{0,av}}$ will vary with ε and ${}^s/_h$. It was also found that the intensity of the increase/decrease vary according to the quantity considered, suggesting that ${}^{\varphi^{av}_{cond}}/_{\varphi^{0,av}_{cond}}$, ${}^{\varphi^{av}_{sp,g}}/_{\varphi^{0,av}_{sp,g}}$ and ${}^{\varphi^{av}_{sp,l}}/_{\varphi^{0,av}_{sp,l}}$ will not necessarily evolve the same way. This section focuses on the sensitivity of ${}^{\phi^{av}}/_{\phi^{0,av}}$ to ε and ${}^s/_h$, and also to ${}^l/_h$, Re_g^{in} and Y_a^{in}. ${}^{\phi^{av}}/_{\phi^{0,av}}$ is averaged over time. In each graph, each point will correspond to a calculation.

The various ratios are shown as a function of ${}^l/_h$ in Fig. 5.10 for Calc. 13. They are found to be nearly constant to 3.1, 1.4 and 0.74, respectively, and therefore independent of ${}^l/_h$. The fact that ${}^{\varphi^{av}_{cond}}/_{\varphi^{0,av}_{cond}}$ and ${}^{\varphi^{av}_{sp,g}}/_{\varphi^{0,av}_{sp,g}}$ are greater than unity is consistent with the intuition from the previous section, which is that these ratios will probably increase with ε. The fact that ${}^{\varphi^{av}_{sp,l}}/_{\varphi^{0,av}_{sp,l}}$ is lower than unity suggests that this ratio will, in contrast, decrease with ε.

The various ratios are shown as a function of ε and ${}^s/_h$ in Fig. 5.10 for Calcs. 37 to 48 and 52 to 54. The intuitions from the previous section and paragraph are confirmed. Indeed, ${}^{\varphi^{av}_{cond}}/_{\varphi^{0,av}_{cond}}$ and ${}^{\varphi^{av}_{sp,g}}/_{\varphi^{0,av}_{sp,g}}$ are found to increase with ε and to decrease with ${}^s/_h$. In contrast, ${}^{\varphi^{av}_{sp,l}}/_{\varphi^{0,av}_{sp,l}}$ is found to decrease with ε and to increase with ${}^s/_h$. For ${}^{\varphi^{av}_{cond}}/_{\varphi^{0,av}_{cond}}$ and ${}^{\varphi^{av}_{sp,g}}/_{\varphi^{0,av}_{sp,g}}$, the global increase with ε is due to an increase in the magnitude of the local increase on top of the roughness elements, and the global decrease with ${}^s/_h$ is due to a decrease in the

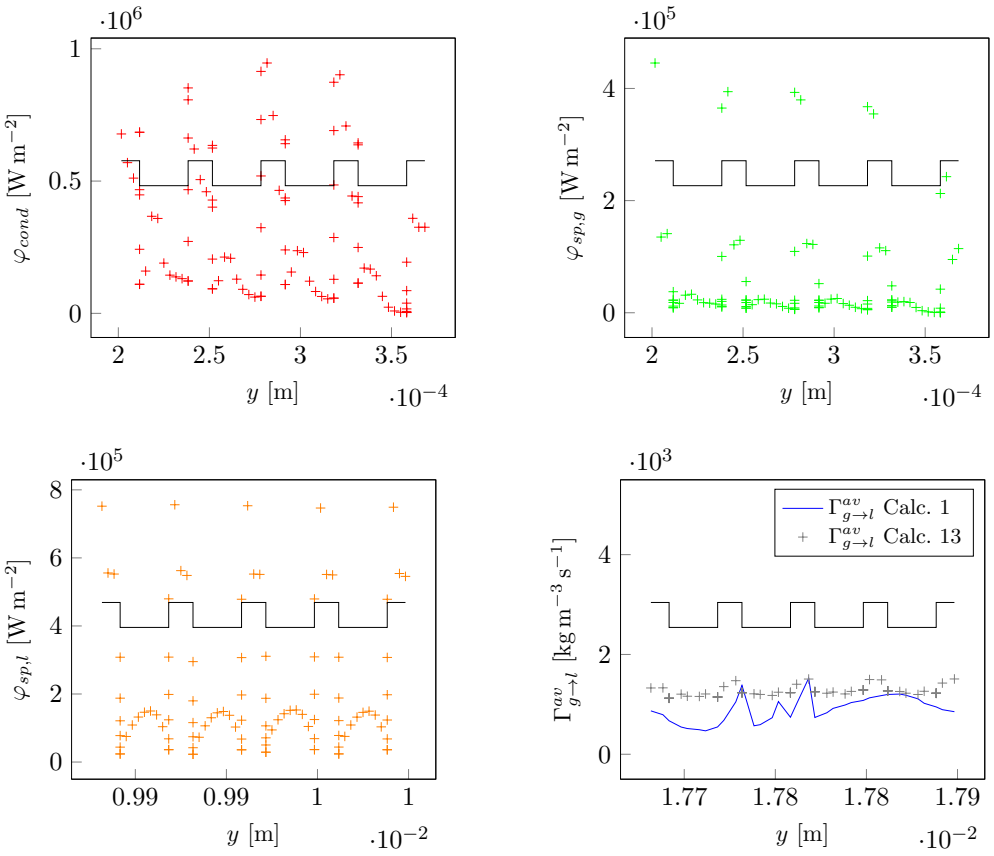

Figure 5.6: Evolution of φ_{cond}, $\varphi_{sp,g}$, $\varphi_{sp,l}$ and $\Gamma^{av}_{g\to l}$ with the y-coordinate for Calc. 13. The averaged quantity $\Gamma^{av}_{g\to l}$ is obtained from Eq. (5.14). φ_{cond}, $\varphi_{sp,g}$, $\varphi_{sp,l}$ and $\Gamma_{g\to l}$ are obtained from the expressions in Section 2.3.2.4. For $\Gamma^{av}_{g\to l}$, a comparison is made with Calc. 1.

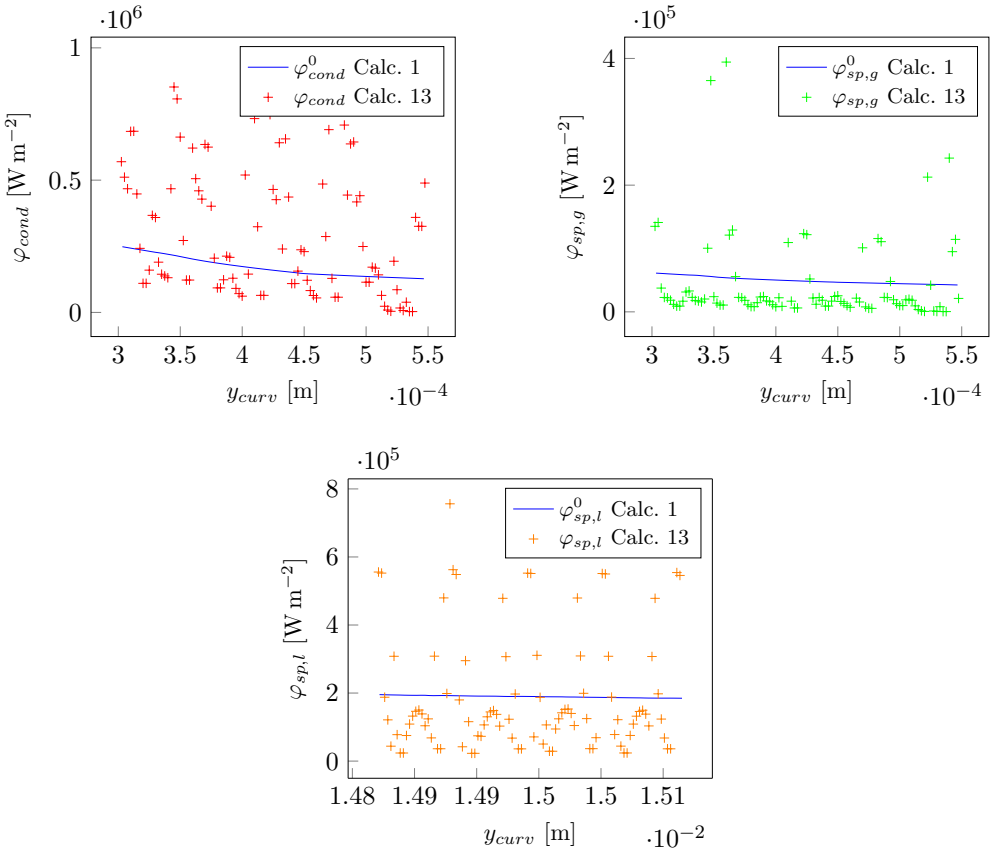

Figure 5.7: Evolution of φ_{cond}, $\varphi_{sp,g}$ and $\varphi_{sp,l}$ with the y_{curv}-coordinate for Calc. 13. The various quantities are obtained from the expressions in Section 2.3.2.4. For each quantity, a comparison is made with Calc. 1.

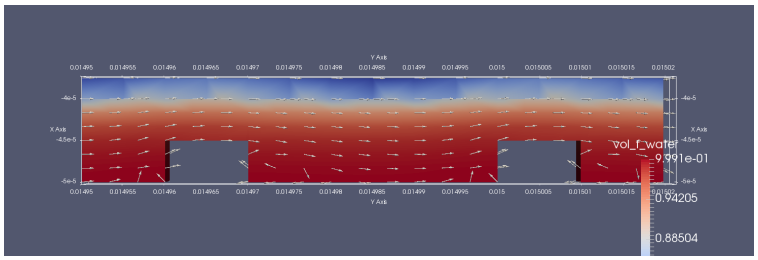

(a)

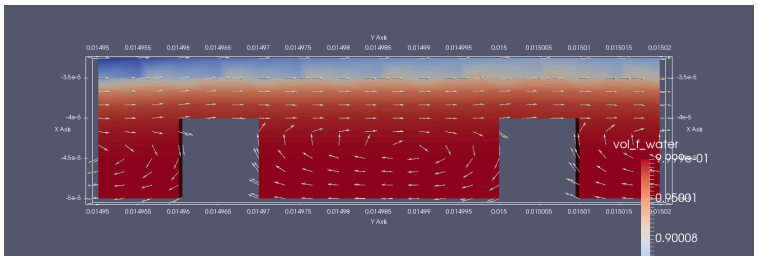

(b)

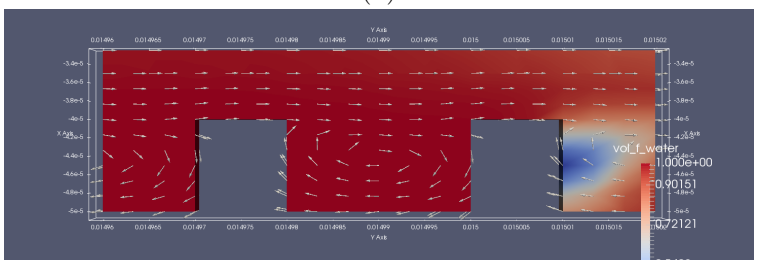

(c)

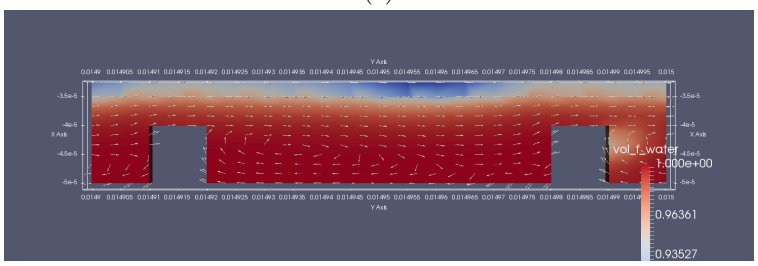

(d)

Figure 5.8: Typical liquid recirculations observed between the roughness elements for $y \in [0.01495, 0.01502]$ m in Calc. 43 (a), Calc. 48 (b), Calc. 47 (c) and Calc. 54 (d) (bulk flow from left to right; gas in blue; liquid in red).

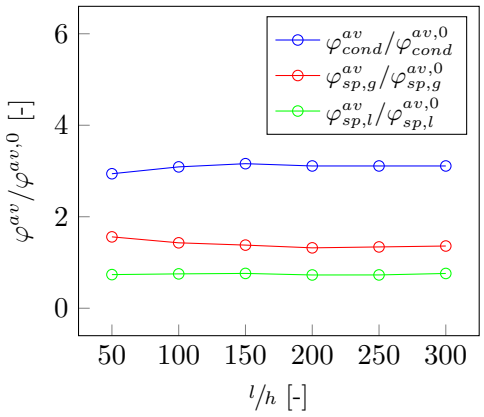

Figure 5.9: Evolution of $\varphi^{av}_{cond}/\varphi^{0,av}_{cond}$, $\varphi^{av}_{sp,g}/\varphi^{0,av}_{sp,g}$ and $\varphi^{av}_{sp,l}/\varphi^{0,av}_{sp,l}$ as a function of l/h for Calc. 13 in Table 5.1. The various quantities appearing in these ratios are averaged quantities and are obtained from Eqs. (5.7) and (5.8). The original quantities φ_{cond}, $\varphi_{sp,g}$ and $\varphi_{sp,l}$ are obtained from the expressions in Section 2.3.2.4.

number of roughness elements and therefore in the fraction of wall area concerned by an increase. For $\varphi^{av}_{sp,l}/\varphi^{0,av}_{sp,l}$, the global decrease with ε is due to an increase in the magnitude of the local decrease where the recirculations occur, and the global increase with s/h is due to a decrease in the number of recirculations and therefore in the fraction of wall area concerned by a decrease.

As a reminder of Section 2.3.2.4, the (local) condensation flux φ_{cond} is obtained from: $\varphi_{cond} = \Gamma_{w\to g} H_{lat}$, with $\Gamma_{w\to g}$ the mass converted from liquid to gas due to condensation and H_{lat} the latent heat. The fact that $\varphi^{av}_{cond}/\varphi^{0,av}_{cond}$ increase with ε implies that φ^{av}_{cond} and therefore $\Gamma_{w\to g}$ increase with ε (in absolute value). In other words, in the present case, roughness is responsible for an increase in the amount of liquid formed at the wall. To our knowledge, such a phenomenon has never been reported in the literature before.

The various ratios are also shown as a function of Re^{in}_g in Fig. 5.11 for Calcs. 3, 13, 16, 19, 29, 32, 38, 48, 54, 57, 67 and 70. For small ε, $\varphi^{av}_{cond}/\varphi^{0,av}_{cond}$ and $\varphi^{av}_{sp,g}/\varphi^{0,av}_{sp,g}$ are found to be nearly constant to unity. This is consistent with the fact that, in Fig. 5.10, the impact of roughness becomes significant for $\varepsilon > 0.05$. For large ε, the two ratios are found to increase with Re^{in}_g, before reaching a plateau at $Re \approx 1250$. The increase at low Re^{in}_g results from the fact that, unlike at high Re^{in}_g, liquid is trapped between the roughness elements located near the entrance. The decrease in the fluxes due to the presence of the liquid is more important than that due to the gas recirculation that would occur if no liquid was trapped. In the latter case, the two ratios would have decreased with Re^{in}_g, due to increasing size of the gas recirculations. $\varphi^{av}_{sp,l}/\varphi^{0,av}_{sp,l}$ is found to slightly decrease with Re^{in}_g, whatever the value of ε. This is consistent with the fact that, in Fig. 5.10, the impact of roughness was found

to be significant for all values of ε, even the lowest ones. The decrease in $\varphi^{av}_{sp,l}/\varphi^{0,av}_{sp,l}$ with Re^{in}_g results from an increase in the size of the liquid recirculations.

The various ratios are finally shown as a function of Y^{in}_a in Fig. 5.12 for Calcs. 48 to 51. $\varphi^{av}_{sp,g}/\varphi^{0,av}_{sp,g}$ and $\varphi^{av}_{sp,l}/\varphi^{0,av}_{sp,l}$ are found to be constant to 1.3 and 0.8, respectively. Conversly, $\varphi^{av}_{cond}/\varphi^{0,av}_{cond}$ is found to slightly decrease with Y^{in}_a, which was not not expected. This would be due to a phenomenon of air rentention between the roughness elements, whose importance increases with Y^{in}_a.

5.1.3.3 Derivation of correlations

In the previous section, it was found that $\varphi^{av}_{cond}/\varphi^{0,av}_{cond}$, $\varphi^{av}_{sp,g}/\varphi^{0,av}_{sp,g}$ and $\varphi^{av}_{sp,l}/\varphi^{0,av}_{sp,l}$ depend on ε, s/h and Re^{in}_g, and that $\varphi^{av}_{cond}/\varphi^{0,av}_{cond}$ also slightly depends on Y^{in}_a. For simplicity, and since not enough data is available, the latter dependence is neglected. Eq. (5.13) can then be rewritten as:

$$\frac{\phi^{av}}{\phi^{0,av}} = g_\phi\left(\varepsilon = \frac{p}{h}, \frac{s}{h}, Re\right) . \tag{5.16}$$

In one-dimensional simulations, it is not possible to model roughness directly, since only one cell is used in the direction perpendicular to the flow. Therefore, it can be useful to have an expression for $\phi^{av}/\phi^{0,av}$, i.e., for g_ϕ. In each cell, it would thus be possible to deduce the flux ϕ that would be computed if roughness was explicitly taken into account from both g_ϕ and the flux ϕ^0 computed by the model, assuming that $\phi^{av}/\phi^{0,av} \approx \phi/\phi^0$ and therefore that $\phi/\phi^0 \approx g_\phi$. A usual way to derive expressions from experimental or numerical data is to perform a regression analysis. We propose to look for g_ϕ in the form of a polynomial of order two in ε, s/h and Re^{in}_g:

$$\begin{aligned} g_\phi\left(\varepsilon = \frac{p}{h}, \frac{s}{h}, Re\right) = {} & a_{\phi,0} + a_{\phi,1}\varepsilon + a_{\phi,2}\frac{s}{h} + a_{\phi,3}Re + a_{\phi,4}\varepsilon^2 + a_{\phi,5}\left(\frac{s}{h}\right)^2 + a_{\phi,6}Re^2 \\ & + a_{\phi,7}\varepsilon\frac{s}{h} + a_{\phi,8}\varepsilon Re + a_{\phi,9}\frac{s}{h}Re + a_{\phi,10}\varepsilon\left(\frac{s}{h}\right)^2 + a_{\phi,11}\varepsilon Re^2 \\ & + a_{\phi,12}\frac{s}{h}Re^2 + a_{\phi,13}\varepsilon^2\frac{s}{h} + a_{\phi,14}\varepsilon^2 Re + a_{\phi,15}\left(\frac{s}{h}\right)^2 Re\,. \end{aligned} \tag{5.17}$$

The regression analysis is performed using MATLAB 9.11.0 (R2021b), more precisely the package Polyfitn (D'Errico, 2021), based on the least-square method. Calculations used are Calcs. 2 to 16, 18 to 32, 37 to 48, 52 to 54 and 56 to 70. The data is presented in Fig. 5.13. The fluxes are shown as a function of ε and s/h for the different Re^{in}_g studied. For each flux, the coefficients a_0 to a_{15} resulting from curve fitting are provided in Table 5.4. A coefficient of determination of 0.8866 is obtained in the case of φ_{cond}, a coefficient of determination of 0.8555 is obtained in the case of $\varphi_{sp,g}$ and a coefficient of determination of 0.9936 is obtained in the case of $\varphi_{sp,l}$, which is indicative of a reasonably good accuracy. A good confidence

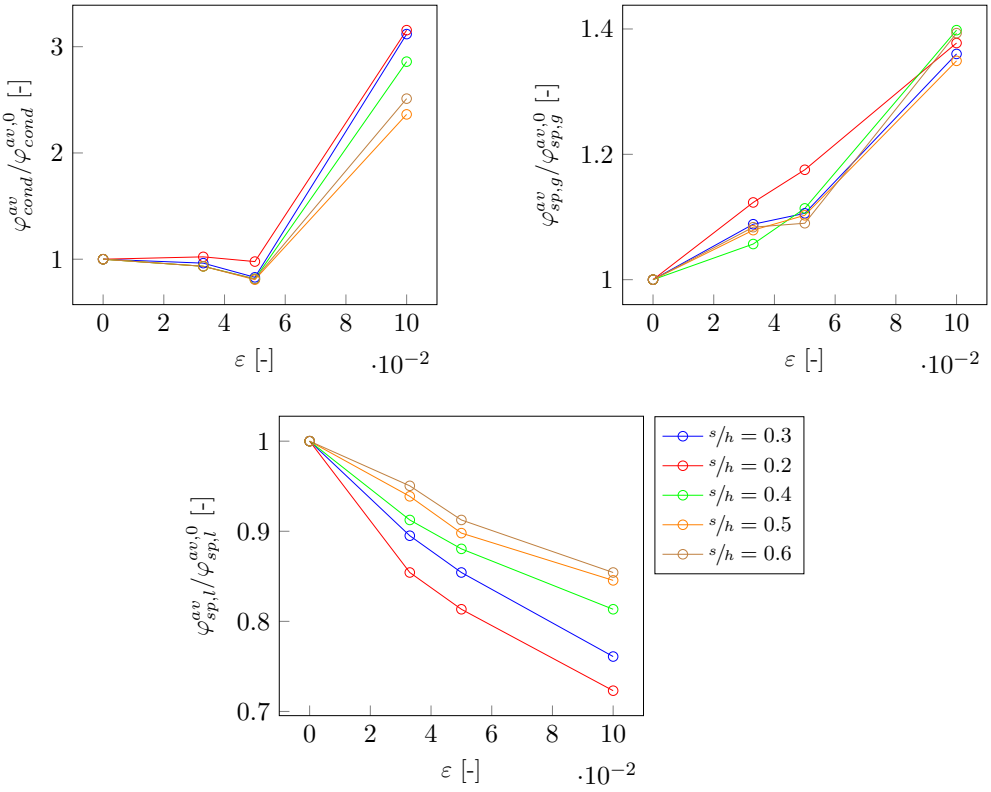

Figure 5.10: Evolution of $\varphi^{av}_{cond}/\varphi^{0,av}_{cond}$, $\varphi^{av}_{sp,g}/\varphi^{0,av}_{sp,g}$ and $\varphi^{av}_{sp,l}/\varphi^{0,av}_{sp,l}$ as a function of ε for Calcs. 37 to 48 and 52 to 54 in Table 5.1. The various quantities appearing in these ratios are averaged quantities and are obtained from Eqs. (5.7) and (5.8). The original quantities φ_{cond}, $\varphi_{sp,g}$ and $\varphi_{sp,l}$ are obtained from the expressions in Section 2.3.2.4.

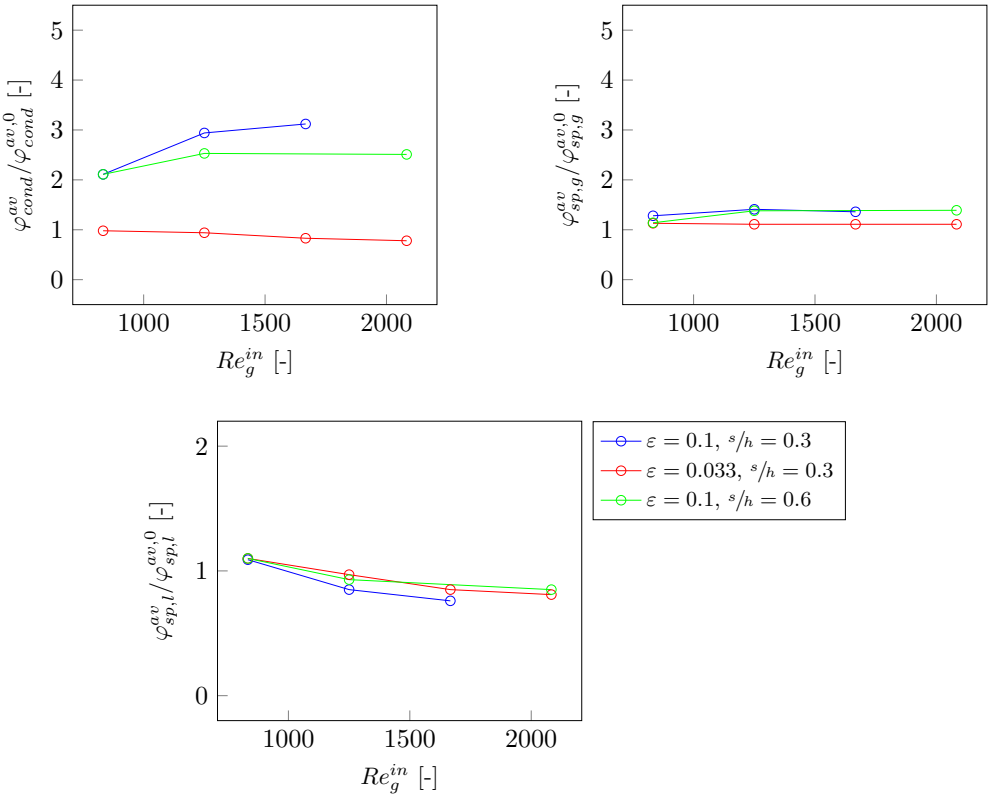

Figure 5.11: Evolution of $\varphi^{av}_{cond}/\varphi^{0,av}_{cond}$, $\varphi^{av}_{sp,g}/\varphi^{0,av}_{sp,g}$ and $\varphi^{av}_{sp,l}/\varphi^{0,av}_{sp,l}$ as a function of Re^{in}_g for Calcs. 3, 13, 16, 19, 29, 32, 38, 48, 54, 57, 67 and 70 in Table 5.1. The various quantities appearing in these ratios are averaged quantities and are obtained from Eqs. (5.7) and (5.8). The original quantities φ_{cond}, $\varphi_{sp,g}$ and $\varphi_{sp,l}$ are obtained from the expressions in Section 2.3.2.4.

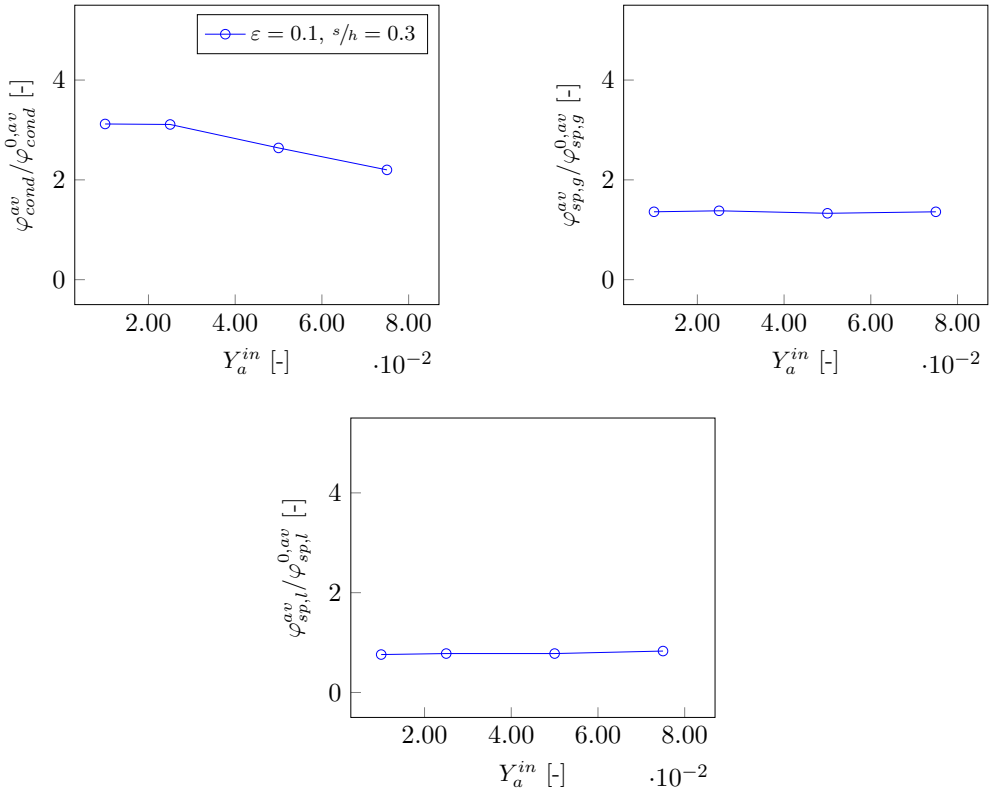

Figure 5.12: Evolution of $\varphi^{av}_{cond}/\varphi^{0,av}_{cond}$, $\varphi^{av}_{sp,g}/\varphi^{0,av}_{sp,g}$ and $\varphi^{av}_{sp,l}/\varphi^{0,av}_{sp,l}$ as a function of Y_a^{in} for Calcs. 48 to 51 in Table 5.1. The various quantities appearing in these ratios are averaged quantities and are obtained from Eqs. (5.7) and (5.8). The original quantities φ_{cond}, $\varphi_{sp,g}$ and $\varphi_{sp,l}$ are obtained from the expressions in Section 2.3.2.4.

Table 5.4: Coefficients $a_{\phi,0}$ to $a_{\phi,15}$ resulting from the regression of $\phi^{av}/\phi^{0,av}$, with $\phi \in \{\varphi_{cond}, \varphi_{sp,g}, \varphi_{sp,l}\}$, in the form given by Eq. (5.17). Calculations used in the regression are Calcs. 2 to 16, 18 to 32, 37 to 48, 52 to 54 and 56 to 70.

ϕ	$a_{\phi,0}$	$a_{\phi,1}$	$a_{\phi,2}$	$a_{\phi,3}$	$a_{\phi,4}$	$a_{\phi,5}$	$a_{\phi,6}$
φ_{cond}	5.9830	−72.2427	−9.0098	−0.0050	665.0711	3.9287	1.4948×10^{-6}
$\varphi_{sp,g}$	2.8643	−31.6721	−3.8768	−0.0024	100.2846	3.4332	7.8565×10^{-7}
$\varphi_{sp,l}$	1.3478	8.3918	−1.1101	-2.6836×10^{-4}	−31.8599	0.4095	2.4571×10^{-8}

ϕ	$a_{\phi,7}$	$a_{\phi,8}$	$a_{\phi,9}$	$a_{\phi,10}$	$a_{\phi,11}$	$a_{\phi,12}$
φ_{cond}	−28.2370	0.0346	0.0102	89.8549	-1.6425×10^{-5}	-2.1504×10^{-6}
$\varphi_{sp,g}$	17.0394	0.0451	0.0029	−34.8952	1.3507×10^{-5}	-7.9305×10^{-7}
$\varphi_{sp,l}$	10.5163	−0.0137	0.0011	−7.1923	3.1976×10^{-6}	-2.0661×10^{-7}

ϕ	$a_{\phi,13}$	$a_{\phi,14}$	$a_{\phi,15}$
φ_{cond}	−646.8324	0.1341	−0.0043
$\varphi_{sp,g}$	45.7290	−0.0855	-8.4137×10^{-4}
$\varphi_{sp,l}$	−14.2740	0.0263	2.7402×10^{-4}

can therefore be placed in the three fits proposed. Note that they are in principle only valid in the analyzed range of control parameters. Even if they may be extrapolated, care has to be taken when using them outside this range.

5.2 Impact of tortuosity on heat transfer with phase change

5.2.1 Introduction

Tortuosity is the state of being tortuous or sinuous, i.e., of having repeated turns. It is usually estimated as the ratio of the actual flow path length to the straight distance between the ends of the flow path. In the previous section, roughness was found to have an impact on the various heat fluxes taking place at the wall, both locally and in average over the length. Since a tortuous channel can be seen as a rough channel with high amplitude, phase-shifted edges, it can be expected that tortuosity will also have an impact on heat transfer with phase change.

No study on the impact of tortuosity on heat transfer in micro- or mini-channels was found in the literature. Nevertheless, a few studies on the impact of tortuosity on turbulent single-phase heat transfer in porous media, more precisely in packed beds, are available. Among them are those of Deen et al. (2014); Gunn (1978); Wilson and Jacobs (1993); Zare and Hashemabadi (2019). Deen et al. (2014); Gunn (1978); Wilson and Jacobs (1993) did

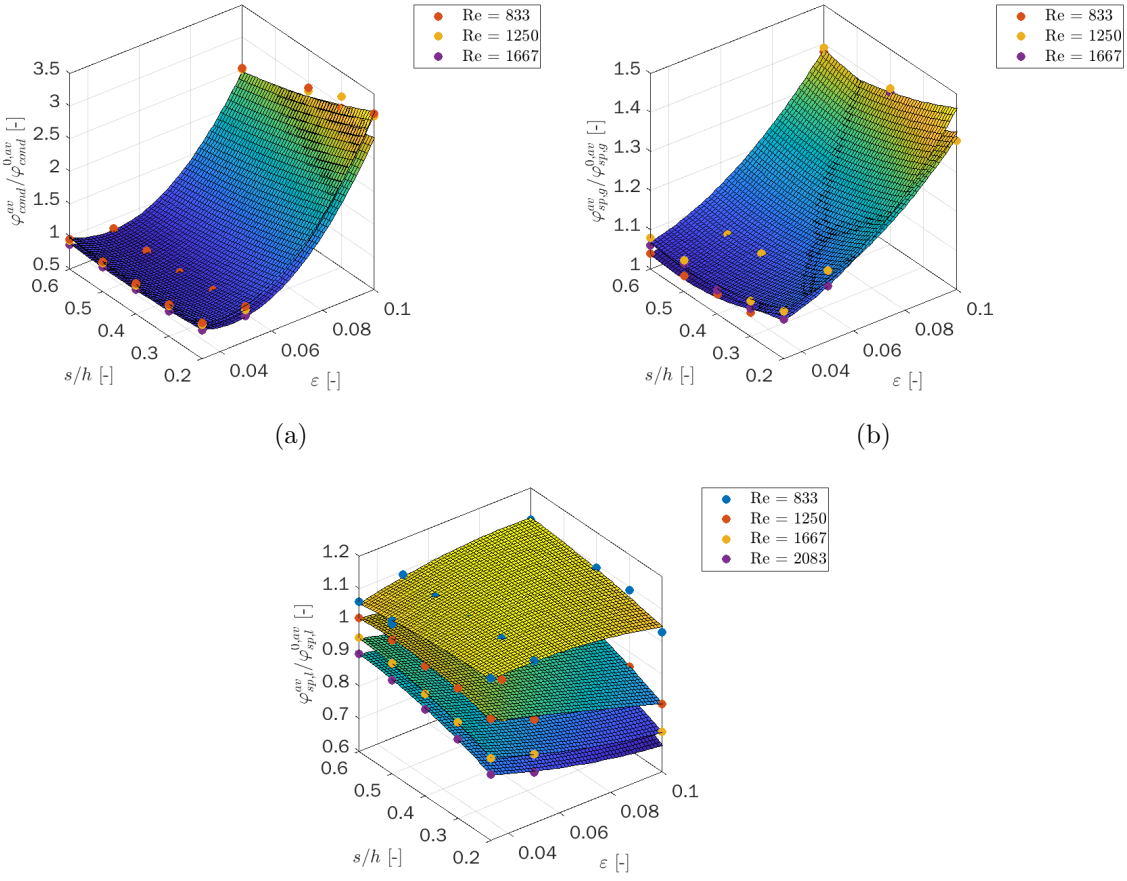

Figure 5.13: Evolution of $\varphi^{av}_{cond}/\varphi^{0,av}_{cond}$ (a), $\varphi^{av}_{sp,g}/\varphi^{0,av}_{sp,g}$ (b) and $\varphi^{av}_{sp,l}/\varphi^{0,av}_{sp,l}$ (c) as a function of ε, s/h and Re^{in}_g for Calcs. 2 to 16, 18 to 32, 37 to 48, 52 to 54 and 56 to 70 in Table 5.1. The various quantities appearing in these ratios are averaged quantities and are obtained from Eqs. (5.7) and (5.8). The original quantities φ_{cond}, $\varphi_{sp,g}$ and $\varphi_{sp,l}$ are obtained from the expressions in Section 2.3.2.4.

not directly consider the effect of tortuosity but that of porosity (ratio of the volume of the pores to the total volume), which, according to most of the existing empirical expressions, is inversely related to tortuosity – see for instance the expression by Ho and Striender (1981). They proposed correlations for the average Nusselt number (dimensionless wall heat flux) over the bed, predicting that this number increases with porosity and therefore decreases with tortuosity. These correlations were found to depend on porosity, Reynolds number (ratio of inertial forces to viscous forces) and Prandtl number (ratio of momentum diffusivity to thermal diffusivity). In constrast, Zare and Hashemabadi (2019) directly considered the effect of tortuosity. They found distinct packed beds of equal porosity to be characterized by different average Nusselt numbers and attributed this difference to tortuosity. Also, they found the correlations of Deen et al. (2014); Wilson and Jacobs (1993) to give incorrect predictions for the average Nusselt number. As a consequence, they proposed a new correlation explicitly depending on tortuosity, predicting that the average Nusselt number increases with this parameter.

This section investigates the effect of tortuosity on laminar single- and two-phase dynamics and heat transfer in mini-channel. Indeed, the studies mentioned only concerns packed beds and were restricted to single-phase flow and to the turbulent flow regime, while, in the present thesis, the case of two-phase flows with phase change in mini-channels and cracks is considered.

5.2.2 Problem setup

5.2.2.1 Computational domain and boundary conditions

The computational domain is shown in Fig. 5.14. It represents a smooth and tortuous mini-channel of height h and rectilinear length l_{rect}. The tortuous path, of length l_{curv}, is generated by a succession of rectangular elements of height p, width w and spacing s. The difference with the domain in Section 5.1 is that p, w and s are larger than h. The flow rate, the temperature and the composition are imposed at the inlet, the pressure is imposed at the outlet and the temperature is imposed at the walls. A total of 9 calculations are carried out (see Table 5.5). h is set to 100 µm and l_{rect} to 3 cm. To simplify the problem, the assumption is made that $w = s$. p is varied between 2 and 8 mm and s between 0.5 and 2 mm. For the same reasons as before, a high pressure is considered. The outlet pressure P^{out} is set to 140 bar. The air inlet mass fraction Y_a^{in} is set to 1 %. The gas inlet temperature T_g^{in} and wall temperature T_w are set to $T_{sat} + 12$ K and $T_{sat} - 15$ K, respectively. The inlet mass flow rate per unit area G is varied between 50 and 100 kg m^{-2} s^{-1}. The physical properties are computed using the CATHARE tables (Emonot et al., 2011). An adaptive time-stepping strategy is adopted. The maximum Courant and Fourier numbers, defined as $\|\underline{U}_k\| \frac{\Delta t}{\Delta x}$ and

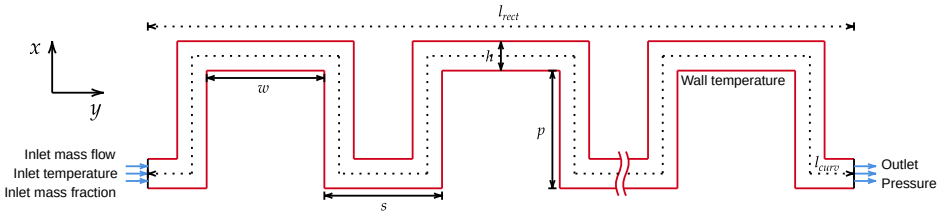

Figure 5.14: Computational domain and boundary conditions. The domain represents a tortuous mini-channel of height $h = 100\,\mu m$ and rectilinear length $l_{rect} = 3\,cm$. The tortuous path, of length l_{curv}, is obtained by successive rectangular elements of height p, width w and spacing s. Mass flow rate, temperature and composition are imposed at the inlet, pressure is imposed at the outlet and temperature is imposed at the walls. p, w and s, as well as the values of the boundary conditions are given in Table 5.5.

Table 5.5: Tortuosity parameter and boundary condition values for the various calculations performed in Section 5.2. p/h is the element relative height and s/h the element relative spacing. G is the gas inlet mass flow rate per unit area, T_g^{in} the gas inlet temperature, Y_a^{in} the air inlet mass fraction and T_w the wall temperature.

p/h	s/h	T_g^{in} [K]	T_w [K]	Y_a^{in} [%]	G [kg m^{-2} s^{-1}]	
					50	200
20	5	650	620	1	–	n°01
20	10	650	620	1	–	n°02
20	20	650	620	1	–	n°03
0	–	622	595	1	n°1	–
20	5	622	595	1	n°2	–
20	10	622	595	1	n°3	–
20	20	622	595	1	n°4	–
40	20	622	595	1	n°5	–
80	20	622	595	1	n°6	–

$\frac{\lambda_k}{\rho_k C p_k}\frac{\Delta t}{\Delta x}$, with Δt the time step and Δx the grid spacing, are set to 1 and 10 for the two phases.

5.2.2.2 Gravity and wettability

For the same reason as in Section 5.1, namely that the Eotvos number, is below the critical values proposed by Suo and Griffith (1964); Griffith and Synder (1964); Cornwell and Kew (1993), gravity is neglected. We are still not interested by the effect of wettability. Therefore, as previously, a neutral contact angle of 90° is used for the large interfaces, which is in fact enforced enforced via the null flux condition applied by the code to the volume fraction at the wall.

Table 5.6: Values of the gas Reynolds number at the inlet (Eq. (5.2)) for the calculations in Table 5.5.

Calculation number	01 to 03	1 to 6
Re_g^{in}	417	1667

5.2.2.3 Turbulence and mesh

For tortuous-wall conditions, no modification of the critical Reynolds number for the transition from laminar to turbulent flow has been reported in the literature. For this reason, and since smooth walls are used, the critical value of about 2000 apply for the present calculations. An estimation of the inlet Reynolds number, defined by Eq. (5.2), is given in Table 5.6. The corresponding values are found to be below 2000, indicating that the flow is laminar and therefore that there is no need for a turbulence model. Cartesian grids are employed, and the same resolution as in Chapter 4 is used, corresponding to $\Delta x = {}^{h}/_{20}$ and $\Delta y = {}^{0.03}/_{6000}$.

5.2.2.4 Single-phase flow verifications

The purpose of this section is to ensure that single-phase dynamics is correctly computed in the presence of geometrical singularities other than those induced by roughness, i.e., with dimensions larger than the channel diameter. For this purpose, Calcs. 01 to 03, in which no liquid is formed, are used. For single-phase flow, in the presence of geometrical singularities with dimensions larger than the channel diameter, Eq. (5.4) becomes:

$$\frac{\Delta P}{l'} = \frac{1}{2}\left(\frac{f_g}{D_h} + \frac{\sum_{N_{sing}} \xi}{l'}\right)\rho_g U_g^2 \,. \tag{5.18}$$

ξ is the singular head loss coefficient. It is the equivalent of f for friction. The quantity $f_g + {}^{D_h}/_{l'}\sum_{N_{sing}} \xi$ resulting from simulation, obtained from the pressure drop and the velocity computed by the code, is shown as a function of ${}^{s}/_{h}$ in Fig. 5.15. A comparison is made with the same quantity but with f_g computed using Eq. (5.5) and with ξ computed using the following empirical expression for sudden elbows of angle θ with rectangular cross-section (Idel'cik, 1969):

$$\xi = C_1 A \xi' \,. \tag{5.19}$$

A is a correction coefficient based on experimental data, which depends on the deviation angle θ, and C_1 is a coefficient depending on the ratio of cross-section width to cross-section height. For $\theta = {}^{\pi}/_{2}$ and an infinite cross-section width, $A = 1.2$ and $C_1 = 0.7$. ξ' can be

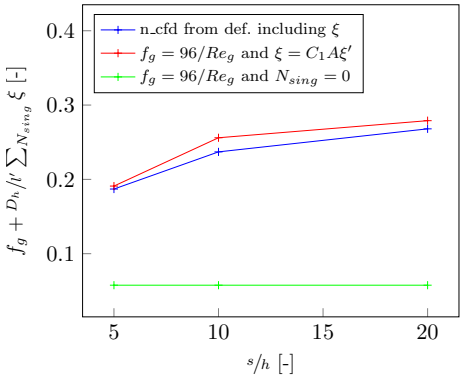

Figure 5.15: Evolution of the equivalent friction factor ${}^{f_g}/_{D_h} + \sum_{N_{sing}} {}^{\xi}/_{l'}$ with element relative spacing for Calcs. 01 to 03. Comparison is made with Eqs. (5.5) and (5.19).

obtained from the equation of Weisbach (1850):

$$\xi' = 0.95 \sin^2 \frac{\theta}{2} + 2.05 \sin^4 \frac{\theta}{2} . \tag{5.20}$$

With the previous values of θ, A and C_1, we get $\xi' = 0.99$ and $\xi = 0.83$. A good agreement is obtained between the curve corresponding to Eq. (5.18) and that corresponding to Eqs. (5.5) and (5.19), which confirms that single-phase dynamics is correctly computed by the code in the presence of geometrical singularities with dimensions larger than the channel diameter. The other curve corresponds to the case where the contribution corresponding to the singular head loss is not taken into account. An important discrepancy with the first two curves is observed, indicating that the latter contribution cannot be neglected in the simulations performed. The magnitude of this contribution would be decreased if the number of singularities was reduced (at fixed length) or if the channel length was increased (at fixed number of singularities). However, for the application targeted in the present thesis, namely concrete cracks, it is to be expected that the ratio of number of singularities to length will be important. This will be further discussed in Chapter 6.

5.2.2.5 Dependence of the wall energy transfers

In the following, the same methodology as in Section 5.1 for the impact of roughness is used. The purpose is to characterize the impact of the tortuosity parameters and other problem variables on ϕ and ${}^{\phi^{av}}/_{\phi^{0,av}}$, $\phi \in \{\varphi_{cond}, \varphi_{sp,g}, \varphi_{sp,l}\}$ referring to tortuous-wall conditions, $\phi^0 \in \left\{\varphi^0_{cond}, \varphi^0_{sp,g}, \varphi^0_{sp,l}\right\}$ referring to smooth-wall conditions and the superscript av referring to the average over the length, computed using the same equations as Eqs. (5.7) and (5.8). As a reminder, φ_{cond} is the condensation heat flux and $\varphi_{sp,g}$ and $\varphi_{sp,l}$ are the single-phase gas and liquid heat fluxes. These fluxes are obtained from the expressions provided in

Section 2.3.2.4.

Using the general non-dimensionalization technique by Ipsen (1960), taking into account the fact that $s = w$, the same dependence as that described by Eqs. (5.9) and (5.10) is obtained for ϕ and ϕ^0. Again, the dependence to the Prandtl number is neglected, and the assumption is made that the variations of ϕ^{av} and $\phi^{0,av}$ with the Eckert number are identical. As a consequence, Eq. (5.13) still apply for ${}^{\phi^{av}}/_{\phi^{0,av}}$. In the next section, the sensitivity of ϕ to ${}^{y_{curv}}/_{h}$ will be assessed. Due to time limitations, only the sensitivity of ${}^{\phi^{av}}/_{\phi^{0,av}}$ to ${}^{l}/_{h}$, ${}^{p}/_{h}$ and ${}^{s}/_{h}$ will be investigated. The sensitivity of the latter ratio to Re_g^{in} and Y_a^{in} should be investigated in future research.

5.2.3 Results

5.2.3.1 Local impact

This section focuses on the sensitivity of $\phi \in \{\varphi_{cond}, \varphi_{sp,g}, \varphi_{sp,l}\}$ to ${}^{y}/_{h}$ and ${}^{y_{curv}}/_{h}$. ϕ is averaged over time, and absolute values are used.

The various quantities are shown as a function of y in Fig. 5.16 for Calc. 4, bottom wall. The range $y \in [2.5 \times 10^{-3}, 4 \times 10^{-3}]$ m is used for all the quantities, corresponding to the third and fourth turns starting from the entrance. For $y \approx 2.81 \times 10^{-3}$ m, the fluxes are found to reach values lower than the values for $y > 2.81 \times 10^{-3}$ m and also values larger than the values for $y < 2.81 \times 10^{-3}$ m. This can be attributed to the geometrical singularities, i.e., the two elbows. Indeed, in the absence of any elbow, the fluxes are found to monotonically decrease with y (see Chapter 4).

The various quantities are shown as a function of y_{curv} in Fig. 5.17 for the same calculation as before, bottom and top walls. Only the third turn starting from the entrance is considered. A comparison is made with Calc. 1, corresponding to smooth-wall conditions. The fact that the elbows are responsible for fluctuations is confirmed. For the bottom wall, φ_{cond} and $\varphi_{sp,g}$ are found to decrease upstream the elbow and to increase downstream the elbow. The opposite behavior is observed for the top wall, i.e., these fluxes are found to increase upstream the elbow and to decrease downstream the elbow. For a given flux, the increase/decrease for the top wall has not necessarily the same amplitude than that for the bottom wall. Except maybe for φ_{cond}, which can be expected to slightly decrease, it is difficult to know if, in average over the length, the fluxes will increase, decrease or stay constant in comparison with Calc. 1. This will be the object of the following section.

The fluctuations of the various quantities considered can be linked with hydrodynamics. As shown in Fig. 5.18, corresponding to the third turn from the entrance, liquid is trapped in the outer corner and right after the inner corner, due to the generation of recirculations.

Because of the liquid, the cross-sectional area is reduced and the gas accelerates. Therefore, in Fig. 5.17, for the bottom wall, the decrease in φ_{cond} and $\varphi_{sp,g}$ observed upstream the elbow is attributed to an increase in the amount of liquid. Conversely, the increase observed downstream the elbow is attributed to a decrease in the amount of liquid, and also to an increase in the gas velocity. The inverse apply for the top wall, i.e., the increase observed upstream the elbow is attributed to a decrease in the amount of liquid and the decrease observed downstream the elbow is attributed to an increase in the amount of liquid. Recirculations generated by elbows have been extensively studied in the literature for adiabatic single-phase flows. Studies can also be found for adiabatic two-phase flows. The latter studies put forward the existence of the same two zones of liquid recirculation. In the case of non-adiabatic two-phase flow, which has never been reported in the literature, the present results show that these zones have a significant impact on wall heat transfer.

5.2.3.2 Global impact

In the previous section, it was found that the elbows are responsible for fluctuations in $\phi \in \{\varphi_{cond}, \varphi_{sp,g}, \varphi_{sp,l}\}$. Therefore, it can be expected that ${}^{\phi^{av}}/_{\phi^{0,av}}$ will vary with ${}^{p}/_{h}$ and ${}^{s}/_{h}$. This section focuses on the sensitivity of ${}^{\phi^{av}}/_{\phi^{0,av}}$ to the latter parameters, and also to ${}^{l}/_{h}$. ${}^{\phi^{av}}/_{\phi^{0,av}}$ is averaged over time. In each graph, each point will correspond to a calculation.

The various ratios are shown as a function of ${}^{l}/_{h}$, ${}^{p}/_{h}$ and ${}^{s}/_{h}$ in Figs. 5.19 to 5.21, respectively, for Calcs. 4 to 6. In each figure, each ratio is found to be nearly constant to unity, meaning that, in average over the length, φ_{cond}, $\varphi_{sp,g}$ and, $\varphi_{sp,l}$ are almost unchanged in comparison with φ^0_{cond}, $\varphi^0_{sp,g}$ and, $\varphi^0_{sp,l}$, despite the fluctuations undergone locally. This is attributed to a compensation effect between the zones where the fluxes increase and those where they decrease.

In one-dimensional simulations, like roughness, tortuosity cannot be directly taken into account, i.e., by means of geometry. In Section 5.1.3, correlations were derived to indirectly take into account the effect of roughness on heat transfer with phase change in this kind of simulation. Concerning tortuosity, the above results show that ${}^{l}/_{h}$, ${}^{p}/_{h}$, ${}^{s}/_{h}$ do not have any impact on ${}^{\phi^{av}}/_{\phi^{0,av}}$ in the range of parameters studied. At this stage no correlation is therefore required for tortuosity. However, as indicated previously, further investigations should be conducted for Re_g^{in} and Y_a^{in}.

5.3 Summary

In this chapter, the effects of roughness and tortuosity, i.e., of geometrical singularities, on laminar two-phase heat transfer with phase change were investigated. The geometrical

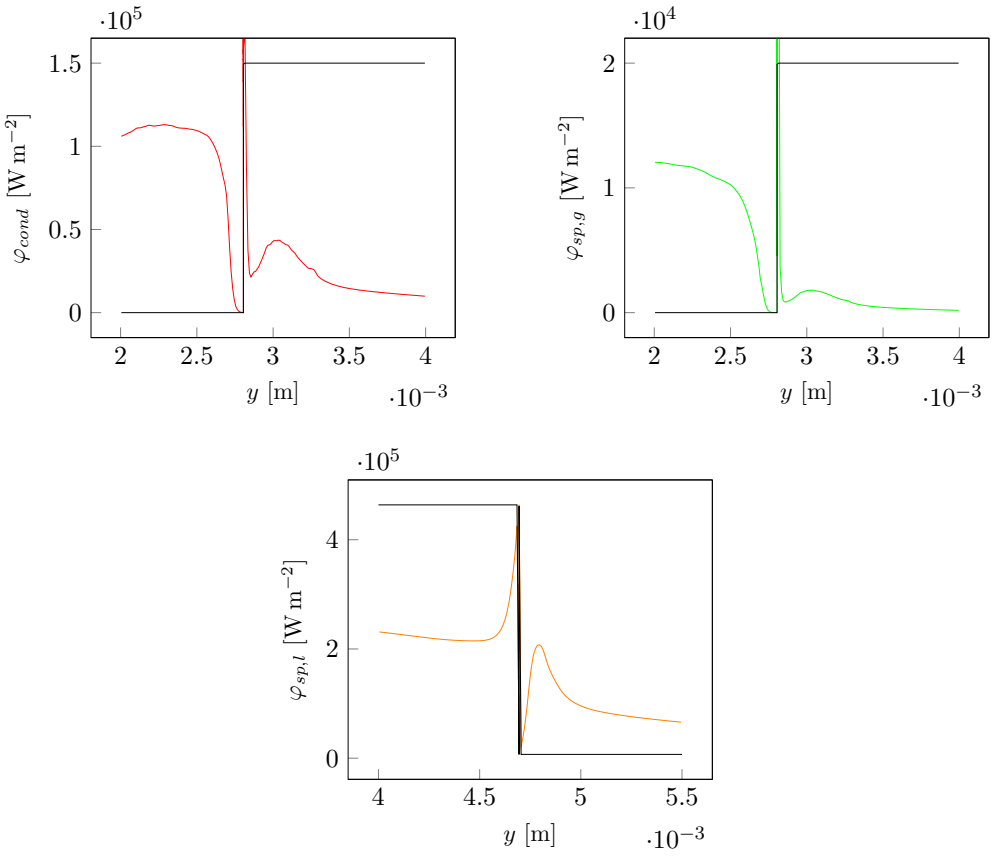

Figure 5.16: Evolution of φ_{cond}, $\varphi_{sp,g}$ and $\varphi_{sp,l}$ with the y-coordinate for Calc. 4. The various quantities are obtained from the expressions in Section 2.3.2.4.

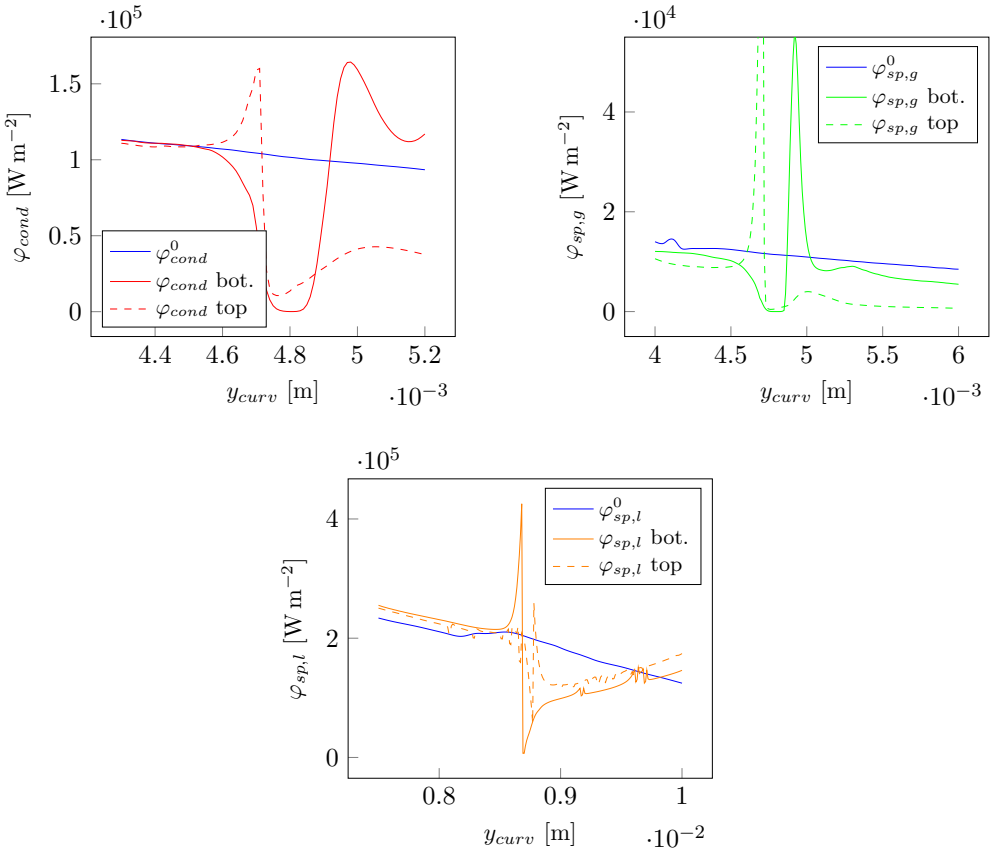

Figure 5.17: Evolution of φ_{cond}, $\varphi_{sp,g}$ and $\varphi_{sp,l}$ with the y_{curv}-coordinate for Calc. 4. The various quantities are obtained from the expressions in Section 2.3.2.4. For each quantity, a comparison is made with Calc. 1.

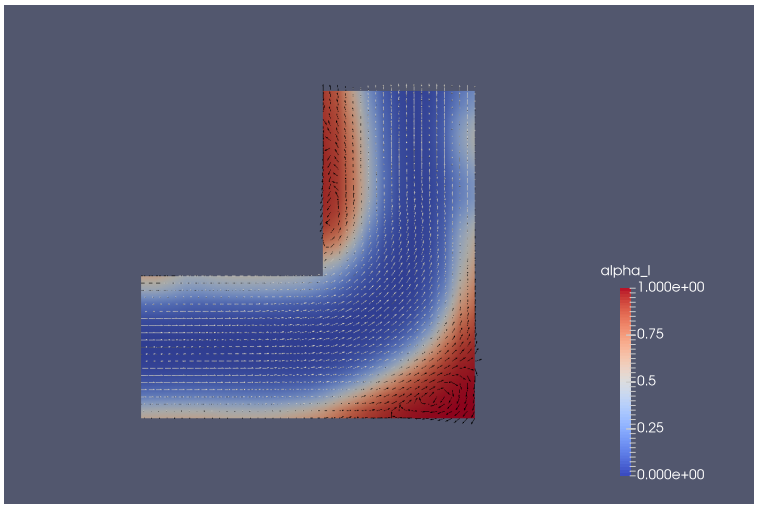

Figure 5.18: Liquid recirculations observed in the vicinity of the third turn in Calc. 4. The gas is represented in blue, while the liquid is repesented in red. The white and black arrows correspond to the gas and liquid velocities, respectively.

singularities were modeled directly, using rectangular elements, with dimensions lower than the channel diameter for roughness and larger than the channel diameter for tortuosity. The quantities considered were ϕ and ${}^{\phi^{av}}/_{\phi^{0,av}}$, $\phi \in \{\varphi_{cond}, \varphi_{sp,g}, \varphi_{sp,l}\}$ – with φ_{cond} the condensation heat flux and $\varphi_{sp,g}$ and $\varphi_{sp,l}$ the single-phase gas and liquid heat fluxes – referring to rough- or tortuous-wall conditions, $\phi^0 \in \left\{\varphi^0_{cond}, \varphi^0_{sp,g}, \varphi^0_{sp,l}\right\}$ referring to smooth wall-conditions and the subscript av referring to the average over the length. It was shown that ${}^{\phi^{av}}/_{\phi^{0,av}}$ can depend on the averaging length, element height and spacing, inlet Reynolds number and air inlet mass fraction.

Concerning roughness, the assumption was made of a constant element width. Unlike for channels of conventional size, the impact of roughness on dynamics cannot be neglected in the laminar flow regime. As a first step, the friction factor was successfully verified against a recent correlation depending on roughness and valid in the latter regime. In comparison with φ^0_{cond}, $\varphi^0_{sp,g}$ and $\varphi^0_{sp,l}$, φ_{cond}, $\varphi_{sp,g}$ and $\varphi_{sp,l}$ were found to decrease between the roughness elements and increase on top of the roughness elements. ${}^{\varphi^{av}_{cond}}/_{\varphi^{0,av}_{cond}}$, ${}^{\varphi^{av}_{sp,g}}/_{\varphi^{0,av}_{sp,g}}$ and ${}^{\varphi^{av}_{sp,g}}/_{\varphi^{0,av}_{sp,g}}$ were found to be independent of the averaging length and the air mass fraction. Also, ${}^{\varphi^{av}_{cond}}/_{\varphi^{0,av}_{cond}}$ and ${}^{\varphi^{av}_{sp,g}}/_{\varphi^{0,av}_{sp,g}}$ were found to increase with element height (relative roughness) and with Reynolds number, and to decrease with element spacing. In contrast, ${}^{\varphi^{av}_{sp,l}}/_{\varphi^{0,av}_{sp,l}}$ was found to decrease with relative roughness and with Reynolds number, and to increase with element spacing. A correlation depending on element height, element spacing and Reynolds number was proposed for each ratio.

Concerning tortuosity, the assumption was made of equal element width and spacing. The dynamics was successfully verified against a standard correlation from the literature.

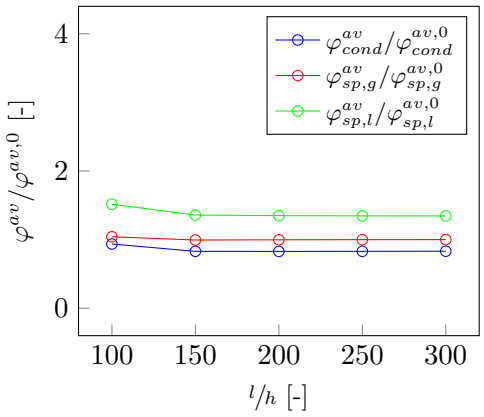

Figure 5.19: Evolution of $\varphi^{av}_{cond}/\varphi^{0,av}_{cond}$, $\varphi^{av}_{sp,g}/\varphi^{0,av}_{sp,g}$ and $\varphi^{av}_{sp,l}/\varphi^{0,av}_{sp,l}$ as a function of l/h for Calc. 2 in Table 5.5. The various quantities appearing in these ratios are averaged quantities and are obtained from Eqs. (5.7) and (5.8). The original quantities φ_{cond}, $\varphi_{sp,g}$ and $\varphi_{sp,l}$ are obtained from the expressions in Section 2.3.2.4.

It was also found that the geometrical singularities are responsible for local fluctuations in φ_{cond}, $\varphi_{sp,g}$ and $\varphi_{sp,l}$. Only the sensitivity to the averaging length and the element height and spacing was assessed for $\varphi^{av}_{cond}/\varphi^{0,av}_{cond}$, $\varphi^{av}_{sp,g}/\varphi^{0,av}_{sp,g}$ and $\varphi^{av}_{sp,l}/\varphi^{0,av}_{sp,l}$. The three ratios were found to be nearly constant to unity, indicating that, in average over the length, for the range of parameter studied, tortuosity has almost no effect on the various heat fluxes exchanged at the wall.

Further work should be conducted to assess the sensitivity of $\varphi^{av}_{cond}/\varphi^{0,av}_{cond}$, $\varphi^{av}_{sp,g}/\varphi^{0,av}_{sp,g}$ and $\varphi^{av}_{sp,l}/\varphi^{0,av}_{sp,l}$ to the inlet Reynolds number and the air inlet mass fraction for tortuous-wall conditions. The impact of the assumptions made concerning geometry should also be investigated, for both rough- and tortuous-wall conditions. More precisely, in the former case, other element widths should be studied and, in the latter case, the element width should be decorrelated from the element spacing. However, in both cases, varying the element width would lead to a significant increase in the number of calculations to perform. Still concerning geometry, other element shapes, e.g., triangular and semi-circular shapes, could be investigated. More realistic alternatives would be to use fractal dimensions or to reconstruct the walls from real mini-channels or cracks. However, this would considerably increase the complexity of the mesh. In addition, roughness and tortuosity could be combined in order to see if the coupled effect is equal to the sum of the individual effects. Finally, the case of three-dimensional roughness and tortuosity should be considered. However, once again, this would significantly increase the number of calculations to perform, since an additional parameter, namely the element depth, would be introduced. This would also increase the number of cells in the domain, but this would not be a problem to the extent that more processors could be used.

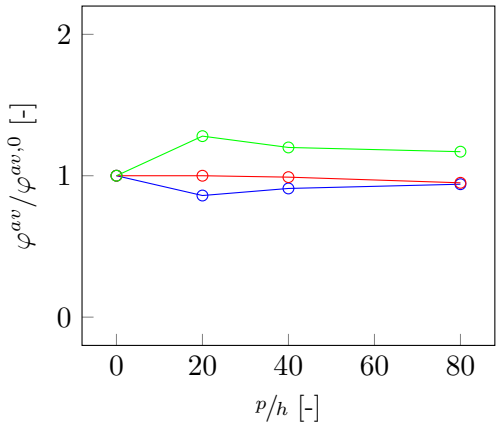

Figure 5.20: Evolution of $\varphi^{av}_{cond}/\varphi^{0,av}_{cond}$, $\varphi^{av}_{sp,g}/\varphi^{0,av}_{sp,g}$ and $\varphi^{av}_{sp,l}/\varphi^{0,av}_{sp,l}$ as a function of p/h for Calcs. 4 to 6 in Table 5.5. The various quantities appearing in these ratios are averaged quantities and are obtained from Eqs. (5.7) and (5.8). The original quantities φ_{cond}, $\varphi_{sp,g}$ and $\varphi_{sp,l}$ are obtained from the expressions in Section 2.3.2.4.

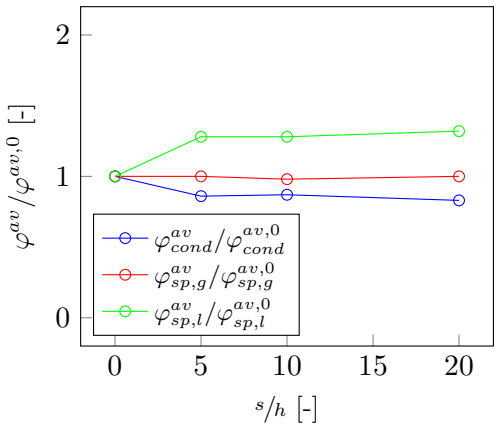

Figure 5.21: Evolution of $\varphi^{av}_{cond}/\varphi^{0,av}_{cond}$, $\varphi^{av}_{sp,g}/\phi^{0,av}_{sp,g}$ and $\varphi^{av}_{sp,l}/\varphi^{0,av}_{sp,l}$ as a function of s/h for Calcs. 2 to 4 in Table 5.5. The various quantities appearing in these ratios are averaged quantities and are obtained from Eqs. (5.7) and (5.8). The original quantities φ_{cond}, $\varphi_{sp,g}$ and $\varphi_{sp,l}$ are obtained from the expressions in Section 2.3.2.4.

Chapter 6

Development of a one-dimensional model based on the correlations derived in three dimensions

Contents

6.1 Introduction 152
6.2 Model description 153
6.2.1 Preamble 153
6.2.2 Equations solved 153
6.2.3 Source and transfer terms 154
6.2.4 Note on the 1DM 158
6.3 Problem setup 159
6.3.1 Computational domain and boundary conditions 159
6.3.2 Averaging procedure for the 2D calculations used for comparison . 159
6.3.3 Single-phase flow basic verifications 161
6.4 Results 162
6.4.1 High pressure 162
6.4.2 Low pressure 165
6.5 Summary 168

6.1 Introduction

In the previous chapters, two-dimensional calculations have been performed using the FGLIM. In addition to two-dimensional calculations, this model also allows for three-dimensional calculations. In practice, the two- and three-dimensional models remain little used for industrial simulations, characterized by large domain sizes and long transients. The reason is that relatively small cells and relatively small time steps are required, which results in heavy meshes and large computation times. When applied to confined geometries like mini-channels and cracks, as shown in the previous chapters, the two- and three-dimensional models require very small time steps. If the physical duration time is short, the computation time will remain acceptable. However, if the physical duration time is long, as is usually the case for industrial simulations, the computation time will reach extremely large values and therefore become prohibitive.

For industrial simulations, an alternative is to use one-dimensional models. Among the various codes using this kind of models are the ATHLET, CAST3M, CATHARE, GOTHIC, RELAP and ECREVISSE codes. Most of them have been developed for nuclear applications – in the latter case, the simulation of the flow inside cracks that could be formed in the walls of the steam generator/the containment building and, in the other cases, the simulation of the flow in the primary and secondary circuits. Examples of studies employing these codes include those of Bahr et al. (2021); Granet (2014); Simon et al. (2004, 2007); Moonesi Shabestary et al. (2020). Moonesi Shabestary et al. (2020) used three different models in the ATHLET code to simulate the COSMEA experiment, corresponding to steam wall and film condensation in a circular pipe of diameter 40 mm – see Bieberle et al. (2020). They found the different models to correctly predict the condensation rate but to underestimate the gas and liquid heat fluxes. Bahr et al. (2021) employed the ATHLET code to simulate the air-steam leakage through a small-scale cracked concrete specimen of opening between 50 and 250 µm. They obtained a relatively good qualitative agreement but a poor quantitative agreement between numerical and experimental data. Granet (2014) used the ECREVISSE code and Simon et al. (2004, 2007) the CAST3M code to simulate the SIMIBE experiment, corresponding to condensation in a model crack of opening between 50 and 370 µm, consisting of two parallel plates – see Caroli et al. (1995) and Chapter 1. They found the results corresponding to the largest openings to be in good agreement with experimental data, and the results corresponding to the lowest openings to be in partial agreement with experimental data.

The one-dimensional code ECREVISSE is based on the homogeous flow assumption, which implies that, in the unique grid cell composing the cross-section, the gas and the liquid have the same velocity and the same temperature (see Chapter 2 for details about

this assumption, which can also be made in two- or three-dimensions). However, Granet (2014); Simon et al. (2004, 2007) have shown that it is not suitable for flows with large droplets and/or slugs, which can establish in cracks. Also, in all the codes mentioned previously, including ECREVISSE, the effects of roughness and tortuosity on dynamics and heat transfer with phase change in the laminar flow regime that have been highlighted in Chapter 5 cannot be taken into account.

In this chapter, a new one-dimensional model, which has been implemented in the neptune_cfd code, is proposed and verified against the FGLIM. Unlike the models mentioned previously, it allows the gas and the liquid to move at different velocities and to have distinct temperatures. It also incorporates the correlations used/developed in Chapter 5 for the effect of roughness and tortuosity on dynamics and heat transfer with phase change in the laminar flow regime.

6.2 Model description

6.2.1 Preamble

The 1D model is detailed here and not in Chapter 2 with the other models since it is based on correlations assessed or developed in Chapters 4 and 5. It is dedicated to the simulation of small-scale laminar condensing flows, like those encountered in mini-channels and cracks (see Chapter 1). It allows to take into account roughness and tortuosity. In both cases, the effect of the geometrical singularities on dynamics and heat transfer with phase change are included in the various correlations used for the source and transfer terms appearing in the equations solved. For compatibility with the correlations for dynamics, in case of a rough mini-channel or crack, the 1D domain length is supposed to be equal to the straight distance between the inlet and the outlet of the mini-channel or crack, whereas in case of a tortuous mini-channel or crack, it is supposed to be equal to the curvilinear distance between the inlet and the outlet of the mini-channel or crack. The equations solved are presented in Section 6.2.2, while the correlations for the source and transfer terms are given in Section 6.2.3.

6.2.2 Equations solved

In the 1D model, as was the case in the FGLIM, two fields are considered, namely a gas field and a liquid field. The following mass, momentum and energy equations are solved for

each of the two fields:

$$\frac{\partial}{\partial t}\left(\alpha_k \rho_k\right) + \frac{\partial}{\partial y}\left(\alpha_k \rho_k U_k\right) = \Gamma_{p\to k} + \Gamma_{w\to k}\,, \tag{6.1}$$

$$\frac{\partial}{\partial t}\left(\alpha_k \rho_k U_k\right) + \frac{\partial}{\partial y}\left(\alpha_k \rho_k U_k U_k\right) = -\alpha_k \frac{\partial P}{\partial y} + I_{p\to k} + S_k^{reg} + S_k^{sing}\,, \tag{6.2}$$

$$\frac{\partial}{\partial t}\left(\alpha_k \rho_k H_k\right) + \frac{\partial}{\partial y}\left(\alpha_k \rho_k H_k U_k\right) = \alpha_k \frac{\partial P}{\partial t} + \Pi^{\Gamma}_{p\to k} + \Pi_{p\to k} + \varphi_{w\to k}\,. \tag{6.3}$$

These equations are obtained from Eqs. (2.37) to (2.39), using the fact that the velocity $\underline{U}_k$ reduces to U_k, and by (i) removing the terms linked with viscous dissipation, (ii) removing the terms linked with heat conduction, (iii) removing the terms linked with gravity and (iv) adding the source terms S_k^{reg} and S_k^{sing} for wall regular friction and singular friction, respectively. As a reminder, H_k, α_k and ρ_k are, respectively, the total enthalpy, volume fraction and density of phase k. P is the pressure, assumed to be the same for both fields. $I_{p\to k}$, $\Gamma_{p\to k}$, and $\Pi_{p\to k}$ denote, respectively, the momentum, mass and energy transfers from phase p to phase k. $\Gamma_{w\to k}$ denotes the mass contribution to phase k induced by wall condensation and $\varphi_{w\to k}$ the energy contribution to phase k induced by wall condensation and/or wall sensible heat transfer. As in the FGLIM and the 4FM, the interfacial transfer terms $\Gamma_{p\to k}$, $I_{p\to k}$, $\Pi^{\Gamma}_{p\to k}$ and $\Pi_{p\to k}$ verify the equalities given by Eqs. (2.40) to (2.42) and the wall transfer terms $\Gamma_{w\to k}$ and $\varphi_{w\to k}$ the equalities given by Eqs. (2.43) and (2.44).

6.2.3 Source and transfer terms

6.2.3.1 Interfacial mass, momentum and energy transfers

In the 1D model, for the interfacial transfer terms, we propose to use closures from the 2-3D models. Indeed, a good confidence is placed in these closures, since they have been found to provide accurate results in a large number of validation cases (see previous chapters and past works mentioned in Chapter 2). More precisely, since no bubbles were detected in the 2D calculations, and since the 1D mesh does not allow for large interfaces, we propose to use the same closures as those for droplets in the Standard Dispersed Model, namely Eq. (2.45) for $I_{p\to k}$ and Eqs. (2.46) to (2.49) for $\Gamma_{p\to k}$ and $\Pi_{p\to k}$ (Mimouni et al., 2010, 2011). A parameter of primary importance in these closures is the droplet diameter. In the 2-3D models, the latter is deduced from the interfacial area concentration, which is obtained by solving an additional transport equation. Exception is made for the wall cells, in which the diameter is computed as:

$$d_l = \left(\frac{6\alpha_l V}{\pi}\right)^{\frac{1}{3}}\,, \tag{6.4}$$

with V the cell volume. In the 1D model, no interfacial area equation is solved. The expression used for the diameter in the unique cell composing the cross-section is:

$$d_l = c_\Delta \left(\frac{6\alpha_l V}{\pi} \right)^{\frac{1}{3}} . \tag{6.5}$$

The purpose of c_Δ is to recover the same order of magnitude of diameter and therefore recover the same level of mass, momentum and energy transfers as in 2D. It is obtained from: $c_\Delta = \left[{}^{N}/_{(N_x N_y)_{resol}} \right]^{1/3}$, with N the number of cells used in the 1D calculation and $(N_x N_y)_{resol}$ the minimal resolution that would be required in 2D. According to the previous chapters, the latter parameter is set to $20 \times 6000 \times {}^{l}/_{0.03} = 4l \times 10^6$, with l the channel length.

6.2.3.2 Wall regular friction

The source terms S_g^{reg} and S_l^{reg} in the momentum equations are obtained from the work of Chisholm (1967), based on that of Lockhart and Martinelli (1947):

$$S_g^{reg} = -\frac{\alpha_g \alpha_l}{\alpha_g \alpha_l + \alpha_g^2 X^2} \left(\frac{dP}{dy} \right)_f , \tag{6.6}$$

$$S_l^{reg} = -\frac{\alpha_g \alpha_l X^2}{\alpha_l^2 + \alpha_g \alpha_l X^2} \left(\frac{dP}{dy} \right)_f , \tag{6.7}$$

with $\left({}^{dP}/_{y} \right)_f$ the total frictional pressure gradient and X the Martinelli parameter. The latter is defined as:

$$X^2 = \frac{\left(\frac{dP}{dy} \right)_{f,l}}{\left(\frac{dP}{dy} \right)_{f,g}} , \tag{6.8}$$

with $\left({}^{dP}/_{y} \right)_{f,g}$ and $\left({}^{dP}/_{y} \right)_{f,l}$ the gas and liquid frictional pressure gradients. These are obtained from:

$$\left(\frac{dP}{dy} \right)_{f,g} = \frac{f_g G^2 x_g^2}{2\rho_g D_h} , \tag{6.9}$$

$$\left(\frac{dP}{dy} \right)_{f,l} = \frac{f_l G^2 \left(1 - x_g\right)^2}{2\rho_l D_h} , \tag{6.10}$$

with D_h the hydraulic diameter, f_k the regular friction factor, G the total mass flow rate per unit area and x_g the flow quality. In 1D, the latter, which is defined as the ratio of vapor mass flow rate to total mass flow rate, simply reads:

$$x_g = \frac{\alpha_g \rho_g U_g}{\alpha_g \rho_g U_g + \alpha_l \rho_l U_l} . \tag{6.11}$$

f_k depends on whether the flow is laminar or turbulent, and also depends on the cross-section geometry. In the present chapter, laminar flows are considered. Based on the single-phase flow verification in Chapter 5, the choice is made to use the correlation of Sentürk and Smits (2019):

$$f_k = \frac{C_f + C'_f}{Re_k}\,, \tag{6.12}$$

with C_f a constant depending on the cross-section geometry, C'_f a correction accounting for roughness and Re_k the Reynolds number. For a semi-infinite cross-section, case considered in the present chapter, $C_f = 96$. C'_f reads: $C'_f = a_1\varepsilon^2 + \left(a_2 + a_3\frac{s+w}{w}\right)\varepsilon$, with $a_1 = 3000$, $a_2 = 520$ and $a_3 = -35$, and with s the roughness element spacing, w the roughness element width and ε the relative roughness (ratio of roughness element height to maximum channel height) – note that if $\varepsilon = 0$, f_k reduces to the standard analytical expression ${}^{C_f}/_{Re_k}$. Re_k is defined as:

$$Re_g = \frac{G x_g D_h}{\mu_g}\,, \tag{6.13}$$

$$Re_l = \frac{G\left(1 - x_g\right) D_h}{\mu_l}\,, \tag{6.14}$$

with μ_k the molecular viscosity. On the other hand, $\left({}^{dP}/_{y}\right)_f$ in Eqs. (6.6) and (6.7) is obtained from:

$$\left(\frac{dP}{dy}\right)_f = \left(\frac{dP}{dy}\right)_{f,g} + C\sqrt{\left(\frac{dP}{dy}\right)_{f,g}\left(\frac{dP}{dy}\right)_{f,l}} + \left(\frac{dP}{dy}\right)_{f,l}\,, \tag{6.15}$$

with C the Chisholm parameter. Based on the results from the two-phase flow calculations in Chapter 4, the choice is made to use the correlation of Zhang et al. (2010b).

6.2.3.3 Wall singular friction

The source terms S_g^{sing} and S_l^{sing} in the momentum equations are obtained from:

$$S_g^{sing} = -\frac{1}{2}\frac{\sum_{N_{sing}}\xi}{l}\frac{G^2 x_g^2}{\alpha_g \rho_g}\,, \tag{6.16}$$

$$S_l^{sing} = -\frac{1}{2}\frac{\sum_{N_{sing}}\xi}{l}\frac{G^2\left(1 - x_g\right)^2}{\alpha_l \rho_l}\,, \tag{6.17}$$

with l the channel length and ξ the singular head loss coefficient. The latter depends on the nature of the geometrical singularities considered. In present chapter, the case of sudden elbows of deviation angle θ with rectangular cross-section is considered. Based on the single-phase flow verification in Chapter 5, the choice is made to use the expression proposed by

(Idel'cik, 1969):

$$\xi = C_1 A \xi' \,. \tag{6.18}$$

A is a correction coefficient based on experimental data, which depends on the deviation angle θ, and C_1 is a coefficient depending on the ratio of cross-section width to cross-section height. For $\theta = \pi/2$ and an infinite cross-section width, $A = 1.2$ and $C_1 = 0.7$. ξ' can be obtained from the equation of Weisbach (1850):

$$\xi' = 0.95 \sin^2 \frac{\theta}{2} + 2.05 \sin^4 \frac{\theta}{2} \,. \tag{6.19}$$

With the previous values of θ, A and C_1, we get $\xi' = 0.99$ and $\xi = 0.83$.

6.2.3.4 Wall mass and energy transfers

The closures for the wall mass and energy transfers are also based on the Standard Dispersed Model for droplets. The reason is the same as before, namely that these closures have been found to provide accurate results in a large number of validation cases. $\Gamma_{w\to k}$ is obtained from the same equation as Eq. (2.53) (Mimouni et al., 2010, 2011). However, the droplet diameter is computed using Eq. (6.5). $\varphi_{w\to k}$ is obtained from the same equations as Eqs. (2.54) and (2.55). However, φ_{cond}, $\varphi_{sp,g}$ and $\varphi_{sp,l}$ are obtained from:

$$\varphi_{cond} = g_{cond} \cdot g' \cdot \Gamma_{w\to g} H_{lat} \,, \tag{6.20}$$

$$\varphi_{sp,g} = g_{sp,g} \cdot g' \cdot (1 - A_l)\, h_g \,(T_w - T_g) \,, \tag{6.21}$$

$$\varphi_{sp,l} = g_{sp,l} \cdot g' \cdot A_l h_l \,(T_w - T_l) \,, \tag{6.22}$$

with A_l the fraction of area affected by the liquid, g_{cond}, $g_{sp,g}$, $g_{sp,l}$ and g' weighting functions for replicating the effect of roughness, h_g and h_l the gas and liquid local heat transfer coefficients, H_{lat} the latent heat of condensation, T_g and T_l the gas and liquid temperatures, and T_w the wall temperature. h_g and h_l are obtained from:

$$h_k = Nu_{sp,k} \frac{\lambda_k}{D_h} \,, \tag{6.23}$$

with $Nu_{sp,k}$ the single-phase Nusselt number and λ_k the thermal conductivity. $Nu_{sp,k}$, defined by $\varphi_{sp,k} / (T_w - T_k) \cdot D_h / \lambda_k$, depends on whether the flow is laminar or turbulent and on whether a single- or a two-phase flow is considered. It can also depend on the cross-section geometry. In Chapter 4, laminar single- and two-phase flows were considered. $Nu_{sp,g}$ and $Nu_{sp,l}$ were computed by the FGLIM from their definition, and compared with analytical values and experimental correlations. The analytical value of 7.54 was employed for $Nu_{sp,g}$ in the part concerning the gas single-phase flow verification – this value assumes an infinite

cross-section and would also have have applied to liquid. In addition, the correlation of Chato (1962) was employed for $Nu_{sp,l}$ in the part concerning the two-phase flow calculations – in fact, for the two-phase flow calculations, the quantity computed was Nu_{tp}, but this quantity reduces to $Nu_{sp,l}$ in the region where the correlation was used. In the present chapter, laminar flows and mini-channels with infinite cross-section are considered. For $Nu_{sp,l}$, the value of 7.54 is retained for single-phase flow and the correlation of Chato (1962) is retained for two-phase flow. For $Nu_{sp,g}$, the value of 7.54 is retained for single-phase flow, and also for two-phase flow, since no correlation was tested in Chapter 4.

The functions g_{cond}, $g_{sp,g}$, $g_{sp,l}$ are set to unity if $\varepsilon = 0$ or otherwise obtained from the correlations derived in Chapter 5, i.e., Eq. (5.17) and Table 5.4, containing the intrinsic effect of roughness. The function g' aims to account for the additional effect of surface increase – remember that, in the case of a rough mini-channel or crack, the domain length is supposed to be equal to the straight distance between the inlet and the outlet. It is set to unity if $\varepsilon = 0$ or otherwise obtained from: $g' \approx {}^{S}/_{S^0}$, with S the surface if roughness was explicitly taken into account and S^0 the surface used in 1D. Note that, at this stage, there is no equivalent of g_{cond}, $g_{sp,g}$, $g_{sp,l}$ for tortuosity, since in Chapter 5 the effect of tortuosity was found to be zero for the range of parameters studied.

6.2.4 Note on the 1DM

In its current state, the 1DM does not account for surface tension and wettability effects. In 1D, unlike in 2D or 3D, no interface can explicitly be solved. Therefore, it is not possible to explicitly compute the surface tension force or control the contact angle made by the liquid on the walls. A solution for indirectly take into account surface tension and wettability in the future could be to develop additional source terms in the form of regular or singular head losses.

In addition to small-scale laminar flows, the 1DM could be used for large-scale laminar flows. However, further developments would be required for turbulent flows. Indeed, some of the relations provided in Section 6.2.3 does not apply in the turbulent flow regime. This is the case of Eq. (6.12) for the regular friction factors, the various correlations for the Nusselt number in Eq. (6.23), but also Eq. (5.17) for the functions g_{cond}, $g_{sp,g}$ and $g_{sp,l}$ used in Eqs. (6.20) to (6.22).

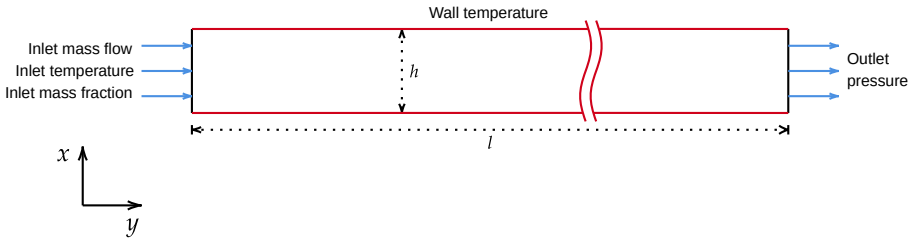

Figure 6.1: Computational domain and boundary conditions. Dimensions are: $h = 100\,\mu m$ and $l = 3\,cm$. Mass flow rate, temperature and composition are imposed at the inlet, pressure is imposed at the outlet and temperature is imposed at the walls.

6.3 Problem setup

6.3.1 Computational domain and boundary conditions

A smooth rectilinear computational domain, of height h and length l is considered. It is shown in Fig. 6.1. The model being able to indirectly take into account roughness and tortuosity, in the following, the domain will represent either a smooth rectilinear mini-channel, a rough rectilinear mini-channel or a smooth and tortuous mini-channel. In the two former cases, l will correspond to the straight distance between the inlet and the outlet of the mini-channel while, in the latter case, it will correspond to the curvilinear distance between the inlet and the outlet of the mini-channel. The flow rate, the temperature and the composition are imposed at the inlet, the pressure is imposed at the outlet and the temperature is imposed at the walls. h is set to $100\,\mu m$. The air inlet mass fraction Y_a^{in} is set to $1\,\%$. The roughness/tortuosity element height p, width w and spacing s, the mass flow rate per unit area G, the gas inlet temperature T_g^{in}, the outlet pressure P_{out}, the wall temperature T_w as well as the model parameters c_Δ, C_f', ξ, g_{cond}, $g_{sp,g}$, $g_{sp,l}$ and g' are varied according to Table 6.1. The physical properties are computed using the CATHARE tables (Emonot et al., 2011). An adaptive time-stepping strategy is adopted. The maximum Courant and Fourier numbers, defined as $\|\underline{U}_k\| \frac{\Delta t}{\Delta x}$ and $\frac{\lambda_k}{\rho_k C p_k} \frac{\Delta t}{\Delta x}$, with Δt the time step and Δx the grid spacing, are set to 1 and 10 for both the gas and the liquid.

6.3.2 Averaging procedure for the 2D calculations used for comparison

In the following, a comparison is made between the 1D and 2D calculations. For this purpose, in 2D, the quantities of interest are averaged over the cross-section. The formulas used are the same as those employed in Chapter 4. They are recalled in Table 6.2. An area-weighted average is performed for volume fraction and pressure. A volume-fraction-

Table 6.1: Geometrical parameter, boundary condition and model parameter values for the various calculations performed/used in the chapter. l is the rectilinear length and l_{curv} the curvilinear length. $^{p}/_{h}$ is the element relative height, $^{s}/_{h}$ the element relative spacing and $^{w}/_{h}$ the element relative width. G is the gas inlet mass flow rate per unit area, T_g^{in} the gas inlet temperature, P_{out} the outlet pressure and T_w the wall temperature. c_Δ, C_f', ξ and g' are used in Eqs. (6.5), (6.12), (6.16) and (6.20) to (6.22), and are given in Section 6.2.3. g_{cond}, $g_{sp,g}$ and $g_{sp,l}$ are used in Eqs. (6.20) to (6.22) and are given by Eq. (5.17) and Table 5.4, except for calculation 1D-4. "I" indicates that the value is imposed and does not correspond to that given by the formula, "–" indicates that the quantity is not defined in the calculation or model, and "∼" indicates that the quantity is defined in the model but the value does not matter in the calculation due to single-phase conditions.

Number	Model	Cell size [m]	l [m]	l_{curv} [m]	$^{p}/_{h}$	$^{s}/_{h}$	$^{w}/_{h}$	G [kg m^{-2} s^{-1}]	T_g^{in} [K]	P_{out} [bar]	T_w [K]	c_Δ	C_f'	ξ	g_{cond}	$g_{sp,g}$	$g_{sp,l}$	g'
2D-00	FGLIM	Chap. 4	0.03	0.03	0	–	–	200	650	140	620	–	–	–	–	–	–	–
1D-00	1DM	10^{-4}	0.03	0.03								∼	0	0	∼	∼	∼	∼
2D-01	FGLIM	Chap. 5.1	0.03	0.035	0.033	0.3	0.1	200	650	140	620	–	–	–	–	–	–	–
1D-01	1DM	10^{-4}	0.03	0.03								∼	15.8	0	∼	∼	∼	∼
2D-02	FGLIM	Chap. 5.1	0.03	0.0375	0.05	0.3	0.1	200	650	140	620	–	–	–	–	–	–	–
1D-02	1DM	10^{-4}	0.03	0.03								∼	26.5	0	∼	∼	∼	∼
2D-03	FGLIM	Chap. 5.1	0.03	0.045	0.1	0.3	0.1	200	650	140	620	–	–	–	–	–	–	–
1D-03	1DM	10^{-4}	0.03	0.03								∼	68.0	0	∼	∼	∼	∼
2D-04	FGLIM	Chap. 5.2	0.03	0.156	20	5	5	200	650	140	620	–	–	–	–	–	–	–
1D-04	1DM	10^{-4}	0.156	0.156								∼	0	0.83	∼	∼	∼	∼
2D-05	FGLIM	Chap. 5.2	0.03	0.09	20	10	10	200	650	140	620	–	–	–	–	–	–	–
1D-05	1DM	10^{-4}	0.09	0.09								∼	0	0.83	∼	∼	∼	∼
2D-06	FGLIM	Chap. 5.2	0.03	0.06	20	20	20	200	650	140	620	–	–	–	–	–	–	–
1D-06	1DM	10^{-4}	0.06	0.06								∼	0	0.83	∼	∼	∼	∼
2D-1	FGLIM	Chap. 4	0.03	0.03	0	–	–	50	622	140	595	–	–	–	–	–	–	–
1D-11	1DM	5×10^{-6}	0.03	0.03								1 (I)	0	0	1	1	1	1
1D-12	1DM	5×10^{-6}	0.03	0.03								0.34	0	0	1	1	1	1
1D-13	1DM	10^{-4}	0.03	0.03								0.14	0	0	1	1	1	1
2D-2	FGLIM	Chap. 5.1	0.03	0.045	0.1	0.3	0.1	200	622	140	595	–	–	–	–	–	–	–
1D-21	1DM	10^{-4}	0.03	0.03								0.14	0 (I)	0	2.5	1.1	0.81	1.5
1D-22	1DM	10^{-4}	0.03	0.03								0.14	68.0	0	1 (I)	1 (I)	1 (I)	1 (I)
1D-23	1DM	10^{-4}	0.03	0.03								0.14	68.0	0	2.5	1.1	0.81	1.5
2D-3	FGLIM	Chap. 4	0.03	0.03	0	–	–	100	442	5	415	–	–	–	–	–	–	–
1D-3	1DM	10^{-4}	0.03	0.03								0.14	0	0	1	1	1	1
2D-4	FGLIM	Chap. 5.1	0.03	0.045	0.1	0.3	0.1	100	442	5	415	–	–	–	–	–	–	–
1D-4	1DM	10^{-4}	0.03	0.03								0.14	68.0	0	1.5	1.2	1.3	1.5

and density-weighted average is performed for velocity, since the conserved quantity is $\alpha_k \rho_k U_k$. A volume-fraction-, density- and heat-capacity-weighted average is performed for temperature, since the conserved quantity is $\alpha_k \rho_k Cp_k T_k$.

Table 6.2: One-dimensional quantities used in the following.

ϕ_k	Cross-sectional averaged ϕ_k
α_k, P	$\frac{1}{h}\int_x \phi_k \mathrm{d}x$
$U_{k,y}$	$\frac{\int_x \alpha_k \rho_k \phi_k \mathrm{d}x}{\int_x \alpha_k \rho_k \mathrm{d}x}$
T_k	$\frac{\int_x \alpha_k \rho_k Cp_k \phi_k \mathrm{d}x}{\int_x \alpha_k \rho_k Cp_k \mathrm{d}x}$

6.3.3 Single-phase flow basic verifications

The 1D model is first verified in case of single-phase flow, by comparison with the FGLIM. Cases 00 to 06 are used for this purpose. For Cases 00 to 03, the quantity used is the gas friction factor f_g. In the two models, it is obtained from (Darcy, 1857; Moody, 1944; Weisbach, 1850):

$$\frac{\Delta P}{l} = \frac{1}{2}\frac{f_g}{D_h}\rho_g U_g^2 \,. \tag{6.24}$$

The results are shown as a function of $\varepsilon = {}^{p}/_{h}$ in Fig. 6.2, each point corresponding to a calculation. The 1D model is found to be in good agreement with the FGLIM, which indicates that wall regular friction (Eqs. (6.6) to (6.15)) is correctly computed for single-phase flow. For Cases 04 to 06, the quantity used is $f_g + {}^{D_h}/_{l}\sum_{N_{sing}} \xi$. In the two models, it is obtained from:

$$\frac{\Delta P}{l} = \frac{1}{2}\left(\frac{f_g}{D_h} + \frac{\sum_{N_{sing}} \xi}{l}\right)\rho_g U_g^2 \,. \tag{6.25}$$

The results are shown as a function of ${}^{s}/_{h}$ in Fig. 6.3. As previously, each point corresponds to a calculation. The 1D model is once again found to be in good agreement with the FGLIM, indicating that wall singular friction (Eqs. (6.16) to (6.19)) is correctly computed for single-phase flow. An additional comparison between the 1D model and the FGLIM is performed for Case 00. The quantity used is the Nusselt number $Nu_{sp,g}$. In both models, it is obtained from:

$$Nu_{sp,g} = \frac{\varphi_{sp,g}}{T_w - T_g}\frac{D_h}{\lambda_g} \,. \tag{6.26}$$

The results are shown as a function of ${}^{4y}/_{D_h Re_g Pr_g}$ in Fig. 6.4. The 1D model is found to be consistent with the FGLIM, which means that wall heat transfer (Eqs. (6.21) to (6.23)) is correctly computed for single-phase flow. These three basic verifications indicate that Eqs. (6.6) to (6.19) and (6.21) to (6.23) properly work for single-phase flow. Two-phase

flow is investigated in the following.

6.4 Results

6.4.1 High pressure

6.4.1.1 Smooth rectilinear

The averaged gas and liquid volume fractions, velocities and temperatures, as well as the pressure, are shown in Fig. 6.5 for Cases 2D-1 and 1D-11 to 1D-13. In comparison with Case 2D-1, Case 1D-11 significantly underestimates the liquid volume fraction and significantly overestimates the gas and liquid velocities and temperatures, as well as the pressure, on the first half of the channel. For Cases 1D-12 and 1D-13, a relatively good agreement with Case 2D-1 is obtained for all the quantities considered. A small discrepancy is nonetheless observed at the entrance for the liquid temperature. The fact that a bad agreement is obtained between Case 2D-1 and Case 1D-11 and that a good agreement is obtained between Case 2D-1 and Cases 1D-12 and 1D-13 confirms that Eq. (6.4) cannot provide accurate results and that Eq. (6.5) has to be used instead. The fact that similar accurate results are obtained in Cases 1D-12 and 1D-13 indicates that the number of cells can be decreased without deteriorating the results (provided that the parameter c_Δ is adapted), which is of great interest since the time step can be increased and therefore the computation time decreased. From Cases 1D-12 and 1D-13, we conclude that the 1D model is predictive in case of two phase flow in smooth rectilinear channel.

6.4.1.2 Rough rectilinear

The cases used in this section are Case 2D-2 and Cases 1D-21 to 1D-23. The average gas and liquid volume fractions, velocities and temperatures, as well as the pressure, are shown in Fig. 6.6. A relatively good agreement is obtained between Case 2D-2 and 1D-21 for all the quantities considered, except for the pressure, which is underestimated by the 1D model on the whole domain, and except for the gas temperature, which is underestimated by the 1D model in the center of the domain. A bad agreement is obtained between Case 2D-2 and Case 1D-22 for all the quantities considered, except the velocities and maybe the gas temperature. The 1D model underestimates the liquid volume fraction and overestimates the liquid temperature and the pressure. The results obtained in Case 1D-23 are similar to those obtained in Case 1D-21, except for the pressure. Indeed, for this quantity, Case 1D-23 is found to be more consistent with Case 2D-2 than Case 1D-21. The fact that a relatively good agreement is obtained between Case 2D-2 and Case 1D-23 and that a bad agreement

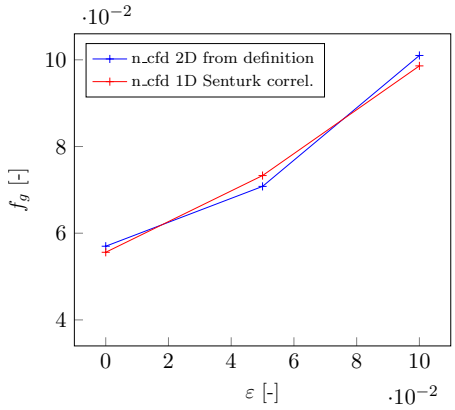

Figure 6.2: Evolution of the friction factor, obtained from Eq. (6.24), with relative element height for Calcs. 2D-00 to 2D-03 and 1D-00 to 1D-03.

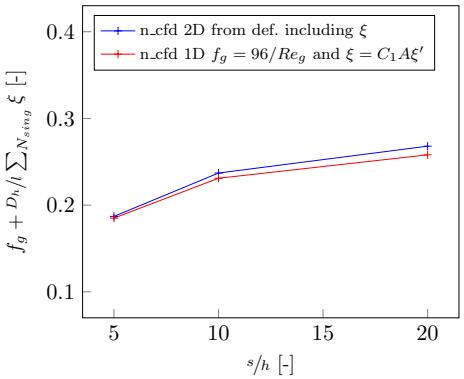

Figure 6.3: Evolution of the quantity $f_g + {}^{D_h}/l \sum_{N_{sing}} \xi$, obtained from Eq. (6.25), with relative element spacing for Calcs. 2D-04 to 2D-06 and 1D-04 to 1D-06.

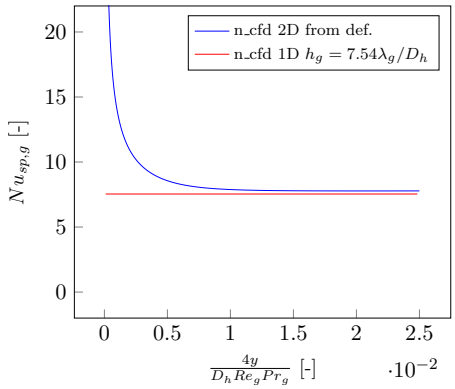

Figure 6.4: Evolution of the Nusselt number, obtained from Eq. (6.26), with ${}^{4y}/_{D_h Re_g Pr_g}$ for Calcs. 2D-00 1D-00.

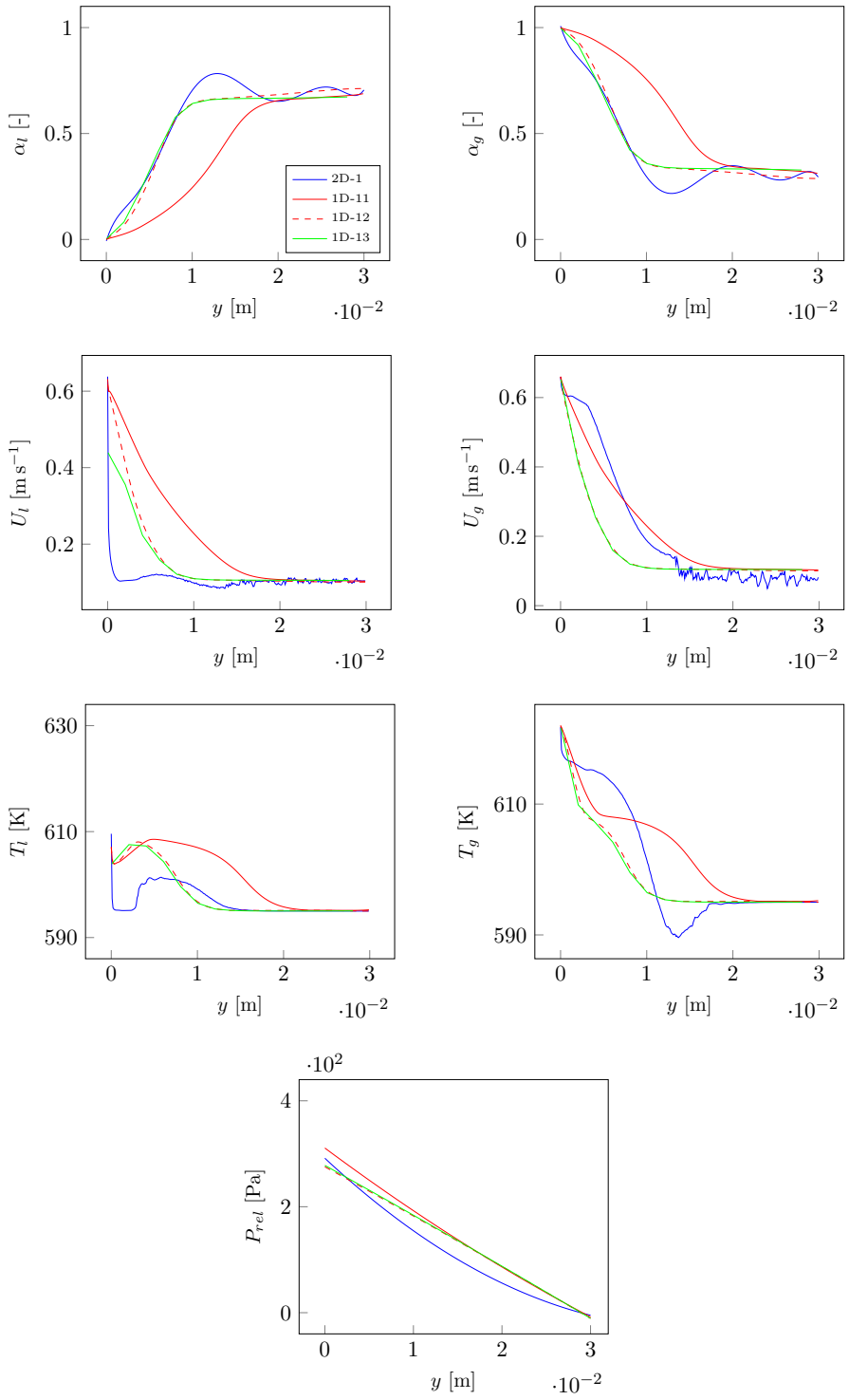

Figure 6.5: Evolution of the quantities α_g, α_l, $U_{g,y}$, $U_{l,y}$, T_g, T_l and P the y-coordinate for Calcs. 2D-1 and 1D-11 to 1D-13. For Calcs. 2D-1, the various quantities are averaged over the cross-section (x-direction) using the expressions given in Table 6.2.

is obtained between Case 2D-2 and Case 1D-21 for the pressure highlights the importance of taking into account the effect of roughness on dynamics via Eq. (6.12). In addition, the fact that a relatively good agreement is obtained between Case 2D-2 and Case 1D-23 and that a bad agreement is obtained between Case 2D-2 and Case 1D-22 for the liquid volume fraction underlines the importance of taking into account the effect of roughness on heat transfer with phase change via the correlations developed in the previous chapter for the weighting factors g_{cond}, $g_{sp,g}$ and $g_{sp,l}$ appearing in Eqs. (6.20) to (6.22). From Case 1D-23, we conclude that the 1D model is predictive in case of two-phase flow in rough rectilinear channel.

6.4.2 Low pressure

6.4.2.1 Smooth rectilinear

The averaged gas and liquid volume fractions, velocities and temperatures, as well as the pressure, are shown in Fig. 6.7 for Cases 2D-3 and 1D-3. Qualitatively speaking, both cases are found to be in good agreement, for all the quantities. Quantitatively speaking, a good agreement is obtained for the gas temperature and for the pressure, and also for the gas and the liquid volume fractions on the first halft of the channel and the liquid temperature on the second half of the channel. As previously in Sections 6.4.1.1 and 6.4.1.2, discrepancies are observed for the gas and liquid velocities on a large part of the domain and for the liquid temperature at the entrance. Again, for the velocities, this is attributed to the interfacial momentum transfer – reducing to the drag force in the present case – which is greater than expected.

6.4.2.2 Rough rectilinear

The cases considered in the present section are Cases 2D-4, 1D-3 and 1D-4. The average gas and liquid volume fractions, velocities and temperatures, as well as the pressure, are shown in Fig. 6.8. Quantitatively speaking, a relatively good agreement is obtained between Cases 2D-4 and 1D-4 for the liquid velocity, the gas temperature and the pressure. A good agreement is also obtained for the gas and liquid volume fractions in the middle of the domain and for the liquid temperature at the entrance. A bad agreement is obtained between Cases 2D-4 and 1D-3 for all the quantities, except the gas temperature. In particular, the liquid volume fraction and the pressure are found to be significantly underestimated on the whole domain. These results are consistent with those in Section 6.4.1.2, in the sense that the best 1D results are obtained when the effect of roughness on dynamics and heat transfer with phase change are taken into account – via Eq. (6.12) with ε different from zero for

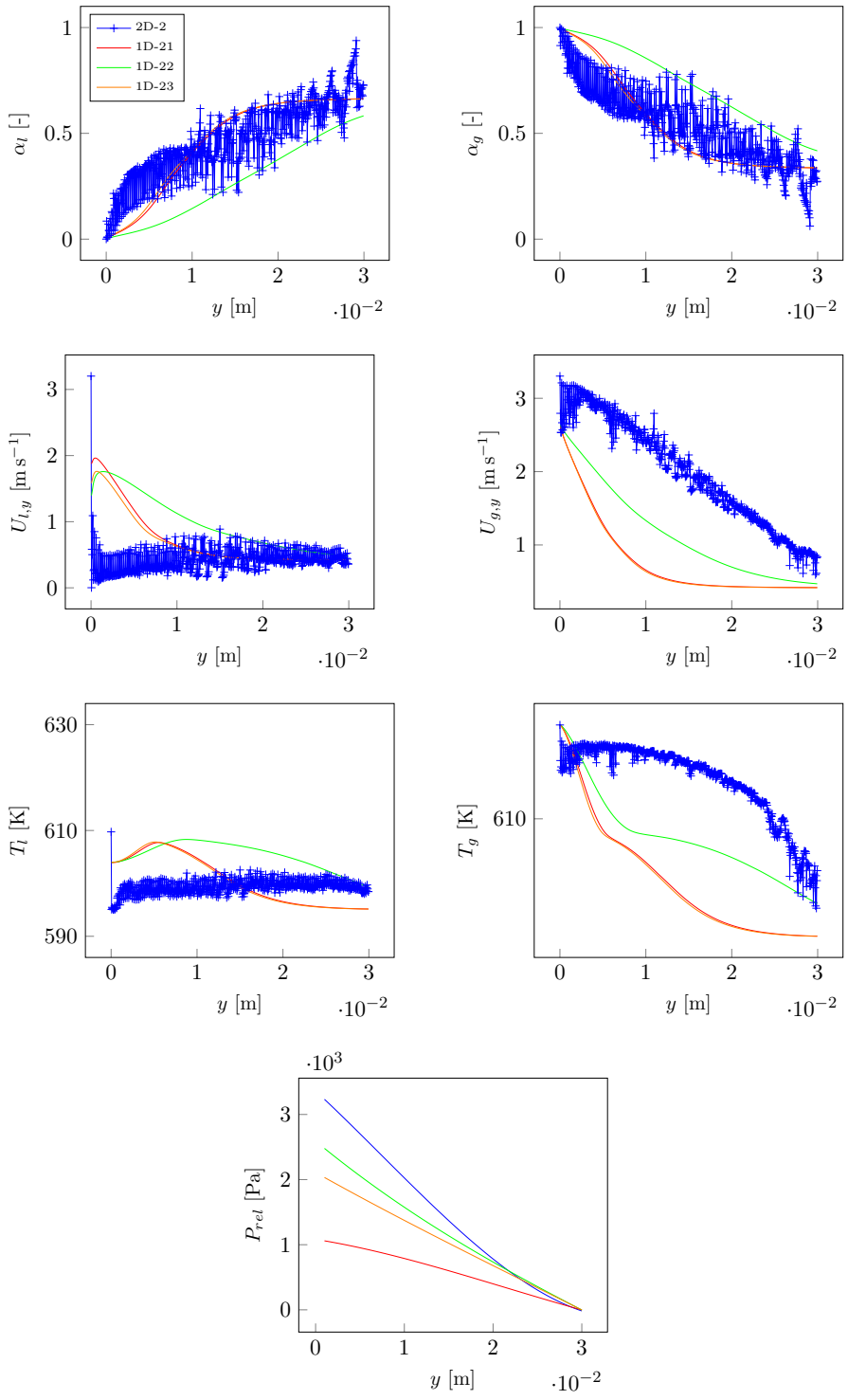

Figure 6.6: Evolution of the quantities α_g, α_l, $U_{g,y}$, $U_{l,y}$, T_g, T_l and P the y-coordinate for Calcs. 2D-2 and 1D-21 to 1D-23. For Calcs. 2D-2, the various quantities are averaged over the cross-section (x-direction) using the expressions given in Table 6.2.

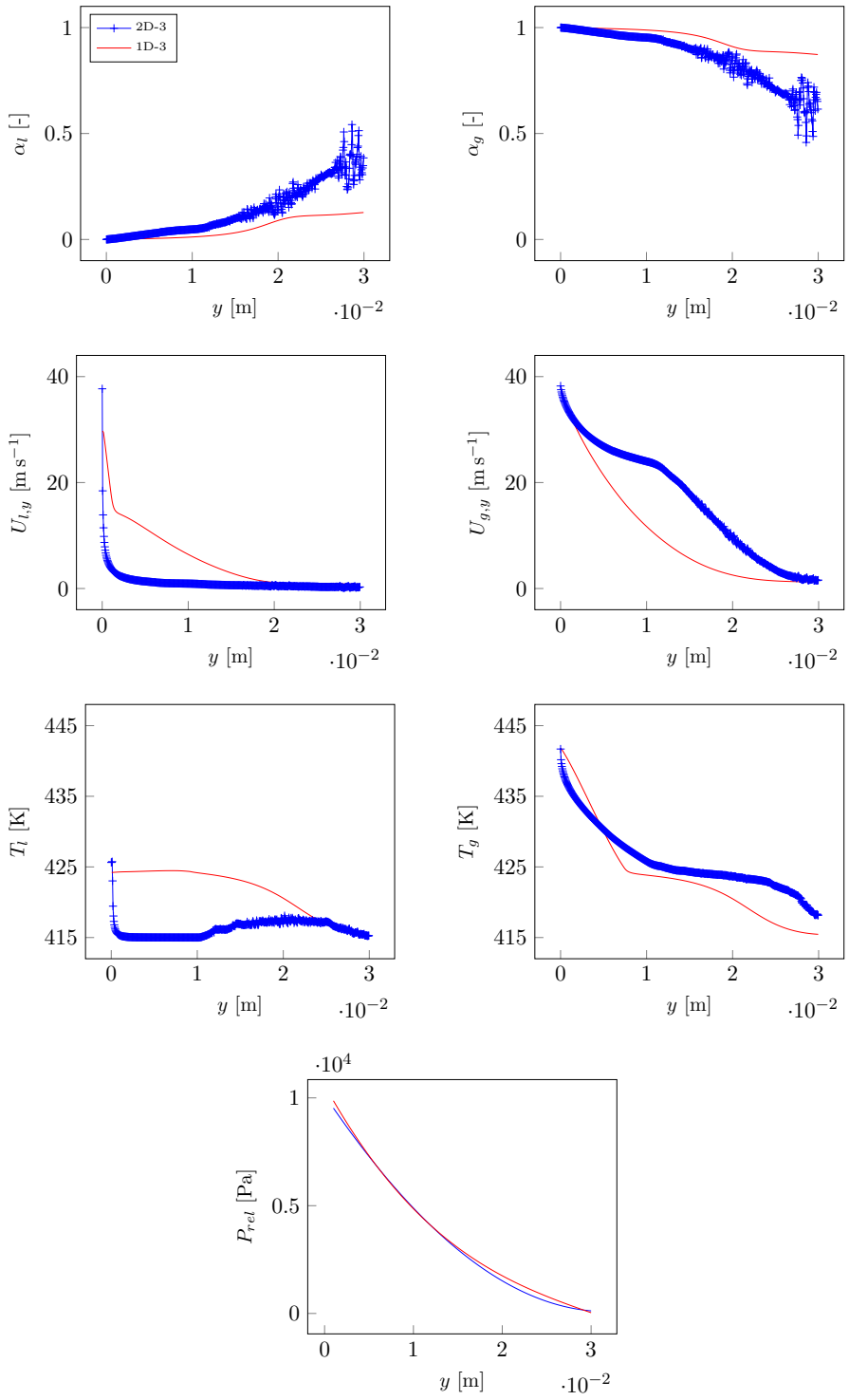

Figure 6.7: Evolution of the quantities α_g, α_l, $U_{g,y}$, $U_{l,y}$, T_g, T_l and P the y-coordinate for Calcs. 2D-3 and 1D-3. For Calcs. 2D-3, the various quantities are averaged over the cross-section (x-direction) using the expressions given in Table 6.2.

dynamics and via Eqs. (6.20) to (6.22) with g_{cond}, $g_{sp,g}$ and $g_{sp,l}$ different from unity for heat transfer with phase change.

6.5 Summary

A one-dimensional model for laminar condensing two-phase flow, allowing to take into account roughness and wettability, has been implemented in the neptune_cfd code. It was developed as an alternative to the FGLIM and the 4FM, which are computationally expensive and could hardly be used for industrial calculations, and to the in-house Ecrevisse code, which is based on the homogeneous flow assumption (and therefore cannot take into account the difference in velocity and temperature between the gas and the liquid) and does not account for the effect of roughness on dynamics and heat transfer with phase change in the laminar flow regime. A mass, a momentum and an energy balance equation is solved for the gas, as well as for the liquid. The equations are similar to those in the FGLIM and the 4FM, with the difference that they do not include the terms for viscous dissipation and heat conduction, and that momentum source terms are introduced for wall regular and singular friction. Wall regular friction is computed using the model of Lockhart and Martinelli (1947) and the correlations of Sentürk and Smits (2019); Zhang et al. (2010b). The interfacial mass, momentum and energy transfers, as well as the wall mass and energy transfers, are based on the Standard Dispersed Model for droplets. Roughness is taken into account by a specific term in the correlation of Sentürk and Smits (2019) and by additional weighting functions based on the correlations from Chapter 5 in the expressions of the wall energy transfers. Tortuosity is taken into account by wall singular friction, which is computed in a standard way.

The 1D model was verified against the FGLIM in 2D, in both smooth- and rough-wall conditions, and at both low and high pressures. The quantities considered were the gas and liquid volume fractions, velocities, temperatures, as well as the pressure. Qualitatively speaking, the 1D model was in good agreement with the FGLIM, for all the calculations performed and all the quantities considered. From a quantitative point of view, some significant discrepancies were found between the 1D model and the FGLIM, especially for the velocities, which was attributed to an underestimation of the interfacial momentum transfer. The impact of taking into account roughness was assessed by deactivating the corresponding terms and weighting functions in the equations for the transfer terms. As expected, the results obtained in these conditions were found to be in bad agreement with the FGLIM, especially for the volume fractions and the pressure.

Perspectives to the work presented in this chapter include investigations on the interfacial momentum transfer, to reduce the discrepancies observed on the velocities. The 1D

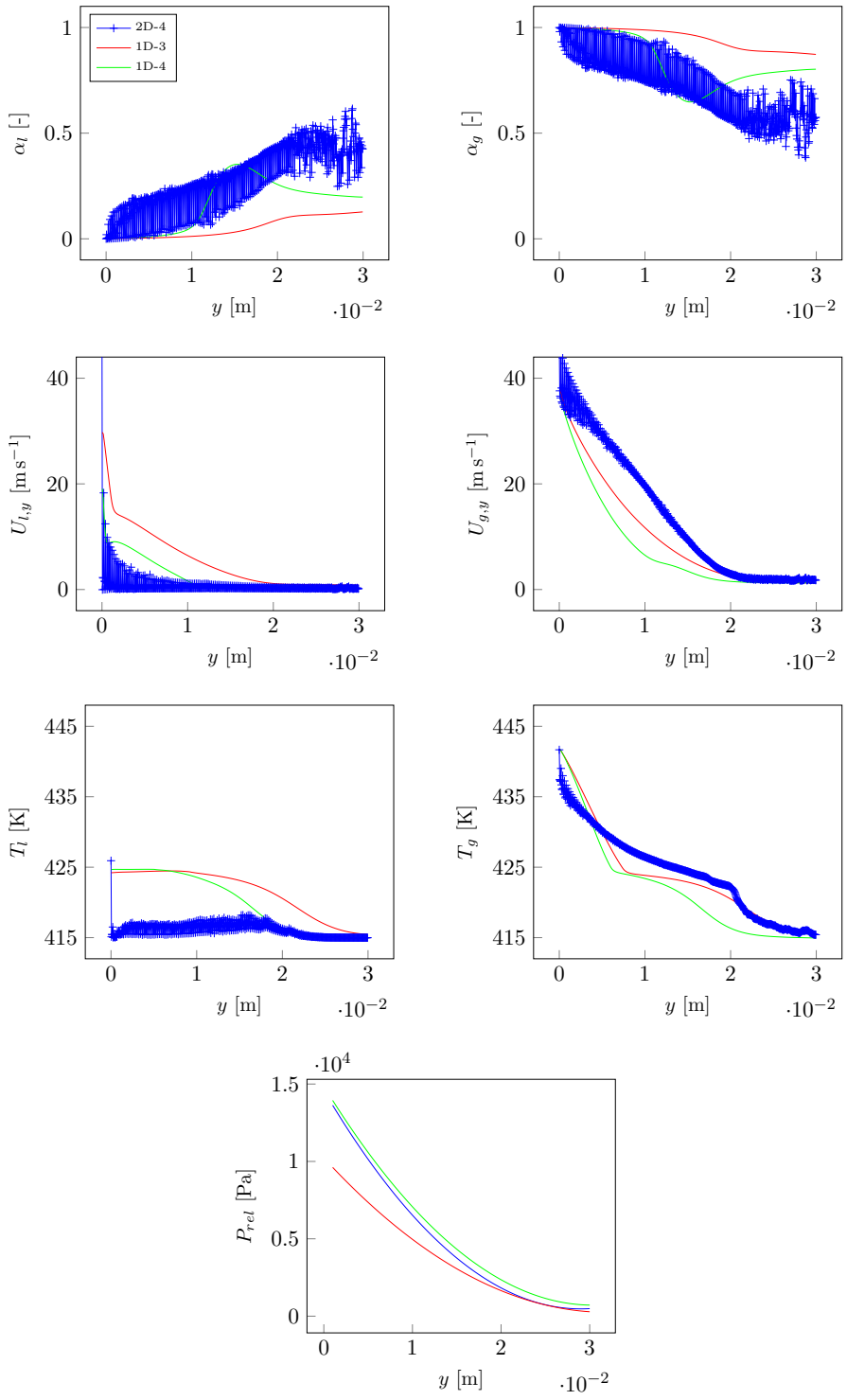

Figure 6.8: Evolution of the quantities α_g, α_l, $U_{g,y}$, $U_{l,y}$, T_g, T_l and P the y-coordinate for Calcs. 2D-4, 1D-3 and 1D-4. For Calcs. 2D-4, the various quantities are averaged over the cross-section (x-direction) using the expressions given in Table 6.2.

model should then be verified in tortuous-wall conditions, and in rough- and tortuous-wall conditions simultaneously. Comparisons between 1D and 3D calculations could also be made. As mentioned previously, one of the drawbacks of the 1D model in its current version is that it does not take into account surface tension and wettability. Source terms could therefore be developed for these two phenomena. Finally, the 1D model could be used for industrial-type calculations, to give an estimation of the leakage rate through a localized crack in the event of a loss-of-coolant accident.

Chapter 7

Conclusions and perspectives

Contents

7.1 Conclusions 172
7.2 Perspectives 174

7.1 Conclusions

This PhD took place in the framework of the CIWAP3 project (Civil Work Assessment Project 3), conducted by EDF R&D, aiming to refine the understanding of the various physical phenomena occurring in the walls of the concrete containment building in the event of a pressurized water reactor loss-of-coolant accident, namely steam condensation in the presence of air – in both the porous media and in localized cracks – and thermal dilatation. Concerning steam condensation, the experiments performed in the past have shown that this phenomenon usually results in a complex two-phase flow, with droplets of variable size, films and slugs. Also, the numerical simulations performed in the past have provided interesting but sometimes inconsistent results in terms of leakage rate. The main purpose of the PhD was to propose an finer modeling approach for the simulation of steam condensation in the presence of air in model cracks, and to implement it in EDF's in-house computational multi-fluid dynamics code neptune_cfd.

The choice has been made of coupling the two main Eulerian approaches for the simulation of two-phase flows, namely the interface capturing/tracking approach and the dispersed flow approach, the former allowing for the simulation of localized large interfaces spreading over several computational cells and the latter allowing for the simulation of dispersed droplets or bubbles of size comparable to the grid spacing. Two models resulting from such a coupling, allowing for flows with droplets, bubbles and large interfaces, were proposed. The first model, called Full Generalized Large Interface Model (FGLIM), is an extension of the Generalized Large Interface Model. It uses two computational fields: one for the gas and another for the liquid, each one being either dispersed or continuous. The second model, called Four-Field Model (4FM), is an extension of the three-field Large Bubble Model. It uses four computational fields: one for the dispersed gas, one for the continuous gas, one for the dispersed liquid and one for the continuous liquid. In comparison with the FGLIM, it has the advantage that a given cell can contain simultaneously dispersed droplets, dispersed bubbles and a portion of large interface.

The FGLIM and the 4FM were then validated against analytical and experimental data in various cases. These cases included one based on the experiments of Bhaga and Weber (1981), corresponding to the rise of a large bubble of air in a viscous liquid, one inspired from the well-known Stefan problem, corresponding to the displacement of a large interface due to direct contact condensation of steam in the presence of air, one based on the COPAIN facility, corresponding to the condensation of steam in the presence of air on a vertical plate, and one based on the BARTOLOMEI facility, corresponding to boiling of water in a circular channel. A parametric study was performed to select the optimal value of the parameters allowing to switch from the dispersed flow approach to the interface capturing approach.

The FGLIM was selected for use in the rest of the PhD, since, on the one hand, the planned simulations were expected to not involve cells containing simultaneously dispersed droplets, dispersed bubbles and large interfaces and, on the other hand, the model was found to be less computationally expensive than the 4FM.

The FGLIM was then used to simulate steam condensation in the presence of air in a smooth, rectilinear model crack/mini-channel. The purpose was to assess the ability of the model to correctly predict steam condensation with non-condensable gases at this scale and also to refine the understanding of the different physical phenomena involved. Low and high pressures were investigated. In both cases, the results were successfully compared with experimental correlations from the literature in terms of pressure drop and Nusselt number (dimensionless wall heat flux). The flow regime was found to vary according to the position in the channel and the various flow patterns were found to be consistent in nature with experiment. Numerically speaking, the model was found to require small time steps and therefore to result in large computation times, especially for the low pressures. It was concluded that, although it is predictive, it could hardly be used for industrial simulations. It was suggested that it could rather serve to develop correlations that could then be used in one-dimensional simulations, allowing for larger time steps.

The effects of roughness and tortuosity on small-scale laminar two-phase heat transfer with phase change was then investigated, using the FGLIM. The assumption was made of rectangular elements, with dimensions lower than the channel diameter in the case of roughness and larger than the channel diameter in the case of tortuosity. The roughness/ tortuosity elements were found to locally modify the various heat fluxes taking place at the wall, namely the condensation heat flux, the single-phase gas heat flux and the single-phase liquid heat flux. The ratio of spatially-averaged condensation flux for rough-wall conditions to spatially-average condensation flux for smooth-wall conditions was found to increase with roughness element height and Reynolds number and to decrease with roughness element spacing. A similar behavior was obtained for the same ratio in the case of the gas heat flux, while an opposite behavior was obtained for the same ratio in the case of the liquid heat flux. Correlations were proposed for these three ratios. In contrast, the ratios of average flux in tortuous-wall conditions to average flux in smooth-wall conditions were found to be approximately constant to unity, indicating that in average over the length tortuosity has no significant impact on heat transfer in the analyzed range of parameters.

Finally, a one-dimensional model was proposed as an alternative to the FGLIM and the 4FM for industrial calculations. The one-dimensional model proposed builds up on the correlations developed in three dimensions for the impact of roughness on dynamics and heat transfer with phase change in the laminar flow regime. It was verified against the FGLIM in various geometrical configurations, including one corresponding to a rectilinear

mini-channel with smooth walls, one corresponding to a rectilinear mini-channel with rough walls and one corresponding to a tortuous mini-channel with smooth walls.

The work on steam condensation in the presence of air in a smooth, rectilinear model cracks/mini-channel resulted in an article in a peer-reviewed *International Journal of Multiphase Flow*. In addition, the FGLIM was integrated to the standard version of the neptune_cfd code by the development team.

7.2 Perspectives

Some perspectives to the work summarized in the previous section are outlined hereafter. Extent the validation of the FGLIM and the 4FM at small-scale could constitute a first axis of improvement. In particular, the two models could be used to simulate the small-scale experiments of steam condensation in the presence of air that are currently being carried out by EDF R&D in the framework of the MACENA2 (MAnagement of the Containment of ENclosures in Accidents 2) project, in partnership with the 3SR laboratory (Sols, Solides, Structures, Risques, Université Grenoble Alpes), the I2M laboratory (Institut de Mécanique et d'Ingénierie, Université de Bordeaux) and the SIAME laboratory (Sciences pour l'Ingénieur Appliquées à la Mécanique et au génie Electrique, Université de Pau et des Pays de l'Adour).

Concerning the impact of roughness and tortuosity on small-scale laminar heat transfer with phase change, other roughness/tortuosity element shapes could be studied. Correlations similar to those proposed for rough mini-channels with rectangular roughness elements could be derived. Element shapes could also be mixed or roughness could be characterized by fractal geometry. One could also imagine reconstructing the walls from real rough surfaces by 3D imaging. The impact of roughness and tortuosity on heat transfer with phase change should also be investigated in three dimensions. However, this would considerably increase the number of calculations to perform for establishing correlations. Finally, roughness and tortuosity could be combined, in order to see if the coupled effect is equal to the sum of the individual effects.

The impact of wettability on small-scale heat transfer with phase change should be investigated, at first in the case of a smooth rectilinear model crack. At this scale, it is well known that wettability can have a significant impact on dynamics. However, little information about its impact on heat transfer with phase change is available in the literature. In the neptune_cfd code, a feature allowing to impose the contact angle made by a large (resolved) interface on the wall boundaries is already available. However, as the FGLIM and the 4FM also consider the case of dispersed droplets, an additional feature allowing to

implicitly take into account wettability for a non-resolved interface should be developed.

So far, wall conduction has been neglected, due to the fact that channels of reduced length were considered. In the future, the impact of wall heat conduction on dynamics and heat transfer with phase change should be investigated for large domain lengths, in industrial conditions, preferably by means of two- or three-dimensional simulations. No additional developments would be required since a feature for 1D wall conduction is already available in the neptune_cfd code. It would even be possible to perform 3D wall conduction, using the coupling with EDF's in-house Syrthès code.

As done for the FGLIM, the 4FM will be integrated in the standard version of the neptune_cfd code. These two models have been proposed in the framework of the CIWAP3 project, about containment tightness, but their field of application is in fact very wide. In particular, the FGLIM is planned to be used in a project on the behavior of fuel rods during the reflood phase of a loss-of-coolant accident. It could also be used in studies on the leakage through micro-cracks that can be formed by corrosion in the tubes of the steam generator located in the secondary circuit of the power plant. The model is expected to provide good results, since these cracks are characterized by a length of the order of the centimeter and the inlet pressure is about 155 bar, which are conditions that have also been studied in the PhD.

Bibliography

L. Bahr, J. Sievers, M. Zemann, and N. Herrmann. Simulation of steam/air leakage through small-scale cracked concrete specimen. *Eur. J. Environ. Civ. Eng.*, pages 1–12, 2021.

G. G. Bartolomei, V. G. Brantov, Y. S. Molochnikov, Y. V. Kharitonov, V. A. Solodkii, G. N. Batashova, and V. N. Mikhailov. An experimental investigation of true volumetric vapour content with subcooled boiling in tubes. *Therm. Eng.*, 29:132–135, 1982.

D. Bhaga and M. E. Weber. Bubbles in viscous liquids: shape, wakes and velocities. *J. Fluid Mech.*, 105:61–85, 1981.

H. Bian, Z. Sun, N. Zhang, Z. Meng, and M. Ding. A new modified diffusion boundary layer steam condensation model in the presence of air under natural convection conditions. *Int. J. Therm. Sci.*, 145:105948, 2019.

A. Bieberle, A. Moonesi Shabestary, T. Geissler, S. Boden, M. Beyer, and U. Hampel. Flow morphology and heat transfer analysis during high-pressure steam condensation in an inclined tube part I: Experimental investigations. *Nucl. Eng. Des.*, 361:110553, 2020.

T. Bonometti and J. Magnaudet. An interface-capturing method for incompressible two-phase flows. Validation and application to bubble dynamics. *Int. J. Multiph. Flow*, 33: 109–133, 2007.

J. Borchman. Heat transfer of high velocity vapor condensing in annuli. *ASHRAE Trans.*, 73, 1967.

J. U. Brackbill, D. B. Kothe, and C. Zemach. A continuum method for modeling surface tension. *J. Comput. Phys.*, 100:335–354, 1992.

T. P. Brackbill and S. G. Kandlikar. Effect of sawtooth roughness on pressure drop and turbulent transition in microchannels. *Heat Transf. Eng.*, 28:662–669, 2007.

N. Brauner and D. Moalem-Maron. Identification of the range of 'small diameters' conduits, regarding two-phase flow pattern transitions. *Int. Commun. Heat Mass Transf.*, 19:29–39, 1992.

V. P. Carey. *Liquid-vapor phase change phenomena: An introduction to the thermophysics of vaporization and condensation process in heat transfer equipment.* Hemisphere, 1992.

C. Caroli, N. Coulon, D. A. V. Morton, and M. M. R. Williams. Theoretical and experimental investigations on the leakage of steam, gas and aerosols through narrow cracks and capillaries. FISA-95 symposium on EU research on severe accidents, Luxembourg, Luxembourg, 1995.

G. P. Celata, M. Cumo, S. J. McPhail, and G. Zummo. Single-phase laminar and turbulent heat transfer in smooth and rough microtubes. *Microfluid. Nanofluid.*, 3:697–707, 2007.

L. Charpin, C. Toulemonde, A. Cherki El Idrissi, S. Michel-Ponnelle, A. Adia, and J.-M. Hénault. Contrat du projet CIWAP3 – Mise à jour 2020. Internal note 6125-2104-2020-01545-FR, EDF R&D, 2020.

J. C. Chato. Laminar condensation in horizontal and inclined tubes. *ASHRAE J.*, 4:52–60, 1962.

D. Chen, R. Cardinaels, and P. Moldenaers. Effect of confinement on droplet coalescence in shear flow. *Langmuir*, 25:12885–12893, 2009a.

M. Chen, Z. Yang, Y. Duan, Y. Chen, and D. Wu. Simulation of condensation flow in a rectangular microchannel. *Int. Commun. Heat Mass Transf.*, 76:60–69, 2014.

Y. Chen, C. Zhang, M. Shi, and G. P. Peterson. Role of surface roughness characterized by fractal geometry on laminar flow in microchannels. *Phys. Rev. E*, 80:026301, 2009b.

Y. Chen, P. Fu, C. Zhang, and M. Shi. Numerical simulation of laminar heat transfer in microchannels with rough surfaces characterized by fractal Cantor structures. *Int. J. Heat Fluid Flow*, 31:622–629, 2010.

X. Cheng, P. Bazin, P. Cornet, D. Hittner, J. D. Jackson, J. López Jiménez, A. Naviglio, F. Oriolo, and H. Petzold. Experimental data base for containment thermalhydraulic analysis. *Nucl. Eng. Des.*, 204:267–284, 2001.

D. Chisholm. A theoretical basis for the Lockhart-Martinelli correlation for two-phase flow. *Int. J. Heat Mass Transf.*, 10:1767–1778, 1967.

S. W. Churchill. Friction-factor equation spans all fluid-flow regimes. *Chem. Eng.*, 7:91–92, 1977.

R. Clift, J. R. Grace, and M. E. Weber. *Bubbles, drops and particles.* Academic Press, 1978.

C. F. Colebrook and C. M. White. Experiments with fluid friction in roughened pipes. *Proc. R. Soc. A: Math. Phys. Eng. Sci.*, 161:367–381, 1937.

K. Cornwell and P. A. Kew. Boiling in small parallel channels. In *Energy efficiency in process technology*. Elsevier Applied Science, 1993.

J.-L. Costaz. Confinement. Enceintes. In *Techniques de l'ingénieur Génie nucléaire*. Editions T.I., 1997.

P. Coste. A large interface model for two-phase CFD. *Nucl. Eng. Des.*, 255:38–50, 2013.

P. Coste and J. Lavieville. A two-phase approach to the PTS problem evaluated on COSI experiment. 16th International Conference on Nuclear Engineering (ICONE-16), Orlando, USA, 2008.

P. Coste and J. Lavieville. A wall function-like approach for two-phase CFD condensation modeling of the pressurized thermal shock. 13th International Topical Meeting on Nuclear Reactor Thermal Hydraulics (NURETH-13), Kanazawa, Japan, 2009.

A. Courtois. Prédiction du taux de fuite diffuse en situation d'épreuve des enceintes à double paroi – Application aux VD2, VD3 et VD4 de Belleville 1. Internal technical report ENGSDS050223, EDF SEPTEN, 2005.

G. Croce and P. D'Agaro. Numerical analysis of roughness effect on microtube heat transfer. *Superlattices and microstruct.*, 35:601–616, 2004.

G. Croce and P. D'Agaro. Numerical simulation of roughness effect on microchannel heat transfer and pressure drop in laminar flow. *J. Phys. D: Appl. Phys.*, 38:1518–1530, 2005.

E. Da Riva and D. Del Col. Effect of gravity during condensation of R134a in a circular minichannel. *Microgravity Sci. Technol.*, 23:87–97, 2011.

E. Da Riva and D. Del Col. Numerical simulation of laminar liquid film condensation in a horizontal circular minichannel. *J. Heat Transf.*, 134:051019, 2012.

E. Da Riva, D. Del Col, S. V. Garimella, and A. Cavallini. The importance of turbulence during condensation in a horizontal circular minichannel. *Int. J. Heat Mass Transf.*, 55: 3470–3481, 2012.

H. Darcy. *Recherches expérimentales relatives au mouvement de l'eau dans les tuyaux*. Mallet-Bachelier, 1857.

G. Davy, E. Reyssat, S. Vincent, and S. Mimouni. CFD modeling of two-phase flows in cracks. 8th Workshop on Computational Fluid Dynamics for Nuclear Reactor Safety (CFD4NRS-8), Paris, France, 2020.

G. Davy, E. Reyssat, S. Vincent, and S. Mimouni. Euler-Euler simulations of condensing two-phase flows in mini-channel: Combination of a sub-grid approach and an interface capturing approach. *Int. J. Multiph. Flow*, 149:103964, 2022.

A. De Santis, M. Colombo, B. C. Hanson, and M. Fairweather. A generalized multiphase modelling approach for multiscale flows. *J. Comput. Phys.*, 436:110321, 2021.

R. DeBar. Fundamentals of the KRAKEN code. Technical report UCIR-760, Lawrence Livermore National Laboratory, 1974.

N. G. Deen, E. Peters, J. T. Padding, and J. Kuipers. Review of direct numerical simulation of fluid–particle mass, momentum and heat transfer in dense gas–solid flows. *Chem. Eng. Sci.*, 116:710–724, 2014.

A. Dehbi, F. Janasz, and B. Bell. Prediction of steam condensation in the presence of noncondensable gases using a CFD-based approach. *Nucl. Eng. Des.*, 258:199–210, 2013.

R. Denèfle, S. Mimouni, J.-P. Caltagirone, and S. Vincent. Multifield hybrid approach for two-phase flow modeling – Part 1: Adiabatic flows. *Comput. Fluids*, 113:106–111, 2015.

R. Denèfle. *Modélisation locale diphasique eau-vapeur des écoulements dans les générateurs de vapeur*. PhD thesis, Université de Bordeaux 1, 2013.

J. D'Errico. MATLAB package Polyfitn for polynomial modeling in 1 or n dimensions. fr.mathworks.com/matlabcentral/fileexchange/34765-polyfitn, 2021. Accessed: 27 dec.

F. Dierich and P. A. Nikrityuk. A numerical study of the impact of surface roughness on heat and fluid flow past a cylindrical particle. *Int. J. Therm. Sci.*, 65:92–103, 2013.

M. K. Dobson and J. C. Chato. Condensation in smooth horizontal tubes. *J. Heat Transf.*, 120:193–213, 1998.

D. Drew. Mathematical modeling of two-phase flow. *Ann. Rev. Fluid Mech.*, 15:261–291, 1983.

EDF. Le nucléaire en chiffres. www.edf.fr/groupe-edf/espaces-dedies/l-energie-de-a-a-z/tout-sur-l-energie/produire-de-l-electricite/le-nucleaire-en-chiffres, 2021a. Accessed: 27 dec.

EDF. Le fonctionnement d'une centrale nucléaire. www.edf.fr/groupe-edf/espaces-dedies/l-energie-de-a-a-z/tout-sur-l-energie/produire-de-l-electricite/le-fonctionnement-d-une-centrale-nucleaire, 2021b. Accessed: 27 dec.

EDF. Finite element Code_Aster, Analysis of Structures and Thermomechanics for Studies and Research. www.code-aster.org, 2021c. Accessed: 27 dec.

P. Emonot, A. Souyri, J. L Grandrille, and F. Barré. CATHARE-3: A new system code for thermal-hydraulics in the context of the NEPTUNE project. *Nucl. Eng. Des.*, 241: 4476–4481, 2011.

B. S. Field and P. S. Hrnjak. Two-phase pressure drop and flow regime of refrigerants and refrigerant-oil mixtures in small channels. Technical report 261, ACRC, 2007.

S. Fleau. *Multifield approach and interface locating method for two-phase flows in nuclear power plant.* PhD thesis, Université Paris-Est, 2017.

S. Fleau, S. Mimouni, N. Mérigoux, and S. Vincent. Validation of multifield approach for the simulations of two-phase flows. *Comput. Therm. Sci.*, 7:441–457, 2015.

M. François, S. J. Cummins, E. D. Dendy, D. B. Kothe, J. M. Sicilian, and M. W. Williams. A balanced-force algorithm for continuous and sharp interfacial surface tension models within a volume tracking framework. *J. Comput. Phys.*, 213:141–173, 2006.

E. M. A. Frederix, D. Dovizio, A. Mathur, and E. M. J. Komen. All-regime two-phase flow modeling using a novel four-field large interface simulation approach. *Int. J. Multiph. Flow*, 145:103822, 2021.

V. H. Gada, M. P. Tandon, J. Elias, R. Vikulov, and S. Lo. A large scale interface multi-fluid model for simulating multiphase flows. *Appl. Math. Model.*, 44:189–204, 2017.

G. Gamrat, M. Favre-Marinet, S. Le Person, R. Bavière, and F. Ayela. An experimental study and modelling of roughness effects on laminar flow in microchannels. *J. Fluid Mech.*, 594:399–423, 2008.

G. Gamrat, M. Favre-Marinet, and S. Le Person. Modelling of roughness effects on heat transfer in thermally fully-developed laminar flows through microchannels. *Int. J. Therm. Sci.*, 48:2203–2214, 2009.

H. Ganapathy, A. Shooshtari, K. Choo, S. Dessiatoun, M. Alshehhi, and M. Ohadi. Volume of fluid-based numerical modeling of condensation heat transfer and fluid flow characteristics in microchannels. *Int. J. Heat Mass Transf.*, 65:62–72, 2013.

S. Ganesan and L. Tobiska. Computation of flows with interfaces using arbitrary Lagrangian-Eulerian method. 4th European Conference on Computational Fluid Dynamics (ECFD-4), Delft, The Netherlands, 2006.

A. Gobin, H. Neau, O. Simonin, J. R. Llinas, V. Reiling, and J. L. Selo. Fluid dynamic numerical simulation of a gas phase polymerization reactor. *Int. J. Numer. Methods Fluids*, 43:1199–1220, 2003.

S. Granet. Modélisation des essais SIMIBE avec le couplage Aster-Ecrevisse. Internal technical report H-T64-2014-02630-FR, EDF R&D, 2014.

S. Granet. Modélisation de la fuite en air-vapeur dans le cadre de l'expérience PACE. Internal technical report H-T65-2016-00193-FR, EDF R&D, 2016.

L. Granger, C. Y. Rieg, J. P. Touret, F. Fleury, G. Nahas, R. Danisch, L. Brusa, A. Millard, C. Laborderie, F. Ulm, P. Contri, K. Schimmelpfennig, F. Barré, M. Firnhaber, J. Gauvain, N. Coulon, L. M. C. Dutton, and A. Tuson. Containment Evaluation under Severe Accidents (CESA): synthesis of the predictive calculations and analysis of the first experimental results obtained on the Civaux mock-up. *Nucl. Eng. Des.*, 209:155–163, 2001.

U. Greiner and W. Ramm. Air leakage characteristics in cracked concrete. *Nucl. Eng. Des.*, 156:167–172, 1995.

P. Griffith and G. A. Synder. The bubble-slug transition in a high velocity two phase flow. Technical report 5003-29 (TID-20947), MIT, 1964.

S. Grohmann. Measurement and modeling of single-phase and flow-boiling heat transfer in microtubes. *Int. J. Heat Mass Transf.*, 48:4073–4089, 2005.

A. Guelfi, D. Bestion, M. Boucker, P. Boudier, P. Fillion, M. Grandotto, J. M. Hérard, E. Hervieu, and P. Péturaud. NEPTUNE: A new software platform for advanced nuclear thermal hydraulics. *Nucl. Sci. Eng.*, 156:281–324, 2007.

D. J. Gunn. Transfer of heat or mass to particles in fixed and fluidised beds. *Int. J. Heat Mass Transf.*, 21:467–476, 1978.

S. Hänsch, D. Lucas, E. Krepper, and T. Höhne. A multi-field two-fluid concept for transitions between different scales of interfacial structures. *Int. J. Multiph. Flow*, 47:171–182, 2012.

N. Herrmann, H. S. Müller, C. Niklasch, S. Michel-Ponnelle, and B. Masson. The PACE-1450 test campaign – Leakage behaviour of a pre-stressed concrete containment wall segment. *Key Eng. Mater.*, 711:863–870, 2016.

C. Hervouet. Simulation d'écoulement air/eau/vapeur à travers une fissure : logiciel ECREVISSE version 3.0 – Note de principe. Internal technical report HI-86/04/005/A, EDF R&D, 2004.

C. Hervouet. Amélioration des modèles de perte de charge et d'échange de chaleur du code ECREVISSE 3.2. Internal technical report H-I81-2011-00919-FR, EDF R&D, 2012.

H. Herwig, D. Gloss, and T. Wenterodt. A new approach to understanding and modelling the influence of wall roughness on friction factors for pipe and channel flows. *J. Fluid Mech.*, 613:35–53, 2008.

J. O. Hinze. Fundamentals of the hydrodynamic mechanism of splitting in dispersion processes. *AIChE J.*, 1:289–295, 1955.

C. W. Hirt and B. D. Nichols. Volume of fluid (VOF) method for the dynamics of free boundaries. *J. Comput. Phys.*, 39:201–225, 1981.

C. W. Hirt, A. A. Amsden, and J. L. Cook. An arbitrary Lagrangian-Eulerian computing method for all flow speeds. *J. Comput. Phys.*, 135:203–216, 1997.

F.-G. Ho and S. Striender. A variational calculation of the effective surface diffusion coefficient and tortuosity. *Chem. Eng. Sci.*, 36:253–258, 1981.

T. Höhne and C. Vallée. Experiments and numerical simulations of horizontal two-phase flow regimes using an interfacial area density model. *J. Comput. Multiph. Flows*, 2: 131–143, 2010.

J. S. Hu and C. Y. H. Chao. An experimental study of the fluid flow and heat transfer characteristics in micro-condensers with slug-bubbly flow. *Int. J. Refrig.*, 30:1309–1318, 2007.

Y. W. Hwang and M. S. Kim. The pressure drop in microtubes and the correlation development. *Int. J. Heat Mass Transf.*, 49:1804–1812, 2006.

I. E. Idel'cik. *Memento des pertes de charge*. Eyrolles, 1969.

F. P. Incropera, D. P. DeWitt, T. L. Bergman, , and A. S. Lavine. *Fundamentals of heat and mass transfer*. Wiley, 2007.

D. C. Ipsen. *Units, dimensions, and dimensionless numbers*. McGraw-Hill, 1960.

IRSN. Parc des réacteurs nucléaires français en exploitation. www.irsn.fr/FR/connaissances/Installations_nucleaires/Les-centrales-nucleaires/reacteurs-nucleaires-France/Pages/0-sommaire-parc-reacteurs-nucleaires-France.aspx, 2021a. Accessed: 27 dec.

IRSN. Fonctionnement d'un réacteur nucléaire. www.irsn.fr/FR/connaissances/Installations_nucleaires/Les-centrales-nucleaires/reacteurs-nucleaires-

France/Pages/1-reacteurs-nucleaires-France-Fonctionnement.aspx, 2021b. Accessed: 27 dec.

IRSN. Visites décennales. www.irsn.fr/FR/connaissances/Installations_nucleaires/Les-centrales-nucleaires/visites-decennales/Pages/0-Sommaire-Reexamens-periodiques-des-reacteurs-nucleaires-et-visites-decennales.aspx, 2021c. Accessed: 27 dec.

M. Ishii. *Thermo-fluid dynamic theory of two-phase flow*. Eyrolles, 1975.

M. Ishii and N. Zuber. Drag coefficient and relative velocity in bubbly, droplet or particulate flows. *AIChE J.*, 25:843–855, 1979.

S. S. Jain. Flow-induced breakup of drops and bubbles. Preprint, arXiv:1701.06157, 2017.

Y. Ji, K. Yuan, and J. N. Chung. Numerical simulation of wall roughness on gaseous flow and heat transfer in a microchannel. *Int. J. Heat Mass Transf.*, 49:1329–1339, 2006.

S. G. Kandlikar, S. Joshi, and S. Tian. Effect of surface roughness on heat transfer and fluid flow characteristics at low reynolds numbers in small diameter tubes. *Heat Transf. Eng.*, 24:4–16, 2003.

S. G. Kandlikar, D. J. Schmitt, A. L. Carrano, and J. B. Taylor. Characterization of surface roughness effects on pressure drop in single-phase flow in minichannels. *Phys. Fluids*, 17: 100606, 2005.

M. Kang, R. Fedkiw, and X.-D. Liu. A boundary condition capturing method for multiphase incompressible flow. *J. Sci. Comput.*, 15:323–360, 2000.

N. Kaushik and N. Z. Azer. A general heat transfer correlation for condensation inside internally finned tubes. *ASHRAE Trans.*, 94:261–279, 1988.

W. M. Kays and M. E. Crawford. *Convection heat and mass transfer*. McGraw-Hill, 1993.

S.-M. Kim and I. Mudawar. Universal approach to predicting two-phase frictional pressure drop for adiabatic and condensing mini/micro-channel flows. *Int. J. Heat Mass Transf.*, 55:3246–3261, 2012.

S.-M. Kim, J. Kim, and I. Mudawar. Flow condensation in parallel micro-channels – Part 1: Experimental results and assessment of pressure drop correlations. *Int. J. Heat Mass Transf.*, 55:971–983, 2012.

B. Lalanne, L. Rueda Villegas, and S. Tanguy. On the computation of viscous terms for incompressible two-phase flows with Level Set/Ghost Fluid Method. *J. Comput. Phys.*, 301:289–307, 2015.

J. Lavieville, N. Mérigoux, M. Guingo, C. Baudry, and S. Mimouni. A generalized turbulent dispersion model for bubbly flow numerical simulation in NEPTUNE_CFD. *Nucl. Eng. Des.*, 312:284–293, 2017.

C. K. Law. *Combustion physics*. Cambridge University Press, 2006.

C. Leau. Physical and numerical modeling of diphasic flows – Dimensionless number-based approach of fluid pattern flow prediction. Master's thesis, ESPCI Paris, 2020.

W. H. Lee. A pressure iteration scheme for two-phase flow modeling. In *Multi-phase transport: Fundamentals, reactor safety, applications*. Hemisphere, 1980.

W. Li and Z. Wu. A general correlation for adiabatic two-phase pressure drop in micro/mini-channels. *Int. J. Heat Mass Transf.*, 53:2732–2739, 2010.

Z. Li, Y. L. He, G. H. Tang, and W. Q. Tao. Experimental and numerical studies of liquid flow and heat transfer in microtubes. *Int. J. Heat Mass Transf.*, 50:3447–3460, 2007.

J. H. Lienhard IV and J. H. Lienhard V. *A heat transfer textbook*. Phlogiston Press, 2017.

Y. Liu, J. Li, and A. J Smits. Roughness effects in laminar channel flow. *J. Fluid Mech.*, 876:1129–1145, 2019.

Z. Liu, C. Zhang, Y. Huo, and X. Zhao. Flow and heat transfer in rough micro steel tubes. *Exp. Heat Transf.*, 20:289–306, 2007.

R. W. Lockhart and R. C. Martinelli. Proposed correlation of data for isothermal two-phase, two-component flow in pipes. *Chem. Eng. Prog.*, 45:39–48, 1947.

R. Manceau and K. Hanjalić. Elliptic blending model: A new near-wall Reynolds-stress turbulence closure. *Phys. Fluids*, 14:744–754, 2002.

M. Manninen, V. Taivassalo, and S. Kallio. On the mixture model for multiphase flow. Technical report 288, VTT Technical Research Centre of Finland, 1996.

E. Manon. *Contribution à l'analyse et à la modélisation locale des écoulements bouillants sous-saturés dans les conditions des Réacteurs à Eau sous Pression*. PhD thesis, Ecole Centrale Paris, 2000.

S. Márques Damián. *An extended mixture model for the simultaneous treatment of short and long scale interfaces*. PhD thesis, Universidad Nacional del Litoral, 2013.

H. Marschall and O. Hinrichsen. Numerical simulation of multi-scale two-phase flows using a hybrid interface-resolving two-fluid model (HIRES-TFM). *J. Chem. Eng. Japan*, 46: 517–523, 2013.

R. C. Martinelli and B. Nelson. Prediction of pressure drop during forced-circulation boiling water. *Trans. ASME*, 70:695–702, 1948.

A. Mathur, D. Dovizio, E. M. A. Frederix, and E. M. J. Komen. A Hybrid Dispersed-Large Interface Solver for multi-scale two-phase flow modelling. *Nucl. Eng. Des.*, 344:69–82, 2019.

S. Mer, O. Praud, H. Neau, N. Mérigoux, J. Magnaudet, and V. Roig. The emptying of a bottle as a test case for assessing interfacial momentum exchange models for Euler–Euler simulations of multi-scale gas-liquid flows. *Int. J. Multiph. Flow*, 106:109–124, 2018.

W. E. Mercer, W. M. Pearce, and J. E. Hitchcock. Laminar forced convection in the entrance region between parallel flat plates. *J. Heat Transf.*, 89:251–256, 1967.

N. Mérigoux, J. Lavieville, S. Mimouni, M. Guingo, and C. Baudry. A generalized large interface to dispersed bubbly flow approach to model two-phase flows in nuclear power plant. 6th Workshop on Computational Fluid Dynamics for Nuclear Reactor Safety (CFD4NRS-6), Cambridge, USA, 2016.

S. Mimouni, J.-S. Lamy, J. Lavieville, S. Guieu, and M. Martin. Modelling of sprays in containment applications with a CMFD code. *Nucl. Eng. Des.*, 240:2260–2270, 2010.

S. Mimouni, A. Foissac, and J. Lavieville. CFD modelling of wall steam condensation by a two-phase flow approach. *Nucl. Eng. Des.*, 241:4445–4455, 2011.

S. Mimouni, S. Fleau, and S. Vincent. CFD calculations of flow pattern maps and LES of multiphase flows. *Nucl. Eng. Des.*, 321:118–131, 2017.

S. Mimouni, P. Baconnier, and G. Davy. Overview of mitigation models dedicated to severe accidents and consequences on flow rate through concrete containment structures. 18th International Topical Meeting on Nuclear Reactor Thermal Hydraulics (NURETH-18), Portland, USA, 2019.

K. Mishima and T. Hibiki. Some characteristics of air-water two-phase flow in small diameter vertical tubes. *Int. J. Multiph. Flow*, 22:703–712, 1996.

L. F. Moody. Friction factors for pipe flow. *Trans. ASME*, 66:671–678, 1944.

A. Moonesi Shabestary, A. Bieberle, D. von der Cron, W. Ding, E. Krepper, D. Lucas, and U. Hampel. Flow morphology and heat transfer analysis for high-pressure steam condensation in an inclined tube part II: Numerical investigations. *Nucl. Eng. Des.*, 362: 110580, 2020.

J. S. Murallidharan, B. V. S. S. S. Prasad, B. S. V. Patnaik, G. F. Hewitt, and V. Badalassi. CFD investigation and assessment of wall heat flux partitioning model for the prediction of high pressure subcooled flow boiling. *Int. J. Heat Mass Transf.*, 103:211–230, 2016.

W. F. Noh and P. Woodward. SLIC (Simple Line Interface Calculation). In *Proceedings of the 5th International Conference on Numerical Methods in Fluid Dynamics*, pages 330–340, 1976.

W. Nusselt. Die oberflachenkondensation des wasserdampfes. *Z. Ver. D. Ing.*, 60:541–546, 1916.

E. S. Oran and J. P. Boris. Detailed modelling of combustion systems. *Prog. Energy Combust. Sci.*, 7:1–72, 1981.

S. Osher and J. Sethian. Fronts propagating with curvature-dependent speed: Algorithms based on Hamilton-Jacobi formulations. *J. Comput. Phys.*, 79:12–49, 1988.

R. K. Pal and R. K. K. Thermo-hydrodynamic modeling of flow boiling through the horizontal tube using Eulerian two-fluid modeling approach. *Int. J. Heat Mass Transf.*, 168: 120794, 2021.

A. E. Perry, W. H. Schofield, and P. N. Joubert. Rough wall turbulent boundary layers. *J. Fluid Mech.*, 37:383–413, 1969.

G. Pianet, S. Vincent, J. Leboi, J. P. Caltagirone, and M. Anderhuber. Simulating compressible gas bubbles with a smooth volume tracking 1-Fluid method. *Int. J. Multiph. Flow*, 36:273–283, 2010.

S. Popinet and S. Zaleski. A front tracking algorithm for accurate representation of surface tension. *Int. J. Numer. Methods Fluids*, 30:775–793, 1999.

W. Qu, G. M. Mala, and D. Li. Heat transfer for water flow in trapezoidal silicon microchannels. *Int. J. Heat Mass Transf.*, 43:3925–3936, 2000.

W. E. Ranz and W. R. Marshall. Evaporation from drops. *Chem. Eng. Prog.*, 48:141–146, 1952.

G. Rastiello. *Influence de la fissuration sur le transfert de fluides dans les structures en béton : stratégies de modélisation probabiliste et étude expérimentale.* PhD thesis, Université Paris-Est, 2013.

G. Rastiello, S. Leclaire, R. Belarbi, and R. Bennacer. Unstable two-phase flow rate in micro-channels and cracks under imposed pressure difference. *Int. J. Multiph. Flow*, 77: 131–141, 2015.

République française. Journal officiel. www.legifrance.gouv.fr/jorf/jo, 2021. Accessed: 27 dec.

P. Ruyer, N. Seiler, M. Weiss, and F. P. Weiss. A bubble size distribution model for the simulation of bubbly flows. 6th International Conference on Multiphase Flow (ICMF-6), Leipzig, Germany, 2007.

G. Ryskin and L. G. Leal. Numerical solution of free-boundary problems in fluid mechanics. Part 1. The finite-difference technique. *J. Fluid Mech.*, 148:1–17, 1984.

Y. Sato and B. Ničeno. A sharp-interface phase change model for a mass-conservative interface tracking method. *J. Comput. Phys.*, 249:127–161, 2013.

D. J. Schmitt and S. G. Kandlikar. Effects of repeating microstructures on pressure drop in rectangular minichannels. 3rd International Conference on Microchannels and Minichannels (ICMM-3), Toronto, Canada, 2005.

U. Sentürk and A. J Smits. Roughness effects in laminar pipe flow. Preprint, arXiv:1905.12479, 2019.

M. M. Shah. An improved and extended general correlation for heat transfer during condensation in plain tubes. *HVAC&R Res.*, 15:889–913, 2009.

S. Shen, J. L. Xu, J. J. Zhou, and Y. Chen. Flow and heat transfer in microchannels with rough wall surface. *Energy Convers. Manag.*, 47:1311–1325, 2006.

H. Simon, N. Tomassian, N. Coulon, and G. Nahas. A model for two-phase flow through small opening cracks. 4th European Thermal Sciences Conference, Birmingham, UK, 2004.

H. Simon, G. Nahas, and N. Coulon. Air–steam leakage through cracks in concrete walls. *Nucl. Eng. Des.*, 237:1786–1794, 2007.

A. Singh, M. M. Ohadi, and S. V. Dessiatoun. Empirical modeling of stratified-wavy flow condensation heat transfer in smooth horizontal tubes. *ASHRAE Trans.*, 102:596–603, 1996.

M. Stegemann, B. Masson, L. Coudert, J.-P. Touret, N. Herrmann, and L. Stempniewski. Experimental investigation of the leakage behaviour of reinforced concrete walls. 18th International Conference on Structural Mechanics in Reactor Technology (SMiRT-18), Beijing, China, 2005.

M. Suo and P. Griffith. Two-phase flow in capillary tubes. *J. Basic Eng.*, 86:576–582, 1964.

M. Sussman and E. G. Puckett. A coupled level-set and volume-of-fluid method for computing 3D axisymmetric incompressible two-phase flow. *J. Comput. Phys.*, 162:301–337, 2000.

Y. Taitel, D. Bornea, and A. E. Dukler. Modelling flow pattern transition for steady upward gas-liquid flow in vertical tubes. *AIChE J.*, 26:345–354, 1980.

S. Tanguy, M. Sagan, B. Lalanne, F. Couderc, and C. Colin. Benchmarks and numericals methods for the simulation of boiling flows. *J. Comput. Phys.*, 264:1–22, 2014.

M. Tavares. *Simulation et modélisation multi-échelle d'écoulements diphasiques*. PhD thesis, Université Paris-Est, 2019.

J. B. Taylor, A. L. Carrano, and S. G. Kandlikar. Characterization of the effect of surface roughness and texture on fluid flow – past, present, and future. *Int. J. Therm. Sci.*, 45: 962–968, 2006.

A. Tomiyama, H. Tamai, I. Zun, and S. Hosokawa. Transverse migration of single bubbles in simple shear flows. *Chem. Eng. Sci.*, 57:1849–1858, 2002.

S. O. Unverdi and G. Tryggvason. A front-tracking method for viscous, incompressible, multi-fluid flows. *J. Comput. Phys.*, 100:25–37, 1992.

G. Černe, S. Petelin, and I. Tiselj. Coupling of the interface tracking and the two-fluid models for the simulation of incompressible two-phase flow. *J. Comput. Phys.*, 171:776–804, 2001.

L. Štrubelj and I. Tiselj. Two-fluid model with interface sharpening. *Int. J. Numer. Meth. Eng.*, pages 575–590, 2011.

R. N. Wagner and S. G. Kandlikar. Effects of structured roughness on fluid flow at the microscale level. *Heat Transf. Eng.*, 33:483–493, 2012.

W. W. Wang, T. D. Radcliff, and R. N. Christensen. A condensation heat transfer correlation for millimeter-scale tubing with flow regime transition. *Exp. Therm. Fluid Sci.*, 26: 473–485, 2002.

J. Weisbach. *Lehrbuch der Ingenieur- und Maschinen-Mechanik. Erster Theil: Theoretische Mechanik*. Friedrich Vieweg & Sohn, 1850.

Wikipedia. PWR nuclear power plant diagram. en.wikipedia.org/wiki/File:PWR_nuclear_power_plant_diagram.svg, 2021. Accessed: 27 dec.

M. Wilson and H. Jacobs. A numerical solution of the heat transfer from a dense array of spherical particles. In *Proceedings of the 7th National Heat Transfer Conference*, pages 225–233, 1993.

C. Wu and P. Cheng. Condensation flow patterns in silicon microchannels. *Int. J. Heat Mass Transf.*, 48:2186–2197, 2005.

H. Y. Wu and P. Cheng. An experimental study of convective heat transfer in silicon microchannels with different surface conditions. *Int. J. Heat Mass Transf.*, 46:2547–2556, 2003.

P. Y. Wu and W. A. Little. Measurement of friction factors for the flow of gases in very fine channels used for microminiature Joule-Thomson refrigerators. *Cryogenics*, 23:273–277, 1983.

K. Yan and D. Che. A coupled model for simulation of the gas-liquid two-phase flow with complex flow patterns. *Int. J. Multiph. Flow*, 36:333–348, 2010.

Z. Yin, Y. Guo, B. Suden, Q. Wang, and M. Zeng. Numerical simulation of laminar film condensation in a horizontal minitube with and without non-condensable gas by the VOF method. *Numer. Heat Transf. A: Appl.*, 68:958–977, 2015.

M. Zare and S. H. Hashemabadi. CFD simulation and experimental validation of tortuosity effects on pellet-fluid heat transfer of regularly stacked multi-lobe particles. *Chem. Eng. J.*, 361:1543–1556, 2019.

C. Zhang, Y. Chen, and M. Shi. Effects of roughness elements on laminar flow and heat transfer in microchannels. *Chem. Eng. Process.: Process Intensif.*, 49:1188–1192, 2010a.

J. Zhang, W. Li, and W. J. Minkowycz. Numerical simulation of condensation for R410A at varying saturation temperatures in mini/micro tubes. *Numer. Heat Transf. A: Appl.*, 69:464–478, 2016a.

J. Zhang, W. Li, and S. A. Sherif. A numerical study of condensation heat transfer and pressure drop in horizontal round and flattened minichannels. *Int. J. Therm. Sci.*, 106: 80–93, 2016b.

J. Zhang, W. Li, and W. J. Minkowycz. Numerical simulation of R410A condensation in horizontal microfin tubes. *Numer. Heat Transf. A: Appl.*, 71:361–376, 2017.

W. Zhang, T. Hibiki, and K. Mishima. Correlations of two-phase frictional pressure drop and void fraction in mini-channel. *Int. J. Heat Mass Transf.*, 53:453–465, 2010b.

Z. Zhao, Y. Zhang, X. Chen, X. Ma, S. Yanga, and S. Li. A numerical study on condensation flow and heat transfer of refrigerant in minichannels of printed circuit heat exchanger. *Int. J. Refrig.*, 102:96–111, 2015.

N. Zuber. On the dispersed two-phase flow in the laminar flow regime. *Chem. Eng. Sci.*, 19:897–917, 1964.

Appendix A

Stefan with NCG

A.1 Prerequisites

The apparent, intrinsic and mixture densities read

$$\tilde{\rho}_i = \lim_{V\to 0} \frac{m_i}{V}\,, \quad \rho_i = \lim_{V\to 0} \frac{m_i}{V_i}\,, \quad \rho = \lim_{V\to 0} \frac{m}{V}\,. \tag{A.1}$$

These quantities are not independent since

$$\rho_i = \lim_{V\to 0} \frac{m_i}{V_i} = \lim_{V\to 0} \left(\frac{m_i}{V}\frac{V}{V_i}\right) = \frac{\tilde{\rho}_i}{\alpha_i}\,, \tag{A.2}$$

$$\rho = \lim_{V\to 0} \frac{m}{V} = \lim_{V\to 0} \frac{\sum_i m_i}{V} = \sum_i \tilde{\rho}_i = \sum_i \rho_i \alpha_i\,. \tag{A.3}$$

Assuming the gases to be ideal, Amagat's law allows writing that

$$\alpha_i = \frac{V_i}{V} = \frac{P_i}{P} = X_i\,. \tag{A.4}$$

It follows from Eqs. (A.2) to (A.4) that

$$Y_i = \frac{\tilde{\rho}_i}{\sum_j \tilde{\rho}_j} = \frac{\rho_i \alpha_i}{\sum_j \rho_j \alpha_j} = \frac{\rho_i}{\rho}\alpha_i = \frac{\rho_i}{\rho} X_i\,, \tag{A.5}$$

and from Eqs. (A.3) and (A.5) that

$$\frac{dY_i}{dx} = \frac{dY_i}{dX_i}\frac{dX_i}{dx} = \frac{d}{dX_i}\left(\frac{\rho_i}{\rho}X_i\right)\frac{dX_i}{dx} = \frac{\rho_i \rho_j}{\rho^2}\frac{dX_i}{dx}\,. \tag{A.6}$$

A.2 Assumptions

1. Eqs. (A.7), (A.10) and (A.11) are derived assuming the process to be quasi-static.[1]
2. Eq. (A.18) is derived assuming the liquid density to be constant.

A.3 Analytical solution

On the one hand, from liquid energy conservation,

$$\frac{d}{dx}\left(\lambda_l \frac{dT_l}{dx}\right) = 0\,. \tag{A.7}$$

Integrating Eq. (A.7) once yields

$$\frac{dT_l}{dx} = \frac{T_\gamma - T_w}{x_\gamma}\,. \tag{A.8}$$

It follows from Fourier's law and Eq. (A.8) that

$$j_\gamma = \frac{q_l}{L} = -\frac{\lambda_l}{L}\frac{dT_l}{dx} = \frac{\lambda_l}{L}\frac{T_w - T_\gamma}{x_\gamma}\,. \tag{A.9}$$

On the other hand, from gas (total and partial) mass conservation,

$$\frac{d}{dx}\left(\rho_g U_g\right) = 0\,, \tag{A.10}$$

$$\frac{d}{dx}\left(\rho_g U_g Y_a - \rho_g D \frac{dY_a}{dx}\right) = 0\,. \tag{A.11}$$

Integrating Eq. (A.10) yields

$$\rho_g U_g = j_\gamma\,, \tag{A.12}$$

and substituting Eq. (A.12) in Eq. (A.11) yields

$$\frac{d}{dx}\left(j_\gamma Y_a - \rho_g D \frac{dY_a}{dx}\right) = 0\,. \tag{A.13}$$

Since $\rho_g(x)$ is a problem, Eq. (A.13) is rewritten using Eqs. (A.5) and (A.6) as

$$\frac{d}{dx}\left(j_\gamma \frac{\rho_a}{\rho_g} X_a - \frac{\rho_a \rho_v}{\rho_g} D \frac{dX_a}{dx}\right) = 0\,. \tag{A.14}$$

[1] This allows to neglect the time derivative.

Integrating Eq. (A.14) twice yields

$$X_a = X_{a,b} \exp\left[\frac{j_\gamma}{\rho_v D}(x - x_b)\right] = X_{a,b} \exp\left[\frac{\lambda_l}{\rho_v D L}\frac{T_w - T_\gamma}{x_\gamma}(x - x_b)\right]. \tag{A.15}$$

Clapeyron's equation allows writing that

$$1 - X_{a,\gamma} = \frac{P_0}{P} \exp\left[\frac{L M_{H_2O}}{R}\left(\frac{1}{T_0} - \frac{1}{T_\gamma}\right)\right]. \tag{A.16}$$

It follows from Eqs. (A.15) and (A.16) that

$$1 - X_{a,b} \exp\left[\frac{\lambda_l}{\rho_v D L}\frac{T_w - T_\gamma}{x_\gamma}(x_\gamma - x_b)\right] = \frac{P_0}{P} \exp\left[\frac{L M_{H_2O}}{R}\left(\frac{1}{T_0} - \frac{1}{T_\gamma}\right)\right]. \tag{A.17}$$

The interface position evolves according to

$$\frac{dx_\gamma}{dt} = -\frac{j_\gamma}{\rho_l} = \frac{\lambda_l}{\rho_l L}\frac{T_\gamma - T_w}{x_\gamma}. \tag{A.18}$$

Eq. (A.18) is solved in the form

$$x_\gamma^{n+1} \approx x_\gamma^n + \frac{\lambda_l}{\rho_l L}\frac{T_\gamma^n - T_w}{x_\gamma^n}\Delta t, \tag{A.19}$$

where T_γ at iteration n (T_γ^n) is obtained from Eq. (A.17).

Table A.1: Physical properties used (analytical solution).

λ_l [W m^{-1} K^{-1}]	ρ_l [kg m^{-3}]	ρ_v [kg m^{-3}]	D [m^2 s^{-1}]	L [J kg^{-1}]	M_{H_2O} [kg mol^{-1}]	R [J mol^{-1} K^{-1}]
0.678	969	0.593	2.86×10^{-5}	2.30×10^6	0.0180	8.31